Carbon dioxide capture from flue gases using dry sorbents

A Jacobs

orcid.org/ 0000-0003-1639-8677

Dissertation submitted in fulfilment of the requirements for the degree *Master of Engineering in Chemical Engineering* at the North West University

Supervisor: Prof RC Everson
Supervisor: Prof JR Bunt
Supervisor: Dr GN Okolo
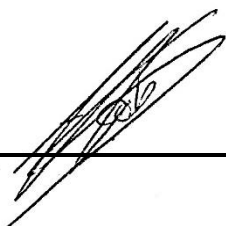
Graduation: Dec 2021
Student number: 25068237

DECLARATION

I, André Jacobs, hereby declare that the dissertation entitled: "*Carbon dioxide capture from flue gases using dry sorbents.*", submitted in the fulfilment of the requirements for the degree of Masters in Chemical Engineering, is my own work except where acknowledged in text, it has been language edited as required and has not been submitted to any other tertiary institution in whole or in part.

I understand that the copies handed in for examination are the property of the North-West University.

Signed at Potchefstroom on the 29th day of March 2021

<table>
<tr><td>A Jacobs (Student)</td><td>25068237
University number</td></tr>
</table>

CONFERENCE PROCEEDINGS

Conference presentations emanating from the investigations conducted in this study include the following.

Jacobs, A., Odendaal, C.J., Everson, R.C., Okolo, G.N. and Bunt, J.R. (2019). Adsorption properties of activated carbon sorbents for carbon capture for development of a dry adsorption process. Presented at the Sixth Eskom Power Plant Engineering Institute Student Workshop Eskom Academy of Learning. 21–22 August 2019, Johannesburg, South Africa. **(Oral presentation)**

Jacobs, A., Odendaal, C.J., Everson, R.C., Okolo, G.N. and Bunt, J.R. (2019). Characterization, adsorption isotherm and adsorption rate modelling of activated carbon sorbents for carbon dioxide capture. Presented at the REPS 2020 Conference. 21–22 September 2020, Potchefstroom, South Africa. **(Oral presentation)**

Jacobs, A., Everson, R.C., and Okolo, G.N. (2019). Carbon dioxide capture from flue gases using dry sorbents. Presented at the Seventh Eskom Power Plant Engineering Institute Student Workshop Eskom Academy of Learning. 12–13 November 2020, Johannesburg, South Africa. **(Oral presentation)**

ACKNOWLEDGEMENTS

The author of this dissertation expresses his appreciation and gratefully acknowledges the following persons:

ABSTRACT

The project entails capturing CO_2 produced from industrial flue gases with dry adsorbents through gas adsorption to mitigate the CO_2 emissions. Four commercially available activated carbon samples (CQ006, CQ30P, CQ650 and PCX1) (available in South Africa, from ChemQuest), derived from coal, coconut fibre and wood, were investigated in this study. The samples were comprehensive characterized using methods such as proximate analysis, ultimate analysis, surface area analysis, pore size distribution and volume analysis, as well as scanning electron microscopy analysis. The CO_2 adsorption isotherms for each activated carbon sample was evaluated at low pressures, ranging from 0 to 114 kPa, at 0, 10, 20, 30, 40 and 55 °C. In efforts to determine the optimal adsorption isotherm model suitable for CO_2 adsorption isotherm modelling on the activated carbon samples, the individual adsorption isotherms were modelled with eight adsorption isotherm models: Langmuir, BET, Dubinin–Radushkevich (D-R), Dubinin–Astakhov (D-A), Toth, Freundlich, Temkin and SIPS. The goodness of fit for each adsorption isotherm model was evaluated with quality of fit and average relative error. D-R presented as the best fitting adsorption isotherm model to describe the experimental adsorption isotherm data of the activated carbon samples. Thermodynamic analysis was conducted on the activated carbon samples to determine the change in enthalpy, entropy, Gibbs free energy and isosteric heat of adsorption. The adsorption rates of the activated carbon samples were evaluated at 40, 55, 70 and 85 °C with inlet CO_2 concentrations of 5, 15 and 25 vol% at a pressure of 1 bar. A fixed bed reactor was designed and built to measure the adsorption rates of the activated carbon adsorbent at each selected temperature and pressure. The individual adsorption rates were modelled with five adsorption rate models: Pseudo first order (P1O), pseudo second order (P2O), Elovich, Avrami and the fractional order adsorption rate models, to find the optimal adsorption rate model suitable for CO_2 adsorption rate modelling on the activated carbon samples. The Avrami adsorption rate model presented as the best fitting adsorption rate model on the experimental adsorption rate data. CQ650 was found to be the most suitable adsorbent for CO_2 adsorption in terms of adsorption capacity and rate. The CQ650 sample is derived from coconut fibres, making it robust and resistant to attrition, which is ideal for the use in a dry carbon capture process.

Key words: carbon capture, CO_2, adsorption, kinetics, thermodynamics, activated carbon

TABLE OF CONTENTS

LIST OF TABLES

LIST OF FIGURES

LIST OF ABBREVIATIONS AND SYMBOLS

Symbol	Description	Unit
A_C	Percentage ash content	%
A_s	Surface area of adsorbent	m^2/g
B	Adsorbent–adsorbate interactions related to heat of adsorption	J/mol
b	Avrami stretching parameter	-
b_T	Related to heat of adsorption ($-\Delta H_{ads}$)	J/mol
B_t	Mathematical function related to q_t/q_e	-
c_F	FOM order constant	-
C	Constant related to heat of adsorption	-
C_{A_i}	Initial CO_2 concentration	%
C_{A_t}	CO_2 concentration at time t	%
$C_{C_{MAX}}$	Maximum CO_2 concentration of the calibration gas	%
$C_{C_{MIN}}$	Minimum CO_2 concentration of the calibration gas	%
$C_{Z_{MAX}}$	Maximum CO_2 concentration read of CO_2 analyser at $C_{C_{MAX}}$	%
$C_{Z_{MIN}}$	Minimum CO_2 concentration read of CO_2 analyser at $C_{C_{MIN}}$	%
$C_{A,b}$	Concentration of CO_2 in bulk phase	%
$C_{A,e}$	Equilibrium CO_2 concentration adsorbed	%
C_{A0}	Initial CO_2 concentration	%
C_D	True steady state CO_2 concentration	%
C_i	Inlet CO_2 concentration	%
C_R	Initial CO_2 concentration measured with the CO_2 analyser	%
C_w	Concentration of water vapour	%
C_X	CO_2 concentration measured with the CO_2 analyser	%
C_Y	Experimental CO_2 concentration	%
d	Particle diameter	m
D_C	Diffusivity of the solid particle	-
D_{DA}	D-A affinity constant	-
D_{DR}	D-R affinity constant	-
d_p	Pore diameter	$Å$
$G°$	Gibbs free energy	kJ/mol
$H°$	Enthalpy	kJ/mol
k_0	Initial adsorption rate constant	$L/s.g$
k_1	Pseudo first order rate constant	$1/s$
k_2	Pseudo second order rate constant	$g.mmol/s$
k_A	Avrami kinetic constant	$1/s$
K	Equilibrium adsorption constant	

K_F	Freundlich equilibrium adsorption constant	$mmol/g.kPa^{1/n}$
k_F	Fractional order adsorption rate constant	
k_i	Intraparticle diffusion rate	$1/s$
K_L	Langmuir equilibrium adsorption constant	$1/kPa$
K_S	SIPS equilibrium adsorption constant	$1/kPa$
K_T	Toth equilibrium constant	$1/kPa$
K_{TEM}	Temkin equilibrium adsorption constant	$1/kPa$
m_{FOM}	FOM order constant	-
M	Moisture content percentage	$\%$
m_1	Mass of empty tray	g
m_2	Mass of tray and sample before drying	g
m_3	Mass of tray and sample after drying	g
M_w	Sorbent mass	g
n_S	SIPS parameter related to surface heterogeneity	-
n_{DA}	D-A heterogeneity parameter	-
n_F	Freundlich heterogeneity parameter	-
n_T	Heterogeneity parameter for Toth model	-
N	Number of experimental data points	-
n_i	Experimental point	-
P_{CO_2}	Pressure of CO_2	kPa
$P_{CO_{2,0}}$	Saturation pressure of CO_2	kPa
q_{CO_2}	CO_2 equilibrium adsorption quantity	$mmol/g$
q_0	Inlet CO_2 quantity	$mmol/g$
q_{BET}	Maximum multilayer adsorption capacity	$mmol/g$
q_{DA}	Maximum adsorption capacity D-A model	$mmol/g$
q_{DR}	Maximum adsorption capacity D-R mode	$mmol/g$
q_e	Adsorption quantity at equilibrium	$mmol/g$
Q_g	Volumetric flow rate of gas through fixed bed	L/s
q_L	Maximum monolayer adsorption capacity of adsorbent	$mmol/g$
q_S	Maximum adsorption capacity SIPS model	$mmol/g$
Q_{st}	Heat of adsorption	kJ/mol
q_T	Maximum adsorption capacity for Toth model	$mmol/g$
q_t	Adsorption quantity at a specific time	$mmol/g$
R	Universal gas constant	$J/mol.K$
r_p	Adsorbent particle radius	m
S	Entropy	kJ/mol
T	Absolute temperature	K
t	Reaction time	s
t_∞	Infinite time	s
V	Volatile matter percentage	$\%$

V_p	Pore volume	cm^3/g
w	Weight of adsorbent	g
x	Modelled data value	-
x_{expt}	Experimental data value	-

Greek letters

α	Initial adsorption rate constant	-
α	Activity of solid reactant	-
β	Desorption rate constant	-
Δ	Change in quantity	-
θ	Fraction of the desorption sites occupied	-
ω_{H_2O}	Moisture content	%

Abbreviations

AC	Activated carbon
AIM	Adsorption isotherm model
ARE	Average relative error
ARM	Adsorption rate model
AUSC	Advanced ultra-supercritical
BET	Brunauer-Emmett-Teller
BPC	Back pressure controller
CCS	Carbon capture and storage
CFB	Circulating fluidized bed
CFBR	Circulating fluidized bed reactor
CO	Carbon monoxide
D-A	Dubinin–Astakhov
DEA	Diethanolamine
DEAT	Department of environmental affairs
D-R	Dubinin–Radushkevich
ESS	Error sum of squares
FBR	Fixed bed reactor
FOM	Fractional order
GC	Gas chromatograph
IEA	International energy agency
IUPAC	International Union of Pure and Applied Chemistry
LEM	Laboratory for Electron Microscopy
LTMS	Long term mitigation scenarios
MEA	Monoethanolamine
MFC	Mass flow controller
MFM	Mass flow meter
MOF	Metal organic framework
NETL	National Energy Technology Laboratory
NWU	North-West University

P1O	Pseudo first order
P2O	Pseudo second order
ppm	Parts per million
PSD	Pore size distribution
QOF	Quality of fit
SE	Secondary electrons
SEM	Scanning electron microscopy
SO_2	Sulphur dioxide
STDV	Standard deviation
XRD	X-ray diffraction

Chapter 1

INTRODUCTION

Chapter 1

(INTRODUCTION)

1.1   BACKGROUND AND RATIONALE

By 2013, the CO_2 concentration had increased from 280 ppm (pre-industrial times) to a reported 400 ppm (Song et al., 2016).

CO_2 emissions from the combustion of fossil fuels is considered to be one of the main contributors to climate change (Balsamo *et al.*, 2013). South Africa has a production rate of about 440 million tons of CO_2 per annum, ranking it as the fourteenth largest CO_2 emitter in the world (Subramoney *et al.*, 2009; Viljoen *et al.*, 2010). Removing CO_2 from the flue gases of coal-fired power stations and other industries forms part of the Long-Term Mitigation Scenarios (LTMS) of the Department of Environmental Affairs, South Africa (DEAT, 2007).

To ensure sufficient mitigation of CO_2 worldwide, and to limit the global temperature increase to between 2 and 3 °C by 2050, a 90% decrease in CO_2 emissions over this period is required. To achieve this enormous undertaking, 3400 large-scale carbon capture and storage (CCS) plants need to be fully functional by 2050 (Barnes, 2015). CCS involves capturing the bulk of the CO_2 produced from industrial processes, then transporting the captured CO_2 to safe geological storage spaces where it cannot escape into the atmosphere (Marsh *et al.*, 2006). Various CCS technologies exist to capture CO_2 from industrial-scale processes (Gibbins & Chalmers, 2008). CO_2 capture can be categorized into two main categories: wet processes such as amine-based absorbers using diglycol amine (DGA) and monoethanolamine (MEA) solutions and dry processes such as circulating fluidized bed reactors (CFBR's) utilizing dry sorbents such as activated carbons and zeolites.

Carbon capture and sequestration can be achieved with capture techniques such as absorption, cryogenic distillation, membrane separation and adsorption. Research and development is more focused on dry processes because dry processes are known to be less expensive than wet processes (Leung *et al.*, 2014). CFBR technology is an example of a dry CO_2 capture process

that offers simultaneous adsorption and desorption of CO_2 with dry sorbents (Abbasi & Arastoopour, 2011). Examples of dry sorbents used in a dry carbon capture processes include the following: activated carbons, potassium carbonates, zeolites, metal organic frameworks and amine-functionalized mesoporous silica (Marsh *et al.*, 2006; Park *et al.*, 2006; Serna-Guerrero & Sayari, 2010).

Adsorption isotherm data is significant for the determination of maximum adsorption capacities and thermodynamic properties and characteristics of adsorbents. Adsorption kinetic rate data are imperative because the residence time required for completion of the CO_2 adsorption process, the adsorption bed size and, consequently, the unit capital costs are significantly influenced by the kinetic rate adsorption considerations (Shafeeyan *et al.*, 2015).

1.2   RESEARCH   PROBLEM,   RESEARCH   PURPOSE   AND   OBJECTIVES

1.2.1   RESEARCH PROBLEM

Setting up a computational fluid dynamics model for a dry carbon capture process requires comprehensive and accurate adsorption rate kinetic data of the adsorbents utilized in the process. The equipment currently available at the research facility (NWU) has shortcomings in terms of measuring the adsorption kinetic rates of gas adsorption onto a solid adsorbent. A more suitable experimental setup is therefore required to quantify the adsorption kinetic rates of gas adsorption onto a solid adsorbent.

1.2.2   RESEARCH PURPOSE

The aims of this project were to quantify the adsorption properties, analyse the CO_2 adsorption isotherms and kinetic rates as well as thermodynamic properties of commercially available activated carbons for the capture of CO_2 from simulated flue gases, suitable for advanced process modelling for the design of a dry industrial-scale carbon capture process, as well as to determine optimal operating conditions with respect to pressure and temperature in such a dry carbon capture process.

CHAPTER 1: GENERAL INTRODUCTION

1.2.3 RESEARCH OBJECTIVES

In order to achieve the overall aims, the following specific objectives will be addressed.

- ➢ Determine the relevant physical/chemical properties of selected dry activated carbon samples relevant for CO_2 capture evaluation (CQ006, CQ30P, CQ650 and PCX1).
- ➢ Determine the adsorption capacities of the dry activated carbon samples with adsorption isotherms—this involves experimentation and modelling.
- ➢ Build a fixed bed reactor to estimate the fractional adsorption kinetics of the activated carbon samples—this involves experimentation and adsorption rate modelling.
- ➢ Rank the studied activated carbon samples in terms of suitability for CO_2 capture in terms of performance: adsorption capacity and kinetic rate.

1.2.4 LAYOUT OF DOCUMENT

The scope of this investigation includes conducting adsorption isotherm experiments on the activated carbon samples to determine the maximum adsorption capacity, as well as adsorption kinetic rate experiments in a fixed bed reactor (FBR) to obtain the fractional adsorption kinetic rate of CO_2 onto the activated carbon samples. The outlay of this dissertation is as follows.

Literature study

In order to achieve the research aims and objectives set out and discussed in Chapter 1, a thorough literature search was conducted on the status of carbon capture, carbon capture processes, carbon capture technologies, adsorbents suitable for carbon capture, and adsorption isotherm models and adsorption kinetic rate models suitable for modelling the experimental adsorption isotherms and kinetic rates of CO_2 adsorption onto dry adsorbents, respectively.

Experimental and methodology

This chapter introduces and explains the materials and methods used to complete the experimental work. The experimental methodology followed to obtain the characterization results, adsorption isotherms and adsorption kinetic rate results, as well as the methods used to

solve the adsorption isotherm models, adsorption kinetic rate models and thermodynamic parameters are discussed in this section. The design and construction of the FBR as well as the experimental procedure followed to obtain the experimental kinetic rates of CO_2 adsorption onto the activated carbon samples are described.

Characterization, adsorption isotherm modelling and thermodynamic property evaluation

The experimental results of adsorbent characterization, adsorption isotherm modelling and thermodynamic evaluation are presented and discussed. Characterization of the four activated carbon samples included proximate analysis, ultimate analysis, surface area analysis, pore size distribution analysis, pore volume analysis, porosity analysis and scanning electron microscopy analysis. Eight adsorption isotherm models were applied to the experimental adsorption isotherm results of the activated carbon samples: Langmuir, BET, Dubinin–Radushkevich, Dubinin–Astakhov, Toth, Freundlich, Temkin and SIPS. The thermodynamic properties investigated are Gibbs free energy, enthalpy, entropy and isosteric heat of adsorption.

Adsorption kinetic rate modelling

The experimental adsorption rate results of the activated carbon samples (CQ006, CQ30P, CQ650 and PCX1), obtained from the experimental FBR setup, are modelled with the five adsorption kinetic rate models (pseudo first order, pseudo second order, Elovich, Avrami and fractional order) and discussed. The best fitting adsorption kinetic rate model will be determined and used to model the experimental kinetic rate results of CO_2 adsorption onto the activated carbon adsorbents. Diffusion from the bulk gas into the adsorbent's micropores will be investigated to determine the rate limiting diffusion step. The activation energies of CO_2 adsorption onto the activated carbon samples will be determined with the adsorption kinetic rate constants determined from fitting the adsorption kinetic rate models to the experimental adsorption kinetic rates of CO_2 adsorption onto the adsorbents. The results and findings of this chapter will be compared with literature report to ascertain how the activated carbon samples measure up to the activated carbon samples reported in literature.

Conclusions and recommendations

CHAPTER 1: GENERAL INTRODUCTION

The conclusions, recommendations and contribution to existing knowledge and the field of science is addressed in this section.

Chapter 2

(LITERATURE REVIEW)

Chapter 2

(LITERATURE REVIEW)

A thorough literature investigation was conducted on the status of carbon capture, carbon capture processes, carbon capture technologies, adsorbents suitable for carbon capture, adsorption isotherm models and adsorption kinetic rate models suitable for modelling the experimental adsorption isotherms and kinetic rates of CO_2 adsorption onto dry adsorbents. These topics are addressed in this chapter.

2.1   INDUSTRIAL EMISSIONS IN SOUTH AFRICA

The greenhouse gas (GHG) system surrounding Earth acts as a global insulator to ensure and maintain habitable surface temperatures for all life on Earth. The GHG system consists mainly of GHGs such as CO_2, N_2O, CH_4 and fluorine, of which CO_2 plays a significant role (Feig *et al.*, 2017). Increasing the amount of GHGs leads to an increase in global surface temperatures; ocean warming, with a reduction in pH; and loss of ice mass over the cryosphere, resulting in increasing sea levels and abnormal seasonal changes (Kweku *et al.*, 2017).

An increase in GHG emissions has been recorded over the period 1990–2016; see Figure 2-1 (Ge & Friedrich, 2020). South Africa produces the seventh largest amount of coal in the world—coal is therefore a significant economic booster, and it is used as the main source of power generation in the country (McSweeney & Timperley, 2018). South Africa operates a fleet of 18 coal-fired power stations, contributing approximately 88% of all the power consumed in South Africa (US-Embassy, 2017). This is complemented by nuclear energy, hydroelectric power, pumped storage schemes, and renewable energies such as solar and wind energy. Thermal power sources will probably remain the main source of energy generation in South Africa, therefore mitigation strategies for CO_2 are required in efforts to ensure continuous sustainable utilization of thermal energy in the country (Metz *et al.*, 2005).

South Africa currently presents as the fourteenth largest GHG emitter in the world. In the years 1990–2018, there has been increases of 89%, 75%, 74% and 73% in building emissions, transportation services, industrial combustion processes and power generation industries, respectively. In 2016, approximately 70% of all the CO_2 produced and emitted in South Africa was attributed to power generation from coal-fired plants. In 2017, a staggering 210 MT of CO_2 was emitted into the atmosphere from the power generation sector. In 2018, South Africa emitted approximately 477 MT of CO_2, of which >50% was attributed to the power- and heat generation sector (dependant on the combustion of coal) (Crippa *et al.*, 2019; McSweeney & Timperley, 2018).
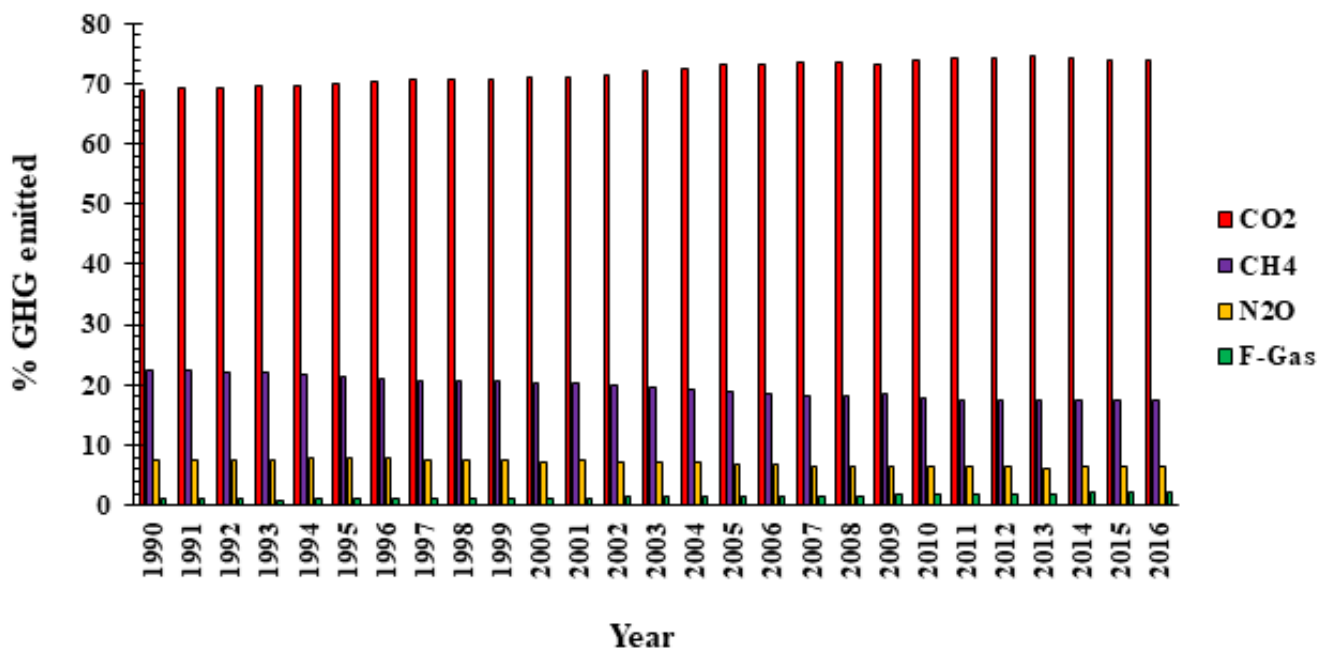
Figure 2-1: Global GHG (CO_2, CH_4, N_2O and fluorine gases) emissions recorded from 1990 to 2016, adapted from (Ge & Friedrich, 2020).

The combustion of fossil fuels for energy, which forms the dominant part of South Africa's power grid, is a major source of CO_2 (Ammendola *et al.*, 2017). The amount of CO_2 produced by a coal-fired plant is greatly dependant on the type of coal-fired plant used. Coal-fired plants can be categorized as follows: subcritical, supercritical, ultra-supercritical and advanced ultra-supercritical (Barnes, 2015). The main difference between the types of coal-fired plant is the operating steam temperature and pressure applied. Table 2-1 distinguishes between the different pressures and temperatures utilized in these two types of coal-fired plants.

Table 2-1: Subcritical, supercritical and ultra-supercritical temperature and pressure (Barnes, 2015).

	Subcritical	Supercritical	Ultra-supercritical
Main steam pressure, MPa	<22.1	22-25	>25
Main steam temperature, °C	Up to 565	540-580	>580
Reheat steam temperature, °C	Up to 565	540-580	>580
Efficiency %	33-39	38-42	>42

Upgrading a subcritical coal-fired plant to a supercritical coal-fired plant can increase the plant efficiency by 4–6% (Barnes, 2015). Subcritical coal-fired plants consume more coal than supercritical and ultra-supercritical coal-fired plants to produce one unit of electricity. Increased consumption of coal means an increased production of CO_2; therefore, the upgrading of existing coal-fired power plants is beneficial to power production from coal and it addresses climate change mitigation (Barnes, 2015).

International Energy Agency (IEA) studies of 2012 concluded that younger and more efficient coal-fired plants are more economically suitable to be retrofitted with carbon capture and storage (CCS) units (Barnes, 2015). It was also found that only 29% of the current operating coal-fired plants, worldwide, are suitable to be retrofitted with such CCS units (Barnes, 2015). Furthermore, ultra-supercritical coal-fired plants are more reliable and have a longer life expectancy than supercritical and subcritical coal-fired plants. The development of state-of-the-art advanced ultra-supercritical (AUSC) coal-fired plants will provide plants operating at steam temperatures between 700 and 760 *°C* and with steam cycle efficiencies of up to 50%. AUSC coal-fired plants will produce 28% less CO_2 than subcritical coal-fired plants and 10% less CO_2 than ultra-supercritical coal-fired plants.

To address the pressing climate change concerns, new high-efficiency, low-emission (Coninck & Benson, 2014) coal-fired plants should be constructed with CCS units, and current subcritical coal-fired plants should be upgraded to supercritical and ultra-supercritical coal-fired plants and retrofitted with CCS units (Barnes, 2015).

CHAPTER 2: LITERATURE REVIEW

2.2   CARBON CAPTURE TECHNOLOGIES AND PROCESSES

Capturing carbon can be accomplished by three main approaches, depending on how/when the capture is performed: pre-combustion, post-combustion and oxyfuel combustion. Separating CO_2 from the flue gas can be accomplished by separation technologies such as adsorption, absorption, membrane separation and cryogenic distillation. A detailed discussion of the carbon capture processes and technologies now follows.

2.2.1   CARBON CAPTURE TECHNOLOGIES

The current carbon capture technologies are pre-combustion capture, post-combustion capture and oxyfuel combustion.

2.2.1.1   PRE-COMBUSTION CAPTURE

Pre-combustion capture of CO_2 requires a specific process known as gasification of coal, prior to combustion. In this process, the coal is sent through a gasification process with a deficient oxygen atmosphere to produce mainly CO and H_2, as represented in Equation 2.1. The gas produced will undergo a water–gas shift reaction with steam to convert CO to CO_2 and to increase the concentration of H_2 in the syngas (Kumar *et al.*, 2015; Leung *et al.*, 2014). The chemical reaction is described by Equations 2-2 and 2-3.

$$Coal \xrightarrow{Gasification} CO + H_2 \tag{2-1}$$

$$CO + H_2O \xrightarrow{Water-gas\,shift} H_2 + CO_2 \tag{2-2}$$

$$CH_4 + H_2O \xrightarrow{Reform} CO + H_2 \tag{2-3}$$
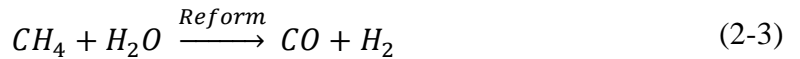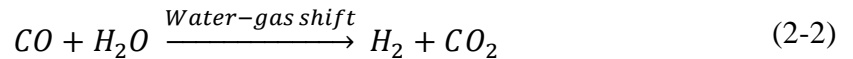
This gasification process produces a high CO_2 concentration (>20%) in the syngas before combustion. Utilizing a CCS plant (before combustion of the syngas) will significantly decrease the amount of CO_2 entering the combustion unit, resulting in a decreased quantity of CO_2 produced by this process (Leung *et al.*, 2014).

Natural gas undergoes a steam reformation process to produce CO and H_2, followed by a water–gas shift reaction to produce more H_2 and convert CO to CO_2. Therefore, natural gas power stations can also benefit from CCS, to decrease CO_2 pollution and avoid the tax associated with CO_2 production (Kumar *et al.*, 2015; Leung *et al.*, 2014). A CO_2 capture efficiency of 80% has been obtained from advanced combined cycle gas turbine plants fitted with pre-combustion CO_2 capturing units (Hoffmann *et al.*, 2008). A schematic of a CO_2 pre-combustion system is shown in Figure 2-2.
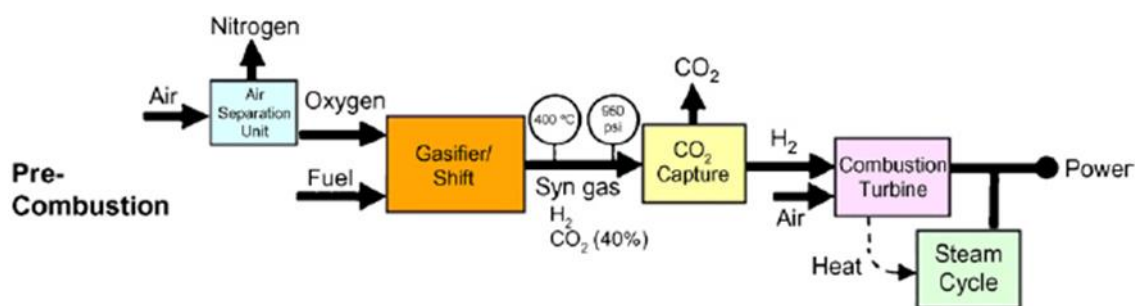
Figure 2-2: Pre-combustion CO_2 capturing process (Figueroa et al., 2008).

2.2.1.2 POST-COMBUSTION CAPTURE

Post-combustion capture consists of a CO_2 capturing unit after the boiler, without inherently changing the process in which it is used (Coninck & Benson, 2014). Post-combustion CO_2 capturing units offers the preferred technology for retrofitting existing power plants with CO_2 capturing units. Extensive amounts of energy is required to capture and produce a >95.5% CO_2 purity stream from a low concentration flue gas containing 7-14% CO_2 (Leung *et al.*, 2014) (where >95.5% is the purity required for economically feasible compression, transport and storage). An analysis of the cost of electricity production was done by the U.S. National Energy Technology Laboratory (NETL)—they estimated a cost increase of 32% and 65% for combustion in gas-fired and coal-fired power plants fitted with post-combustion CO_2 capturing units, respectively (Kanniche *et al.*, 2010).

Flue gas contains low CO_2 concentrations (<15%) close to atmospheric pressure which requires large amounts of energy to capture the CO_2 from the flue gas. At these conditions, the thermodynamic driving force for CO_2 capture from flue gas is low, with the partial pressure of CO_2 usually <0.15 atm (Figueroa *et al.*, 2008). This property of flue gas increases the difficulty of developing a cost-effective advanced capturing system to be applied to existing coal-fired

power stations and development of future coal-fired power stations and to, which generate two thirds of the CO_2 emissions in the power sector (Figueroa *et al.*, 2008). A schematic of a CO_2 post-combustion system is shown in Figure 2-3.
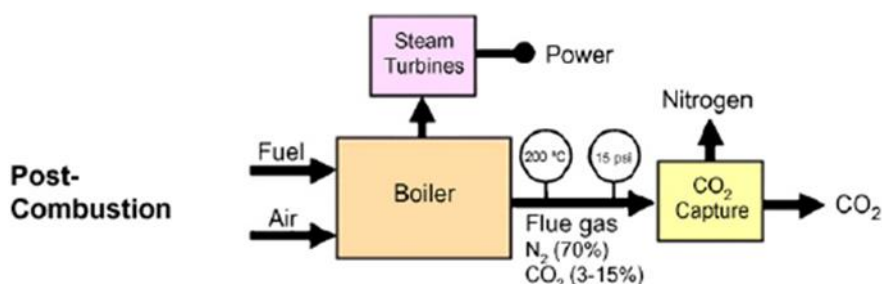
Figure 2-3: Post-combustion CO_2 capturing process setup (Figueroa *et al.,* 2008).

2.2.1.3   OXYFUEL COMBUSTION

Oxyfuel combustion is carried out in the absence of nitrogen, meaning that combustion is carried out in a pure oxygen atmosphere. The absence of nitrogen in the flue gas stream eases the sequestration of CO_2 from the flue gas mixture and also has the advantage of reduced formation of thermal NO_x gases. The flue gas of an oxyfuel combustion unit consists mainly of CO_2, water, SO_2 and particulates. Electrostatic precipitators and desulfurization methods can be utilized to remove the particulates and SO_2, respectively. After treating the flue gas for particulates and SO_2, the remaining flue gas consists mainly of CO_2 (>80%), depending on the fuel used for combustion and the water content (Leung *et al.*, 2014). The purity of the CO_2 in the flue gas can, inexpensively, be increased to required standards (>95.5%) for transport and storage. Oxyfuel combustion produces less flue gas during the combustion process than either the pre- or post-combustion processes (Kanniche *et al.*, 2010). The higher CO_2 concentration attributed to the smaller volume of flue gas produced contributes to the economic aspects of capturing CO_2 from the flue gas (Kanniche *et al.*, 2010).

Currently available materials of construction are unsuitable for high temperatures, due to the very high combustion temperatures reached from coal combustion in the presence of pure oxygen. Therefore, prior to combustion, the oxygen is mixed with recycled flue gas produced from the process, or in the boiler during combustion, to ensure reasonable operating conditions (Figueroa *et al.*, 2008). The air separation unit, required for the vital demand of O_2 in combustion, together with the recycled flue gas for bearable combustion conditions in the

boiler, reduces the economic attractiveness of this combustion configuration. A basic schematic of a CO_2 oxy-combustion system is shown in Figure 2-4.
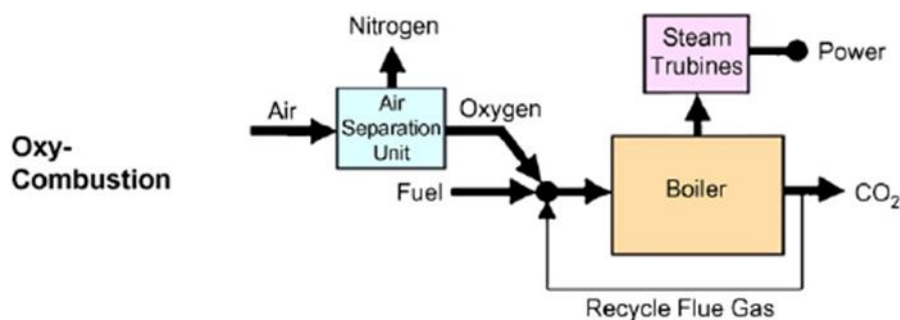
Figure 2-4: Oxyfuel combustion CO_2 capturing process setup (Figueroa *et al.,* 2008).

2.2.2 CARBON CAPTURE TECHNIQUES

Carbon capture and sequestration can be achieved with separation techniques such as absorption, cryogenic distillation, membrane separation and adsorption. These separation techniques are discussed in this section.

2.2.2.1 ABSORPTION

The separation of CO_2 from an industrial flue gas can be accomplished by dissolving the CO_2 in a liquid-phase sorbent. The sorbent is regenerated after each cycle, either with a temperature or pressure swing (Leung *et al.*, 2014). Typical sorbents used to accomplish successful separation of CO_2 from flue gases include monoethanolamine (MEA), diethanolamine (DEA) and potassium carbonate. MEA was found to be the most efficient aqueous sorbent, with an absorption efficiency >90% (Veawab *et al.*, 2002).

Piperazine is presented as a sorbent that reacts faster than MEA, but with an increased volatility factor; it is more costly than MEA in the application to CO_2 capture, and still under development (Ben-Mansour *et al.*, 2016; Leung *et al.*, 2014). An illustration of CO_2 absorption is given in Figure 2-5.
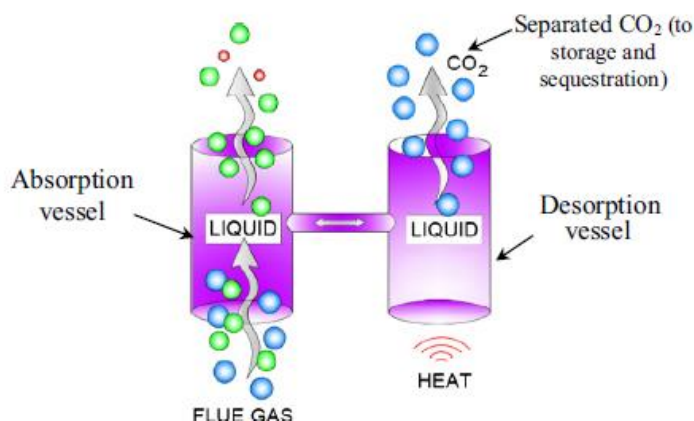
Figure 2-5: Illustration of CO_2 separation accomplished with absorption ((Ben-Mansour *et al.*, 2016).

2.2.2.2   MEMBRANE SEPARATION

Membrane technology is an attractive option because it does not require a separating agent (solvent or adsorbent) or involve any phase changes (Kargari & Ravanchi, 2012). Furthermore, there are no costs associated with regeneration of the material and low maintenance is required (Kargari & Ravanchi, 2012). The compact and lightweight properties of membranes enables their horizontal and vertical positioning (Kargari & Ravanchi, 2012). Membrane technology can easily be applied to the separation of CO_2 from flue gas because of CO_2's inherent permeation properties (Ebner & Ritter, 2009). Membranes such as glassy and rubbery polymers, molecular sieves and various inorganic materials are excellent for application in CO_2 separation because of the rapid diffusion of CO_2 across them (Ebner & Ritter, 2009). CO_2 has a large quadruple moment, enabling fast adsorption or dissolution over these membrane materials (Kargari & Ravanchi, 2012). Such properties enable increased permeation rates and selectivity towards CO_2, making membrane technology a very useful option for the separation of CO_2 from flue gas. A separation efficiency of 82–88% has been achieved in the development of highly efficient membranes made from ceramic and metallic substances by (Audus, 2000; Gielen, 2003). Low pressure and the CO_2 concentration in industrial flue gases have a significant impact on membrane separation efficiency. Significant developments in gas separation are still required, however, before suitable application of membranes to industrial-scale CO_2 separation units can is realized (Leung *et al.*, 2014). A visual illustration of CO_2 separation accomplished with membrane technology is given in Figure 2-6.
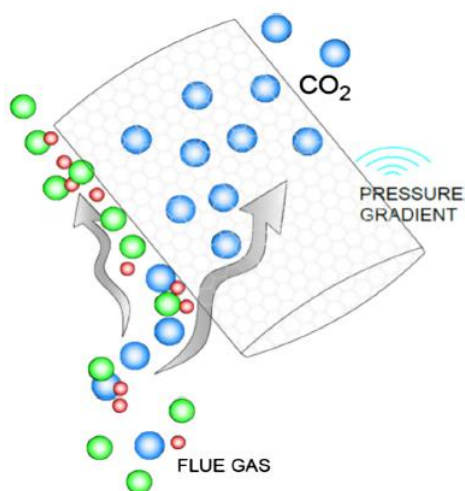
Figure 2-6: A visual illustration of CO_2 separation in a membrane, obtained from (Ben-Mansour *et al.*, 2016).

2.2.2.3   CRYOGENIC DISTILLATION

Cryogenic distillation entails the separation of gases using extremely low temperatures and high pressures. The difference in the boiling point of different constituents in the flue gas enables the successful separation of CO_2 from other gases present (Leung *et al.*, 2014). The flue gas is cooled down to desublimation temperatures (-100 to -135 °C), where CO_2 solidifies, and is then compressed at high pressures of 100–200 atm (Leung *et al.*, 2014). The separation efficiency can reach an astonishing 90–95%, with the added advantage of production of very pure CO_2 liquid, ready for transport (Kargari & Ravanchi, 2012; Leung *et al.*, 2014).

The downside of using cryogenic distillation is the high energy requirement per ton of CO_2 (~600–660 kWh) (Leung *et al.*, 2014). The amount of water and heavy hydrocarbons, which also freeze at the temperatures involved, tend to block the heat exchangers, leading to the requirement for frequent maintenance (Kargari & Ravanchi, 2012). The technology is limited to gas streams containing >50 vol% CO_2 and preferably >90 vol% for economical application and therefore, not applicable on flue gases from gas-fired and coal-fired power plants (Kargari & Ravanchi, 2012). An illustration of cryogenic distillation applied to CO_2 separation is given in Figure 2-7.
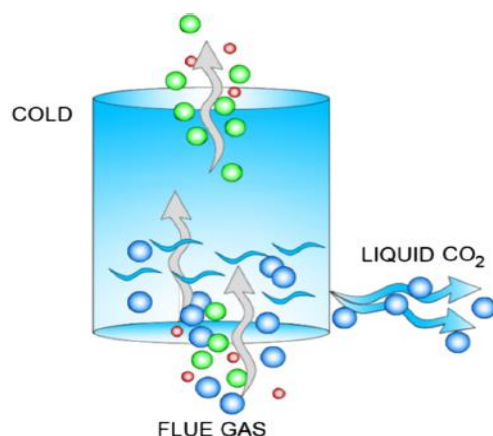
Figure 2-7: Illustration of CO_2 separation utilizing cryogenic distillation, obtained from (Ben-Mansour *et al.*, 2016)

2.2.2.4   ADSORPTION

Adsorption can be defined as the 'sticking' of gas and liquid molecules to the surface of a solid material. This surface phenomenon can occur at any temperature and pressure. The gas molecules to be adsorbed can vary considerably, due to the size, structure and electric properties of the gases. The surface of the sorbents also presents different types of sites, resulting in complex interactions between the gas and the surface of the solids. Dynamic equilibria are reached when the number of molecules adsorbed matches the number of desorbed molecules and, if the flows to and from the surface are not equal, either adsorption or desorption will take place. The type of adsorption can be categorized by the strength (interaction energy between the adsorbate and adsorbent), depending on the way in which the adsorbed molecules are bound to the sorbents' surface (Keller & Staudt, 2005).

2.2.3   WET, DRY AND SEMI-DRY CO_2 CAPTURE PROCESSES

CO_2 capture processes can be classified as wet, dry or semi-dry process. Advantages and disadvantages of each of these processes are now discussed.

2.2.3.1   WET CARBON CAPTURE PROCESSES

Wet CO_2 absorption processes make use of aqueous solvents such as MEA, DEA, sodium carbonate solutions and potassium carbonate solutions. MEA has been found to be the most

efficient aqueous sorbent, with an absorption efficiency >90% (Czerw *et al.*, 2017; Goel *et al.*, 2011; Leung *et al.*, 2014; Silva *et al.*, 2013; Veawab *et al.*, 2002). Utilization of an absorption unit consuming amine solvents presents important challenges, including the following:

➢ Potential amine degradation, resulting in solvent loss.

➢ Equipment corrosion leading to regular shut-downs and maintenance.

➢ Generation of atmospheric pollutants due to degradation of volatile compounds.

➢ Health and environmental issues arising from amine degradation.

➢ Substantial amounts of energy required for the regeneration of the solvent after each CO_2 adsorption cycle.

2.2.3.2 DRY AND SEMI-DRY CARBON CAPTURING PROCESSES

Capturing CO_2 with dry solid adsorbents is industrially preferred because of its low capital cost, low operational costs, easy retrofitting to existing industrial processes, low energy requirements and secondary waste generation (Coninck & Benson, 2014; Leung *et al.*, 2014). South Africa is a water-scarce country, therefore, a dry process presents as an ideal solution for carbon capture in South Africa. Examples of adsorbents used in dry and semi-dry CO_2 capture processes are presented in Table 2-2.

Table 2-2: Adsorbents used for CO_2 adsorption in dry and semi-dry carbon capturing processes (Dantas *et al.*, 2011; Hauchhum & Mahanta, 2014a; Singh *et al.*, 2019; Singh & Kumar, 2016).

Dry process adsorbents	Semi-dry adsorbents
Molecular sieves	Metal oxides
Activated carbon	Alkali carbonates
Zeolites	
Magnetite	
Metal organic frameworks	
Amine-modified silica	

2.2.3.3 COMPARING WET, DRY AND SEMI-DRY CARBON CAPTURING PROCESSES

An example of a wet carbon capturing process, is a CO_2 absorber utilizing MEA as solvent. Both dry and semi-dry carbon capture can be accomplished in a circulating fluidized bed reactor (CFBR). The advantages and disadvantages of the wet, dry and semi-dry carbon capturing processes are indicated in Table 2-3. It is evident that a dry or semi-dry carbon capturing process utilizing a CFBR is superior to a wet carbon capturing process, particularly when evaluating parameters such as capital cost, operational cost, water consumption, adsorbent/solvent regeneration, carbon capture operation footprint and energy consumption.

Table 2-3: The advantages and disadvantages of wet, dry and semi-dry carbon capturing processes (Abd *et al.*, 2020; Coninck & Benson, 2014; Jafari *et al.*, 2020; Leung *et al.*, 2014; Song *et al.*, 2016; Yates & Lettieri, 2016; Zanco *et al.*, 2018; Zhang *et al.*, 2017).

Characteristic	Wet process(absorption)	Dry, semi-dry process
Capital cost	🟥	🟩
Operational cost	🟥	🟩
CO_2 capture to meet low permit limits	🟩	🟩
Low water consumption	🟥	🟩
Compact system footprint	🟥	🟩
Minimum maintenance	🟥	🟩
Adsorbent/solvent regeneration efficiency	🟥	🟩

Green – Advantage, Red - Disadvantage

2.3 CIRCULATING FLUIDIZED BED REACTOR PROCESS SUITABLE FOR CARBON CAPTURE

Circulating fluidized bed (CFB) technology originates from its use in coal combustion, where it was initially used for its ability to handle low-quality coals containing large amounts of sulphur. CFBR's have been frequently employed in a wide variety of industrial processes over the past century (Zanco *et al.*, 2018). To capture CO_2 from the emissions generated from a coal-fired plant, a CFBR can be implemented as a post-combustion carbon capturing process. This implementation simplifies the industrial application because it can easily be retrofitted to existing coal-fired plants. It has been experimentally confirmed that an adsorption-based post-

combustion capturing step performed in a CFB, offers a promising solution (Choi *et al.*, 2020). CFBRs offer certain advantages over fixed bed reactors (FBRs). Examples include the following:

➢ Continuously and simultaneously capturing CO_2 and regenerating the adsorbent (Choi *et al.*, 2020)

➢ Increased interaction and contact time between the adsorbent and gas for increased carbon capture (Jafari *et al.*, 2020)

➢ Increased amounts of gas can be processed due to more efficient gas–solid interactions (Grace and Bi, 1997)

➢ Isothermal conditions along the reactor bed length can be more easily achieved due to the CFBR's design (Zhang *et al.*, 2017)

➢ Decreased pressure drops along the CFBR bed are achieved with an optimal gas velocity to bed height ratio (Yates & Lettieri, 2016)

➢ Increased mass and heat transfer rates (Zanco *et al.*, 2018).

A simple schematic of a CBFR is shown in Figure 2-8. The flue gas emitted from a combustion process enters at the bottom of the rizer section. The flue gas fluidizes the adsorbent particles present in the riser section. CO_2 adsorbs onto the adsorbent in this section as the adsorbent is forced to the regeneration section of the CFBR. The excess gas, consisting primarily of N_2 and O_2, is separated from the saturated adsorbent with a mesh. The saturated adsorbents pass through a cyclone process to separate spent adsorbent particles from reusable adsorption particles, and enter the regenerator. To liberate the CO_2 from the adsorbent, the adsorbent is heated to a predetermined temperature for optimal desorption. The CO_2 is extracted from the adsorbent particles and ready for storage or utilization. The adsorbents circulate back to the riser section through a loop seal, where fresh adsorbents are added to maintain carbon capturing efficiency. This process is repeated continuously (Benjaprakairat *et al.*, 2020).
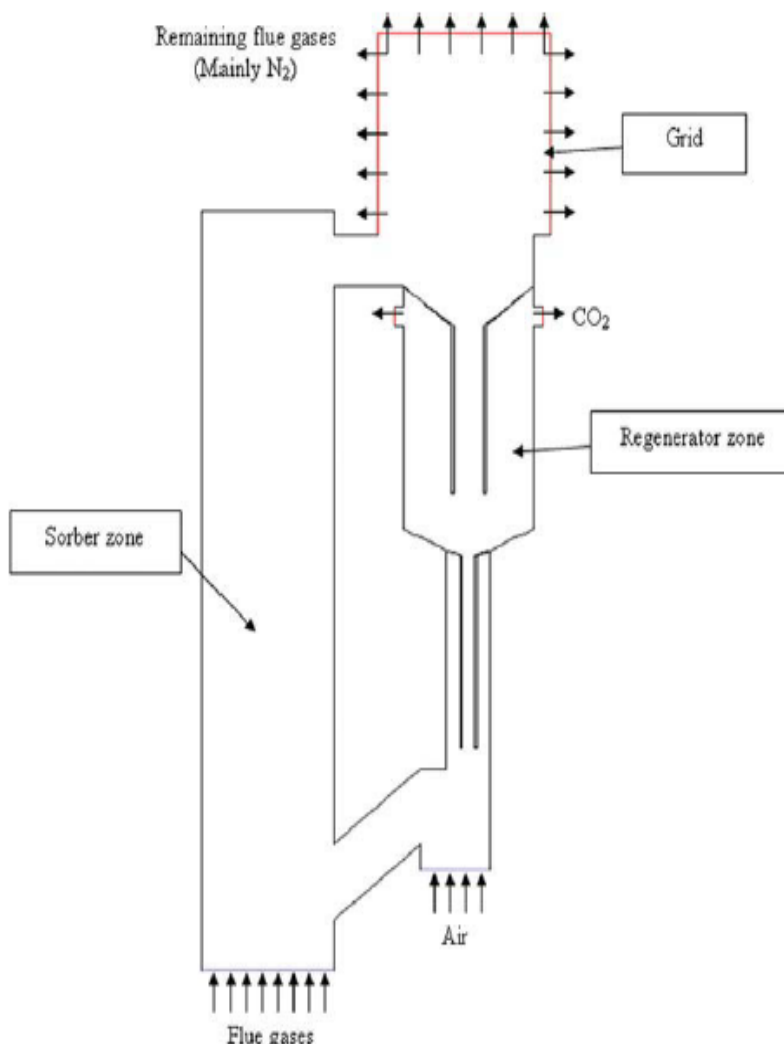
Figure 2-8: Schematic of a CFB reactor for capturing CO_2 with dry sorbents
(Chalermsinsuwan et al., 2010).

2.4 ADSORBENTS SUITABLE FOR CARBON CAPTURE

To successfully separate CO_2 from a flue gas in a circulating fluidized bed reactor, a suitable and efficient adsorbent is required. There are various suitable adsorbents available, each with their own adsorption properties and capabilities. Thus, investigating the adsorption capacity, adsorption kinetics, structural surface properties and characteristics of these available adsorbents should yield more accurate design specifications towards the development of a circulating fluidized bed reactor.

CHAPTER 2: LITERATURE REVIEW

2.4.1 INTRODUCTION TO ADSORBENTS

Large single-point CO_2 producing processes are primarily targeted for carbon capture (Ruthven, 2006). Current industrial-scale processes for carbon capture exist only in the form of liquid-based scrubbing systems. Further development of dry carbon capture processes, such as the use of re-generable adsorbents in a CFBR, offers as a less costly operation.

2.4.1.1 IMPORTANT PROPERTIES OF ADSORBENTS FOR CO_2 CAPTURE

Comprehensive knowledge about the adsorbent's adsorption capacity and adsorption kinetic behaviour is mandatory to ensure an efficient carbon capture system design. Knowledge of the adsorbent's structural surface properties (surface area, pore volume, micropore volume and pore type) will aid in the search for a sorbent suitable for the carbon capture process. To facilitate adequate CO_2 adsorption, the pore size distribution of an adsorbent should accommodate CO_2 without extreme diffusion inhibiting the adsorption rate. Towards an economically feasible design, in order to be deemed suitable in a continuous carbon capture system, the adsorbent should exhibit excellent regenerative characteristics, be selective towards CO_2 and abrasion resistant.

2.4.1.2 PHYSICAL SURFACE ADSORPTION

There are two main categories of adsorption: physical adsorption (physisorption) and chemical adsorption (chemisorption). Electrostatic forces exist in all matter and can be seen as a field in which a molecule experiences a force. Dispersion–repulsion forces, otherwise referred to as van der Waals forces, form the basis upon which a molecule attaches to a porous sorbent in physisorption. Further contributions of electrostatic forces, such as polarization, field dipole and field gradient-quadrupole forces, can increase the strength of the attachment between the molecule and the porous sorbent. The maximum adsorption capacity of a porous sorbent for physisorption is directly related to surface structural properties of the porous sorbent, such as the specific micropore volume, surface area, micropore surface area and porosity (Ruthven, 2006). Absolute physisorption yields a change in magnitude of the enthalpy (ΔH^0) of <20 kJ/mol (Zhou *et al.*, 2012). Physisorption onto porous solid adsorbents is industrially applied in processes such as water treatment, adsorption-based cooling systems, gas purification and

storage, and separation of gases (Singh & Kumar, 2016). A representation of the physisorption adsorption mechanism is given in Figure 2-9.
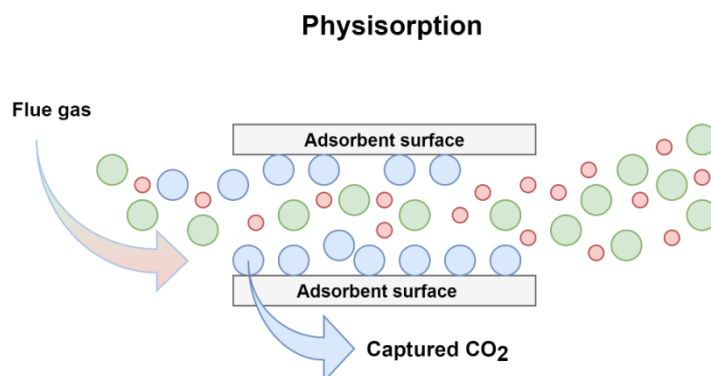
Figure 2-9: An illustration of the physisorption adsorption mechanism, obtained from (Ben-Mansour *et al.*, 2016).

2.4.1.3   CHEMICAL SURFACE ADSORPTION

Chemisorption entails a chemical reaction occurring between the adsorbate and adsorbent which makes the adsorption strength of the adsorbate to the adsorbent inherently stronger, compared to physisorption. When chemisorption takes place, substantial electron transfer or electron sharing occurs, resulting in higher adsorption energies experienced for chemisorption than for physisorption, slower adsorption times and, in some cases, an irreversible adsorption reaction.

Chemisorption is highly specific, meaning that a certain adsorbent can only remove a certain impurity; for example, K_2CO_3 will be used to remove CO_2 in the presence of water (Ruthven, 2006; Zhou *et al.*, 2012). The change magnitude in enthalpy for chemisorption is 80–200 kJ/mol, which is significantly higher than the change magnitude in enthalpy observed for physisorption (Zhou *et al.*, 2012). A visual illustration of the chemisorption adsorption mechanism is given in Figure 2-10.
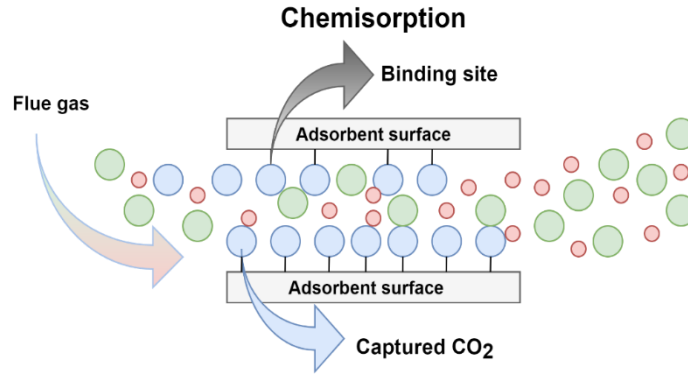
Figure 2-10: A visual illustration of the chemisorption adsorption mechanism, obtained from (Ben-Mansour *et al.*, 2016)

2.4.2 CLASSIFICATION OF ADSORBENTS

This section will discuss all possible sorbents available for the capture of CO_2 from flue gases, in both dry and semi-dry processes. Semi-dry processes require an adsorbent and water to adsorb CO_2 from a flue gas. This type of adsorption is defined as chemical adsorption, or chemisorption, which indicates a chemical reaction taking place between the adsorbent, water and CO_2, to then adsorb the CO_2 onto the adsorbent.

2.4.2.1 SODIUM CARBONATE (ALKALI CARBONATE)

Sodium bicarbonate ($NaHCO_3$) has been used to capture hydrogen chloride (HCl) and SO_2 from dilute flue gases, but it has not been used for CO_2 (Green *et al.*, 2004). Sodium bicarbonate presents as semi-dry sorbent for the capture of CO_2; its carbonation and decarbonation reaction are given in Equations 2-4 and 2-5.

$$Na_2CO_3(s) + CO_2(g) + H_2O(g) \rightarrow 2NaHCO_3(s) \qquad (2\text{-}4)$$

$$2NaHCO_3(s) \rightarrow Na_2CO_3(s) + CO_2(g) + H_2O(g) \qquad (2\text{-}5)$$
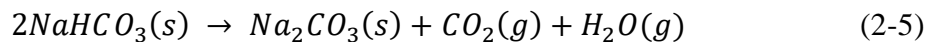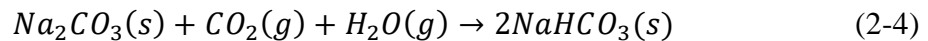
The adsorption of CO_2 from a flue gas follows as in Equation 2-4, with the subsequent regeneration step given in Equation 2-5. Regeneration of the adsorbent is accomplished by heating of the adsorbent after the adsorption of CO_2 has taken place, followed by liberation of the CO_2 from the adsorbent, to produce a concentrated stream of CO_2, which can then be utilized or sequestrated (Green *et al.*, 2004).

The adsorption of HCl and SO_2 also takes place and follows the reaction equations given in Equations 2-6 and 2-7 (Green *et al.*, 2004).

$$Na_2CO_3(s) + 2HCl(g) \rightarrow 2NaCl(s) + CO_2(g) + H_2O(g) \qquad (2\text{-}6)$$

$$Na_2CO_3(s) + SO_2(g) + \frac{1}{2}O_2 \rightarrow Na_2SO_4(s) + CO_2(g) \qquad (2\text{-}7)$$
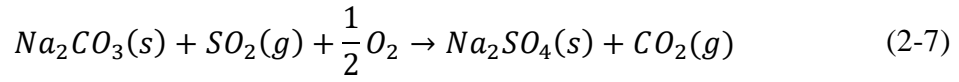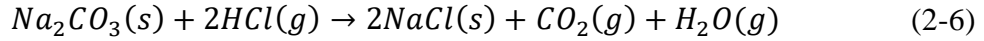
Sodium bicarbonate is an expensive adsorbent, if only used once; it is therefore generally not accepted in the utility industry as a viable sequestration technique (Green *et al.*, 2004). This could change, however, if the process in which the adsorbent is used can provide for the regeneration and reuse of the adsorbent, continuously (Green *et al.*, 2004).

2.4.2.2 MAGNESIUM OXIDE (METAL OXIDE)

Magnesium oxide (MgO) has the ability to adsorb CO_2 at temperatures <200 °C and can be regenerated at a low temperature of 550 °C. The water vapour present in flue gases will not inhibit CO_2 adsorption, as the case may be for adsorbents such as activated carbons, zeolites, metal organic frameworks (MOFs), etc., and act as a favourable constituent in the adsorption interaction between the MgO and CO_2. MgO can easily be synthesized in large quantities from magnesium-based minerals commonly available in nature; it is therefore possibly an economically feasible adsorbent (Kumar *et al.*, 2015; Song *et al.*, 2016). The chemical reaction between MgO and CO_2 is given in Equation 2.8.

$$MgO(s) + CO_2(g) \rightarrow MgCO_3(s) \qquad (2\text{-}8)$$
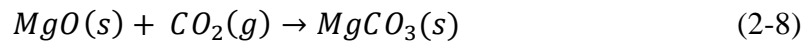
Song *et al.* (2016) investigated the rate-limiting step present in the adsorption of CO_2 onto MgO and found that there are two rate-limiting steps present: the first occurred rapidly and the second slowly. Film diffusion from the bulk gas phase to the exterior of the adsorbent formed the first step, while intensive interparticle diffusion resistance dominated and mitigated the CO_2 adsorption onto the MgO adsorbent for the remainder of the adsorption process. The strong interparticle diffusion resistance is due to the extremely narrow pores present in MgO.

2.4.2.3   ACTIVATED CARBON

Marsh *et al.* (2006) describe activated carbon as a processed form of carbon, with abundant pores in the carbon structure, resulting in high surface areas, which is advantageous for adsorption. Activated carbon is mainly used for the purification of water and for the separation of liquid and gas mixtures. These carbons can be made from a variety of materials, including hard woods, coconut shells, fruit stones, coals and synthetic macromolecular systems.

Activated carbon consist of cavities (voids, sites, pores) the size of molecules with zero electron density, but it exhibits intense van der Waals forces, responsible for the adsorption (Lu *et al.*, 2018; Marsh *et al.*, 2006). The use of activated carbons in industry offers numerous benefits, such as good regenerative capability, low cost, insensitivity towards moisture, high adsorption capacity of CO_2 at ambient conditions, high specific surface area, adequate pore size distribution, high mechanical strength and a low energy requirement (Ammendola *et al.*, 2017; Ogungbenro *et al.*, 2017; Rashidi *et al.*, 2014). Activated carbon has a high affinity for CO_2 and presents as a good adsorbent for the use in an industrial CO_2 separation process from flue gases produced from coal-fired power plants.

Prior to its industrial use, activated carbon needs to be activated, synthetically (Marsh *et al.*, 2006). Further activation affords the formation of additional porosity, widening of existing pores, modifications to the pore surfaces and to the carbonization process(es). Thermal activation of activated carbon involves the removal of carbon atoms within the activated carbon structure, using CO_2 or steam or a mixture of both, at temperatures of 800–900 °C (Marsh *et al.*, 2006). Chemical activation involves other techniques to chemically activate the carbon further, such as co-carbonization with zinc chloride, phosphoric acid and potassium hydroxide.

Activated carbons from coal

Coal is a sedimentary rock composed of a combination of organic and mineral substances, derived from plant debris deposits that underwent a coalification process over an extended time period (Marsh *et al.*, 2006). The coalification transformation of plant material takes place in two steps, involving an initial biochemical degradation followed by physico-chemical degradation. Coals possesses an inherent microporosity, making it a unique parent material for the production of activated carbon (Marsh *et al.*, 2006).

Activated carbons from coconut shells and wood

The abundant supply of wood and coconut shells from the coconut oil and desiccated coconut industry ensures economic viability for the production of activated carbons from coconut shells (Gratuito *et al.*, 2008). Coconut shells can be seen as an amorphous form of carbon, which can adsorb gases, vapours and colloidal solids. Further advantages of using coconut shells instead of other precursor materials include its high density, high purity and virtually dust-free nature. These properties results in a harder and more robust activated carbon. which is more resistant to attrition (Gratuito *et al.*, 2008; Lozano-Castelló *et al.*, 2009).

The activated carbons produced from coconut shells and wood can be further activated through chemical or physical activation. Physical activation entails carbonization, at high temperatures in an inert gas atmosphere, followed by subjection to either steam or CO_2 at high temperatures (as activation agent) (Gratuito *et al.*, 2008). Chemical activation is commonly preferred over physical activation because the latter usually results in lower yields due to mass loss associated with oxidation at high temperatures. Chemical activation also results in higher specific surface areas, with the added benefit of a more economical process due to the lower temperatures required for activation (Gratuito *et al.*, 2008).

2.4.2.4   ZEOLITES

Zeolite sorbents are tetrahedral building structures which give rise to ring-like 3D structures with either micropore or mesopore structures or a combination architecture of both micropores and mesopores. Zeolites are composed of a ratio of SiO_4 and AlO_4 linked by shared oxygen ions (Flanigen *et al.*, 2010). Zeolites with porous attributes are capable of yielding high surface areas, making them powerful structures for the use in adsorbent-related processes. Zeolites have catalytic properties due to their high inherent surface areas and the ability to control acid–base properties due to mobile ions present in the adsorbent (Ullah *et al.*, 2018). A simplified 3D schematic, given in Figure 2–11, illustrates the tetrahedral building structures of ZSM-5 zeolite adsorbent sample.

The secondary building unit in the synthesis process of producing zeolites determines the shape, architecture and structure of the zeolite. CO_2 possesses an elevated quadruple moment which interacts with the zeolite's electron field produced by the cationic structure of the zeolite

and is responsible for the adsorption of CO_2 on the surface of the zeolite (Nie *et al.*, 2018). Characteristics such as the structure, architecture, aluminium-to-silicon composition ratio of the framework, cationic structure and purity can influence the zeolite's CO_2 adsorption
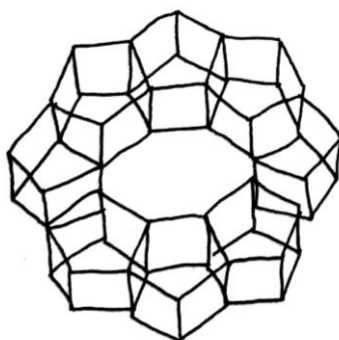
Figure 2-11: Crystal structure of a ZSM5 zeolite.

efficiency (Abd *et al.*, 2020).

2.4.2.5   METAL ORGANIC FRAMEWORKS

Metal-organic frameworks were discovered in 1989 by Hoskins and Robson and they present a new addition to the porous material family (Abd *et al.*, 2020; Khraisheh *et al.*, 2020). MOFs are synthesized from metal ions and organic ligand to produce a unique network structure with a remarkable combination of structural and chemical properties (Ghanbari *et al.*, 2020; Mohamedali *et al.*, 2016; Samokhvalov, 2015). See Figure 2-12

A wide range of metals and organic ligands is available to modify and manipulate the surface area, structure, architecture, pore size distribution and selectivity to adjust MOFs for certain applications, such as CO_2 adsorption (Abd *et al.*, 2020; Ben-Mansour *et al.*, 2016; Styring, 2015). Due to the limitless adjustments, manipulation and modifications that can be applied,

Metal Ion + **Organic Ligand**   =   **Metal Organic Framework**
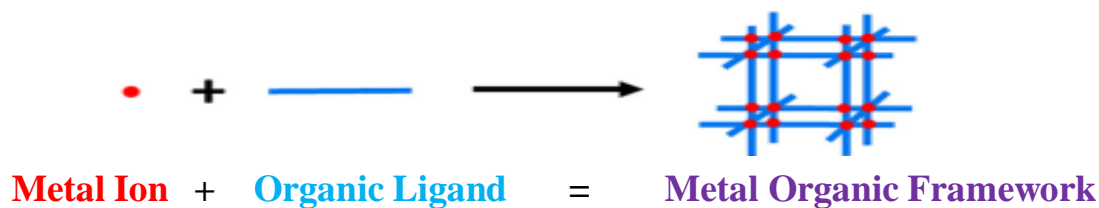
Figure 2-12: Visual representation of the synthesis of MOFs obtained from (Ghanbari *et al.*, 2020).

MOFs have the highest recorded surface area and porosity per unit mass, as a result of the absence of any dead volume present in the framework (Khraisheh *et al.*, 2020; Müller *et al.*, 2008; Tekalgne *et al.*, 2020).

2.4.2.6   AMINE-FUNCTIONALIZED MESOPOROUS SILICA

Amine solvent CO_2 scrubbing technology, currently utilized in industry for carbon capture, has inspired the innovative impregnation of amine-functionalized groups on mesoporous silicas. Mesoporous silica displays favourable adsorption characteristics such as high surface area, narrow pore size distribution (in the nanometre range) and large pore volumes (Sayari, 1996; Yang, 2003). These characteristics of mesoporous silica can be modified and manipulated to suit a specific application, such as CO_2 adsorption, by increasing the affinity as well as the capacity for CO_2 adsorption. CO_2 adsorption capacity increases with an increase in the functional groups attached to the surface of the silica. The amine efficiency is only favourable when an open pore structure is maintained in the silica (Serna-Guerrero & Sayari, 2010). The synthetic process for amine-functionalized mesoporous silica is shown in   Figure 2-13.
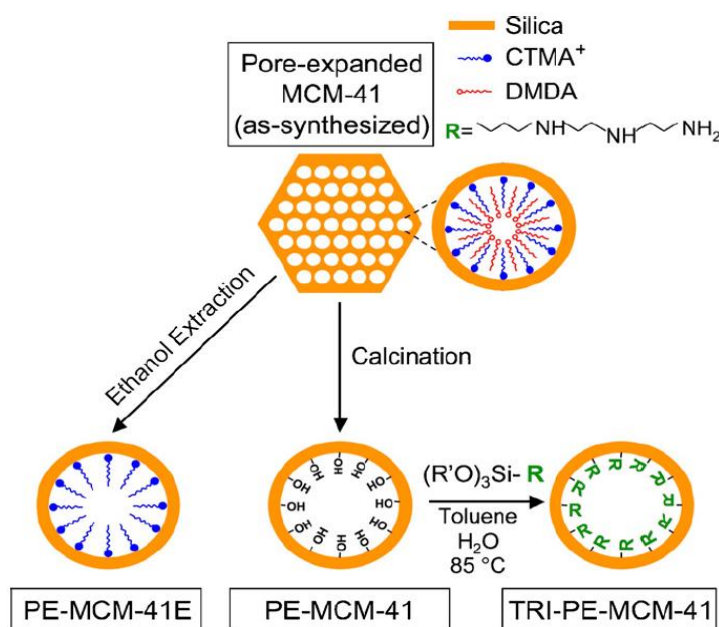
Figure 2-13: Schematic of the synthetic process for amine-functionalized mesoporous silica (Serna-Guerrero & Sayari, 2010).

2.4.2.7   SUMMARY OF THE ADSORBENTS INVESTIGATED

The adsorption mechanisms, and advantages and disadvantages, of the adsorbents investigated in this study are summarised in table form in Table 2-4. It is evident that all the adsorbents adsorbing CO_2, with physisorption as the adsorption mechanism to adsorb the CO_2, are sensitive to humid conditions. This presents as a major drawback, since moisture will always be present in flue gases produced from coal-fired plants. The presence of moisture in the flue gas poisons the adsorbent by concealing the active sites and blocking passageways to micropore structures.

Adsorbents such as alkali carbonates and metal oxides, which make use of chemisorption as the adsorption mechanism to adsorb CO_2, require the presence of moisture so that the chemical reaction between the adsorbent and adsorbate can take place, to adsorb the CO_2 from the gas bulk phase. Although stability in humid conditions can be achieved with these adsorbents, the adsorption kinetic rate of the chemical reactions to occur in the adsorbent–adsorbate system is slow compared to in the case of physical adsorption adsorbents. This presents as a serious disadvantage because the residence times in these carbon capture processes are then extremely short.

Table 2-4:   The adsorption mechanism: summary of advantages and disadvantages of sorbents used for CO_2 adsorption.

Adsorbent type	Adsorption mechanism	Advantages	Disadvantages
Activated carbon	► Physisorption	► Commercially available ► Lower energy requirement for regeneration ► Low production cost ► Chemically and thermodynamically stable ► Stable under humid conditions ► Fast adsorption rate kinetics	► Low operational temperature; low selectivity at high temperature ► Applicable only to high-pressure gases ► Lower adsorption capacity ► Reduced adsorption ability in humid conditions
Zeolite	► Physisorption	► Fast adsorption rate kinetics ► Low production cost ► Commercially available	► Low CO_2 selectivity ► High regeneration energy required ► Unstable under humid conditions ► Reduced adsorption ability in humid conditions
Amine-functionalized mesoporous silica	► Physisorption ► Chemisorption	► High adsorption capacity ► Adjustable pore sizes ► High surface areas	► High synthesis production cost ► Non-reversible adsorption reactions occur ► Unstable under humid conditions ► Present relatively slow CO_2 adsorption rate kinetics ► Commercially available
MOFs	► Physisorption	► High CO_2 selectivity ► Adjustable pore sizes ► High adsorption capacity ► High surface area	► High synthesis production cost ► Unstable in moisture conditions ► Operational limitation ► Reduced adsorption capacity in gas mixtures ► Unstable under humid conditions
Metal oxides	► Chemisorption	► Stable under humid conditions ► Commercially available	► Slow adsorption rate kinetics ► High regeneration energy required ► Not fully regenerated after each adsorption cycle
Alkali carbonates	► Chemisorption	► Stable under humid conditions ► Commercially available	► Slow adsorption rate kinetics ► High inset energy required to regenerate ► Not fully regenerated after each adsorption cycle

2.5   ADSORBENT CHARACTERIZATION

Certain characteristics/properties of adsorbents determine the material's adsorption capacity and kinetic performance characteristics. Characterization of adsorbents reveals correlations between the adsorbent's characteristics and the adsorbent's adsorption capacity and the kinetic performances. Various types of characterization methods can be carried out to obtain the characteristics of the adsorbents to compare with each other and with adsorbents used in literature. The characterization methods discussed in this section are applicable for the characterization of activated carbon adsorbents.

2.5.1   PROXIMATE AND ULTIMATE ANALYSES FOR CARBON BASED ADSORBENTS

Proximate analysis represents a sample in four main constituent categories: moisture content, volatile matter, ash content and fixed carbon. Proximate analysis quantifies the ratio of the combustible to incombustible constituent in a sample tested, and can give insight into the quality of the carbonaceous material (Mayoral *et al.*, 2001). The ash yield after complete combustion represents the residual incombustible metal oxides and salts present in the sample. The activation of carbon takes place at high temperatures, which dissipates remaining gases present in the sample. The adsorption capability of a sorbent decreases with an increasing moisture content (Mayoral *et al.*, 2001). A low inherent moisture content is therefore desirable for maximum adsorption capability of the sorbents.

Ultimate analysis, is a more comprehensive analysis of the sample; it breaks down the sample into its elemental composition of carbon content, hydrogen content, nitrogen content and oxygen content.

2.5.2   DETERMINATION OF SURFACE STRUCTURAL PROPERTIES

Various methods exist for the analysis and characterization of the porosity of a porous dry sorbent, such as mercury intrusion porosimetry, helium measurements and gas adsorption (Keller & Staudt, 2005). Amongst these characterization techniques, gas adsorption is the most

widely employed method for the characterization of dry sorbent porosity and surface area properties (Cazorla-Amorós *et al.*, 1996).

Gases such as N_2, CO_2, Ar, He and CH_4 are frequently used to characterize the surface area of a porous sorbent. From the economic aspect, gas adsorption is the preferred method of measuring surface area, pore structure (consisting of pore size, pore size distribution and pore volume) and porosity (Thommes, 2010). The pores existing in a porous sorbent can be distributed over three ranges: there are micropores ($d_p \leq 20$ Å), mesopores (20 Å $< d_p \leq 500$ Å) and macropores ($d_p > 500$ Å) (Everett, 1972; Sing, 1985). The gas used for determining the surface area is highly dependent on the pore range to be analysed.

Complete wetting occurs when N_2 adsorption at 77 K is utilized for surface area analysis (Thommes, 2010). Phase transition and pore condensation are associated with adsorption onto mesopores, giving rise to hysteresis (see also Section 2.6) (Thommes, 2010). A technique for determining the surface area with N_2 is the Brunauer–Emmett–Teller (BET) surface area determination. The BET surface serves as a characterization parameter for porous sorbents. This parameter is determined through gas adsorption experiments at constant temperature (Keller & Staudt, 2005). The BET surface is the surface of a monolayer adsorbate of N_2 molecules at 77 K, the latter being the boiling temperature of N_2 at 1 atm (Keller & Staudt, 2005). Upon fitting data to the adsorption isotherm equation, developed by Brunauer *et al.* (1938), the maximum adsorption capacity of the monolayer load can be determined from Equation 2-9 (Keller & Staudt, 2005; Valenzuela & Myers, 1984)

$$\frac{P}{(P_0 - P)q_{BET}} = \frac{C - 1}{C q_{CO_2}}\left(\frac{P_{CO_2}}{P_{CO_2,0}}\right) + \frac{1}{C q_{CO_2}} \tag{2-9}$$

where C and q_{BET} are determined with a non-linear regression procedure which is restricted to the region $0 < \frac{P}{P_0} < 0.3$ (Brunauer *et al.*, 1938).

With the elevated temperature of adsorption at 273 K, CO_2 possesses a larger kinetic energy (up to 10^5 times higher), resulting in the penetration of narrow pores, such as micropores (Cazorla-Amorós *et al.*, 1996; Thomas & Damberger, 1976). Therefore, surface areas and porosities obtained using CO_2 results in higher values than those obtained from N_2 adsorption.

The total pore volume can be determined by converting the known amount of adsorptive gas adsorbed at a relative pressure close to 1, to the corresponding volume of adsorbate at the temperature of the adsorption measurement (Gil *et al.*, 2008; Kruk & Jaroniec, 2001). Pore size distribution can be analysed with reasonable accuracy using adsorption data for N_2 and CO_2 (Marsh *et al.*, 2006). The diameter (d) of materials with uniform cylindrical pores can be related to their volume and their geometric surface area, as shown in Equation 2.10 (Kruk & Jaroniec, 2001).

$$d = \frac{4V_p}{A_s} \qquad\qquad (2\text{-}10)$$

2.5.3   SCANNING ELECTRON MICROSCOPY

Scanning electron microscopy is a characterization technique used for analysis of the surface of a sample. Electrons are produced via a V-shaped tungsten wire, known as the thermionic cathode, at vacuum conditions. A strong electric field between the thermionic cathode and anode accelerates the liberated electrons downwards, and they are focused with electromagnetic lenses (Cychosz & Thommes, 2018; Keller & Staudt, 2005). At the point of impact, primary electrons knock out secondary electrons (SEs) from the specimen sampled, then detected with a SE detector. The latter is fitted with a positively biased grid to attract more SEs towards the detector. Further manipulation of the electron beam is achieved with the Raster scan generator to produce an image on screen (Keller & Staudt, 2005; Kruk & Jaroniec, 2001)

2.6   ADSORPTION ISOTHERMS

The amount of adsorbate that is adsorbed at thermodynamic equilibrium is fundamental for the design of a carbon capture system and it can be determined by studying the adsorption isotherms of the adsorbent. Binding forces between the adsorbate and adsorbent interactions are weak forces, leading to significant decreases in adsorption capacity as the adsorption temperatures increases (Singh & Kumar, 2016).

Adsorption isotherms can be viewed as the thermal equation of state for the adsorbed phase from a thermodynamic point of view. The mass adsorbed is a function of the partial pressure

of the components present in the gas, the temperature and the mass of the sorbent material (Keller & Staudt, 2005). Adsorption isotherms are used for the characterization of porous sorbents as well as the design and modelling of industrial adsorption processes. Industrial processes produce multi-component gases, which entails complex interactions with molecules and atoms of the adsorbent (Al-Ghouti & Da'ana, 2020). Industrial adsorption isotherms cannot be calculated from statistical data or by phenomenological methods based on macroscopic and microscopic data of an adsorptive–adsorbent system. Experimental data containing accurate values for adsorbed amounts at well-defined conditions is of paramount importance. Adsorption isotherms obtained from experimental data exhibit, or at least give an indication of, the adsorption mechanism, which then enables correlation to analytical adsorption isotherms to be used for extrapolation to desired process conditions as required for process design (Al-Ghouti & Da'ana, 2020; Gottipati, 2012; Keller & Staudt, 2005).

Adsorption isotherms can be classified into six categories (Types I–VI), five of which (Type I–V) are IUPAC recognized classifications. A Type I isotherms indicates that adsorption occurs in the micropores due to strong adsorbent–adsorbate interactions. A Type I isotherm can also be obtained from mesoporous materials, because the pore diameter of mesopores are close to that of micropores. Therefore, the Type I isotherm must level off at an approximate relative pressure of 0.1, to indicate an exclusive microporous material (Kruk & Jaroniec, 2001; Yahia *et al.*, 2013).

Types II and III isotherms indicate the presence of macropores in the sample material. Adsorption onto macroporous materials proceeds via multilayer formation that increases as the relative pressure increases, with the adsorption–desorption branches of the isotherm coinciding, indicating no hysteresis (Kruk & Jaroniec, 2001; Yahia *et al.*, 2013).

Adsorption onto mesoporous materials proceeds via multilayer adsorption, followed by capillary condensation, attributed to Types IV and V isotherms (Kruk & Jaroniec, 2001). Initially, the Types IV and V look similar to macroporous adsorption isotherms, but then capillary condensation takes place in the mesopores, thus increasing the amount adsorbed at higher relative pressures (Al-Ghouti & Da'ana, 2020; Kruk & Jaroniec, 2001). Capillary condensation and evaporation do not always take place at the same temperature; therefore, the

adsorption–desorption branches do not coincide, presenting hysteresis loops (Gil *et al.*, 2008; Kruk & Jaroniec, 2001; Yahia *et al.*, 2013).

The different pore diameter ranges for micro-, meso- and macropores are given in Table 2-5. See Figure 2-15 for examples of Types I–V isotherm plots (Al-Ghouti & Da'ana, 2020; Kruk & Jaroniec, 2001). An illustration of the sizes of micro-, meso- and macropores is given in Figure 2-14.

Table 2-5: Pore classifications with corresponding diameters (Kruk & Jaroniec, 2001)

Pore classification	Diameter
Micropores	$d_p < 20$ Å
Mesopores	20 Å $\leq d_p \leq 500$ Å
Macropores	$d_p > 500$ Å
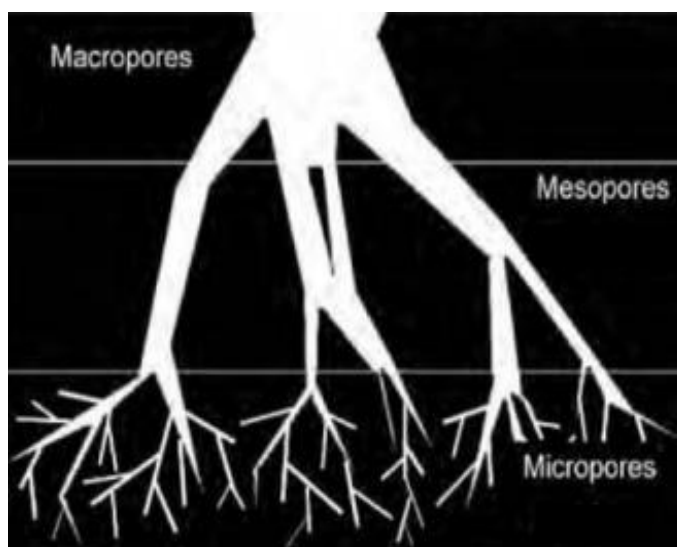
Figure 2-14: Illustration of macropores, mesopores and micropores, obtained from ((Bubanale & Shivashankar, 2017).
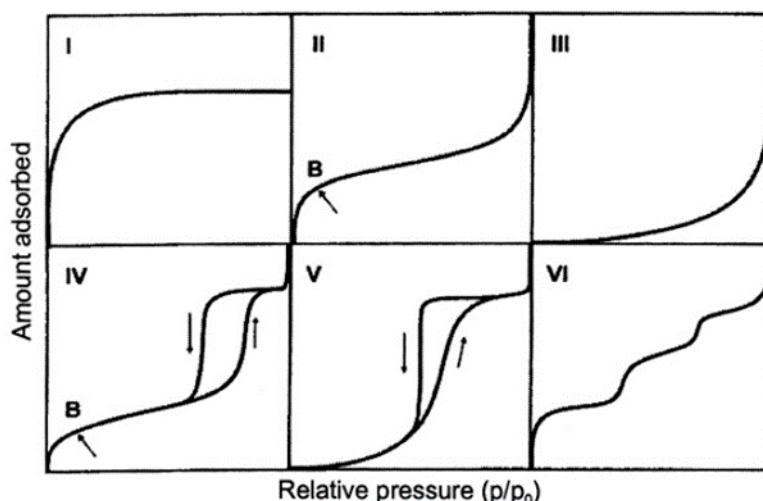
Figure 2-15: Main types of adsorption isotherms (Sing, 1985).

2.6.1 EXPERIMENTAL METHODS

2.6.1.1 VOLUMETRY / MANOMETRY

Volumetry is the oldest method used to determine the adsorption capacity of sorbents. Here, a known amount of sorptive gas is injected into a vessel containing the sorbent sample and the gas then adsorbs to the pore surfaces of the sorbent. A mass balance can then determine the amount of gas adsorbed if the void volume of the sorbent is known. This results in an adsorbed mass per unit mass of sorbent, which can be used to further characterize the adsorbent. The surface area can then be calculated, assuming a characteristic area per single molecule adsorbed onto the surface, which is 0.162 nm^2 and 0.152 nm^2, respectively, for N_2 at 77 K and Ar at 87 K (Ghoufi *et al.*, 2009; Keller & Staudt, 2005).

2.6.1.2 GRAVIMETRY

Gravimetry itself is old, dating back to Biblical times, but it only became feasible in the 20th century when the technology of balances progressed to accurately measure extremely small changes in mass. This technique can be used to characterize adsorbents, much in the same way as volumetry, but it also offers a technique for investigating the adsorption kinetics fairly accurately. Gravimetry can be used in parallel with volumetry to analyse a binary mixture of

adsorptives on an adsorbent without analysing the remnant gas after equilibrium is reached in the adsorption system (Keller & Staudt, 2005).

2.6.1.3   OSCILLOMETRY

Oscillometry is an experimental technique used to measure gas adsorption, with the slow oscillations of a rotational pendulum or relaxed motion of a freely floating rotor. This method is based on the inertia of mass against acceleration. Applying this method to gas adsorption presents challenges, for example, the masses adsorbed are normally small, therefore measuring changes are increasingly difficult, and these can be dampening of the samples motion due to the gas atmosphere surrounding the sample, especially under pressure. Accounting for these challenges, restrictions such as slow rotational oscillations of the adsorbent mass in the presence of the adsorptive gas is considered so that the masses moving geometrically are neglected. The respective flows can then be calculated with the Navier–Stokes equations at laminar flow conditions, which is only induced at low non-linear frequencies (Keller *et al.*, 1999; Keller & Staudt, 2005).

2.6.2   REVIEW OF ADSORPTION ISOTHERM MODELS

Understanding the fundamentals of adsorption equilibria offers powerful insight into understanding adsorption isotherm behaviour of porous structures, which is strongly influenced by resistances to mass transfer and intra-crystalline diffusion (Ruthven, 2006). Adsorption isotherms offer a general understanding of the adsorption equilibria experienced for a particular adsorbent. This is addressed here, as will specific characteristic properties that will promote adsorption of specified gases—with emphasis on CO_2. A summary of the adsorption isotherm models (AIM's) investigated in this study is given in Table 2-6. An in-depth discussion about each adsorption isotherm model follows.

Table 2-6: Summary of the adsorption isotherm models investigated in this study

AIM	Intrinsic adsorption rate model equation	Model parameters	Author(s)
Langmuir	$$q_{CO_2} = \frac{q_L K_L P_{CO_2}}{1 + K_L P_{CO_2}}$$		Langmuir (1916)
BET	$$q_{CO_2} = \frac{q_{BET} C \left(\frac{P_{CO_2}}{P_{CO_2,0}}\right)}{\left(1 - \left(\frac{P_{CO_2}}{P_{CO_2,0}}\right)\right)\left[1 + (C-1)\left(\frac{P_{CO_2}}{P_{CO_2,0}}\right)\right]}$$	q_L = Langmuir maximum adsorption capacity [$mmol/g$] q_{BET} = BET maximum adsorption capacity [$mmol/g$] q_T = Toth maximum adsorption capacity [$mmol/g$] q_{DR} = D-R maximum adsorption capacity [$mmol/g$] q_{DA} = D-A maximum adsorption capacity [$mmol/g$]	Brunauer *et al.* (1938)
Freundlich	$$q_{CO_2} = K_F P_i^{\frac{1}{n_F}}$$	q_S = SIPS maximum adsorption capacity [$mmol/g$] K_L = Langmuir adsorption constant [$1/kPa$] K_F = Freundlich adsorption constant [$mmol/g.kPa^{(1/n)}$]	Freundlich (1906)
Toth	$$q_{CO_2} = \frac{q_T K_T P_{CO_2}}{\left(1 + (K_T P_{CO_2})^t\right)^{1/n_T}}$$	K_T = Toth adsorption constant [$1/kPa$] K_S = SIPS adsorption constant [$1/kPa$]	Toth (1971)
D-R	$$q_{CO_2} = q_{DR} \exp\left[-\left(D_{DR} \, ln\left(\frac{P_{CO_2,0}}{P_{CO_2}}\right)\right)^2\right]$$	K_{TEM} = Temkin adsorption constant [$1/kPa$] n_F = Freundlich heterogeneity parameter n_{DA} = D-A heterogeneity parameter	Dubinin (1960)
D-A	$$q_{CO_2} = q_{DA} \exp\left[-\left(D_{DA} \, ln\left(\frac{P_{CO_2,0}}{P_{CO_2}}\right)\right)^{n_{DA}}\right]$$	n_S = SIPS heterogeneity parameter n_T = Toth heterogeneity parameter C = Constant related to heat of adsorption	Dubinin and Astakhov (1971)
SIPS	$$q_{CO_2} = \frac{q_{SIPS}(K_S P_{CO_2})^{\frac{1}{n_S}}}{1 + (K_{SIPS} P_{CO_2})^{\frac{1}{n_S}}}$$	D_{DR} = D-R affinity constant D_{DA} = D-A affinity constant β = Constant incorporating adsorbate-adsorbent interactions	Sips (1948)
Temkin	$$q_{CO_2} = B \ln (K_{TEM} P_{CO_2})$$		

2.6.2.1   LANGMUIR ADSORPTION ISOTHERM MODEL

The Langmuir adsorption isotherm model, given in Equation 2-11, represents the simplest theoretical model for monolayer gas adsorption onto homogenous surfaces (Ammendola *et al.*, 2017; Zhou *et al.*, 2012). The derivation of the model is based on the following assumptions:

> ➢ Molecules are adsorbed onto a fixed number of well-defined localized sites
> ➢ Monolayer adsorption is as illustrated in Figure 2-16
> ➢ Each available site can host one adsorbate molecule, without the possibility of shifting to another site
> ➢ The surfaces of the adsorbent are homogenous, with each site energetically equivalent, ensuring uniform adsorption energy over all the available adsorption sites
> ➢ No interaction is assumed between molecules adsorbed onto neighbouring sites;
> ➢ The adsorption process is in dynamic equilibrium with the rate of adsorption equal to the rate of desorption (Ammendola *et al.*, 2017; Langmuir, 1916).

$$q_{CO_2} = \frac{q_L K_L P_{CO_2}}{1 + K_L P_{CO_2}} \qquad (2\text{-}11)$$

In Equation 2-11, q_{CO2} represents the equilibrium adsorption of CO_2 onto the adsorbent, q_L is the maximum monolayer adsorption capacity of the adsorbent, K_L is the Langmuir adsorption constant, or it can be seen as the affinity constant, and P_{CO2} is the equilibrium pressure of CO_2 (Ammendola *et al.*, 2017; Langmuir, 1916; Ruthven, 2006).
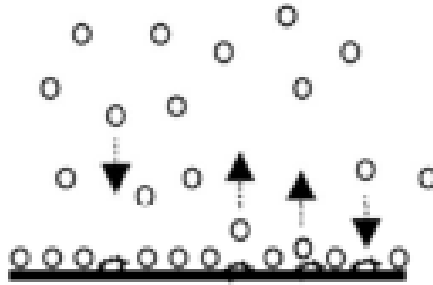
Figure 2-16: Visual illustration of monolayer gas adsorption onto a solid adsorbent, adapted from (Ozdemir, 2005).

2.6.2.2   BET ADSORPTION ISOTHERM MODEL

(Brunauer *et al.*, 1938) extended the Langmuir monolayer adsorption isotherm model to a multilayer adsorption isotherm model, given in Equation 2-12, with all of the same assumptions made, to derive the Langmuir equation, including the following assumptions:

> ➢ Multilayer adsorption where each adsorbate molecule in the initial layer serves as an adsorption site for an adsorbate molecule into the consecutive layer as visually illustrated in Figure 2-17

> ➢ Attractive forces between adsorbate molecules are negligible

> ➢ The heat of adsorption of the second and subsequent layers is equal to the heat of condensation or liquefaction of the adsorbate and different from the heat of adsorption of the first layer (Brunauer *et al.*, 1938; Okolo, 2017).

$$q_{CO_2} = \frac{q_{BET} C \left(\frac{P_{CO_2}}{P_{CO_2,0}}\right)}{\left(1 - \left(\frac{P_{CO_2}}{P_{CO_2,0}}\right)\right)\left[1 + (C-1)\left(\frac{P_{CO_2}}{P_{CO_2,0}}\right)\right]} \tag{2-12}$$

Above, C is a constant related to the heat of adsorption, q_{BET} is the maximum multilayer adsorption capacity and $P_{CO2,0}$ is the saturation pressure of CO_2 at the experimental temperature (Brunauer *et al.*, 1938; Okolo, 2017).
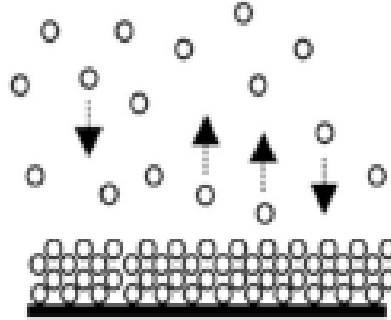
Figure 2-17: Illustration of multi-layer gas adsorption onto a solid adsorbent adapted from (Ozdemir, 2005).

2.6.2.3   FREUNDLICH ADSORPTION ISOTHERM MODEL

The Freundlich adsorption isotherm model, given in Equation 2-13, is one of the earliest isotherm models developed for multilayer non-ideal reversible adsorption that involves

heterogeneous adsorption (Freundlich, 1906; Zhou *et al.*, 2012). The Freundlich isotherm model further incorporates the enthalpy change as the surface loading increases, which entails that the adsorption energy decreases exponentially as the surface loading progresses. It further incorporates the case where the strength in bonds is not homogenous, due to physicochemical adsorption site characteristics or the forces experienced from molecules already adsorbed onto the adsorbent. The higher the surface loading (i.e. the greater the number of molecules adsorbed on the surface), the lower the probability will be for a molecule to adsorb onto the surface, due to the increased amount of energy needed to adsorb (Ammendola *et al.*, 2017; Freundlich, 1906).

$$q_{CO_2} = K_F P_i^{\frac{1}{n_F}}$$

(2-13)

In Equation 2-13, K_F represents the Freundlich isotherm constant and, as it increases, the adsorption capacity of the adsorbent used will also increase; n_F is the heterogeneity parameter that can be used to distinguish between chemisorption ($n_F < 1$) and physisorption ($n_F > 1$), it is also a measure of adsorption, favourability indicated by ($1/n_F < 1$), as a favourable adsorption process (Ammendola *et al.*, 2017; Freundlich, 1906).

2.6.2.4   TOTH ADSORPTION ISOTHERM MODEL

The Toth adsorption isotherm model, given in Equation 2-14, is a well-known isotherm model used to specifically represent equilibrium adsorption data of activated carbon samples (Ruthven, 2006; Toth, 1971). The Toth adsorption isotherm model is based on the Langmuir adsorption isotherm and is commonly utilized to describe heterogeneous adsorption processes incorporating a quasi-Gaussian distribution of available site affinities (LeVan *et al.*, 1997; Shafeeyan *et al.*, 2015; Toth, 1971).

$$q_{CO_2} = \frac{q_T K_T P_{CO_2}}{\left(1 + \left(K_T P_{CO_2}\right)^{n_T}\right)^{1/n_T}}$$

(2-14)

Above, q_T represents the maximum adsorption capacity according to the Toth adsorption isotherm model, K_T represents the Toth equilibrium constant, and n_T is the heterogeneity parameter (LeVan *et al.*, 1997; Shafeeyan *et al.*, 2015; Toth, 1971).

2.6.2.5   DUBININ–RADUSHKEVICH (D-R) ADSORPTION ISOTHERM MODEL

Dubinin *et al.* (1947) applied the Polanyi theory to the extent of micropore filling, in micropore spaces, illustrated in Figure 2-18, and obtained the adsorption isotherm model given in Equation 2-15

$$q_{CO_2} = q_{DR} \exp\left[-\left(D_{DR}\ ln\left(\frac{P_{CO_2,0}}{P_{CO_2}}\right)\right)^2\right] \qquad (2\text{-}15)$$

where q_{DR} represents the maximum adsorption capacity determined according to D-R and D_{DR} is the D-R affinity constant for a particular adsorbate–adsorbent system (Dubinin & Astakhov, 1971; Dubinin *et al.*, 1947; Nguyen & Do, 2001; Okolo, 2017; Tsai *et al.*, 2000).
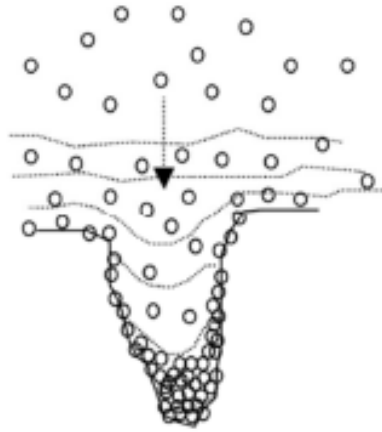
Figure 2-18: Illustration of gas adsorption onto a solid adsorbent by pore filling (Ozdemir, 2005).

2.6.2.6   DUBININ–ASTAKHOV (D-A) ADSORPTION ISOTHERM MODEL

(Dubinin & Astakhov, 1971) further developed the D-R adsorption isotherm model incorporating the Polayni theory of micropore filling, illustrated in Figure 2-18, by introducing a surface heterogeneity parameter n_{DA}, and obtained a physisorption adsorption isotherm equation given in Equation 2-16

$$q_{CO_2} = q_{DA} \exp\left[-\left(D_{DA}\, ln\left(\frac{P_{CO_2,0}}{P_{CO_2}}\right)\right)^{n_{DA}}\right] \tag{2-16}$$

where D_{DA} represents the D-A affinity constant for a particular adsorbate–adsorption system and n_{DA} is the surface heterogeneity parameter (Dubinin & Astakhov, 1971; Okolo, 2017).

2.6.2.7   SIPS ADSORPTION ISOTHERM MODEL

The SIPS adsorption isotherm model is derived from the Langmuir and Freundlich adsorption isotherm models to predict the behaviour of heterogeneous adsorption processes. The SIPS adsorption isotherm reduces to the Freundlich adsorption isotherm at low surface coverages. At high adsorbate concentrations it predicts the monolayer adsorption capacities, resembling the Langmuir adsorption isotherm model (LeVan *et al.*, 1997; Shafeeyan *et al.*, 2015; Sips, 1948). The SIPS adsorption isotherm model is given in Equation 2-17

$$q_{CO_2} = \frac{q_S(K_S P_{CO_2})^{\frac{1}{n_S}}}{1 + (K_S P_{CO_2})^{\frac{1}{n_S}}} \tag{2-17}$$

where q_{SIPS} represents the maximum adsorption capacity according to the SIPS adsorption isotherm model, K_{SIPS} is the SIPS equilibrium constant, and m_{SIPS} is a heterogeneity related to the surface of the adsorbent (LeVan *et al.*, 1997; Park *et al.*, 2016; Shafeeyan *et al.*, 2015; Sips, 1948).

2.6.2.8   TEMKIN ADSORPTION ISOTHERM MODEL

The Temkin adsorption isotherm model contains a factor that specifically incorporates the interactions occurring in adsorbate–adsorbent systems. As adsorbate–adsorbent surface coverage interactions progress, a linear decrease in heat of adsorption of all molecules occurs. A uniform distribution of binding energies is used to characterize this type of adsorption. It is taken into account by the Temkin adsorption isotherm model given in Equation 2-18 (Garnier *et al.*, 2011; Goel *et al.*, 2011; Temkin, 1940)

$$q_{CO_2} = \beta \ln (K_{TEM} P_{CO_2}) \tag{2-18}$$

$$\beta = \frac{RT}{b_T} \qquad\qquad (2\text{-}19)$$

where β, given in Equation 2-19, represents a parameter incorporating adsorbent–adsorbate interactions (which is related to the heat of adsorption), R the universal gas constant (8.314×10^{-1} kJ/mol.K) (where the absolute temperature is measured in K), b_T is related to the heat of adsorption and is equivalent to $-\Delta H_{ads}$ (calculated in kJ/mol), and K_{TEM} is the Temkin equilibrium constant (Garnier *et al.*, 2011; Temkin, 1940).

2.7 ADSORPTION KINETICS

Chemical reaction engineering was initially developed to accomplish the task of sizing a reactor unit and determining the optimal operating conditions for the production of specific chemicals from a petrochemical application. The theory and principles of chemical reaction rates was further developed and evolved so that it can be applied to almost all (if not all) reactor systems, of which the reaction rates of an adsorption system will be specifically focused on (Davis & Davis, 2012).

2.7.1 EXPERIMENTAL METHODS USED TO OBTAIN CO_2 ADSORPTION KINETIC DATA FROM DRY ADSORBENTS

A comprehensive literature study of experimental fixed bed reactor (FBR) design parameters used to conduct CO_2 adsorption rate experiments on dry adsorbents, is discussed in this section.

2.7.1.1 FBR DESIGN AND OPERATING PARAMETERS: INFORMATION OBTAINED FROM LITERATURE

Information on the design of and operating parameters for an experimental fixed bed reactor (FBR) setup is given in Table 2-7. Information includes the reactor length, reactor diameter, operating temperature, operating pressure, operating flow rate, inlet CO_2 concentration and adsorbent mass loaded in the FBR. An average design is obtained from the parameters listed in literature and also given in Table 2-7.

Table 2-7: Fixed bed reactors used for CO2 adsorption (reported in literature).

Parameter	(Singh & Kumar, 2017)	(Hauchhum & Mahanta, 2014b)	(Shafeeyan et al., 2015)	(Balsamo et al., 2013)	(Dantas et al., 2011)	(Park et al., 2006)	Average design parameters
Bed weight, g	53.0	20.0	5.50	15.0	35.2	32.0	21.5
Reactor length, mm	100	200	200	150	171	200	170.2
Reactor diameter, mm	16.0	30.0	10.0	20.0	22.0	-	19.6
Inlet CO_2 concentration, $vol\%$	0–100	13.8	15.0	1.00–15.0	0–100	12.0	0–100
Inlet flow rate, dm^3/min	-	15.0	0.0500–0.100	1.50	0.0300	0.250	0.0300–15.0
Bed porosity	-	0.500	0.560	-	0.520	0.485	0.500
Adsorption temperature, $°C$	50.0– 0.0	25.0–60.0	30.0–60.0	30.0–80.0	30.0–100	50.0–70.0	25.0–100
Adsorption pressure, bar	0–69.0	1.00	1.00	1.00	1.02	1.00	1.00

2.7.1.2 FBR EXPERIMENTAL SETUP DESIGN: INFORMATION OBTAINED FROM LITERATURE

Figure 2-19 shows an experimental FBR setup used to obtain CO_2 adsorption rate experiments on potassium carbonate in the presence of moisture (Park *et al.*, 2006). A 12 vol% CO_2 binary gas mixture with the balance N_2 is mixed with mass flow controllers (MFCs) controlling the mass flow of CO_2 and N_2 and then it is combined with moisture from a micro-syringe pump. This saturated binary gas mixture is then fed to the FBR loaded with 32 g potassium carbonate at 1 *bar*, over the temperature range 50-70 °C. A gas chromatograph measures the outlet CO_2 concentration after the removal of moisture with a moisture trap, to obtain breakthrough adsorbed CO_2 concentration curves (Park *et al.*, 2006).

1. gas bomb   6. packed column
2. mass flow controller   7. temperature probe
3. flow indicator   8. temperature controller
4. micro syringe   9. GC (gas chromatograph)
5. heating line   10. personal computer
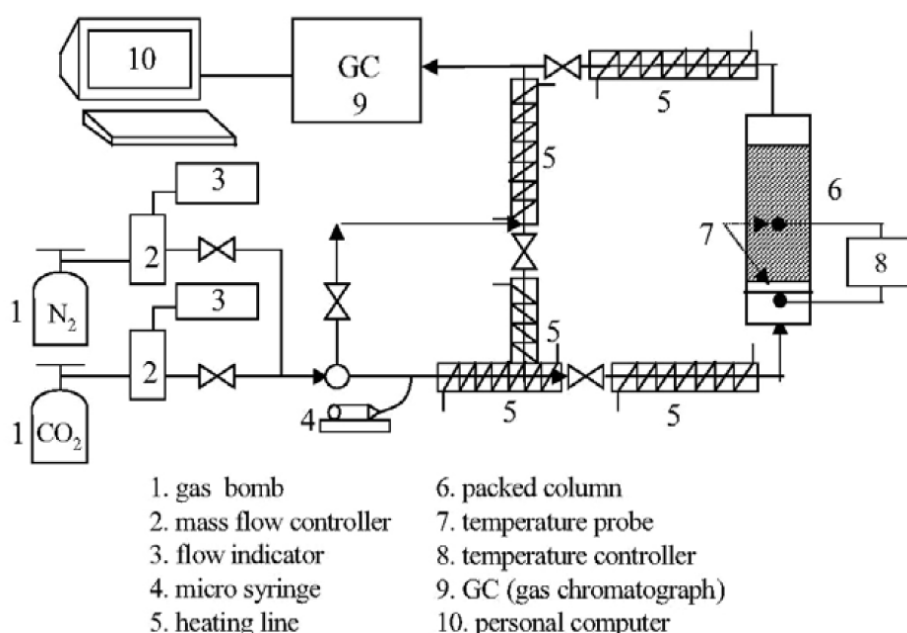
Figure 2-19: Experimental FBR setup used to determine the adsorption kinetic rate of CO_2 adsorption onto K_2CO_3 (Park *et al.*, 2006).

Figure 2-20 illustrates an experimental FBR setup used to determine the adsorption rate kinetics of activated carbon adsorbents. Two digital MFCs regulate the flow of CO_2 and N_2 to obtain a 15 vol% CO_2 gas mixture (with the balance being N_2) to the FBR loaded with 5.5 g sorbent. A Type-K thermocouple measures the temperature of the adsorbent bed and feeds data to a tubular furnace to obtain isothermal conditions at specified temperatures. A CO_2 analyser continuously measures the outlet CO_2 concentration, to obtain the breakthrough adsorbed CO_2 concentration curves (Shafeeyan *et al.*, 2015). Pre-treatment of the adsorbents prior to loading

them into the FBR entailed passing 300 mL/min N_2 through the adsorbent bed at 130 °C and 1 bar for 3 h, to complete the degassing of the adsorbent sample. The design also incorporates a FBR bypass line to the CO_2 analyser to measure the CO_2 concentration and ensure steady state flow before sending the CO_2 through the adsorbent bed (Shafeeyan *et al.*, 2015). The operating parameters, with regard to the inlet CO_2 concentration, operating pressure, operating temperature, operating flow rates fed to the FBR and mass loaded into the FBR, is given in Figure 2-20.
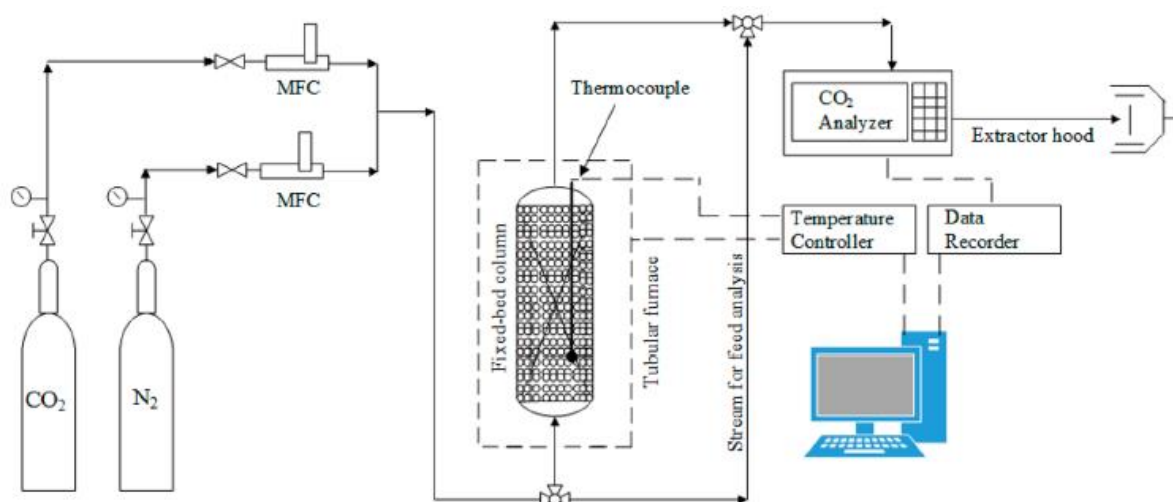
Figure 2-20: Experimental FBR setup used to determine the adsorption kinetic rate of CO_2 adsorption onto activated carbon adsorbents (Shafeeyan *et al.*, 2015).

2.7.2   REVIEW OF INTRINSIC ADSORPTION KINETIC RATE MODELS

In the development of a carbon capture system, the time required to adsorb an optimal amount of the adsorbate is critical. It can be calculated by investigating the adsorption kinetics of an adsorbent. For the industrial application of an adsorbent, the dominant prerequisite is a rapid adsorption rate with reasonable adsorption capacity rather than high adsorption capacity with reasonable adsorption rates (Song *et al.*, 2016). The applicability of an adsorbent in an adsorption process is greatly dependant on the amount of adsorbate gas adsorbed, but limited to the amount of gas adsorbed per unit time. The focus of this section is the modelling of the reaction rates obtained experimentally for the adsorbents. A summary of the intrinsic and diffusion adsorption kinetic rate models (ARM's) investigated in this study is given in Table 2-8. An in-depth discussion about each intrinsic adsorption kinetic rate model follows thereafter.

Table 2-8: Summary of the intrinsic and diffusion adsorption kinetic rate models investigated in this study.

ARM	Intrinsic adsorption rate model equation	Model parameters	Author(s)
Pseudo first order	$\dfrac{q_t}{q_e} = [1 - \exp(-k_1 t)]$	k_1 = Pseudo first order rate constant [s^{-1}] k_2 = Pseudo second order rate constant [$g/mmol.s$]	Lagergren (1898)
Pseudo second order	$q_t = \dfrac{q_e^2 k_2 t}{1 + q_e k_2 t}$	k_A = Avrami kinetic constant [s^{-1}] k_F = Fractional order kinetic constant c_F = Fractional order	Ho and McKay (1999)
Avrami	$\dfrac{q_t}{q_e} = 1 - \exp[-((k_A t)^b)]$	m_F = Fractional order β = Desorption rate constant	Avrami (1939)
Elovich	$q_t = \dfrac{1}{\beta}\ln(1 + \beta \alpha t)$	α = Initial adsorption rate constant b = Avrami stretching parameter	Elovich and Larinov (1962)
Fractional order	$q_t = q_e - \dfrac{1}{\left((n-1)\dfrac{k_F}{m_F}t^{m_F} + \dfrac{1}{q_e^{\,c_F-1}}\right)^{\frac{1}{c_F-1}}}$	q_t = Adsorption capacity at time t [$mmol/g$] q_e = Equilibrium adsorption capacity [$mmol/g$] t = Adsorption time [s]	Heydari-Gorji and Sayari (2011)
ARM	Diffusion adsorption rate model equation	Model parameters	
Film diffusion	$\dfrac{q_t}{q_e} = 1 - \dfrac{6}{\pi^2}\sum_{n=1}^{\infty}\dfrac{1}{n^2}\exp\left(-n^2 B_t\right)$ $\dfrac{q_t}{q_e} < 0.85 \quad B_t = \left[\sqrt{\pi} - \sqrt{\pi - \dfrac{\pi^2 \dfrac{q_t}{q_e}}{3}}\,\right]^2$ $\dfrac{q_t}{q_e} > 0.85 \quad B_t = -0.4997 - \ln\left(1 - \dfrac{q_t}{q_e}\right)$	B_t = Mathematical function of q_t/q_e D_C = Diffusivity in the solid adsorbent r_p = Radius of solid adsorbent particles [m] k_i = Intraparticle diffusion rate constant [$mmol/g.s^{0.5}$]	Boyd et al. (1947)
Interparticle diffusion	$\dfrac{q_t}{q_e} = 1 - \dfrac{6}{\pi^2}\sum_{n=1}^{\infty}\dfrac{1}{n^2}\exp\left(-\dfrac{n^2\pi^2 D_c t}{r_p^2}\right)$		Ruthven (1984)
Intraparticle diffusion	$q_t = k_i t^{0.5} + C$		Weber Jr and Morris (1963)

2.7.2.1   PSEUDO FIRST ORDER KINETIC MODEL

The reversible reaction between adsorbent and adsorbate, which is applicable in the prediction of CO_2 adsorption behaviour, can be modelled using the pseudo first order kinetic model (Ammendola *et al.*, 2017; Lagergren, 1898; Shafeeyan *et al.*, 2015). This model assumes that the rate of adsorption is directly proportional to the number of free active sites available on the adsorbent surface (Ammendola *et al.*, 2017; Goel *et al.*, 2011; Lagergren, 1898). The mathematical expression of the pseudo first order model is given in Equation 2-20. Equation 2-21 represents the integral form of Equation 2-20 with boundary conditions $q_t = 0$ at $t = 0$ and $q_t = q_e$ at $t = t_\infty$.

$$\frac{dq_t}{dt} = k_1(q_e - q_t) \tag{2-20}$$

$$\frac{q_t}{q_e} = [1 - \exp(-k_1 t)] \tag{2-21}$$

In Equations 2-20 and 2-21, q_e and q_t are the adsorption capacity at equilibrium and at a specific time, respectively, and k_1 is the pseudo first order rate constant (Ammendola *et al.*, 2017; Lagergren, 1898; Qiu *et al.*, 2009).

2.7.2.2   PSEUDO SECOND ORDER KINETIC MODEL

The pseudo second order kinetic model assumes that the interactions between the adsorbate and adsorbent are caused by a strong binding of gas to the surface of the adsorbent and chemical interactions control the overall adsorption kinetics (Ammendola *et al.*, 2017; Ho & McKay, 1999; Shafeeyan *et al.*, 2015; Silva *et al.*, 2013). With this assumption, a better fit can be obtained when the CO_2 adsorption process involves some chemical interactions with the adsorbent (Ammendola *et al.*, 2017). Equation 2-22 presents the pseudo second order kinetic model. Integrating Equation 2-22 with boundary conditions $q_t = 0$ at $t = 0$ and $q_t = q_e$ at $t = t_\infty$ yields Equation 2-23 (Ammendola *et al.*, 2017; Ho & McKay, 1999; Lopes *et al.*, 2003).

$$\frac{dq_t}{dt} = k_2(q_e - q_t)^2 \tag{2-22}$$

$$q_t = \frac{q_e^2 k_2 t}{1 + q_e k_2 t} \qquad (2\text{-}23)$$

The constant k_2 represents the pseudo second order rate constant (Ho & McKay, 1999).

2.7.2.3   AVRAMI KINETIC MODEL

The Avrami kinetic adsorption rate model was initially intended to model phase transitions and crystal growth of materials. Wang and Guo (2020) and Shafeeyan *et al.* (2015) successfully applied the Avrami kinetic model to CO_2 adsorption modelling onto an amine-functionalized adsorbent. This kinetic model introduces a stretching parameter b ($0 < b < 1$) with a value of 1, or close to 1, indicating a narrow relaxation time; the value increases as the value of b deviates from 1 (Czerw *et al.*, 2017). The Avrami kinetic adsorption rate model is described in Equation 2-24. Integrating Equation 2-24 with boundary conditions $q_t = 0$ at $t = 0$ and $q_t = q_e$ at $t = t_\infty$ yields Equation 2-25 (Ammendola *et al.*, 2017; Avrami, 1939; Shafeeyan *et al.*, 2015).

$$\frac{dq_t}{dt} = k_A^b t^{b-1}((q_e - q_t) \qquad (2\text{-}24)$$

$$\frac{q_t}{q_e} = 1 - \exp[-((k_A t)^b)] \qquad (2\text{-}25)$$

The constant k_A represents the Avrami kinetic constant and b is a stretching parameter (Avrami, 1939).

2.7.2.4   ELOVICH ADSORPTION RATE MODEL

The Elovich kinetic adsorption rate model is an empirical adsorption model; it is adequate to describe the chemisorption of gas onto a solid sorbent. The adsorption model assumes energetic heterogeneity adsorption sites. This model is given in Equation 2-26 (Elovich & Larinov, 1962; Wang & Guo, 2020).

$$q_t = \frac{1}{\beta} \ln(1 + \beta \alpha t) \qquad (2\text{-}26)$$

where α is the initial adsorption rate constant and β is the desorption rate constant (Elovich & Larinov, 1962; Wang & Guo, 2020).

2.7.2.5   FRACTIONAL ADSORPTION RATE MODEL

The fractional order rate model was developed from the Avrami adsorption rate model, which is based on particle nucleation, and was originally utilized to describe CO_2 adsorption onto mesoporous silicas (Heydari-Gorji & Sayari, 2011). The differential equation is given in Equation 2-30, where the adsorption rate is directly proportional to the nth power of the driving force and the mth power of the adsorption time

$$\frac{dq_t}{dt} = k_{FOM}t^{m_F-1}(q_e - q_t)^{c_F} \tag{2-27}$$

where k_{FOM} represents the fractional order adsorption rate constant, and c_F and m_F represent model constants. Assuming that θ presents a fraction of the adsorption sites occupied by the adsorbed gas, where $\theta = q_t/q_e$, and substituting θ into Equation 2-27, we obtain Equation 2-28 (Heydari-Gorji & Sayari, 2011).

$$\frac{dq_t}{dt} = k_{FOM}t^{m_F-1}q_e^{c_F-1}(1 - \theta)^{c_F} \tag{2-28}$$

Integration of Equation 2-28 yields Equation 2-29 (Heydari-Gorji & Sayari, 2011).

$$q_t = q_e - \frac{1}{\left((n-1)\frac{k_F}{m_F}t^{m_F} + \frac{1}{q_e^{c_F-1}}\right)^{\frac{1}{c_F-1}}} \tag{2-29}$$

2.7.3   DIFFUSION ADSORPTION KINETIC RATE MODELS

To determine the rate-limiting step for adsorption onto a sorbent, diffusion adsorption kinetic rate models can be applied to the experimental adsorption kinetic data (Çağlayan & Aksoylu, 2016; Raganati *et al.*, 2019; Song *et al.*, 2016). The Boyd film-diffusion model, intraparticle diffusion model and interparticle diffusion model, describing film diffusion, interparticle diffusion and intraparticle, respectively, are discussed in this section. A representation of the

regions where film, interparticle and intraparticle diffusion occur, is given in Figure 2-21. A summary of the diffusion adsorption kinetic rate models investigated in this study is given in Table 2-8. An in depth discussion about each diffusion adsorption kinetic rate model follows.
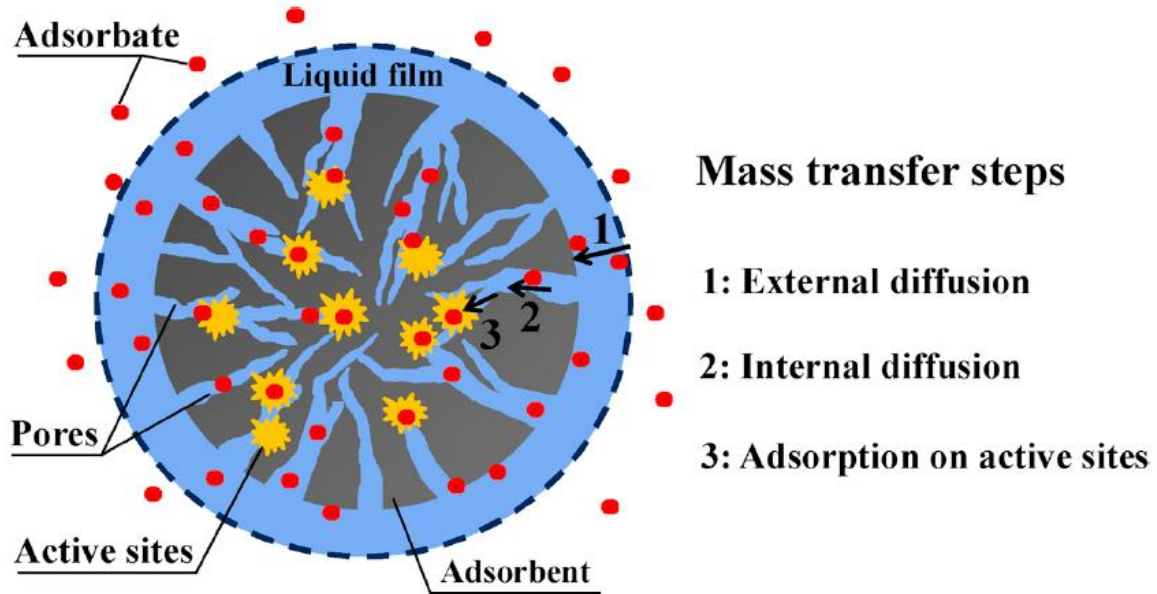
Figure 2-21: Illustration of film, interparticle and intraparticle diffusion mechanism as well as the region where each respective diffusion mechanism occurs, adapted from (Wang & Guo, 2020).

2.7.3.1 BOYD'S FILM-DIFFUSION MODEL

Application of Boyd's film-diffusion model, expressed in Equation 2.30, to the adsorption rate data of CO_2 adsorbed on the adsorbent can be used to determine whether the resistance that exists around the sorbent is the rate-limiting step. The model assumes that the gas film around the adsorbent is the sole resistance (Boyd *et al.*, 1947; Raganati *et al.*, 2019; Song *et al.*, 2016).

$$\frac{q_t}{q_e} = 1 - \frac{6}{\pi^2} \sum_{n_i=1}^{\infty} \frac{1}{n_i^2} \exp\left(-n^2 B_t\right) \tag{2-30}$$

Here, B_t represents a mathematical function related to fractional uptake (q_t/q_e), defined in Equation 2-31 for $q_t/q_e < 0.85$ and in Equation 2-32 for $q_t/q_e > 0.85$.

$$B_t = \left[\sqrt{\pi} - \sqrt{\pi - \frac{\pi^2 \frac{q_t}{q_e}}{3}} \right]^2 \tag{2-31}$$

$$B_t = -0.4997 - \ln\left(1 - \frac{q_t}{q_e}\right) \tag{2-32}$$

To determine the adsorption-rate-controlling diffusion mechanism, a plot of B_t against time is determined. A linear line that does not pass through the origin or a non-linear plot indicates that the adsorption process is controlled by film diffusion. If the plot is linear and passes through the origin, the adsorption process is controlled by intraparticle diffusion (Boyd *et al.*, 1947; Raganati *et al.*, 2019; Song *et al.*, 2016).

2.7.3.2 INTERPARTICLE DIFFUSION MODEL

To evaluate interparticle diffusion, the interparticle diffusion model, given in Equation 2-33, can be applied with an approximation assumption that all the adsorbent particles are equivalent spheres and the assumption of constant diffusivity in spherical coordinates (Ruthven, 1984; Song *et al.*, 2016).

$$\frac{q_t}{q_e} = 1 - \frac{6}{\pi^2} \sum_{n_i=1}^{\infty} \frac{1}{n_i^2} \exp\left(-\frac{n^2 \pi^2 D_c t}{r_p^2}\right) \tag{2-33}$$

Here, D_C represents the diffusivity of the solid particle and r_p the radius of the solid particle sphere. When $q_t/q_e < 0.7$, Equation 2-33 can be simplified to Equation 2-34.

$$1 - \frac{q_t}{q_e} \approx \frac{6}{\pi^2} \exp\left(-\frac{\pi^2 D_c t}{r_p^2}\right) \tag{2-34}$$

To determine whether the interparticle diffusion is the rate-limiting step, a plot of $\ln(1-q_t/q_e)$ against time is examined. A linear line with slope $-\pi(D_c/r_p^2)$ and intercept $\ln(6/\pi^2)$ will indicate interparticle diffusion (Raganati *et al.*, 2019; Ruthven, 1984; Song *et al.*, 2016). If this is not the case observed from the plot, then the adsorption rate is controlled by another diffusion rate-limiting step.

2.7.3.3   INTRAPARTICLE DIFFUSION MODEL

Intraparticle diffusion exists when adsorption takes place onto extremely porous sorbents or sorbents with particularly narrow pores. Weber Jr and Morris (1963) proposed an intraparticle diffusion model based on Fick's second law. The intraparticle diffusion model is expressed in Equation 2-35 (Morris & Weber jr, 1964; Raganati *et al.*, 2019; Song *et al.*, 2016)

$$q_t = k_i t^{0.5} + C \qquad (2\text{-}35)$$

where k_i represents the intraparticle diffusion rate constant, and C represents the intercept and is associated with boundary layer thickness. To predict whether intraparticle diffusion is the rate-limiting step, a plot of q_t against $t^{1/2}$ is evaluated. A linear line passing through the origin implies intraparticle diffusion takes place (Çağlayan & Aksoylu, 2016; Raganati *et al.*, 2019; Song *et al.*, 2016; Weber Jr & Morris, 1963).

2.8   THERMODYNAMIC ANALYSIS OF THE ADSORPTION PROCESS

Thermodynamic analysis of the adsorption process, for an adsorbent, provides information about the adsorption process taking place on that adsorbent—to then deduce whether the adsorption taking place is exothermic or endothermic, physisorption or chemisorption, and if the adsorption occurs spontaneously. Evaluation of the thermodynamic parameters involved in CO_2 adsorption onto adsorbents, is discussed in this section.

2.8.1   ISOSTERIC HEAT OF ADSORPTION

Heat of adsorption is considered to be an important thermodynamic property in the design and optimisation of gas separation processes. It represents the average binding energy of a gas particle at a specific surface coverage. In other words, the heat of adsorption represents the strength of the interaction between the adsorbate and the adsorbent (Ammendola *et al.*, 2017). The isosteric heat of adsorption (Q_{st}) can be quantified for specific amounts adsorbed using Equation 2-36.

$$\left[\frac{\partial ln P_{CO_2}}{\partial \left(\frac{1}{T}\right)} \right]_V = -\frac{Q_{st}}{R} \qquad\qquad (2\text{-}36)$$

Heat of adsorption is associated with the interaction between the surface of the sorbent, and the molecular forces associated with adsorption. These forces may include dipole–dipole interactions, Van der Waals forces, hydrogen bonds, and others. At the commencement of adsorption, there is a large number of available pores. The adsorbate gas comes into close contact with the adsorbent and this creates strong forces between the sorbent and the adsorbate gas. Values for heat of adsorption are thus at a maximum at low adsorbed volumes and will decrease as the adsorption process continues (Ammendola et al., 2017). The isoteric heat of adsorption can be determined from a $ln(P_{CO2})$ versus q_t.

2.8.2   GIBBS FREE ENERGY

The Gibbs free energy ($\Delta G°$) is used to determine to which degree a process occurs spontaneously. If the change in the total free energy of the process at a certain temperature is negative ($\Delta G° < 0$) then the process will occur spontaneously. If the change in the total free energy is positive, the process will be non-spontaneous and not practical, as external energy will be required for adsorption to occur (Ammendola *et al.*, 2017). The Gibbs free energy can be calculated using Equation 2-37, where *K* is the adsorption constant of Langmuir or Freundlich.

$$\Delta G° = -RT ln(1/K) \qquad\qquad (2\text{-}37)$$

2.8.3   ENTHALPY

Enthalpy ($\Delta H°$) determines whether the process is exothermic or endothermic. An exothermic process exhibits a negative value of $\Delta H°$ and is associated with the release of energy to the surroundings, in the form of heat. A negative $\Delta H°$ value occurs due to less energy being absorbed during bond cleavage than there was released during bond creation. In comparison, an endothermic process exhibits a positive value of $\Delta H°$ and heat from the surroundings is absorbed (Ammendola et al., 2017). $\Delta H°$ is commonly <20 kJ/mol for physisorption and 80–

200 kJ/mol for chemisorption. $\Delta H°$ can be calculated from the slope of the van't Hoff equation, given in Equation 2-38.

2.8.4   ENTROPY

According to (Ammendola *et al.*) (2017), the magnitude of the change in entropy ($\Delta S°$) specifies whether the organization of the adsorbate inside the gas/solid interface becomes more random or less random during the adsorption process. If the value of $\Delta S°$ is positive then the organization becomes more random and if the value becomes negative then the organisation becomes less random(Ammendola *et al.*, 2017)(Ammendola *et al.*, 2017)(Ammendola *et al.*, 2017)(Ammendola *et al.*, 2017)(Ammendola *et al.*, 2017)(Ammendola *et al.*, 2017)(Ammendola *et al.*, 2017)(Ammendola *et al.*, 2017)(Ammendola *et al.*, 2017). The intercept of the van't Hoff equation, given in Equation 2-38, is used to calculate $\Delta S°$.

$$\ln\,(1/\mathrm{K}) = \left(\frac{\Delta S°}{R}\right) - \left(\frac{\Delta H°}{RT}\right) \tag{2-38}$$

Chapter 3

(EXPERIMENTATION AND MODELLING)

Chapter 3

(EXPERIMENTATION AND MODELLING)

This chapter introduces, and explains, the materials and methods used to complete the characterization, adsorption isotherm and adsorption kinetic rate experimental work. An experimental procedure is described in this chapter, in an effort to contribute to on the experimental method and experimental repeatability.

3.1 ADSORBENTS

Four activated carbon samples were used to complete the experimental work. Pure N_2 (99.99%) and pure CO_2 (99.99%) were obtained from Afrox (South Africa) and used in pure form, as well as in binary mixtures of 5%, 15% and 25% CO_2 (balance N_2).

3.1.1 ACTIVATED CARBON SAMPLES

The four activated carbon samples—CQ006, CQ650, CQ30P and PCX1—were obtained from ChemQuest (Germiston, South Africa). A comparison between the samples with regard to their respective materials of origin and activation methods is given in Table 3–1.

Table 3-1: Activated carbon samples CQ006, CQ650, CQ30P and PCX1: parent material and activation method.

	CQ006	CQ650	CQ30P	PCX1
Material of origin				
Coal	X		X	
Wood				X
Coconut		X		
Activation method				
Steam	X	X	X	
Chemical				X
Acid washed	X			
KOH impregnation		X	X	
Extra high activity	X			X

Depending on the material of origin, these activated carbons display different inherent characteristics, with regard to pore size and applicability. Wood-based activated carbons are predominantly rich in macropores, making them suitable for the adsorption of large molecules, such as colour bodies. Coconut-based activated carbons are inherently hard, abrasion resistant and microporous, making them suitable for the adsorption of small molecules such as CO_2, and precious metal recovery. Coal-based sorbents are tri-dispersed—they contain micropores, mesopores and macropores—making them suitable for the adsorption of a range of small to large molecules, and thy can be used to treat potable and effluent water.

Physical activation is a combination of carbonization and activation. Carbonization entails the devolatilization/charring process, taking place in an inert atmosphere at temperatures in the range 250–650 °C. Activation entails controlled oxidation in the presence of steam or another oxidizing agent at temperatures in the range 750-1200 °C for long retention times, with exact control. This ensures a well-developed internal pore structure, uniform activation and abrasion resistance.

Chemical activation replaces the oxidizing step in physical activation, partly, where lower temperatures are used in the presence of phosphoric acid or zinc chloride. Chemical activation yields an activated carbon with a well-developed macropore and mesopore structure.

3.2   CHARACTERIZATION OF ACTIVATED CARBON

Characterization experiments are necessary to quantify, and compare, the physical properties of the different samples selected for use in this study. This enable the making of informed assumptions on the adsorption and kinetic ability of a sorbent based on the physical properties of the sorbent.

3.2.1   PROXIMATE ANALYSIS

A proximate analysis quantitatively describes a material in terms of moisture, volatile matter, ash and fixed carbon. A standard experimental procedure was followed to calculate the moisture content, volatile matter, ash content and fixed carbon and discussed in this section.

3.2.1.1   MOISTURE CONTENT

A sample of each sorbent (1 ± 0.1 g) was weighed and dried in an oven for 3 h. The moisture content was then calculated. This experiment was repeated three times for each sorbent and the average value was recorded. The moisture content was calculated with the formula presented in Equation 3-1

$$M = \frac{m_2 - m_3}{m_2 - m_1} \times 100 \qquad (3\text{-}1)$$

where M is the calculated moisture content percentage, m_1 is the mass of the empty tray, m_2 is the mass of the tray and sample before drying, and m_3 is the mass of the sample and tray after drying (SABS, 2009).

3.2.1.2   VOLATILE MATTER

A sample of each sorbent (1 ± 0.1 g) was weighed and heated to a temperature of 900 °C for 7 min in the absence of air. Air is excluded to prevent oxidation, which would ultimately result in an inaccurate experiment. The sample was then removed from the oven and left for 4 min to equilibrate with room temperature. The sample was then weighed and the volatile matter content calculated with the formula presented in Equation 3-2

$$V = \frac{100 \times (m_2 - m_3)}{m_2 - m_1} - M \qquad (3\text{-}2)$$

where M is the mass percentage moisture content calculated in Equation 3.2 (SABS, 2011). This experiment was repeated three times for each sorbent and the average was recorded.

3.2.1.3   ASH CONTENT

A sample of each sorbent (1 ± 0.1 g) was weighed and loaded into an oven at room temperature. The temperature was gradually increased to 500 °C within 1 h and then kept steady at 500 °C for 30 min. Thereafter, temperature was gradually increased to an incineration temperature of 815 °C and held there, until full combustion of the sample was complete. After total

combustion, the sample was left to cool to room temperature and then weighed. The ash content was calculated with the formula presented in Equation 3-3

$$A_C = \frac{m_2 - m_3}{m_2 - m_1} \times 100 \qquad\qquad (3\text{-}3)$$

where A_C represents the percentage ash content (SABS, 2011).

3.2.2   ULTIMATE ANALYSIS

The ultimate analysis was outsourced to Bureaus Veritas and the methodology followed to determine the carbon, nitrogen, hydrogen, oxygen and total sulphur was determined by the methods given in Table

Table 3-2: Ultimate analysis methodology.

Constituent	Method	Laboratory
Carbon (wt.%)	ISO 29541: 2010 (SANS 29541, 2014)	
Nitrogen (wt.%)	ISO 29541: 2010 (SANS 29541, 2014)	
Hydrogen (wt.%)	ISO 29541: 2010 (SANS 29541, 2014)	**Bureaus Veritas**
Oxygen (wt.%)	By difference	
Sulphur (wt.%)	ISO 19579: 2007 (SANS 19579, 2007)	

3.2.3   SURFACE AREA ANALYSIS

The surface area of the activated carbons was determined from low pressure CO_2 and N_2 adsorption at 0 °C and -196 °C, respectively, on a Micromeritics ASAP 2020 analyser. The amount of the adsorbate gas corresponding to the monomolecular layer on the surface of the material could be calculated and then the surface area of the material determined. The adsorption isotherm was measured as a function of partial pressure (P/P_0), ranging from 0-0.03 for CO_2 adsorption, and 0–0.3 for N_2 adsorption. The Dubinin–Radushkevich (D-R) and the Brunauer–Emmet–Teller (BET) theories, respectively, were then applied to calculate the surface area of the sorbent (Micromeritics, 2004).

3.2.3.1   SAMPLE PREPARATION

The sample tube was thoroughly cleaned with acetone to ensure that no particles from a previous experiment could influence the analysis. The sample tube was inserted into a drying oven to ensure that all the acetone evaporated and none remained to affect the experiment. A sample (0.3 ± 0.01 g) was weighed and carefully inserted into the tube. A filler rod was used to improve the accuracy of the experiment by reducing dead space for samples with surface areas <100 m^2/g (Micromeritics, 2004). The sample was then inserted in the degassing port of the ASAP 2020 Micromeritics apparatus and degassed for 12 h at vacuum of 3 µm Hg and a temperature of 380 °C, prior to analysis.

3.2.3.2   SAMPLE ANALYSIS

The exact mass of gas in the storage vessel is known prior to the analysis. The gas expands over an expansion valve into the sample tube and partially adsorbs onto the external and internal surface areas of the sorbent material. The basis for the calculation of the mass adsorbed onto the sorbent material is taken when thermodynamic equilibrium is reached. Thermodynamic equilibrium is reached when consistencies in the pressure and temperature are observed and no further changes are noticed in either. An equilibration time of 100 s was employed to analyse the activated carbon sample's surface area.

Applying the Horvath–Kawazoe pore size analysis method, the maximum pore volume (cm^3/g) and median pore width (Å) were determined at a final partial pressure ($P_{CO2}/P_{CO2,0}$) of 0.3.

3.3   DETERMINATION OF ADSORPTION ISOTHERMS

The same sample preparation procedures as detailed in Section 3.2.2.1 were applied in the preparation of samples for the adsorption experiments on the Micromeritics ASAP 2020 instrument. The adsorption capacity experiments for the four sorbents were conducted at four temperatures (40, 55, 70 and 85 °C) with two different gasses: pure CO_2 and pure N_2. A standard pressure range of 0–1.19 bar was selected for each experiment, to ensure uniformity and valid comparison in this study. The saturation vapour pressures of the gases at the different temperatures are presented in Table 3-3. The saturation vapour pressure for N_2 were obtained

from the fitting function in Aspen Plus V8.6. Experimental real-time data, including relative pressure ($P_{CO2}/P_{CO2,0}$), absolute pressure, volume of adsorptive adsorbed, and experimental time, were logged automatically from the equipment.

Table 3-3: CO_2 saturation pressures at various temperatures.

Temperature, $^{\circ}C$	CO_2 Saturation pressure, kPa
0	3485
10	4501
20	5727
30	7211
55	8967
70	12131

3.3.1 ADSORPTION ISOTHERM MODELLING

The experimental data obtained from the adsorption experiments were used to generate the adsorption isotherms of the samples. Eight different adsorption isotherm models were fitted to the experimental data: Langmuir, BET, D-R, D-A, Toth, Freundlich, Temkin and SIPS adsorption isotherm models (see Table 2-6). The unknown adsorption isotherm parameters of the adsorption isotherm models were fitted and adjusted to the experimental data using non-linear regression analysis implemented in Excel with Excel Solver in combination with error sum of squares (ESS) (Fylstra *et al.*, 1998; Shafeeyan *et al.*, 2015).

3.4 THERMODYNAMIC EVALUATION OF CO_2 ADSORPTION

The change in enthalpy, entropy and Gibbs free energy can be determined with the adsorption constants obtained from adsorption isotherm modelling with either the Langmuir or Freundlich adsorption isotherm models (Ammendola *et al.*, 2017; Goel *et al.*, 2011; Shafeeyan *et al.*, 2015).

The change in enthalpy and entropy is determined from Equation 3-4 and solved by taking the slope and intercept of plotting $\ln(K_F)$ against *1/T*.

$$\ln(K_F) = -\frac{\Delta H^0}{RT} + \frac{\Delta S^0}{R} \qquad (3\text{-}4)$$

The change in enthalpy and entropy is calculated from the slope and intercept with Equation 3-5 and Equation 3-6.

$$\Delta H^0 = \frac{-R \times Slope}{1000} \qquad (3\text{-}5)$$

$$\Delta S^0 = \frac{R \times Intercept}{1000} \qquad (3\text{-}6)$$

The Gibbs free energy is evaluated at each temperature with Equation 3-7.

$$\Delta G^0 = \Delta H^0 - T\Delta S^0 \qquad (3\text{-}7)$$

3.5   DETERMINATION OF ADSORPTION KINETICS

An fixed bed reactor was designed and constructed at the North-West University in Laboratory G15, to measure the CO_2 adsorption kinetics of adsorbents. The fixed bed reactor (FBR) design and experimental procedure for carrying out the CO_2 adsorption kinetic experiments are now described.

3.5.1   REACTOR DESIGN

Photographs of an experimental FBR setup are shown in Figure 3-1. Figure 3-2 shows a detailed piping and instrumentation diagram (P&ID) of the adsorption reactor that was designed and constructed by myself (A. Jacobs) and D. Vosloo at the North-West University. The adsorption reactor design had to incorporate SO_2 adsorption in order for it to also be suitable for use for SO_2 adsorption kinetic experiments. Thus, the design was subject to the consideration of moisture conditions and the possible formation of sulphuric acid (H_2SO_4). The available CO_2 analyser (MGA 3000) is limited to measure 0–5% CO_2 concentrations, with an inlet flow limit of 1 nL/min.

CHAPTER 3: EXPERIMENTATION AND MODELLING

A specific binary gas mixture of CO_2 and N_2 is regulated with mass flow controllers (MFCs) (**4,5**) connected to the CO_2 and N_2 gas cylinders (**1,2**). This binary gas mixture is combined with moisture (**6**) and fed to the FBR with a length of 200 mm and a 1-inch diameter constructed from SS316 (**9**) with the loaded adsorbent, then sent to a condenser (**13**) to remove the moisture from the gas. A back pressure controller (BPC) (**12**) controls the pressure in the FBR to ensure isobaric conditions. The FBR is positioned in an oven to maintain isothermal conditions at a set point. The temperature of the adsorbent bed is measured with a Type-K thermocouple to ensure that the correct temperature is reached and maintained. The dry gas is then diluted (**3,14**) with N_2 to obtain a CO_2 concentration that can be measured with the CO_2 analyser. Any remaining moisture is then adsorbed in the moisture trap (**15**) onto a 3 Å molecular sieve bed. A MFC (**16**) controls the mass flow of the gas to the CO_2 gas analyser at 0.8 nL/min, the excess gas goes through a mass flow meter (MFM) (**17**) and vented. The CO_2 concentration is logged in intervals of 2 s, on an Endress & Hauser data logger (**19**). A bypass line (**8**) is used to bypass the FBR. The binary gas mixture is sent directly to the CO_2 analyser to ensure that the correct CO_2 concentration is recorded.

Prior to carrying out experiments, the adsorbent sample is degassed and a weighed sample positioned in the FBR. The FBR (**10**) is placed in a tubular furnace, maintained at 90 $°C$ and under a vacuum (**11**) of 0.5 bar, for 3 h.
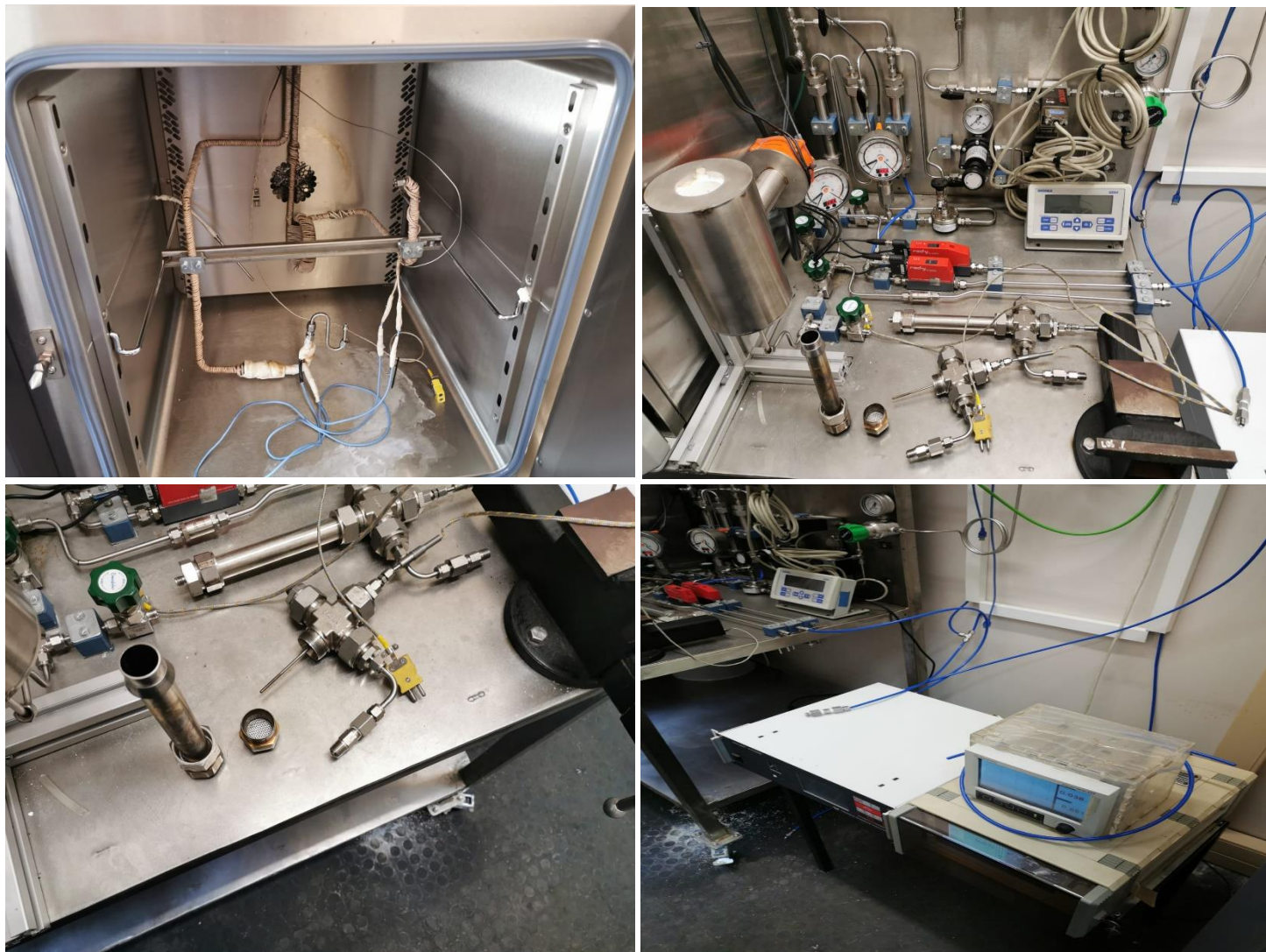
Figure 3-1: Experimental adsorption rate FBR setup in Laboratory G15 (NWU).
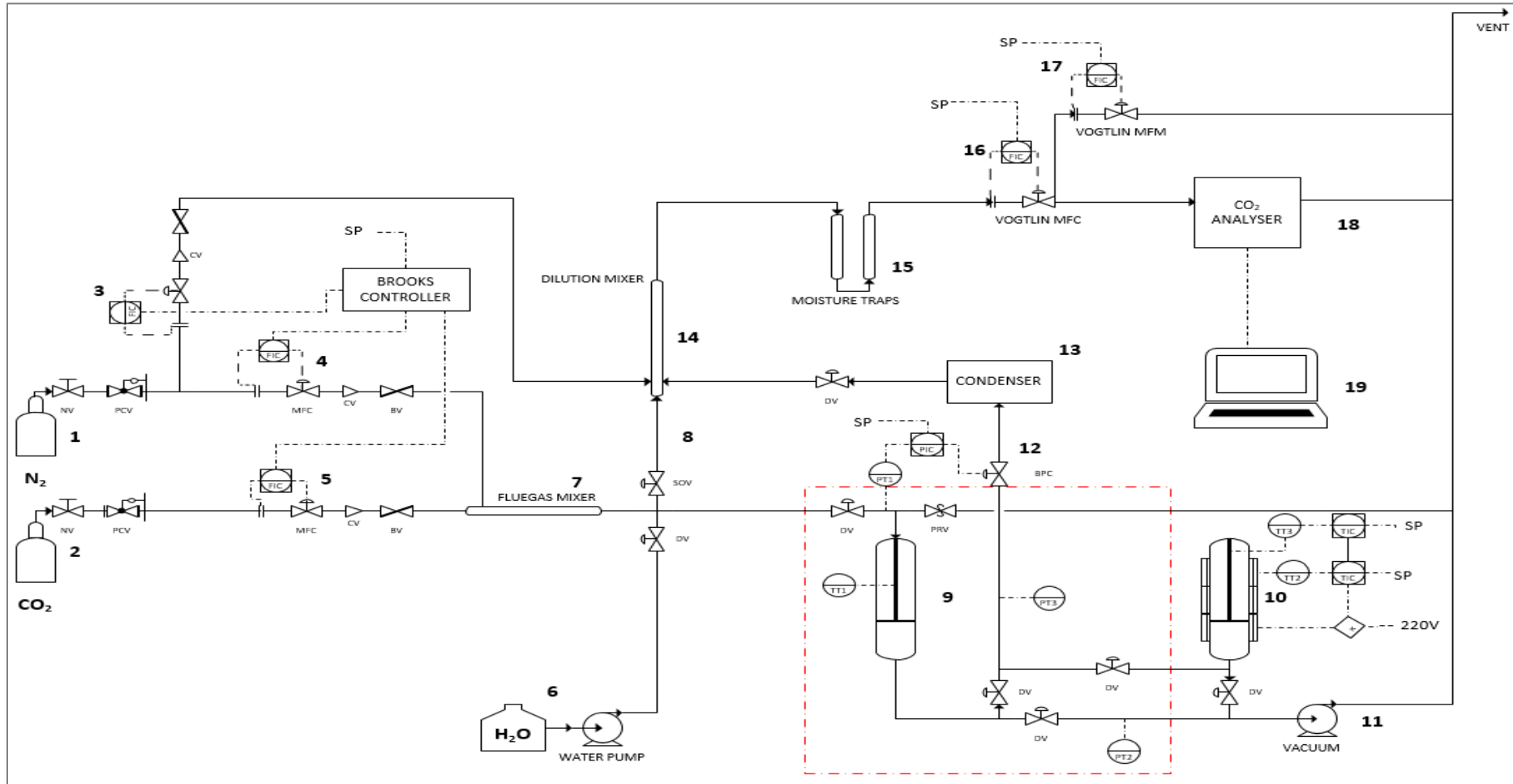
Figure 3-2: Experimental adsorption kinetic rate FBR setup P&ID. (1) N_2 gas cylinder, (2) CO_2 gas cylinder, (3, 4 and 5) mass flow controllers, (6) H_2O pump, (7) flue gas mixer, (8) by-pass line, (9) FBR, (10) degas port for FBR, (11) vacuum line, (12) BPC, (13) condenser, (14) dilution mixer, (15) moisture traps, (16) MFC, (17) mass flow meter (MFM), (18) CO_2 analyser and (19) computer.

3.5.2 EXPERIMENTAL PROCEDURE

The CO_2 analyser was calibrated prior to each experiment. This involved sending pure N_2 through the CO_2 analyser to obtain the minimum CO_2 concentration value and then sending it through a calibration gas with a known CO_2 concentration of 2.85 vol% (with the balance being N_2) to obtain the maximum CO_2 concentration. The calibration gas was obtained from Afrox (South Africa).

To prepare the adsorbent sample for experimentation, 3 g of the adsorbent sample was degassed in the FBR, where the FBR was placed in a tubular furnace, and maintained at 90 °C and under vacuum of 0.5 bar for 3 h.

The FBR is removed from the degassing pod and inserted in the oven. N_2 is used to purge the sample for 5 min and pressurize the FBR to 1 bar. A fixed flow rate of 250 mL/min and pressure of 1 bar were used for each experiment. The CO_2 flow rate was mixed with the dilution 1 N_2 flow rate and sent directly through the bypass line to be diluted again with the dilution 2 N_2 flow rate, and then to the CO_2 analyser, to ensure perfect dilution and steady-state concentration. The flow rates for each concentration (5 vol%, 15 vol% and 25 vol%) investigated are given in Table 3-4. After the set point temperature (40, 55, 70 and 85 °C) was reached in the FBR, the bypass line was closed and the gas fed to the FBR with the loaded sorbent.

Table 3-4: Operating flow rates for each CO_2 concentration investigated.

Gas	5 *vol%* CO_2	15 *vol%* CO_2	25 *vol%* CO_2
CO_2 flow rate, *mL/min*	12.5	37.5	62.5
Dilution 1 N_2 flow rate, *mL/min*	238	213	188
Dilution 2 N_2 flow rate, *mL/min*	750	1250	2250
Dilution to CO_2-analyser, *%*	1.25	2.50	2.50

3.5.3 INTRINSIC ADSORPTION KINETIC RATE MODELLING

The experimental concentration data obtained from the experimental adsorption rate FBR were processed, as discussed in Appendix A, to obtain a plot of a dimensionless quantity adsorbed (q_t/q_e) versus time measured in seconds. The experimental data were then modelled with the

adsorption rate models given in Table 2-8. The unknown adsorption rate parameters of the adsorption rate models, given in Table 2-8, were fitted and adjusted to the experimental data using non-linear regression analysis implemented in Excel with Excel Solver in combination with the ESS (Fylstra *et al.*, 1998; Raganati *et al.*, 2019; Shafeeyan *et al.*, 2015).

3.5.4   DIFFUSION ADSORPTION KINETIC RATE MODELS

The rate-limiting step was determined with the kinetic diffusion rate models, as further explained in this section.

3.5.4.1   BOYD'S FILM-DIFFUSION MODEL

To determine the adsorption-rate-controlling diffusion mechanism, a plot of B_t against time was evaluated. A linear line that does not pass through the origin or a non-linear plot concludes that the adsorption process is controlled by film diffusion. If the plot that passes through the origin is linear, the adsorption process is controlled by intraparticle diffusion.

3.5.4.2   INTERPARTICLE DIFFUSION MODEL

To determine whether interparticle diffusion is the rate-limiting step, a plot of $\ln(1-q_t/q_e)$ against time was examined. A linear line with slope $-\pi(D_c/r_p^2)$ and intercept $\ln(6/\pi^2)$ will indicate interparticle diffusion. If this is not the case (as observed from the plot), then the adsorption rate is controlled by another diffusion rate-limiting step.

3.5.4.3   INTRAPARTICLE DIFFUSION MODEL

To predict whether intraparticle diffusion is the rate-limiting step, a Weber-Morris plot of q_t against $t^{1/2}$ was evaluated. A linear line passing through the origin implies intraparticle diffusion takes place.

3.6 STATISTICAL ANALYSIS OF THE EXPERIMENTAL AND MODELLED DATA

The repeatability and reproducibility of the experimental adsorption capacity and adsorption kinetic data obtained from the Micromeritics ASAP 2020 and the FBR was calculated by repeating experiments at pre-determined conditions with regards to temperature and pressure. The repeats were then analysed with Equation 3-8, to determine the experimental error (Shafeeyan *et al.*, 2015).

$$\% \, Experimental \, Error = \frac{(95\% \, Conf. \, Int.) \times STDV \times 100}{Average} \tag{3-8}$$

Equation 3.8 utilizes a 95% confidence interval, where *STDV* represents the standard deviation of the experimental data and *Average* represents the average of the experimental data. The accuracy of the adsorption isotherm and kinetic models was analysed with a quality of fit (QOF%) performance for each adsorption isotherm model adsorption kinetic rate model applied to the experimental adsorption isotherm and rate data. The QOF% for each model was calculated with Equation 3-9

$$QOF\% = 100 \times \left[1 - \frac{\sum_1^N \frac{|x_{expt} - x|}{x_{expt}}}{N} \right] \tag{3-9}$$

where *N* represents the number of experimental data points, x_{expt} represents the experimental data value, and *x* represents the modelled data value (Shafeeyan *et al.*, 2015). An average relative error (ARE) was also calculated for each adsorption isotherm and rate model applied to the experimental adsorption isotherm and rate data. The ARE% of each adsorption isotherm and adsorption kinetic rate model was calculated using Equation 3-10 (Park *et al.*, 2016; Shafeeyan *et al.*, 2015).

$$ARE\% = \frac{100}{N} \sum_{i=1}^{N} \frac{|x_{expt} - x|}{x_{expt}}_i \tag{3-10}$$

Chapter 4

(ADSORBENT CHARACTERIZATION, ADSORPTION ISOTHERM MODELLING AND THERMODYNAMICS)

Chapter 4

(ADSORBENT CHARACTERIZATION, ADSORPTION ISOTHERM MODELLING AND THERMODYNAMICS)

This study comprises four aspects: adsorbent characterization, adsorption isotherm modelling, thermodynamic evaluation and adsorption rate modelling. The experimental results of adsorbent characterization, adsorption isotherm modelling and thermodynamic evaluation are addressed here (Chapter 4). The experimental adsorption rate results are discussed in the following chapter (Chapter 5).

4.1 ADSORBENT CHARACTERIZATION

First, results of adsorbent characterization are discussed: specifically results obtained for the proximate and ultimate analyses, surface area properties and scanning electron microscopy (SEM) analysis.

4.1.1 PROXIMATE AND ULTIMATE ANALYSES

The activation of carbon takes place at high temperatures, which dissipates remaining gases present in the sample; therefore, a low volatile matter content is observed for both activated carbon samples. The adsorption capability of the sorbents decreases with an increasing moisture content (Mayoral *et al.*, 2001). Therefore, a low inherent moisture content is desirable for maximum adsorption capability of the sorbents.

Ultimate analysis is a more comprehensive analysis of a sample; it breaks down the sample into its elemental composition of carbon, hydrogen content, nitrogen content and oxygen content.

The proximate and ultimate analysis results for the samples—CQ006, CQ30P, CQ650 and PCX1—are reported in Table 4-1, on an air-dried basis for the proximate analysis and on a dry ash-free basis for the ultimate analysis. CQ006 has the highest fixed carbon content of 87.9%

while PCX1 has the lowest fixed carbon content of 76.3%. CQ650 has the highest inherent moisture content of 6.50%, compared with the other activated carbon samples. The highest ash content was reported for the PCX1 sample at 18.6%.

On a dry-ash-free basis, CQ30P displayed the highest carbon content of 96.3%. PCX1 had the lowest carbon content of 87.5%. Regarding the carbon content results obtained from the ultimate analyses, CQ006, CQ30P and CQ650 compared well with each other.

Table 4-1: Proximate and ultimate analysis results for CQ006, CQ30P, CQ650 and PCX1.

Proximate analysis results (wt.%, air dried basis)				
Sample ID / properties	**CQ006**	**CQ30P**	**CQ650**	**PCX1**
Inherent moisture	6.10	4.10	6.50	2.73
Ash yield	2.40	9.70	4.00	18.60
Volatile matter	3.60	2.20	5.20	2.37
Fixed carbon	87.9	84.0	84.3	76.3
Ultimate analysis results (wt.%, dry ash free base)				
Sample ID / properties	**CQ006**	**CQ30P**	**CQ650**	**PCX1**
Carbon	95.20	96.30	94.10	87.5
Hydrogen	0.40	0.48	0.37	0.51
Nitrogen	0.43	0.59	0.48	0.37
Oxygen	3.84	2.11	4.89	11.42
Total sulphur	0.13	0.52	0.16	0.21

4.1.2 SURFACE AREA, PORE SIZE DISTRIBUTION, PORE VOLUME AND POROSITY ANALYSIS

The micropore size distribution was evaluated with CO_2 adsorption at 273 K. The micropore size distribution of CQ006, CQ30P, CQ650 and PCX1 is shown in Figure 4-1. CQ650 had the largest presence of micropores, PCX1 had the fewest. It is evident that CQ650 and CQ006 have well developed microporous architecture and structure.

Mesopores and macropores are evaluated with N_2 adsorption at 77 K and displayed in Figure 4-2. The significant spikes observed for PCX1, CQ006 and CQ30P at values lower than 100 Å, is a clear indication that a significant number of mesopores are present in these samples. No macropores were observed in CQ006, CQ30P and CQ650, but were observed in PCX1. The

pore size distribution analysis of CQ006, CQ30P, CQ650 and PCX1 differs immensely; therefore, a differences in surface area, pore volume and CO_2 adsorption capacity are expected.
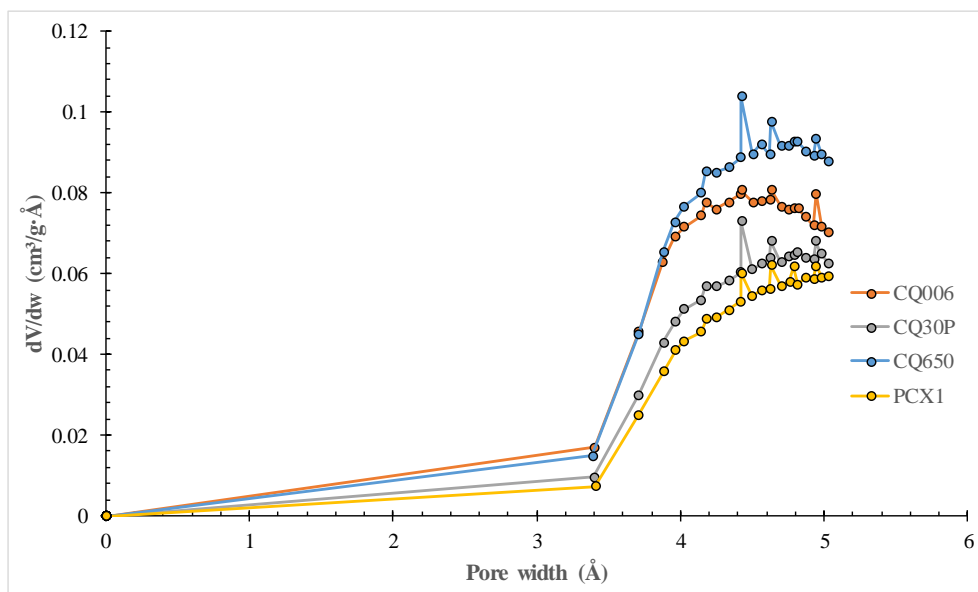
Figure 4-1: Micropore size distribution of CQ006, CQ30P, CQ650 and PCX1 evaluated from CO_2 adsorption at 273 *K*.
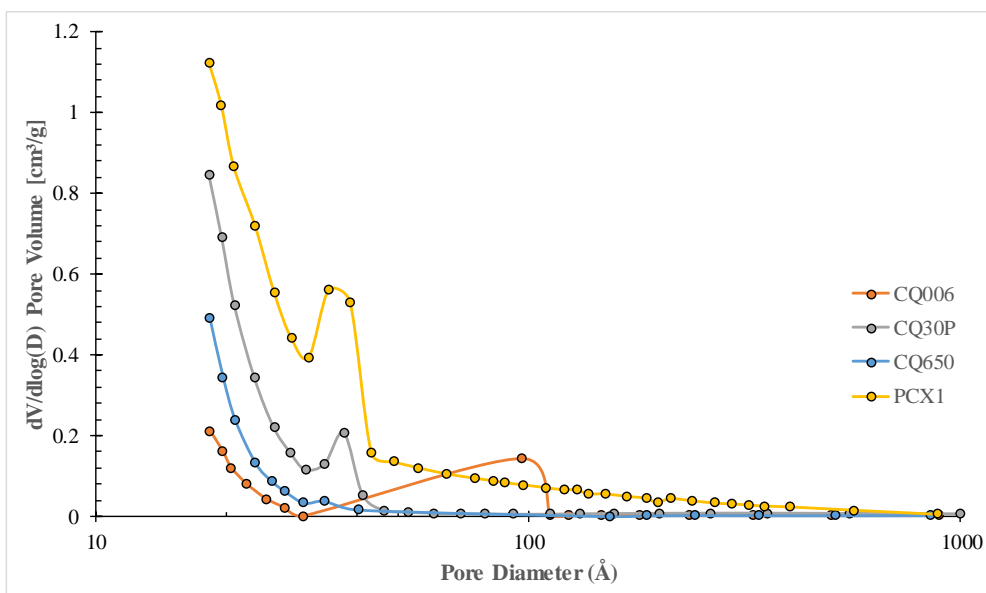
Figure 4-2: Pore size distribution of CQ006, CQ30P, CQ650 and PCX1 evaluated with N_2 adsorption at 77 *K*.

The micropore surface area of an adsorbent gives a good indication of its inherent porosity and potential CO_2 adsorption capacity. The adsorbent properties in terms of micropore surface area, Brunauer–Emmett–Teller (BET) surface area, average pore diameter, micropore volume and porosity are given in Table 4-2. CQ650 had the highest micropore surface area and BET surface area (735 and 517 m^2/g, respectively), therefore, CQ650 is expected to have the highest adsorption capacity.

The porosity is determined from the area under a pore volume (cm^3/g) versus pore width (Å) curve obtained from CO_2 adsorption at 273 *K*. This is displayed graphically Figure A- 7 (Appendix A). CQ006 had the highest porosity of 27.7%. CQ650 had a porosity of 26.3%. Although CQ650 is considered to have the most developed microporous architecture and structure, it did not display any mesopores (seen from Figure 4-2), while CQ006 had a significant number of micropores as well as mesopores. Therefore, a higher porosity was expected for the CQ006 adsorbent.

Table 4-2: Surface area, micropore volume, average pore diameter and porosity recorded for CQ006, CQ30P, CQ650 and PCX1.

	CQ006	CQ30P	CQ650	PCX1
D-R micropore surface area, *m^2/g*	671	532	735	454
BET surface area, *m^2/g*	473	369	517	316
H-K average pore diameter, *Å*	3.92	4.10	4.03	4.13
D-R limiting micropore volume, *cm^3/g*	0.170	0.118	0.177	0.0993
Porosity, *% ($3Å \leq d_p \leq 5$ Å)*	27.7	16.8	26.3	13.4

4.1.3   SCANNING ELECTRON MICROSCOPY ANALYSIS

SEM images of CQ006, CQ30P, CQ650 and PCX1 were obtained from the North-West University Laboratory for Electron Microscopy (LEM), Potchefstroom. The micrographs of the activated carbon samples (used as received) are shown in Figure 4-3 to Figure 4-6. The images show a heterogeneous and irregular surface morphology with a well-developed pore structure. The external surface shows intricate cracks and crevices with different pore shapes and sizes over the entire surface of the activated carbon samples. The samples have different particle sizes—the difference is clearly visible on the micrographs. The CQ30P has the largest particle sizes ranging from 3 – 5 mm, CQ650 with a particle size of 1 – 3 mm, CQ006 with a

particle size of 0.5 – 1.5 mm and PCX1 with the smallest particle sizes with a d_{50} of 42 µm. The d_{50} of PCX1 was determined with a Malvern Mastersizer at the North-West University.
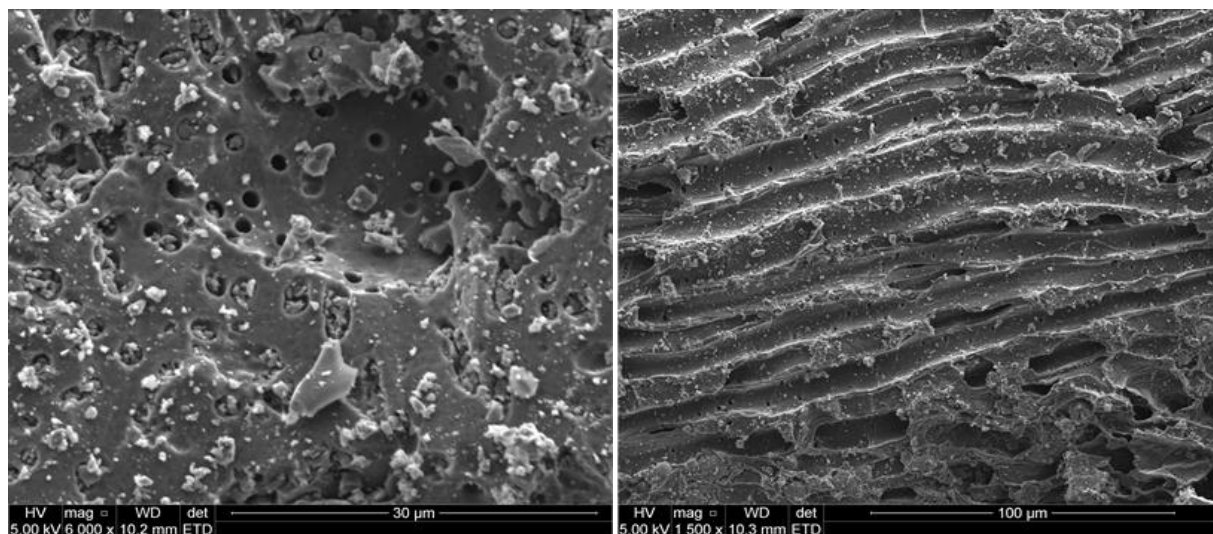
Figure 4-3: SEM micrographs of CQ006.
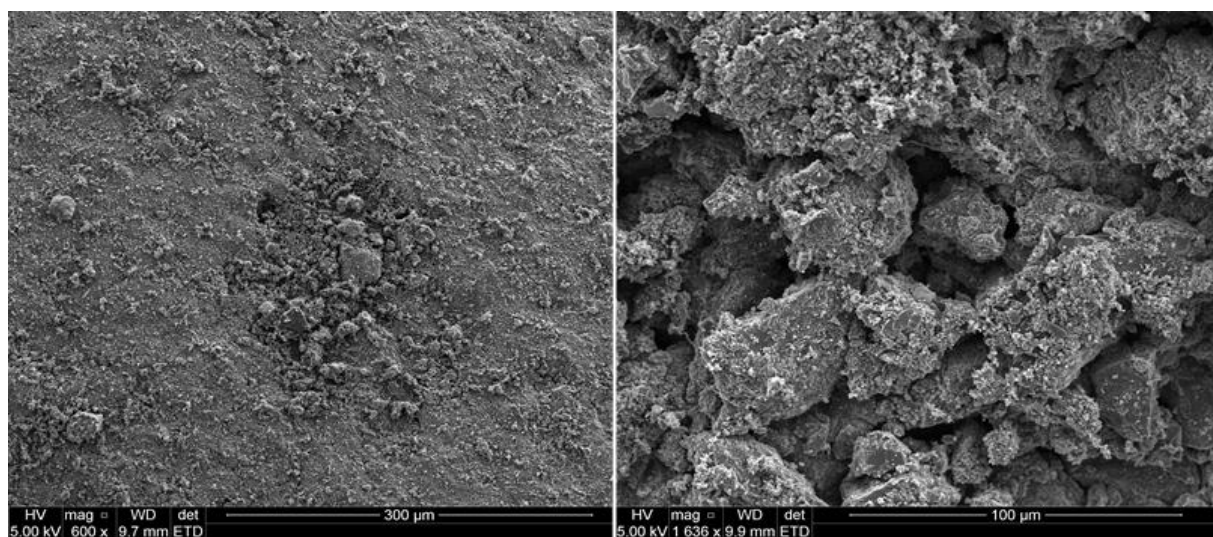
Figure 4-4: SEM micrographs of CQ30P.
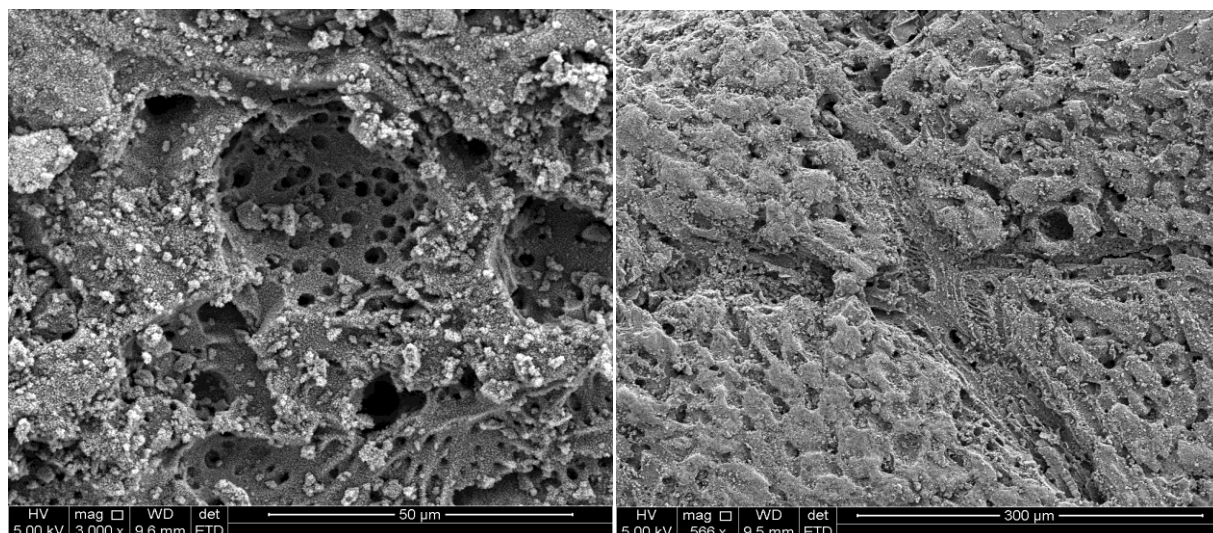
Figure 4-5: SEM micrographs of CQ650.
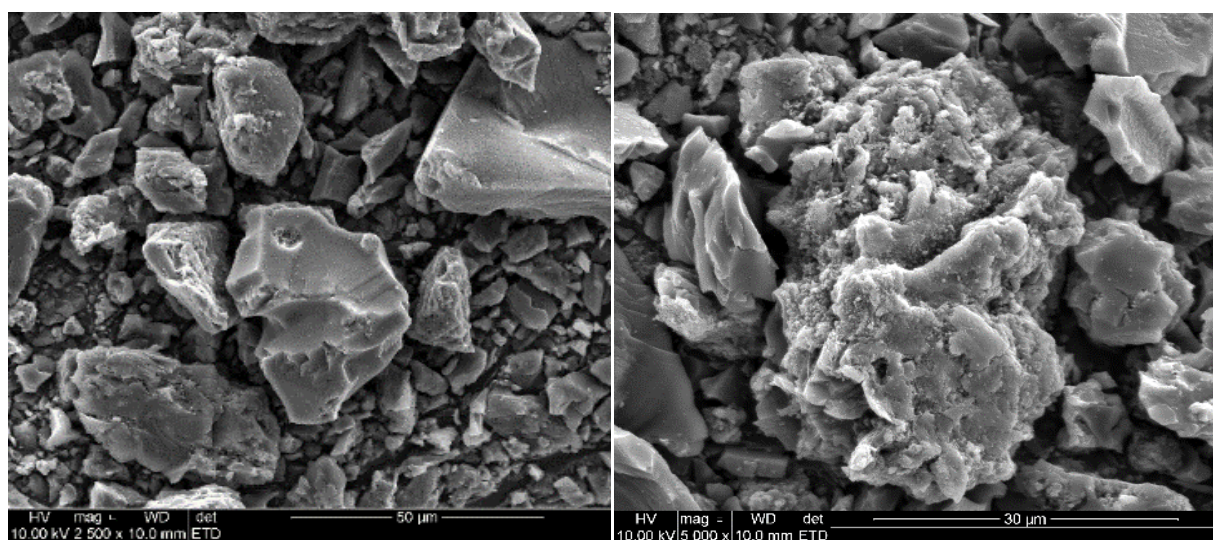
Figure 4-6: SEM micrographs of PCX1.

4.1.4   ACTIVATED CARBON CHARACTERIZATION RESULTS RECORDED IN THIS STUDY COMPARED WITH RESULTS FOUND IN LITERATURE

Results of the characterization of the activated carbon samples that were investigated in this study compared rather well with characterization results reported for other activated carbon, silica and zeolite samples as reported in literature. See Table 4-3.

Shafeeyan *et al.* (2015) investigated the equilibrium adsorption of CO_2 on ammonia-modified activated carbon samples and reported the activated carbon sample (GAC) with a BET surface area of 768 m^2/g, which is greater than what was experimentally obtained for the activated carbon samples investigated in the present study. The adsorbent with the highest BET surface area investigated in the present study was CQ650, with a BET surface area of 517 m^2/g, which is smaller than what was reported for GAC.

The ash and carbon content reported for sample GAC was 5.2% and 92.4%, respectively, which agrees well with the ash and carbon content obtained for CQ006, CQ30P and CQ650. The commercially available activated carbon sample Norit SX2, investigated by Rashidi *et al.* (2016), in his study of the isotherm and thermodynamic analysis of CO_2 on activated carbon samples, had a BET surface area of 660 m^2/g and a pore volume of 0.67 cm^3/g. The BET surface area and pore volume are significantly greater than the values reported for the activated carbon samples investigated in this study.

The activated carbon sample F50, investigated by Balsamo *et al.* (2013), had the highest BET surface area and pore volume, 1071 m^2/g and 0.486 cm^3/g, respectively. A carbon content of 90.9% was obtained for F50, which agrees well with the samples investigated in this study.

The CO_2 adsorption on zeolite 13X, 4A and 5A was determined by Hauchhum and Mahanta (2017). Surface areas of 720, 650 and 434 m^2/g, respectively, were reported. Here, zeolite 13X and 5A outperformed the activated carbons. Both CQ006 and CQ650 had greater BET surface areas than did zeolite 4A. Results of the CO_2 adsorption investigation conducted by Heydari-Gorji and Sayari (2011) on silica adsorbent samples compared well with the activated carbon samples investigated in the present study.

Table 4-3: Adsorbent characterization: Comparison of results recorded in the present study with the results reported in literature.

Sample type	Sample name	Activation method	Sorbent size, μm	Commercially Available [Y/N]	Pressure, bar	Temperature range, °C	BET surface area, m^2/g	Average pore diameter, nm	Pore volume, cm^3/g	Ash content, %	C, %	N, %	H, %	S, %	O, %	Author(s)
Activated carbon	CQ006	Steam, acid washed	1000-3000	Y	1.0	40-85	473.0	0.39	0.17	2.40	95.20	0.43	0.40	0.13	3.80	
Activated carbon	CQ30P	Steam, KOH impregnated	1000-3000	Y	1.0	40-85	369.0	0.41	0.12	9.70	96.30	0.59	0.48	0.52	2.12	This study
Activated carbon	CQ650	Steam, KOH impregnated	1000-3000	Y	1.0	40-85	517.0	0.40	0.18	4.00	94.10	0.48	0.37	0.16	4.87	
Activated carbon	PCX1	Chemically activated	42	Y	1.0	40-85	316.0	0.41	0.099	18.6	87.500	0.365	0.510	0.206	11.4	
Activated carbon	GAC	Ammonia-modified	20 - 35	Y	1.0	30	768.0	-	0.39	5.20	92.40	0.30	1.20	0.20	5.90	Shafeeyan et al. (2015)
Activated carbon	DARCO FGD	-	0.39	N	1.0	18-130	1060.0	-	-	-	-	-	-	-	-	Ammendola et al. (2017)
Activated carbon	C-500	HMMM resin	0.045	N	1.0	30-100	-	3.50	-	2.88	63.90	21.20	1.90	-	12.90	
Activated carbon	C-600	HMMM resin	0.045	N	1.0	30-100	-	3.50	-	3.65	63.10	15.90	2.60	-	18.40	Goel et al. (2016)
Activated carbon	C-700	HMMM resin	0.045	N	1.0	30-100	463.0	3.50	0.48	2.91	61.70	13.60	1.40	-	23.20	
Activated carbon	C-800	HMMM resin	0.045	N	1.0	30-100	112.0	3.50	0.120	2.67	64.20	9.200	1.90	-	24.70	
Activated carbon	Norit® SX2	Steam activated & acid wash	-	Y	1.0	25-120	660.7	4.05	0.67	-	77.48	0.33	1.61	0.05	20.53	Rashidi et al. (2016)
Activated carbon	AC1	Washed, 2N HCL	-	Y	0 - 20	25-200	856.0	-	-	-	-	-	-	-	-	Çağlayan and Aksoylu (2016)
Activated carbon	AC4-200	Impregnated, Na2CO3	-	Y	0 - 20	25-200	687.0	-	-	-	-	-	-	-	-	
Zeolite	13X	-	2000	Y	1.0	25-60	720.0	10.00	-	-	-	-	-	-	-	Hauchhum and Mahanta (2014a)
Activated carbon	Coconut fibre	-	920	N	1.0	25-60	214.0	-	0.068	4.8	41.280	-	-	-	-	
Zeolite	4A	-	1500	Y	1.0	25-60	434.0	4.00	-	-	-	-	-	-	-	
Zeolite	13X	-	2000	Y	4.0	25-60	720.0	10.00	-	-	-	-	-	-	-	Hauchhum and Mahanta (2017)
Zeolite	5A	-	2000	Y	4.0	25-60	650.0	5.00	-	-	-	-	-	-	-	
Zeolite	4A	-	1500	Y	4.0	25-60	434.0	4.00	-	-	-	-	-	-	-	
Activated carbon	Coconut fibre	-	920	N	4.0	25-60	354.0	1.50	-	-	-	-	-	-	-	
Silica	PME	-	-	Y	1.0	25-75	570.0	-	1.590	-	-	-	-	-	-	Heydari-Gorji and Sayari (2011)
Silica	PME-PEI(20)	-	-	Y	1.0	25-75	269.0	-	0.68	-	-	-	-	-	-	
Silica	PME-PEI(30)	-	-	Y	1.0	25-75	16.7	-	0.040	-	-	-	-	-	-	
Silica	PME-PEI(50)	-	-	Y	1.0	25-75	<1	-	<0.005	-	-	-	-	-	-	
Activated carbon	F50	Steam	1800–2360	Y	1.0	30-80	1071.0	-	0.486	-	90.9	0.900	4.95	0.500	2.75	Balsamo et al. (2013)

4.2 ADSORPTION ISOTHERM MODELLING

The experimental adsorption isotherm data of the four activated carbon samples (CQ006, CQ30P, CQ650 and PCX1) obtained from experimental work (discussed in Section 3.3) was modelled with eight adsorption isotherm models: Langmuir, BET, Dubinin-Radushkevich (D-R), Dubinin-Astakhov (D-A), Toth, Freundlich, Temkin and SIPS. The fitted adsorption isotherm model parameters and goodness of fit for each adsorption isotherm model are now discussed.

4.2.1 SELECTING THE MOST ACCURATE ADSORPTION ISOTHERM MODEL

The adsorption mechanisms employed in the Langmuir, BET, SIPS, Freundlich and Toth adsorption isotherm models are monolayer adsorption (Langmuir), multilayer adsorption (BET, Freundlich and Temkin) and a combination of monolayer and multilayer adsorption (SIPS and Toth) (Ammendola *et al.*, 2017; Brunauer *et al.*, 1938; Garnier *et al.*, 2011; Langmuir, 1916; LeVan *et al.*, 1997; Park *et al.*, 2016; Ruthven, 2006; Shafeeyan *et al.*, 2015; Temkin, 1940). The adsorption mechanism employed by the D-R and D-A adsorption isotherm models extends the Polanyi theory to micropore filling. CO_2 adsorption takes place in micropores; it adheres to the theory of micropore filling (Dubinin & Astakhov, 1971; Dubinin, 1975; Nguyen & Do, 2001; Tsai *et al.*, 2000).

The adsorption isotherm models were fitted to the experimental CO_2 adsorption isotherm data of CQ650 at 0, 10, 20 and 30 ℃; see Figure 4-7. The adsorption isotherm model parameters for all the fitted adsorption isotherm models to the experimental CO_2 adsorption isotherm data of CQ650 at 0, 10, 20 and 30 ℃ are given in Table 4-4.

The best fitting adsorption isotherm models with regard to quality of fit (QOF%) and average relative error (ARE%) were found to be D-R, D-A, Toth and SIPS, with their maximum adsorption capacity at each experimental adsorption temperature given in Table 4-5. The Toth adsorption isotherm model was discarded from the study because the maximum adsorption quantity determined from the adsorption isotherm model did not correlate with the maximum adsorption capacity determined from D-R, D-A and SIPS. D-R presents two parameters to be fitted and adjusted to the experimental adsorption isotherm data, while both D-A and SIPS

present three parameters each to be fitted and adjusted to the experimental adsorption isotherm data. The viability of the D-A and SIPS adsorption isotherm models were tested by fixing q_{DA} and q_{SIPS} to 18, 20 and 22 mmol/g and fitting D_{DA} and n for the D-A adsorption isotherm model and m and K_{SIPS} for the SIPS adsorption isotherm model; results are given in

Table 4-6.

It was observed that the averages for QOF% and ARE%, 94.62% and 0.83%, respectively, were obtained for the D-A adsorption isotherm model; while 96.97% and 0.13%, respectively, were obtained for the SIPS adsorption isotherm model. Because a great fit is still obtained for the individual adsorption isotherm models at fixed values of 18, 20 and 22 mmol/g for q_{DA} and q_{SIPS}, the D-A and SIPS adsorption isotherm models were discarded; they were considered biased. Increasing the number of parameters to be solved will increase the accuracy of the model. Although more accurate ARE% and QOF% was obtained, inconsistencies were noted in the parameters leading to the conclusion that they should be discarded. Thus, the D-R
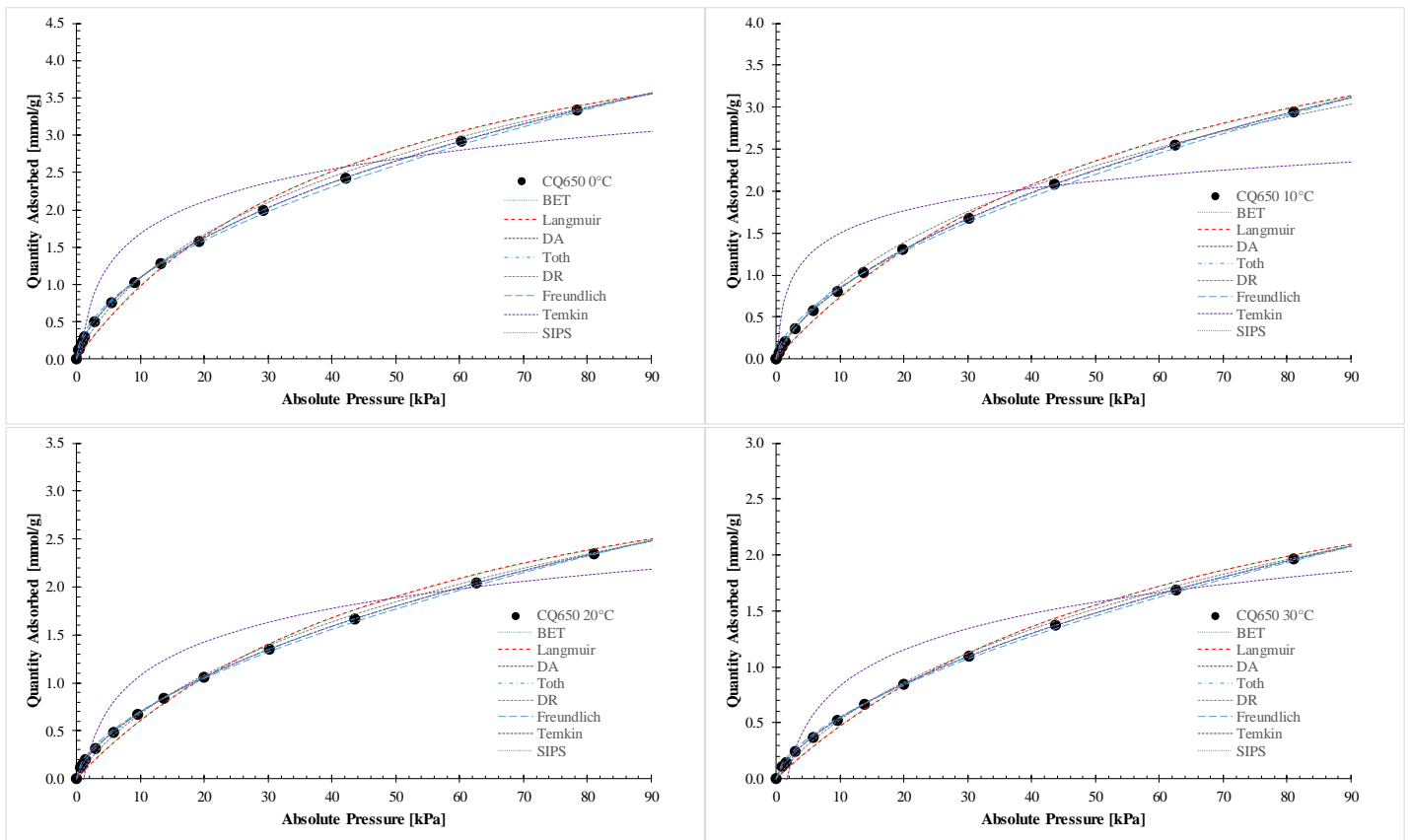
Figure 4-7: Experimental CO_2 adsorption isotherm data of CQ650 at 0, 10, 20 and 30 °C modelled with Langmuir, BET, D-A, D-R, Toth, Freundlich, Temkin and SIPS adsorption isotherm models.

adsorption isotherm model will hereafter be employed to model all of the experimental CO_2 adsorption isotherm data, as described in this section.

Table 4-4: Experimental CO_2 adsorption isotherm data of CQ650 at 0, 10, 20 and 30 °C modelled with Langmuir, BET, D-A, D-R, Toth, Freundlich, Temkin and SIPS adsorption isotherm model (AIM) parameters.

AIM	Parameter	0 °C	10 °C	20 °C	30 °C
Langmuir	q_L, *mmol/g*	5.340	5.313	4.121	3.720
	K_L, *1/kPa*	0.02218	0.01602	0.01714	0.01437
	ARE%	10.68	6.97	7.05	4.64
	QOF%	77.87	78.96	81.76	85.29
BET	P_o, *kPa*	3485	4501	5727	7211
	C	83.90	77.79	103.6	109.6
	q_{BET}, *mmol/g*	5.019	5.010	3.945	3.563
	ARE%	10.28	6.700	6.863	4.539
	QOF%	78.32	79.40	82.04	85.59
D-R	P_o, *kPa*	3485	4501	5727	7211
	q_{DR}, *mmol/g*	7.598	7.148	6.553	6.240
	D_{DR}	0.2387	0.2363	0.2373	0.2391
	ARE%	5.337	5.112	3.550	2.297
	QOF%	86.27	87.63	89.16	91.50
D-A	P_o, *kPa*	3485	4501	5727	7211
	q_{DA}, *mmol/g*	12.91	12.85	12.29	12.53
	D_{DA}	0.3282	0.3239	0.3383	0.3493
	n_{DA}	1.385	1.473	1.381	1.374
	ARE%	0.3501	0.09379	0.3187	0.2107
	QOF%	98.97	96.45	98.62	99.08
Toth	K_{TOTH}, *1/kPa*	0.01397	0.00458	0.00530	0.002838
	t_T	0.1727	0.1940	0.1750	0.1825
	q_T, *mmol/g*	176.1	176.0	190.8	191.6
	ARE%	0.5217	0.5554	0.4009	0.2457
	QOF%	98.47	96.01	98.33	98.87
Freundlich	k_F, *mmol/g.kPa$^{(1/n)}$*	0.3162	0.2188	0.1858	0.1373
	n_F	1.856	1.695	1.736	1.656
	ARE%	3.711	0.000	2.113	1.496
	QOF%	91.34	80.08	94.68	95.47
Temkin	K_{TEM}, *1/kPa*	1.470	4.810	0.832	0.588
	B	0.6241	0.3866	0.5072	0.4679
	ARE%	39.48	54.85	27.08	19.12
	QOF%	17.08	-1828	36.26	41.87
SIPS	K_{SIPS}, *1/kPa*	0.002000	0.001929	0.001327	0.001663
	m_{SIPS}	1.568	1.447	1.519	1.433

qSIPS, *mmol/g*	14.2084	13.5879	12.5614	9.9196
ARE%	0.0482	0.2611	0.0082	-0.0427
QOF%	99.42	95.49	99.68	99.53

Table 4-5: D-R, D-A, Toth and SIPS adsorption isotherm models with maximum adsorption capacity at 0, 10, 20 and 30 °C, average relative error (ARE%) and quality of fit (QOF%).

AIM	Parameter	0 °C	10 °C	20 °C	30 °C
D-R	**q**DR, *mmol/g*	7.598	7.148	6.553	6.240
	ARE%	5.337	5.112	3.550	2.297
	QOF%	86.27	87.63	89.16	91.50
D-A	**q**DA, *mmol/g*	12.91	12.85	12.29	12.01
	ARE%	0.3501	0.09379	0.3187	0.2028
	QOF%	98.97	96.45	98.62	98.87
Toth	**q**T, *mmol/g*	176.1	176.0	190.8	191.6
	ARE%	0.5217	0.5554	0.4009	0.2457
	QOF%	98.47	96.01	98.33	98.87
SIPS	**q**SIPS, *mmol/g*	14.2084	13.5879	12.5614	9.9196
	ARE%	0.0482	0.2611	0.0082	-0.0427
	QOF%	99.42	95.49	99.68	99.53

Table 4-6: The D-A and SIPS adsorption isotherm model parameters, when fixing q_{DA} and q_{SIPS} to 18, 20 and 22 mmol/g.

AIM	Parameter	q DA, q SIPS = 18 *mmol/g*	q DA, q SIPS = 20 *mmol/g*	q DA, q SIPS = 22 *mmol/g*
D-A	**P**o, *kPa*	3485	3485	3485
	qDA, *mmol/g*	18.00	20.00	22.00
	DDA	0.4125	0.4453	0.4779
	nDA	1.170	1.115	1.070
	ARE%	2.0458	0.4117	0.0235
	1-ESS	0.991	0.986	0.981
	QOF%	95.95	94.66	93.26
SIPS	**K**SIPS, *1/kPa*	0.001140	0.000891	0.000715
	mSIPS	1.629	1.652	1.671
	qSIPS, *mmol/g*	18.0000	20.0000	22.0000
	ARE%	0.3076	0.0638	0.0097
	1-ESS	0.9983	0.9970	0.9956
	QOF	97.67	97.00	96.26

4.2.2 CO₂ ADSORPTION ISOTHERM MODELLING

The experimental adsorption isotherm data obtained for CQ006, CQ30P, CQ650 and PCX1 at 0, 10, 20, 30, 40 and 55 °C was modelled with the D-R adsorption isotherm model; see Figure 4-8. A summary of the maximum adsorption capacities for CQ006, CQ30P, CQ650 and PCX1 is given in Table 4-7. The D-R model parameters for CQ006, CQ30P, CQ650 and PCX1 at 0, 10, 20, 30, 40 and 55 °C, is given in Table 4-8.
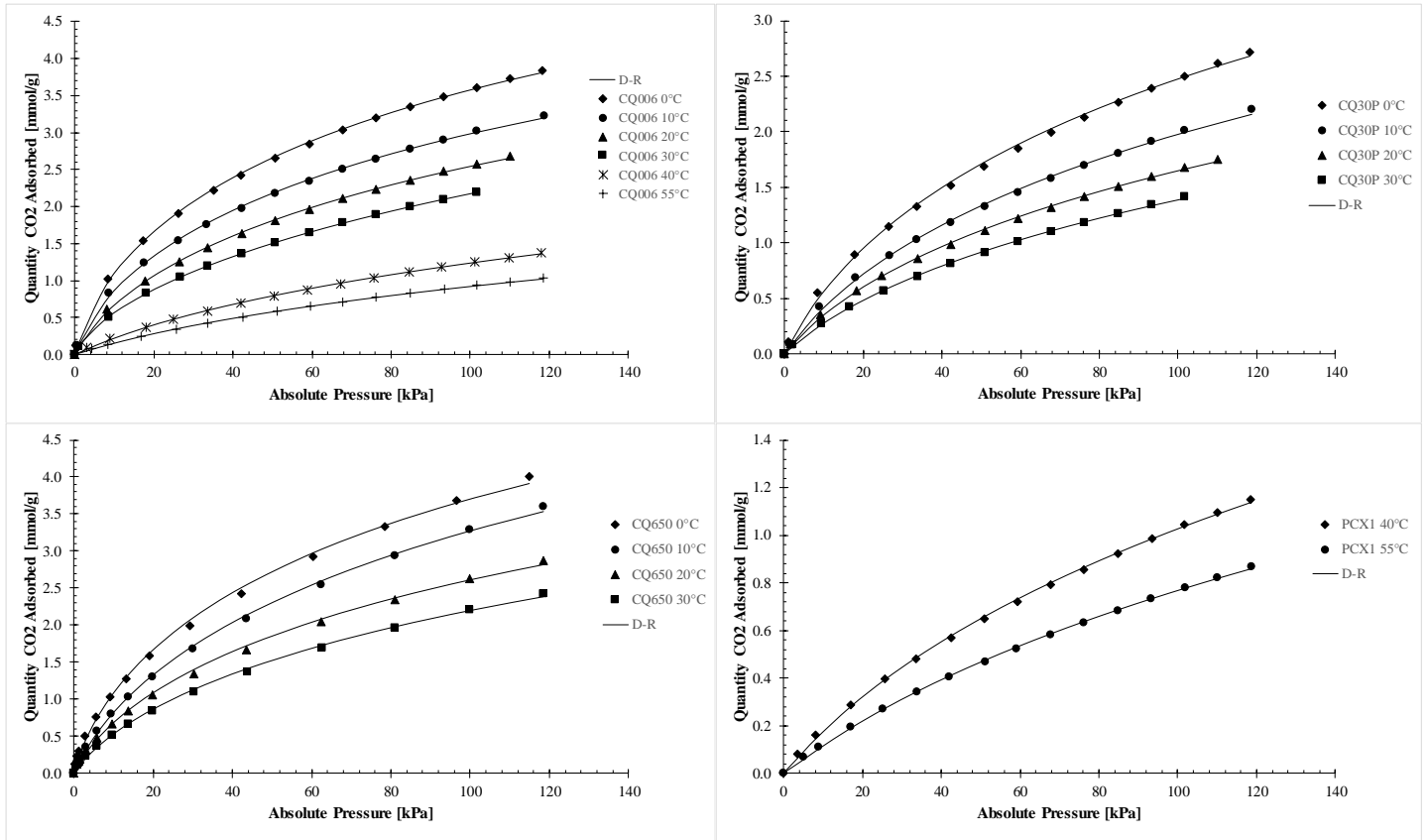
Figure 4-8: Experimental adsorption isotherm data at 0, 10, 20, 30, 40 and 55 °C for samples CQ006, CQ30P, CQ650 and PCX1 modelled with the D-R adsorption isotherm model.

Table 4-7: Maximum adsorption capacity (q_{DR}) determined with the D-R adsorption isotherm model for CQ006, CQ30P, CQ650 and PCX1 at 0, 10, 20, 30, 40 and 55 °C.

Sample	0 °C	10 °C	20 °C	30 °C	40 °C	55 °C
CQ650	7.598	7.148	6.553	6.240	-	-
CQ006	7.143	6.572	6.369	5.947	4.728	4.207
CQ30P	5.859	5.329	4.771	4.543	-	-
PCX1	-	-	-	-	4.090	3.829

It is evident that the adsorption quantity of the experimental adsorption isotherm data of CQ006, CQ30P, CQ650 and PCX1 at 0, 10, 20, 30, 40 and 55 °C decreases as the temperature increases. The weak adsorption forces adsorbing the CO_2 onto the adsorbent is overcome when the gas has increased kinetic energy at the higher temperatures; therefore, the CO_2 adsorption quantity decreases as the temperature increases. A similar observation has been reported by Ammendola *et al.* (2017), Goel *et al.* (2016), Heydari-Gorji and Sayari (2011) and Shafeeyan *et al.* (2015).

Table 4-8: Experimental adsorption isotherm data at 0, 10, 20, 30, 40 and 55 °C for samples CQ006, CQ30P, CQ650 and PCX1 modelled with the D-R adsorption isotherm model parameters.

Sample	Parameters	0 °C	10 °C	20 °C	30 °C	40 °C	55 °C
CQ006	P_o, kPa	3485	4501	5727	7211	8967	12131
	q_{DR}, mmol/g	7.143	6.572	6.369	5.947	4.728	4.207
	D_{DR}	0.2343	0.2336	0.2365	0.2352	0.2576	0.2565
	ARE%	2.103	1.769	1.399	0.990	0.698	0.405
	QOF%	95.91	96.08	96.55	96.71	97.42	98.02
CQ30P	P_o, kPa	3485	4501	5727	7211	-	-
	q_{DR}, mmol/g	5.859	5.329	4.771	4.543	-	-
	D_{DR}	0.2617	0.2614	0.2546	0.2544	-	-
	ARE%	2.503	1.884	1.221	0.717	-	-
	QOF%	95.13	95.45	96.66	97.20	-	-
CQ650	P_o, kPa	3485	4501	5727	7211	-	-
	q_{DR}, mmol/g	7.598	7.148	6.553	6.240	-	-
	D_{DR}	0.2387	0.2363	0.2373	0.2391	-	-
	ARE%	5.337	5.112	3.550	2.297	-	-
	QOF%	86.27	87.63	89.16	91.50	-	-
PCX1	P_o, kPa	-	-	-	-	8967	12131
	q_{DR}, mmol/g	-	-	-	-	4.090	3.829
	D_{DR}	-	-	-	-	0.2615	0.2642
	ARE%	-	-	-	-	0.769	0.463
	QOF%	-	-	-	-	97.07	97.47

Results in Table 4-7 and Figure 4-9 indicate that CQ650 has the highest adsorption capacity, ranging from 7.598 to 4.543 mmol/g over the temperature range 0–30 °C, compared with the other adsorbent samples. CQ006 has the second highest adsorption capacity, ranging from 7.143 to 4.207 mmol/g over the entire temperature range considered here (0–55 °C). The decrease in adsorption capacity with an increase in temperature is attributed to the increased kinetic ability of the gas at higher temperature.

A total experimental error of 1.75% was determined for the experimental CO_2 adsorption isotherm data done on the CQ650 sample at 10 °C.
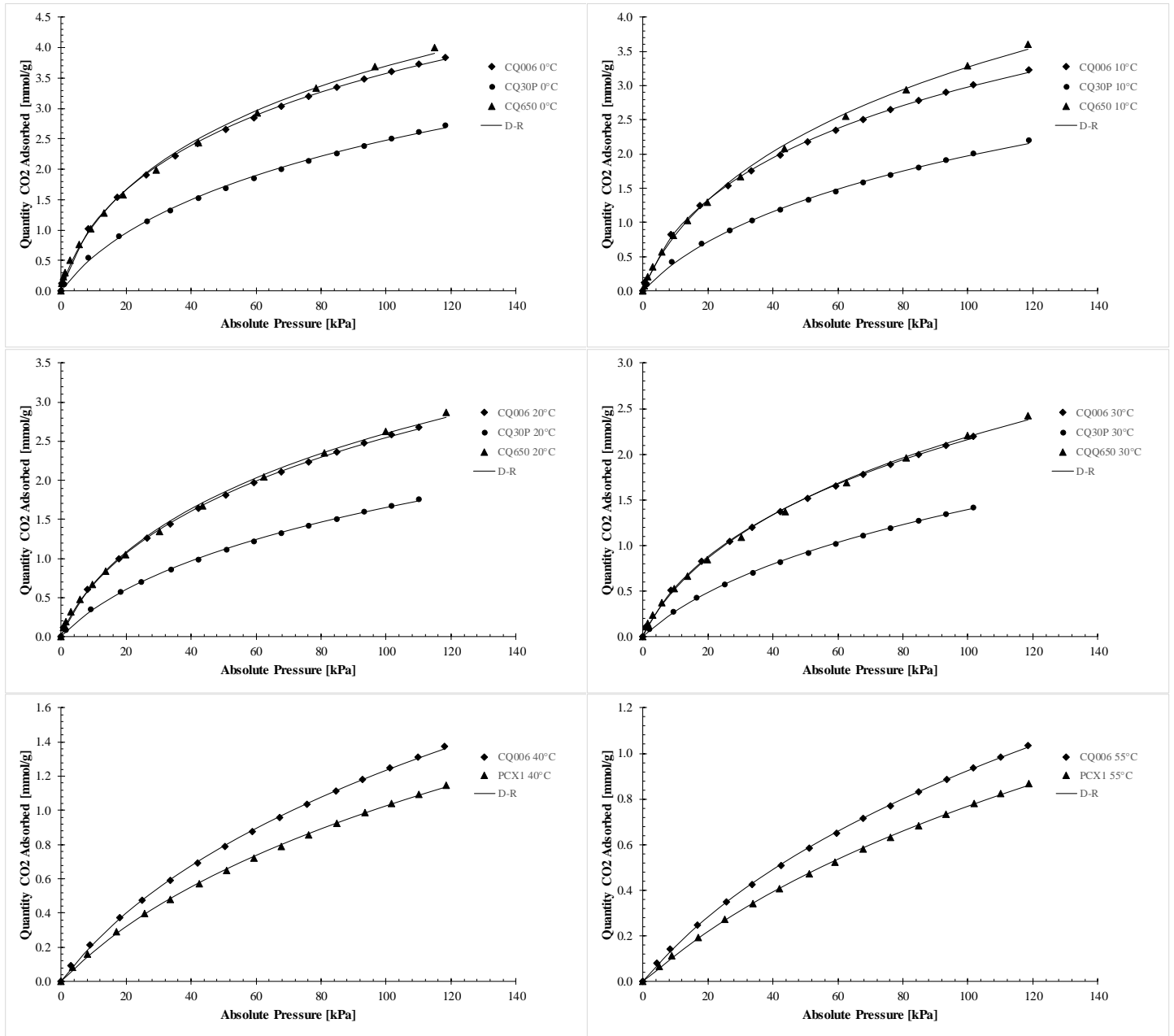
Figure 4-9: Experimental adsorption isotherm data of CQ006, CQ30P, CQ650 and PCX1 compared with each other at 0, 10, 20, 30, 40 and 55 °C, modelled with the D-R adsorption isotherm model.

4.2.3   COMPARISON WITH LITERATURE

The maximum adsorption capacity determined with the D-R adsorption isotherm model, q_{DR}, measured in mmol/g, compares well with adsorption isotherm results reported in literature for activated carbon and zeolite samples. A summary of the adsorption isotherm results determined in this study and what is reported in literature is given in Table 4-9.

Çağlayan and Aksoylu (2016) studied the adsorption of CO_2 on chemically modified activated carbon samples. Chemical activations such as HNO_3 oxidation, alkali impregnation, air oxidation and heat treatment under a He atmosphere were applied to the activated carbon samples to determine the effect of the activation methods on the adsorption capacity and kinetic behaviour. The adsorption capacity was determined in the temperature range 25–200 °C and pressure range 0–20 bar. The activated carbon samples AC4-200 and AC4-250 were impregnated with 10% Na_2CO_3 and calcined in a 5% O_2 atmosphere at 200 and 250 °C, respectively. The highest adsorption capacities for AC4-200 and AC4-250 were reported as 6.77 and 6.06 mmol/g at 25 °C and 1 bar, respectively. This is in good agreement with the maximum adsorption capacity of CQ006 and CQ650, determined as 6.55 and 6.37 mmol/g at 20 °C and 1 bar, respectively. The activated carbon sample studied by Çağlayan and Aksoylu (2016) outperformed the activated carbon samples investigated in this study.

Hauchhum and Mahanta (2017) investigated CO_2 adsorption onto zeolite samples (13X, 4A and 5A) in a bubbling fluidized bed reactor. The adsorption experiments were conducted in the temperature range 25–60 °C, at a pressure of 4 bar and an inlet CO_2 concentration of 13.8 vol%. The best performing zeolite sample was 13X; adsorption capacity was 6.24 mmol/g at 25 °C and 4 bar. The 13X zeolite sample outperformed the CQ006 activated carbon sample, but not the CQ650 sample.

Table 4-9: Adsorption isotherm results obtained from literature to compare to the results obtained in this study.

Sample type	Sample name	Pressure, *bar*	Temperature range, *°C*	Inlet CO_2 concentration, *vol%*	Adsorption Isotherm Model	Temperature, *°C*	Maximum adsorption capacity, *mmol/g*	AIM parameter symbol	AIM parameter value	AIM parameter symbol	AIM parameter value	Author(s)
Activated carbon	CQ006	1	0-55	100	D-R	0 10 20 30 40 55	7.14 6.57 6.37 5.95 4.73 4.21	q_{DR}, *mmol/g*	7.14 6.57 6.37 5.95 4.73 4.21	D_{DR}	0.234 0.234 0.237 0.235 0.258 0.257	**This study**
Activated carbon	CQ30P	1	0-30	100	D-R	0 10 20 30	5.86 5.33 4.77 4.54	q_{DR}, *mmol/g*	5.86 5.33 4.77 4.54	D_{DR}	0.262 0.261 0.255 0.254	
Activated carbon	CQ650	1	0-30	100	D-R	0 10 20 30	7.60 7.15 6.55 6.20	q_{DR}, *mmol/g*	7.60 7.15 6.55 6.24	D_{DR}	0.239 0.236 0.237 0.239	
Activated carbon	PCX1	1	40-55	100	D-R	40 55	4.09 3.83	q_{DR}, *mmol/g*	4.09 3.83	D_{DR}	0.262 0.264	
Activated carbon	AC4-250	0 - 20	25-200	-	D-R	25 180 200	6.77 4.62 2.01	q_{DR}, *mmol/g*	6.77 4.62 2.01	D_{DR}	0.296 0.612 0.783	Çağlayan and Aksoylu (2016)
Activated carbon	AC4-200	0 - 20	25-200	-	D-R	25 120 200	6.06 3.14 1.73	q_{DR}, *mmol/g*	6.06 3.14 1.73	D_{DR}	0.300 0.547 0.781	
Activated carbon	DARCO FGD	1	18-130	15.0	Freundlich	18 40 70 100 130	0.508 0.411 0.394 0.306 0.267	K_F, *mmol/g.atm$^{1/n}$*	0.913 0.788 0.725 0.674 0.500	n	2.52 1.91 1.48 1.23 1.16	Ammendola *et al.* (2017)
Activated carbon	C-700	1	30-100	100	Temkin	30 50 75 100	0.800 0.483 0.424 0.284	K_T, *1/bar*	1054 178 118 44.1	b, *kJ/mol*	22.0 29.2 32.5 43.2	Goel *et al.* (2016)
Activated carbon	Norit® SX2	1	25-120	-	Freundlich	25 50 100	1.88 1.29 0.610	K_F, *mmol/g.atm$^{1/n}$*	1.77 1.17 0.525	n	1.69 1.45 1.20	Rashidi *et al.* (2016)
Activated carbon	ACF	1	50-90	100	Freundlich	50 70 90	0.350 - -	K_F, *mmol/g.atm$^{1/n}$*	0.0513 0.0316 0.0237	n	1.29 1.21 1.22	Zhou *et al.* (2012)

Table 4-10: Adsorption isotherm results obtained from literature to compare to the results obtained in this study (*continued*).

Sample type	Sample name	Pressure, *bar*	Temperature range, *°C*	Inlet CO_2 concentration, *vol%*	Adsorption Isotherm Model	Temperature, *°C*	Maximum adsorption capacity, mmol/g	AIM parameter symbol	AIM parameter value	AIM parameter symbol	AIM parameter value	Author(s)
Zeolite	13X	1	25-60	100	Langmuir	25	4.25	q_L, *mmol/g*	4.25	K_L, *1/bar*	19.0	Hauchhum and Mahanta (2014a)
						35	3.97		3.97		16.9	
						45	3.52		3.52		13.7	
						60	3.17		3.17		11.2	
Activated carbon	ACCF	1	25-60	100	Freundlich	25	2.83	K_F, *mmol/g.atm$^{1/n}$*	0.505	n	1.70	
						35	2.71		0.447		1.55	
						45	2.59		0.383		1.39	
						60	2.49		0.346		1.32	
Zeolite	4A	1	25-60	100	Langmuir	25	3.26	q_L, *mmol/g*	3.26	K_L, *1/bar*	19.0	
						35	3.07		3.07		16.9	
						45	2.92		2.92		13.7	
						60	2.62		2.62		11.2	
Zeolite	13X	4	25-60	13.8	Langmuir	25	6.24	q_L, *mmol/g*	6.24	K_L, *1/bar*	22.0	Hauchhum and Mahanta (2017)
						35	5.97		5.97		20.3	
						45	5.52		5.52		17.6	
						60	5.17		5.17		15.6	
Zeolite	5A	4	25-60	13.8	Langmuir	25	5.26	q_L, *mmol/g*	5.26	K_L, *1/bar*	22.0	
						35	5.07		5.07		21.3	
						45	4.92		4.92		18.6	
						60	4.61		4.61		16.9	
Zeolite	4A	4	25-60	13.8	Langmuir	25	4.26	q_L, *mmol/g*	4.26	K_L, *1/bar*	20.6	
						35	4.07		4.07		18.5	
						45	4.92		4.92		16.6	
						60	4.61		4.61		15.9	
Activated carbon	CF	4	25-60	13.8	Freundlich	25	4.03	K_F, *mmol/g.atm$^{1/n}$*	2.51	n	4.03	
						35	3.81		1.84		3.72	
						45	3.59		1.08		3.49	
						60	3.49		0.840		3.24	

4.3   THERMODYNAMIC ANALYSIS

A thermodynamic evaluation carried out on the activated carbon samples CQ006, CQ30P, CQ650 and PCX1 is now presented. Changes in enthalpy, entropy and Gibbs free energy can be determined with the adsorption constants obtained from adsorption isotherm modelling, with either the Langmuir or Freundlich adsorption isotherm models (Ammendola *et al.*, 2017; Goel *et al.*, 2011; Shafeeyan *et al.*, 2015).

Evaluating the average QOF% and ARE% for the Langmuir and Freundlich adsorption isotherm models given in Table 4-4 yields results now presented in Table 4-10. The Freundlich adsorption isotherm model is more accurate in describing the experimental adsorption isotherm data and, therefore, used to determine the changes in enthalpy, entropy and Gibbs free energy.

Table 4-10: The QOF% and ARE% of the Langmuir and Freundlich adsorption isotherm models when applied to the experimental adsorption isotherm data for CQ006, CQ30P, CQ650 and PCX1.

AIM	Sample	QOF%			ARE%		
Langmuir	CQ006	94.1	±	5.80	3.5	±	6.7
	CQ30P	94.3	±	2.64	2.7	±	3.3
	CQ650	81.0	±	9.13	7.3	±	6.9
	PCX1	96.7	±	1.83	0.8	±	0.8
Freundlich	CQ006	95.4	±	3.80	1.5	±	3.63
	CQ30P	96.3	±	0.362	0.8	±	1.66
	CQ650	90.4	±	19.6	1.8	±	4.23
	PCX1	97.2	±	0.103	0.6	±	0.218

The adsorption constants obtained from fitting the Freundlich adsorption isotherm model to the experimental adsorption isotherm data of CQ006, CQ30P, CQ650 and PCX1 at 0, 10, 20, 30, 40 and 55 °C are given in Figure 4-9. The Freundlich constants were used to obtain $\ln(K_F)$ versus $1/T$ plots, now displayed in Figure 4-10. The Freundlich adsorption isotherm constant, K_F, for the activated carbon samples and the mentioned temperature range, is presented in Table 4-12. The change in enthalpy, entropy and Gibbs free energy was then calculated from the slopes and intercepts, as discussed in Section 3.4, and now reported in Table 4-12.

Table 4-11: Freundlich adsorption isotherm constant, K_F (mmol/g.kPa$^{(1/n)}$), for CQ006, CQ30P, CQ650 and PCX1 at 0, 10, 20, 30, 40 and 55 °C.

Sample	0 °C	10 °C	20 °C	30 °C	40 °C	55 °C
CQ006	0.402	0.298	0.211	0.160	0.0532	0.0344
CQ30P	0.170	0.116	0.0947	0.0677	-	-
CQ650	0.316	0.219	0.186	0.137	-	-
PCX1	-	-	-	-	0.0404	0.0237
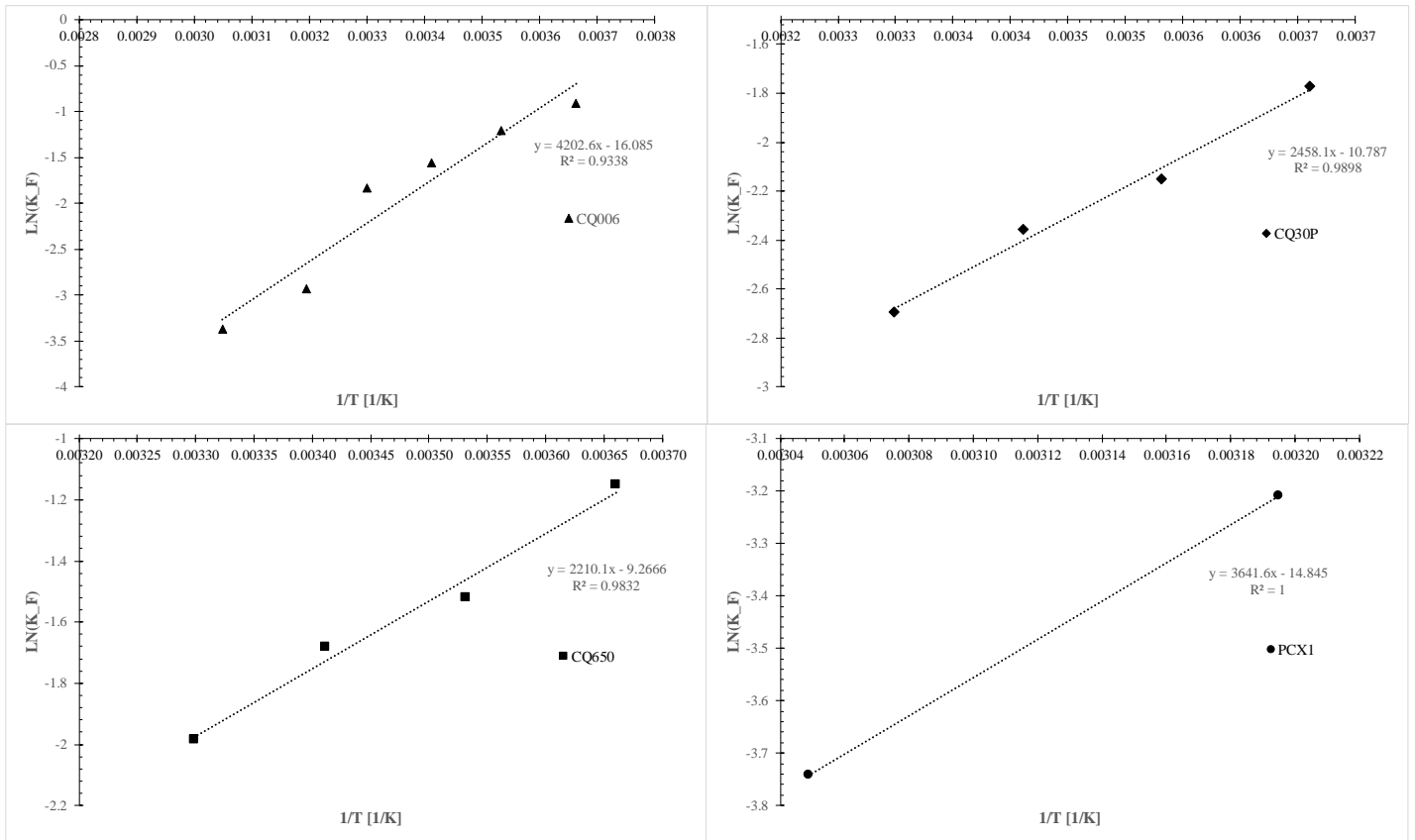
Figure 4-10: Plot of ln(K_F) versus $1/T$ for CQ006, CQ30P, CQ650 and PCX1

Table 4-12: The change in enthalpy, entropy and Gibbs free energy for CQ006, CQ30P, CQ650 and PCX1.

Thermodynamic property	CQ006	CQ30P	CQ650	PCX1
ΔH^0, *kJ/mol*	-34.9	-20.4	-18.4	-30.3
ΔS^0, *kJ/mol*	-0.0763	-0.0323	-0.0196	-0.0660
$\Delta G^0_{0\,°C}$, *kJ/mol*	-14.1	-11.6	-13.0	-
$\Delta G^0_{10\,°C}$, *kJ/mol*	-13.3	-11.3	-12.8	-
$\Delta G^0_{20\,°C}$, *kJ/mol*	-12.6	-11.0	-12.6	-
$\Delta G^0_{30\,°C}$, *kJ/mol*	-11.8	-10.7	-12.4	-
$\Delta G^0_{40\,°C}$, *kJ/mol*	-11.1	-	-	-9.62
$\Delta G^0_{55\,°C}$, *kJ/mol*	-9.91	-	-	-8.63

The ΔH^0 value was found to be negative for each adsorbent, indicating that the adsorption is exothermic in nature. The ΔH^0 result for each adsorbent revealed the type of adsorption process as being physical adsorption. The value for ΔH^0 associated with chemical adsorption is usually 80–200 kJ/mol, while the ΔH^0 value associated with physical adsorption is <20 kJ/mol.

The negative ΔS^0 value found for each adsorbent suggests a high orderliness behaviour of the CO_2 molecules during adsorption onto the activated carbon samples from a disordered and random circumstance in the gas. The low value for ΔS^0 indicates a very small to insignificant change in entropy. The orderly adsorption behaviour can be attributed to a lesser degree of freedom experienced by the CO_2 molecules due to minimum free space on the activated carbon surface.

The ΔG^0 increases in value as temperature increases, indicating that adsorption becomes less feasible at higher temperatures and most favourable at low temperatures. The negative value found for the Gibbs free energy at each temperature for each adsorbent sample, indicates favourable spontaneous adsorption.

Upon evaluating the heterogeneity parameter (*n*) of the Freundlich adsorption isotherm model (see Table 4-13) it is evident that *n* is >1 at each temperature, for each sample, meaning that physical adsorption takes place. Furthermore, 1/*n* (given in Table 4-14) is <1 at each temperature, for each sample, indicating therefore that the CO_2 adsorption is favourable onto the activated carbon samples.

Table 4-13: Freundlich adsorption isotherm heterogeneity parameter, n, for CQ006, CQ30P, CQ650 and PCX1 at 0, 10, 20, 30, 40 and 55 °C.

Sample	0 °C	10 °C	20 °C	30 °C	40 °C	55 °C
CQ006	2.10	1.99	1.84	1.76	1.46	1.40
CQ30P	1.72	1.62	1.60	1.51	-	-
CQ650	1.86	1.69	1.74	1.66	-	-
PCX1	-	-	-	-	1.42	1.32

Table 4-14: Freundlich adsorption isotherm heterogeneity parameter, $1/n$, for CQ006, CQ30P, CQ650 and PCX1 at 0, 10, 20, 30, 40 and 55 °C.

Sample	0 °C	10 °C	20 °C	30 °C	40 °C	55 °C
CQ006	0.476	0.503	0.544	0.569	0.684	0.715
CQ30P	0.583	0.617	0.623	0.660	-	-
CQ650	0.539	0.590	0.576	0.604	-	-
PCX1	-	-	-	-	0.704	0.756

4.3.1 ISOTERIC HEAT OF ADSORPTION

The Q_{ST} value can be determined from the slopes when plotting ln(P) against $1/T$ at specific fixed adsorbed amounts of CO_2, ranging from 0.05 to 3 mmol/g, as displayed in Figure 4-11. The slopes obtained for all the sorbents displays a R^2 value >0.94, indicating a good linear correlation, and functional data to be used to calculate the isosteric heat of adsorption. The slopes obtained were multiplied with the universal gas constant (R) and divided by 1000 to obtain kJ/mol. The Q_{ST} values were then plotted against fixed specific quantities of adsorbed CO_2 (see Figure 4-12). The maximum and minimum isosteric heat of adsorption values obtained for CQ006, CQ30P, CQ650 and PCX1 are given in Table 4-15.
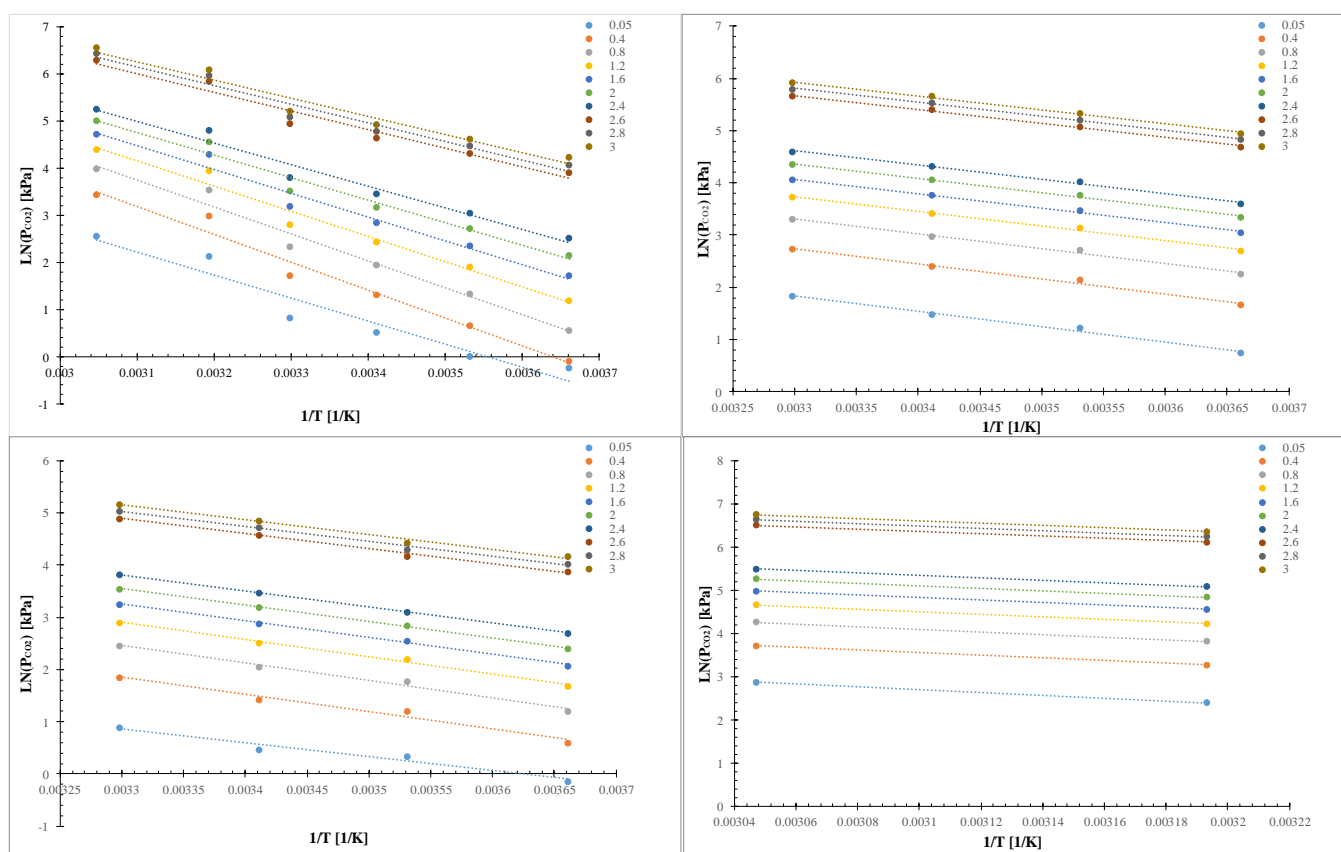
Figure 4-11: ln(P) versus $1/T$ at fixed specified quantities of CO_2 adsorbed for CQ006, CQ30P, CQ650 and PCX1.

Table 4-15: Minimum and maximum isoteric heat of adsorption values for CQ006, CQ30P, CQ650 and PCX1.

Sample	Minimum Q_{ST}, kJ/mol	Maximum Q_{ST}, kJ/mol
CQ006	30.83	49.41
CQ30P	22.03	24.49
CQ650	22.76	27.91
PCX1	21.37	27.12
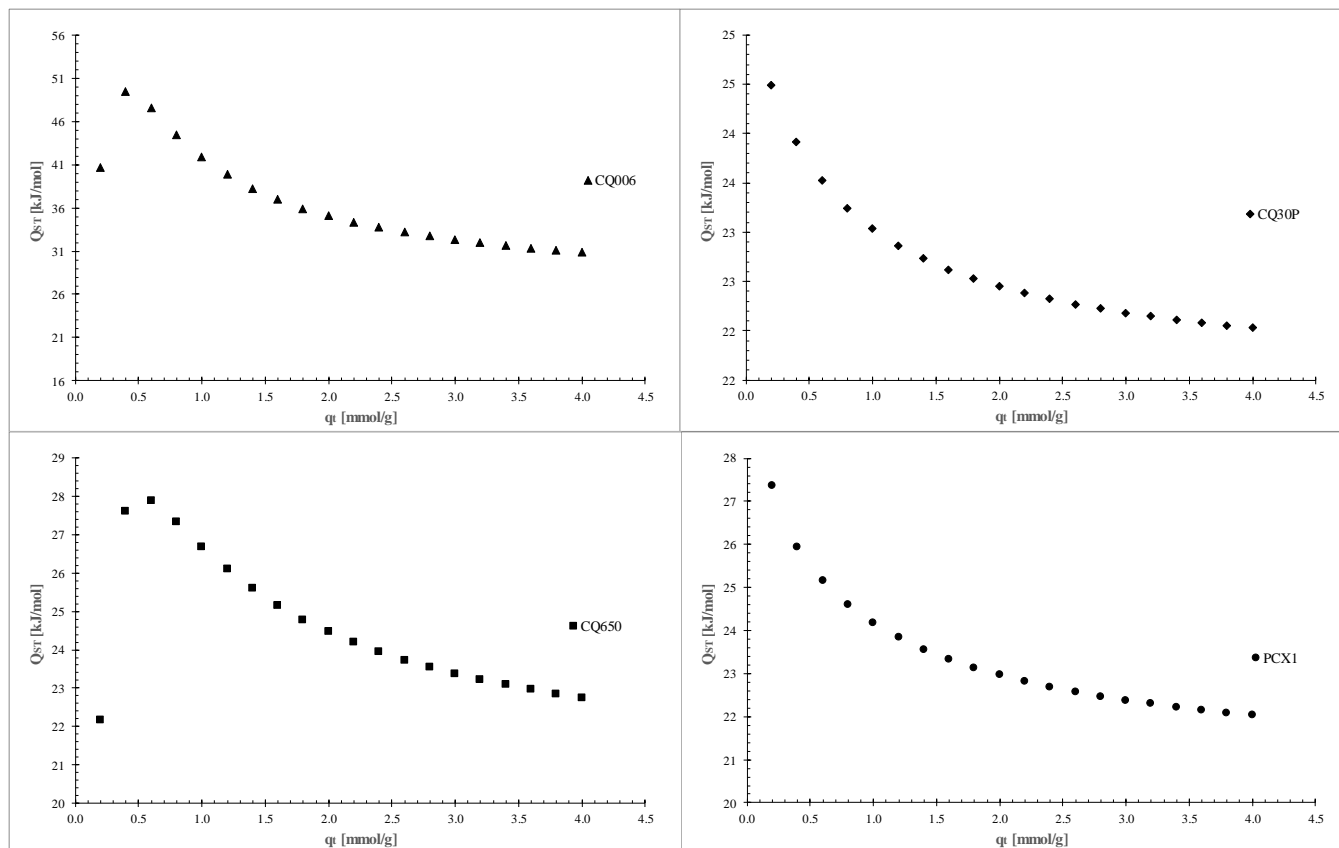
Figure 4-12: Isosteric heat of adsorption displayed (Q_{ST}) as a function of surface loading (q_t) for CQ006, CQ30P, CQ650 and PCX1.

The negative slopes observed in Figure 4-11 suggest that the adsorption process is exothermic in nature. All the maximum isosteric heat of adsorption values are <80 kJ/mol, indicating that the CO_2 adsorption onto the adsorbent is physical adsorption. Analysing Q_{ST} as a function of surface loading illustrates that the maximum isosteric heat of adsorption is obtained at levels of low surface loading. The Langmuir adsorption isotherm model employs an assumption that adsorption occurs homogenously, thus we expect a constant isosteric heat of adsorption over surface loading. The isosteric heat of adsorption decreases to the minimum isosteric heat of

adsorption value (see Table 4-15) as the surface loading increases. This difference may be attributed to surface irregularities and heterogeneity of adsorption sites, in combination with variable adsorbate–adsorbent and adsorbate–adsorbate interactions. Adsorbate–adsorbate interactions (lateral interactions) is a cause of attractive and repulsive forces exerted from CO_2 molecules on other CO_2 molecules (Ammendola *et al.*, 2017; Heydari-Gorji & Sayari, 2011).

Before CO_2 is introduced to the adsorbent, an abundance of active sites is available for CO_2 adsorption. When CO_2 is introduced to the adsorbent, CO_2 comes into direct contact with the adsorbent and forms strong bonds with van der Waals forces and dipole–dipole interactions on the adsorbent; thus, the initial isosteric heat of adsorption at low surface loading presents as the maximum. As adsorption of CO_2 on the adsorbent proceeds, fewer CO_2 molecules come into direct contact with the adsorbent (as the number of active sites decreases with increasing surface loading), leading to weaker interaction forces between CO_2 and the adsorbent, and consequently resulting in a decrease in the isosteric heat of adsorption (Ammendola *et al.*, 2017; Singh & Kumar, 2016).

An interesting phenomenon regarding the isosteric heat of adsorption was observed for CQ006 and CQ650 (see Figure 4-12). The initial isosteric heat of adsorption presents a low value, compared with the isosteric heat of adsorption values determined at higher surface loadings for the adsorbent. This may be due to highly developed micropore surface areas, which both adsorbents have. When the CO_2 molecules are initially introduced to the adsorbent at low pressure, they adsorb onto the outside surface of the adsorbent and then diffuse into the adsorbent's extensive micropore structure at higher pressures, where abundant active sites for CO_2 adsorption present. The highest isosteric heat of adsorption is then experienced.

4.3.2   COMPARISON WITH LITERATURE

The thermodynamic results determined for the activated carbon samples CQ006, CQ30P, CQ650 and PCX1 in this study were compared with thermodynamic results reported for activated carbon and zeolite samples in literature; see Table 4-16. The thermodynamics of CO_2 adsorption on the activated carbon samples Norit SX2 and C700 were investigated by Rashidi *et al.* (2016) and Goel *et al.* (2016). Changes in enthalpy and entropy of -19.66 and -39.56 and -0.059 and 0.075 kJ/mol, respectively, are reported. Results compare well with the changes in

enthalpy and entropy values obtained for the activated carbon samples investigated in this study, where results ranged from -18.38 to -34.94 and -0.077 to -0.13 kJ/mol, respectively. The activated carbon sample C700 had an isosteric heat of adsorption of 53.9 kJ/mol, which is in agreement with the isosteric heat of adsorption values obtained for the activated carbon samples (range 24.5–49.4 kJ/mol). The CO_2 adsorption thermodynamic analysis conducted on zeolite samples (13X, 4A and 5A) by Hauchhum and Mahanta (2017) revealed changes in enthalpy values ranging from -22.85 to -37.15, which compares well with results recorded for the activated carbon samples in this study.

Table 4-16: Adsorption thermodynamic results obtained from literature to compare to the results obtained in this study.

Sample type	Sample name	Pressure, *bar*	Temperature range, °C	Inlet CO$_2$ concentration, *vol%*	Flow rate, *L/min*	Gibbs Temperature, °C	ΔG^0, *kJ/mol*	ΔH^0, *kJ/mol*	ΔS^0, *kJ/mol*	Isosteric heat of adsorption, *kJ/mol*	Author(s)
Activated carbon	CQ006	1	0-55	100	0.25	0 10 20 30 40 55	-14.1 -13.3 -12.6 -11.8 -11.1 -9.91	-34.94	-0.13	30.8-49.4	This study
Activated carbon	CQ30P	1	0-30	100	0.25	0 10 20 30	-11.6 -11.3 -11.0 -10.7	-20.44	-0.090	22.0-24.5	
Activated carbon	CQ650	1	0-30	100	0.25	0 10 20 30	-13.0 -12.8 -12.6 -12.4	-18.38	-0.077	22.8-27.9	
Activated carbon	PCX1	1	40-55	100	0.25	40 55	-9.62 -8.63	-30.29	-0.12	21.4-27.1	
Activated carbon	Norit SX2	1	25-120	-	-	25 50 75 100 120	-1.79 -0.557 0.855 2.12 4.17	-19.66	-0.059	-	Rashidi *et al.* (2016)
Activated carbon	C-700	1	30-100	1	0.050	30 50 75 100	-17.5 -13.9 -13.8 -11.7	-39.56	0.075	53.9	Goel *et al.* (2016)
Activated carbon	DARCO FGD	1	30-100	1 - 15	1.0	18 40 70 100 130	-3.58 -3.07 -2.39 -2.11 -1.93	-7.98	-0.016	5.33–16.6	Ammendola *et al.* (2017)

Table 4-17: Adsorption thermodynamic results obtained from literature to compare to the results obtained in this study (*continued*).

Sample type	Sample name	Pressure, *bar*	Temperature range, °C	Inlet CO$_2$ concentration, *vol%*	Flow rate, *L/min*	Gibbs Temperature, °C	ΔG^0, *kJ/mol*	ΔH^0, *kJ/mol*	ΔS^0, *kJ/mol*	Isosteric heat of adsorption, *kJ/mol*	Author(s)
Zeolite	13X	1	25-60	1.0	15	25 35 45 60	-7.93 -7.69 -6.30 -6.24	-11.27	18	-	Hauchhum and Mahanta (2014a)
Activated carbon	Coconut fibre	1	25-60	1.0	15	25 35 45 60	-7.65 -7.56 -7.25 -6.82	-12.85	18	-	
Zeolite	4A	1	25-60	1.0	15	25 35 45 60	-7.30 -7.24 -6.93 -6.69	-14.98	24	-	
Zeolite	13X	4	25-60	14	15	25 35 45 60	-7.93 -7.69 -6.30 -6.24	-35.27	38	-	Hauchhum and Mahanta (2017)
Zeolite	5A	4	25-60	14	15	25 35 45 60	-7.54 -7.15 -6.96 -6.76	-37.15	39	-	
Zeolite	4A	4	25-60	14	15	25 35 45 60	-7.30 -7.24 -6.93 -6.69	-22.85	24	-	
Activated carbon	Coconut fibre	4	25-60	14	15	25 35 45 60	-7.65 -7.56 -7.25 -6.82	-14.98	26	-	

Chapter 5

(ADSORPTION KINETIC RATE MODELLING, VALIDATION AND ANALYSIS)

Chapter 5

(ADSORPTION KINETIC RATE MODELLING, VALIDATION AND ANALYSIS)

The experimental adsorption rate results of the activated carbon samples (CQ006, CQ30P, CQ650 and PCX1) obtained from the experimental FBR setup, (discussed in Section 3.5.1) are now modelled with the five adsorption kinetic rate models: pseudo first order (P1O) pseudo second order (P2O), Elovich, Avrami and fractional order), as discussed now in this chapter. The best fitting adsorption kinetic rate model will be determined and used to model the experimental kinetic rate results of CO_2 adsorption onto the activated carbon adsorbents. Diffusion from the bulk gas into the adsorbent's micropores will be investigated to determine the rate-limiting diffusion step and order of CO_2 diffusion onto the activated carbon sample. The activation energies of CO_2 adsorption onto the activated carbon samples will be determined, with the adsorption kinetic rate constants determined from fitting the adsorption kinetic rate models to the experimental adsorption kinetic rates measured for the CO_2 adsorption onto the activated carbon samples. The results and findings of this study will be compared with literature, to see how the activated carbon samples compare with the activated carbon samples reported in literature.

5.1 EXPERIMENTAL CO₂ ADSORPTION KINETIC RATE RESULTS

The experimental CO_2 adsorption kinetic rate concentration results measured with the FBR are first discussed. The concentration (C_A), measured from the FBR, is plotted against time t in seconds; results are given in Figure 5-1 to Figure 5-3. Applying the data processing procedure (discussed in Appendix A), the quantity adsorbed (q_t) is determined for each sample at each selected temperature and inlet CO_2 concentration. The normalized dimensionless adsorption quantity (q_t/q_e) is displayed in Figure 5-4 to Figure 5-6. The q_t/q_e data represented in these figures, are fitted with the adsorption kinetic rate models, discussed in Section 3.5. The absolute CO_2 adsorbed quantity (q_t) versus time t is plotted; results are given in Figure C- 9 and Figure C- 10 (Appendix C).
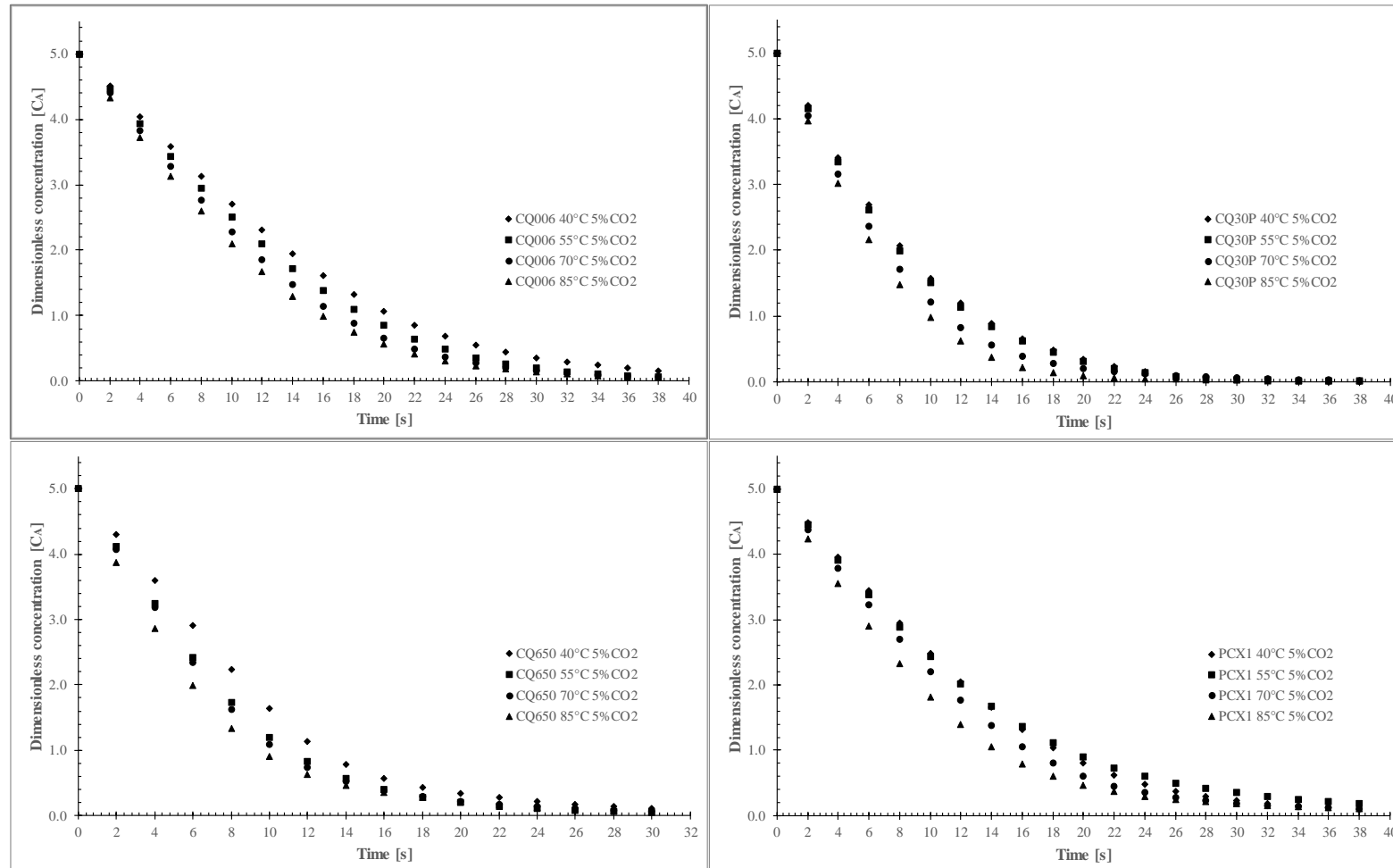
Figure 5-1: Measured experimental CO_2 outlet concentration (C_A in vol%) at 40, 55, 70 and 85 °C for CQ006, CQ30P, CQ650 and PCX1 at a fixed inlet CO_2 concentration of 5 vol% and fixed flow rate of 250 cm^3/min.
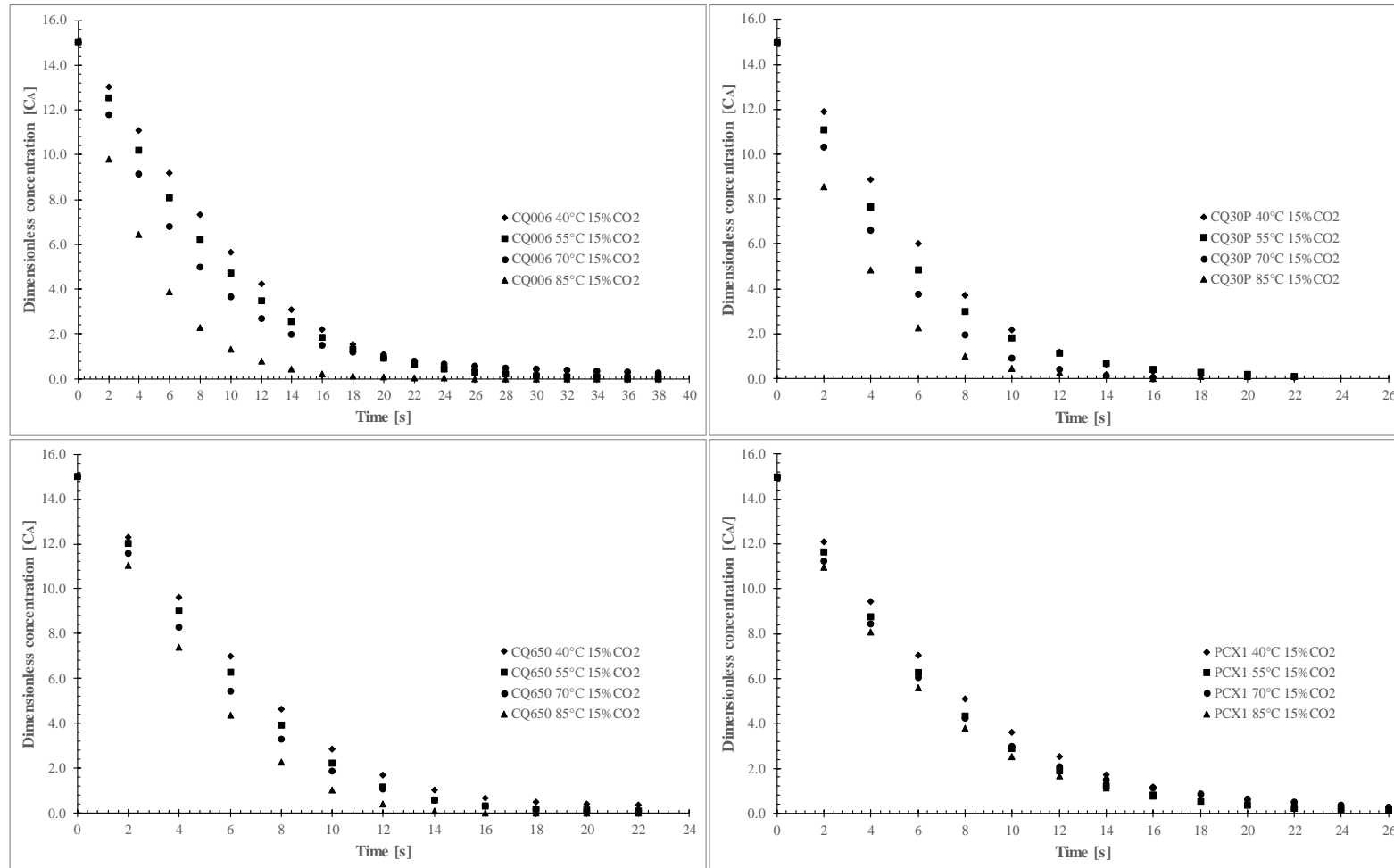
Figure 5-2: Measured experimental CO_2 outlet concentration (C_A in vol%) at 40, 55, 70 and 85 °C for CQ006, CQ30P, CQ650 and PCX1 at a fixed inlet CO_2 concentration of 15 vol% and fixed flow rate of 250 cm^3/min.
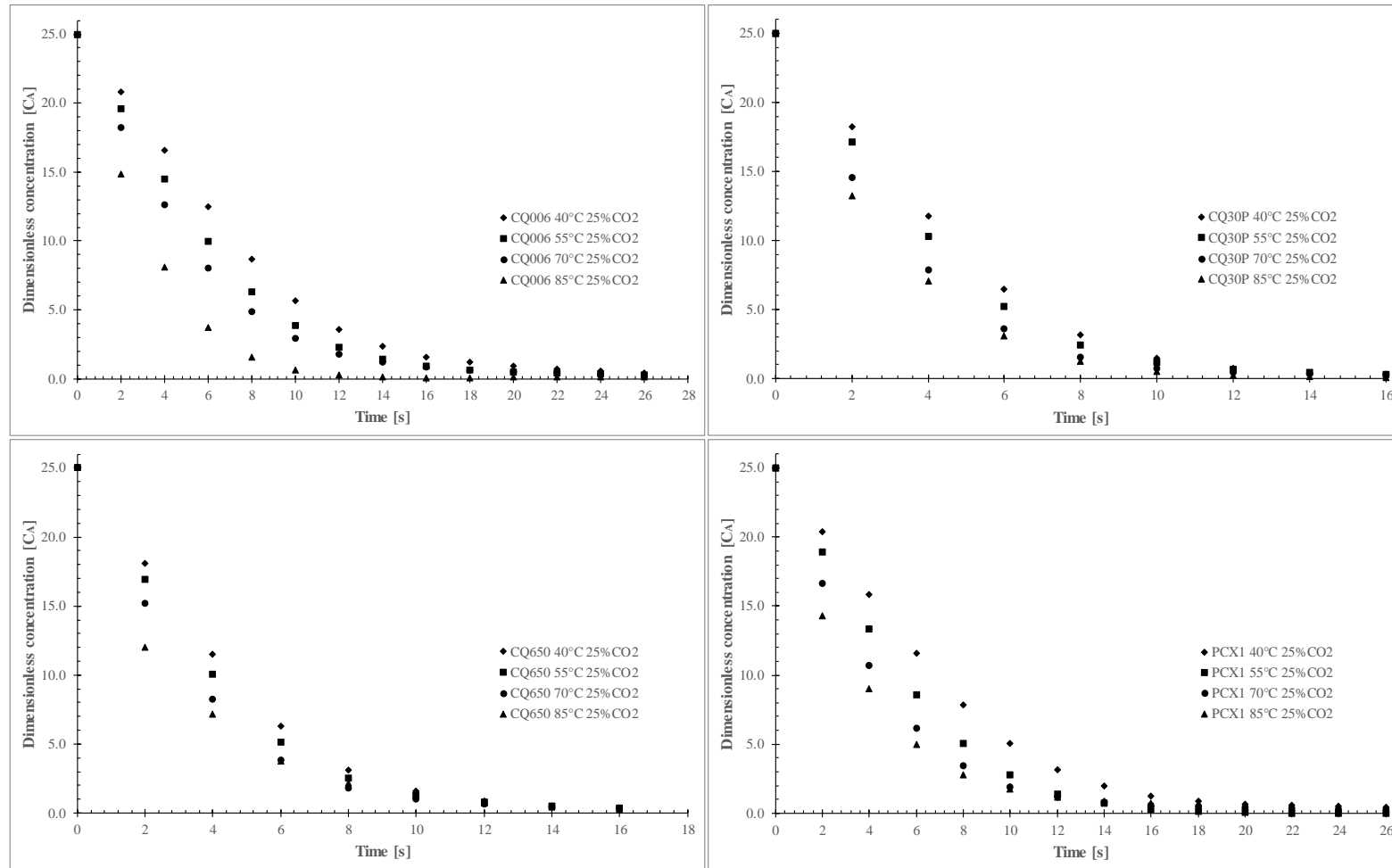
Figure 5-3: Measured experimental CO_2 outlet concentration (C_A in vol%) at 40, 55, 70 and 85 °C for CQ006, CQ30P, CQ650 and PCX1 at a fixed inlet CO_2 concentration of 25 vol% and fixed flow rate of 250 cm^3/min.
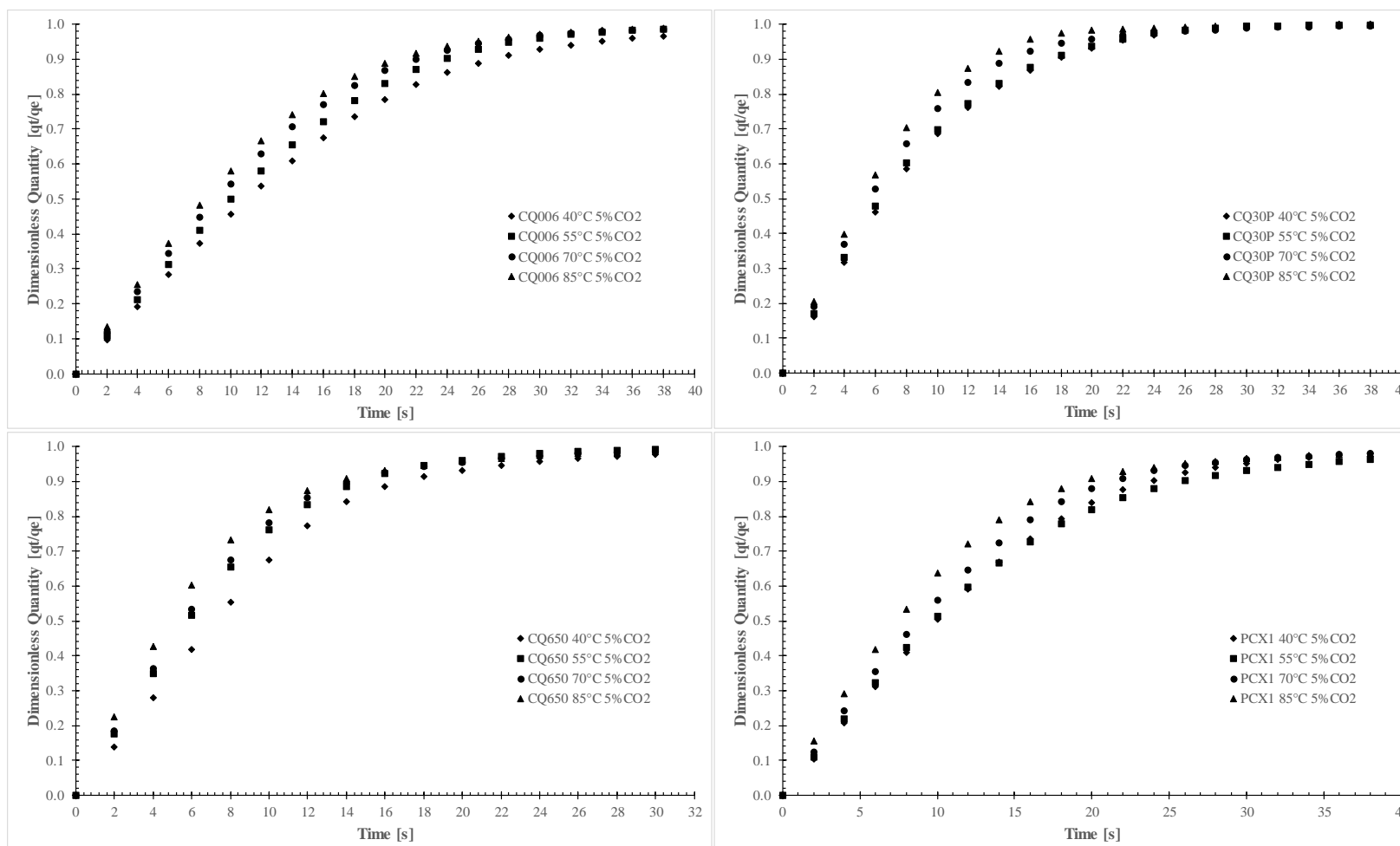
Figure 5-4: Dimensionless quantity CO_2 adsorbed (q_t/q_e) at 40, 55, 70 and 85 °C for CQ006, CQ30P, CQ650 and PCX1 at a fixed inlet CO_2 concentration of 5 vol% and fixed flow rate of 250 cm^3/min.

Figure 5-5: Dimensionless quantity CO_2 adsorbed (q_t/q_e) at 40, 55, 70 and 85 °C for CQ006, CQ30P, CQ650 and PCX1 at a fixed inlet CO_2 concentration of 15 vol% and fixed flow rate of 250 cm^3/min.

Figure 5-6: Dimensionless quantity CO_2 adsorbed (q_t/q_e) at 40, 55, 70 and 85 °C for CQ006, CQ30P, CQ650 and PCX1 at a fixed inlet CO_2 concentration of 25 vol% and fixed flow rate of 250 cm^3/min.

5.2 SELECTING THE MOST ACCURATE ADSORPTION KINETIC RATE MODEL

The experimental adsorption rate data of CQ006, CQ30P, CQ650 and PCX1 at 40, 55, 70 and 85 °C with inlet CO_2 concentrations of 5, 15 and 25 vol%, was modelled with five adsorption rate models: P1O, P2O, Elovich, Avrami and the fractional order (FOM) adsorption rate models.

The optimal adsorption rate model was selected based on quality of fit (QOF%) and the model's average relative error (ARE%), compared to the experimental adsorption rate data. The five adsorption rate models are fitted to the experimental adsorption rate results of CQ650 at 40 °C with a 5% CO_2 inlet concentration. Results are displayed in Figure 5-7, which is a good example of the fittings observed for the other adsorbents at other temperatures. The model parameters are given in Table 5-1.

The P2O adsorption rate model is associated with chemical adsorption and examining the fitting to the experimental adsorption rate data in Figure 5-7, it is conclusive that chemical adsorption do not take place.

The three best fitting adsorption rate models are the P1O, Avrami and the fractional adsorption rate model. The FOM adsorption rate is a three parameter adsorption rate model and presented the same phenomenon experienced with the D-A and Toth adsorption isotherm models applied to the adsorption isotherm data. The FOM adsorption rate model is thus, discarded and considered biased. The QOF% and ARE% of P1O and Avrami adsorption rate models are given in Table 5-2. The Avrami adsorption rate model is deemed the most accurate adsorption rate model and therefore, used as the adsorption rate model to model the adsorption rate data of CQ006, CQ30P and PCX1.
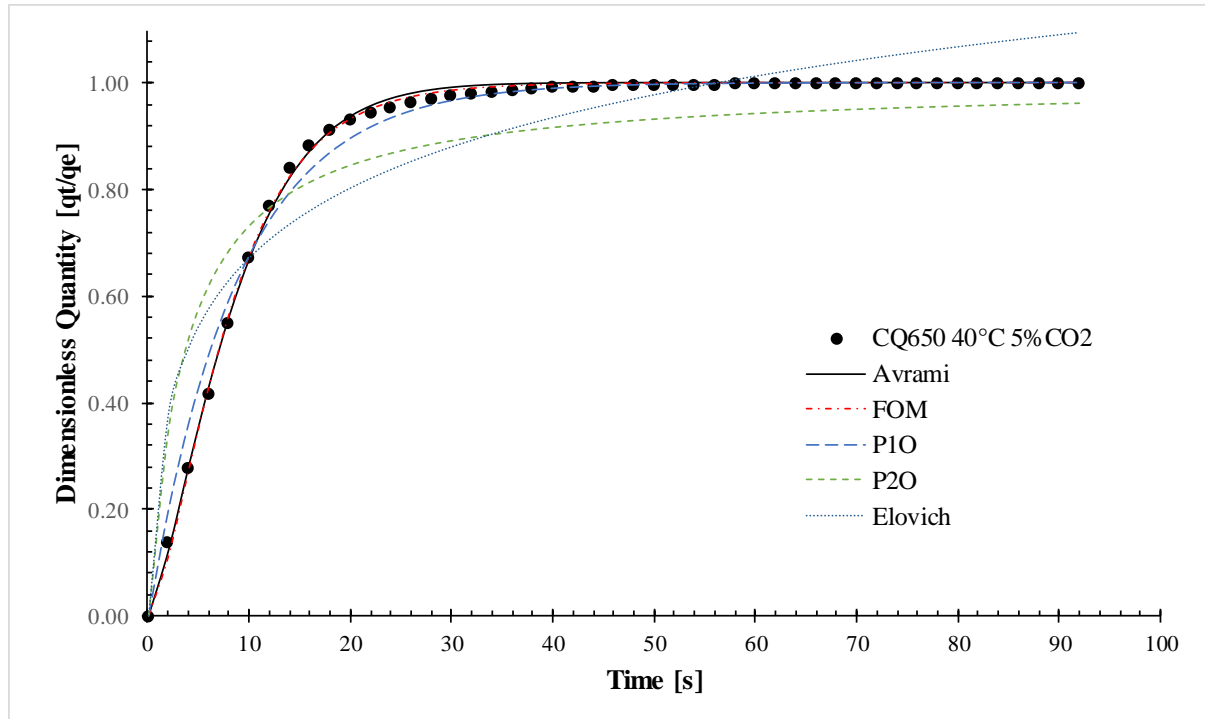
Figure 5-7: Pseudo first order (P1O), pseudo second order (P2O), Elovich, Avrami and fractional order adsorption rate model parameters when fitted to the experimental adsorption rate data of CQ650 at 40 °C and an inlet CO_2 concentration of 5 vol%.

Table 5-1: Pseudo first order (P1O), pseudo second order (P2O), Elovich, Avrami and fractional order adsorption rate model parameters when fitted to the experimental adsorption rate data of CQ650 at 40, 55, 70 and 85 °C and an inlet CO_2 concentration of 5, 15 and 25 vol%.

Sample	Parameter	5 vol% CO_2				15 vol% CO_2				25 vol% CO_2			
		40 °C	55 °C	70 °C	85 °C	40 °C	55 °C	70 °C	85 °C	40 °C	55 °C	70 °C	85 °C
P1O	k_1, $1/s$	0.113	0.136	0.141	0.157	0.148	0.166	0.180	0.212	0.221	0.246	0.286	0.327
	ARE%	1.34	0.960	0.782	0.470	1.14	1.20	0.913	0.977	0.745	0.530	0.350	0.320
	QOF%	**96.9**	**98.0**	**98.2**	**99.0**	**97.6**	**97.6**	**98.3**	**98.4**	**98.7**	**99.1**	**99.5**	**99.6**
P2O	k_2, $mmol/g.s$	0.274	0.338	0.363	0.396	0.369	0.418	0.460	0.554	0.572	0.647	0.775	0.926
	ARE%	7.21	6.33	6.38	5.31	6.31	6.08	5.49	5.14	4.64	4.14	3.56	2.75
	QOF%	**89.8**	**89.8**	**90.0**	**92.2**	**89.8**	**90.5**	**91.8**	**92.7**	**93.4**	**94.4**	**95.5**	**96.8**
Elovich	α	0.617	1.22	1.39	2.38	1.67	2.78	4.64	13.0	16.7	36.2	88.1	154
	β	5.19	5.98	6.14	6.76	6.33	6.90	7.49	8.63	8.94	9.79	10.7	11.3
	ARE%	7.16	6.84	6.63	6.06	7.00	6.94	6.48	6.25	5.72	5.32	4.97	4.44
	QOF%	**87.3**	**88.8**	**89.2**	**90.8**	**88.5**	**89.0**	**90.1**	**90.9**	**91.7**	**92.7**	**93.8**	**95.1**
Avrami	k_A, $1/s$	0.109	0.131	0.136	0.154	0.141	0.156	0.171	0.199	0.211	0.236	0.277	0.342
	b	1.32	1.26	1.23	1.13	1.37	1.41	1.32	1.37	1.33	1.26	1.17	0.87
	ARE%	0.482	0.208	0.365	0.376	0.357	0.231	0.121	0.234	0.273	0.218	0.205	0.129
	QOF%	**99.2**	**99.7**	**99.5**	**99.7**	**99.4**	**99.5**	**99.7**	**99.6**	**99.7**	**99.8**	**99.8**	**99.8**
FOM	k_{FOM}, $g^{n-1}/s^m g^{n-1}$	0.065	0.095	0.099	0.132	0.093	0.102	0.124	0.150	0.167	0.207	0.272	0.344
	n_{FOM}	1.15	1.07	1.20	1.27	1.02	1.01	1.01	1.01	1.06	1.16	1.19	1.01
	m_{FOM}	1.43	1.31	1.38	1.33	1.39	1.42	1.36	1.38	1.37	1.38	1.32	0.877
	ARE%	0.379	0.168	0.246	0.202	0.355	0.235	0.112	0.241	0.263	0.186	0.169	0.130
	QOF%	**99.2**	**99.7**	**99.5**	**99.7**	**99.4**	**99.5**	**99.7**	**99.6**	**99.7**	**99.8**	**99.8**	**99.8**

Table 5-2: QOF% and ARE% of P1O and Avrami adsorption rate models fitted to the experimental adsorption rate data of CQ650 at 40, 55, 70 and 85 °C with a 5, 15, 25 vol% CO_2 inlet concentration.

Inlet CO_2 concentration	Adsorption rate model	QOF%			ARE%		
5 *vol%* CO_2	P1O	98.0	±	2.39	0.889	±	1.00
	Avrami	**99.5**	**±**	**0.640**	**0.358**	**±**	**0.311**
15 *vol%* CO_2	P1O	98.0	±	1.14	1.058	±	0.374
	Avrami	**99.5**	**±**	**0.413**	**0.236**	**±**	**0.266**
25 *vol%* CO_2	P1O	99.2	±	1.14	0.486	±	0.540
	Avrami	**99.8**	**±**	**0.212**	**0.206**	**±**	**0.163**

5.3 CO_2 ADSORPTION KINETIC RATE MODELLING

The experimental adsorption rate data obtained for CQ006, CQ30P, CQ650 and PCX1 at 40, 55, 70 and 85 °C, with CO_2 inlet concentrations of 5, 15 and 25 vol%, are modelled with the Avrami adsorption rate model and discussed in this section.

This data is reported as a normalized dimensionless adsorption quantity (q_t/q_e) as a function of time (s) in Figure 5-8, Figure 5-9 and Figure 5-10. The Avrami adsorption rate model parameters given in Table 5-3. These figures, together with the Avrami adsorption rate constant (k_A), indicate that the adsorption rate increases with temperature increase for each adsorbent. This phenomenon is attributed to the increased kinetic energy CO_2 possesses at increased temperature where the CO_2 migrates faster through the micropore structure inside the adsorbent.

With the increased kinetic energy of CO_2 at increased temperatures, a concomitant decrease in adsorption quantity is expected (as observed for the adsorption isotherms in Section 4.2.2). This hypothesis is proved upon examination of the equilibrium adsorption quantity (q_e) reported in Table 5-3. The decrease in equilibrium adsorption quantity is also attributed to the exothermic nature of CO_2 adsorption (discussed in Section 4.3) onto the adsorbents. The minimum and maximum adsorption rate for CQ006, CQ30P, CQ650 and PCX1, is achieved at 40 and 85 °C, respectively.

The adsorbent samples reached maximum adsorption capacity within the first 40 *s* of CO_2 exposure at 40, 55, 70 and 85 °C with an inlet CO_2 concentration of 5, 15 and 25 vol% and flow rate of 250 cm^3/g, which is remarkably fast, when compared to the literature data (discussed in Section 5.4).
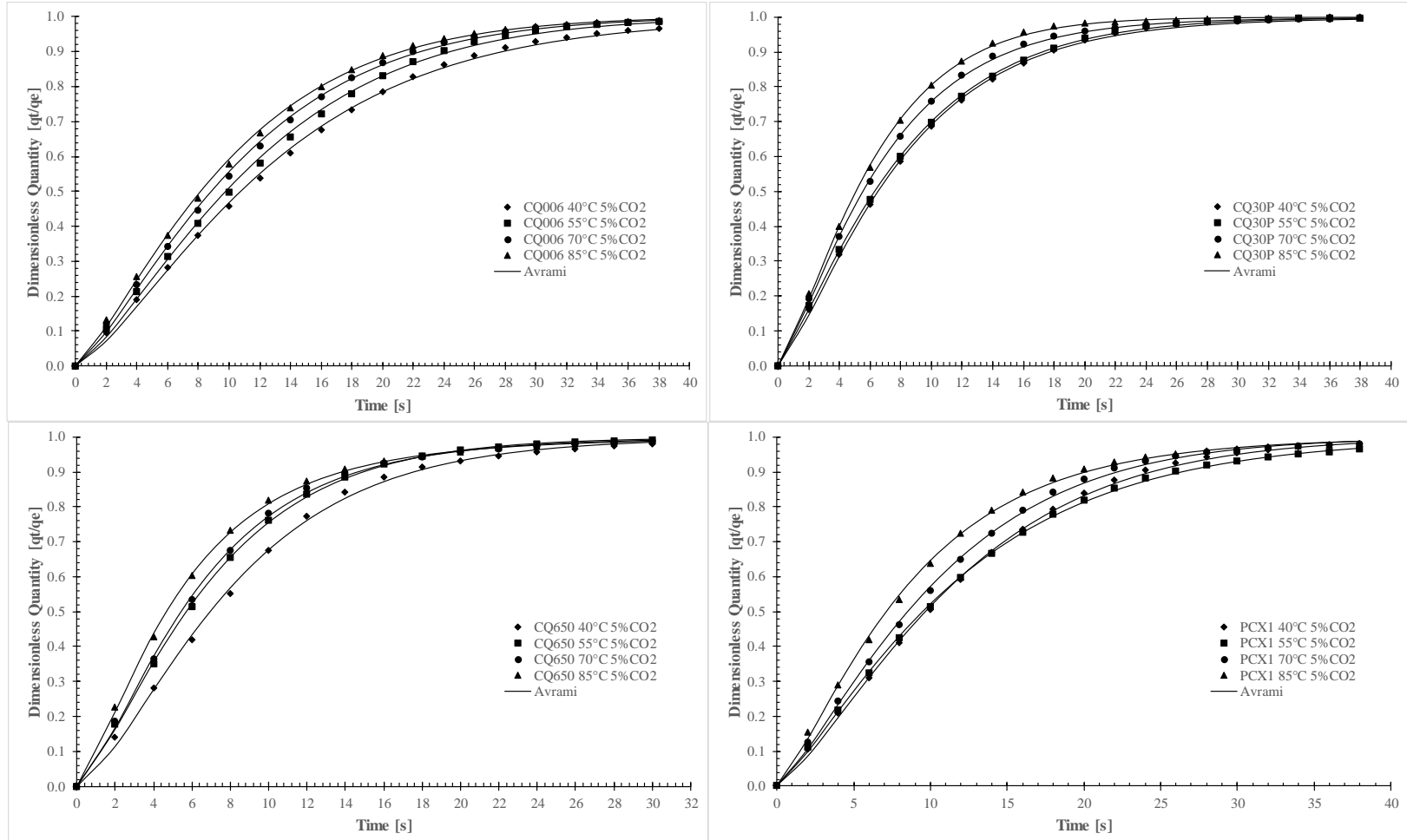
Figure 5-8: Dimensionless quantity adsorbed (q_t/q_e) at 40, 55, 70 and 85 °C for CQ006, CQ30P, CQ650 and PCX1 at a fixed inlet CO_2 concentration of 5 vol% and fixed flow rate of 250 cm^3/min, modelled with the Avrami adsorption rate model.
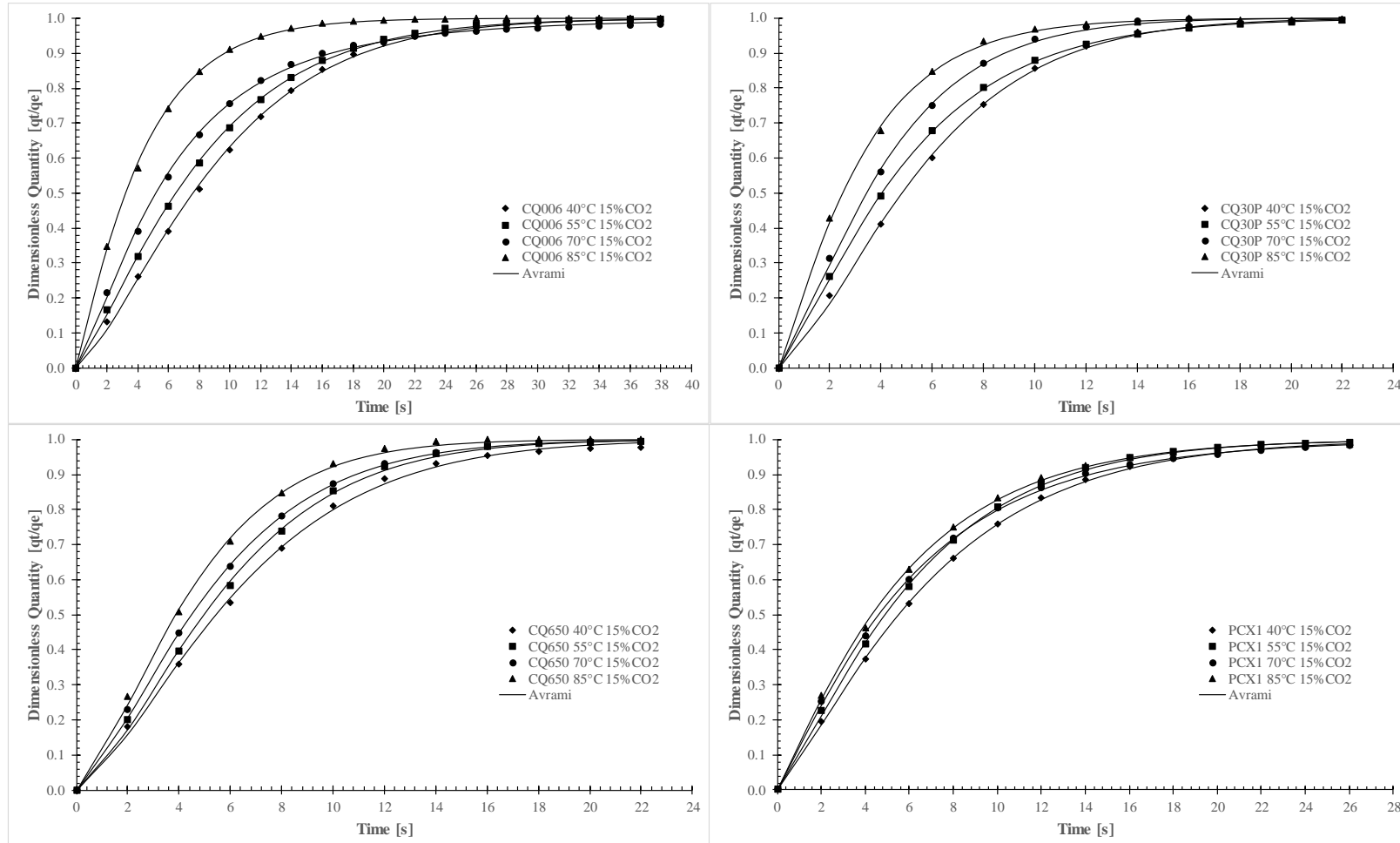
Figure 5-9: Dimensionless quantity adsorbed (q_t/q_e) at 40, 55, 70 and 85 °C for CQ006, CQ30P, CQ650 and PCX1 at a fixed inlet CO_2 concentration of 15 vol% and fixed flow rate of 250 cm^3/min, modelled with the Avrami adsorption rate model.
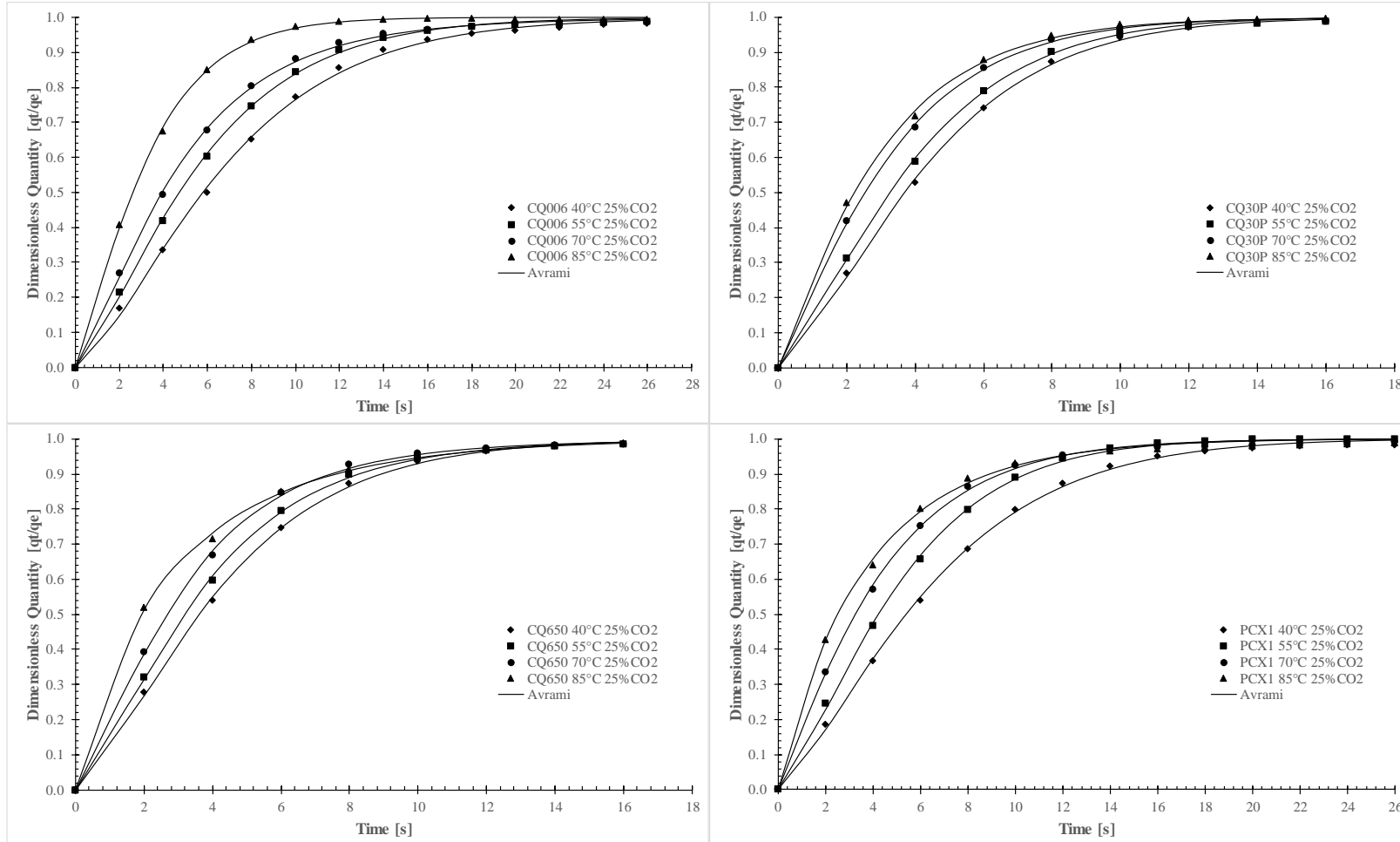
Figure 5-10: Dimensionless quantity adsorbed (q_t/q_e) at 40, 55, 70 and 85 °C for CQ006, CQ30P, CQ650 and PCX1 at a fixed inlet CO_2 concentration of 25 vol% and fixed flow rate of 250 cm^3/min, modelled with the Avrami adsorption rate

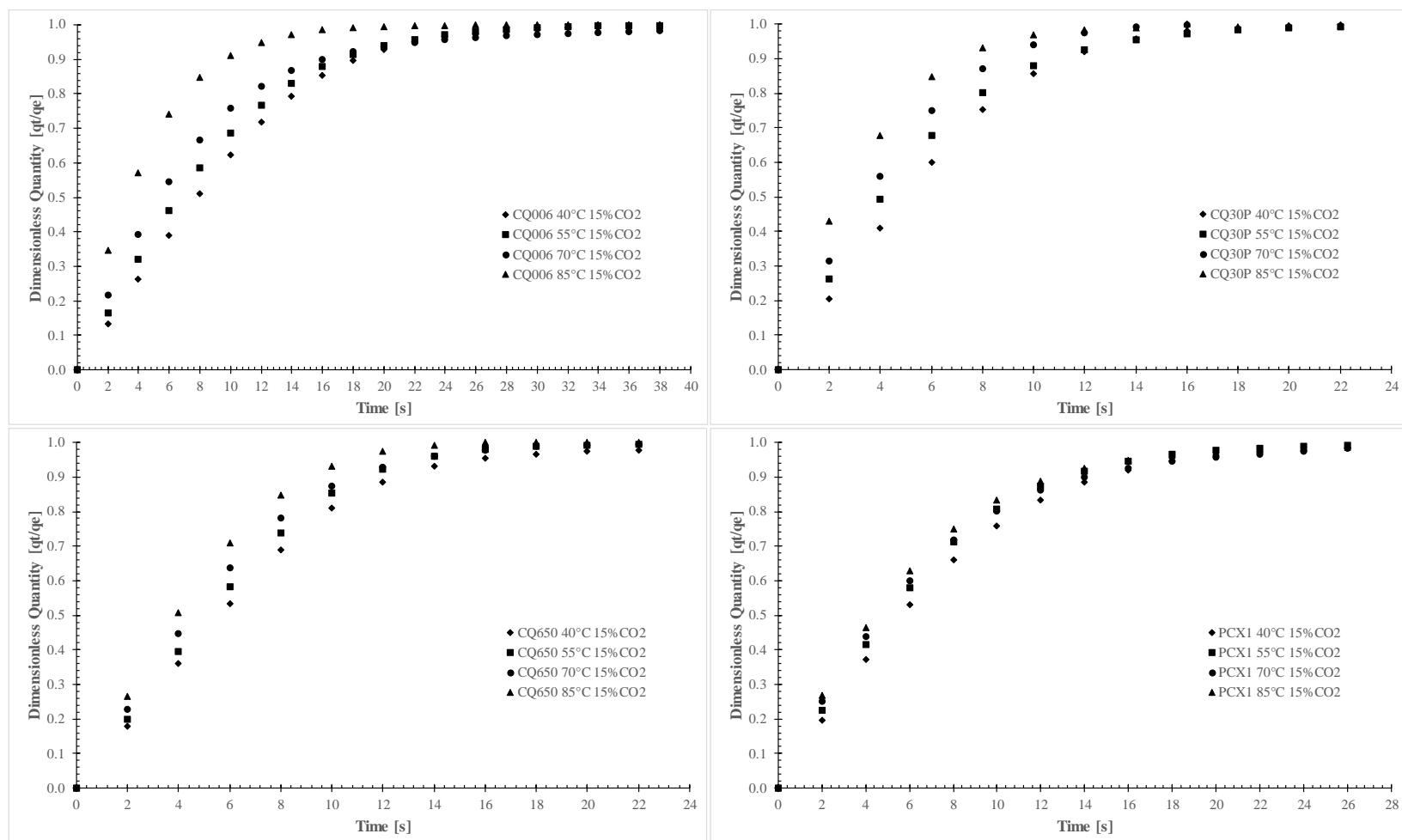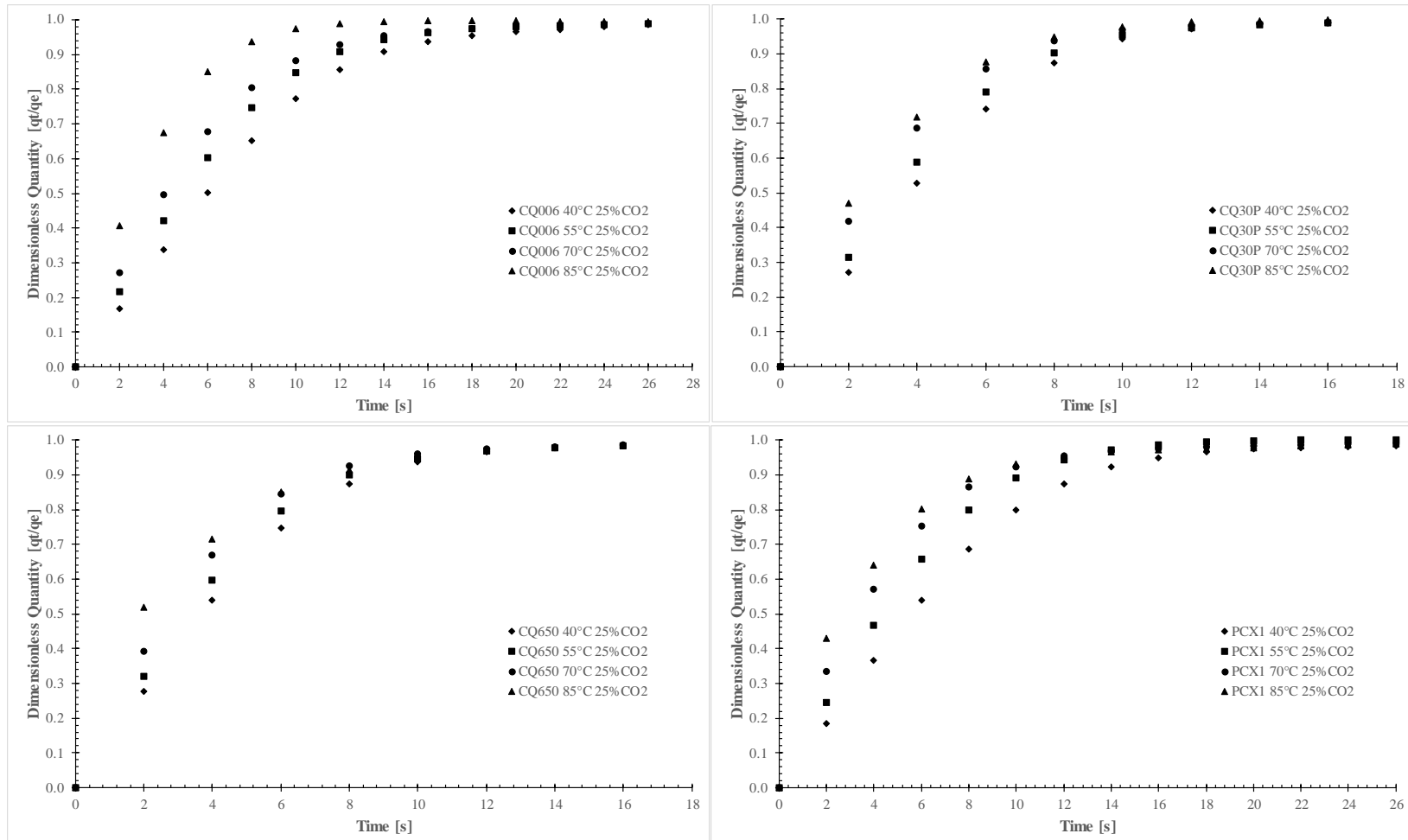Table 5-3: Avrami adsorption rate model parameters of the experimental adsorption rate data at 40, 55, 70 and 85 °C for CQ006, CQ30P, CQ650 and PCX1 at a fixed inlet CO_2 concentration of 5, 15 and 25 vol% and fixed flow rate of 250 cm^3/g.

Sample	Parameter	Inlet CO₂ concentration: 5 *vol%*				Inlet CO₂ concentration: 15 *vol%*				Inlet CO₂ concentration: 25 *vol%*			
		40 °C	55 °C	70 °C	85 °C	40 °C	55 °C	70 °C	85 °C	40 °C	55 °C	70 °C	85 °C
CQ006	k_A, *1/s*	0.07	0.077	0.085	0.091	0.1	0.114	0.134	0.221	0.131	0.159	0.185	0.284
	b	1.28	1.31	1.29	1.25	1.34	1.22	1.05	1.09	1.35	1.29	1.18	1.19
	q_e, *mmol/g*	0.109	0.0971	0.0872	0.0789	0.237	0.19	0.146	0.0905	0.311	0.243	0.194	0.129
	ARE%	0.317	0.427	0.317	0.279	0.244	0.131	0.655	0.097	0.353	0.306	0.319	0.166
	QOF%	98.7	98.8	99.1	99.3	99.3	99.6	99.4	99.8	99.4	99.5	99.6	99.8
CQ30P	k_A, *1/s*	0.113	0.117	0.133	0.147	0.16	0.184	0.219	0.291	0.208	0.233	0.29	0.323
	b	1.21	1.19	1.21	1.27	1.38	1.21	1.26	1.12	1.38	1.3	1.16	1.1
	q_e, *mmol/g*	0.0652	0.0614	0.055	0.0509	0.153	0.12	0.1	0.0733	0.194	0.167	0.125	0.112
	ARE%	0.135	0.136	0.246	0.181	0.167	0.105	0.186	0.193	0.132	0.163	0.217	0.122
	QOF%	99.5	99.7	99.6	99.7	99.6	99.9	99.7	99.8	97.2	98	98.5	99.8
CQ650	k_A, *1/s*	0.109	0.131	0.136	0.154	0.141	0.156	0.171	0.199	0.211	0.236	0.277	0.342
	b	1.32	1.26	1.23	1.13	1.37	1.41	1.32	1.37	1.33	1.26	1.17	0.87
	q_e, *mmol/g*	0.075	0.0595	0.0568	0.0466	0.174	0.158	0.138	0.119	0.189	0.163	0.133	0.101
	ARE%	0.482	0.208	0.365	0.376	0.357	0.231	0.121	0.234	0.273	0.218	0.205	0.129
	QOF%	99.2	99.7	99.5	99.7	99.4	99.5	99.7	99.6	99.7	99.8	99.8	99.8
PCX1	k_A, *1/s*	0.078	0.077	0.088	0.102	0.134	0.151	0.154	0.167	0.14	0.18	0.223	0.269
	b	1.3	1.19	1.26	1.17	1.2	1.2	1.07	1.1	1.32	1.32	1.13	0.95
	q_e, *mmol/g*	0.1	0.0952	0.0847	0.0679	0.161	0.14	0.125	0.117	0.284	0.214	0.156	0.122
	ARE%	0.298	0.329	0.474	0.504	0.244	0.146	0.196	0.249	0.394	0.148	0.312	0.364
	QOF%	99.1	99.4	99.1	99.2	99.6	99.7	99.7	99.6	99.4	96.1	97.7	99.6

A summary of data pertaining to the experimental saturated adsorption quantities for the adsorbent samples at 40, 55, 70 and 85 °C and CO_2 inlet concentrations of 5, 15 and 25 vol%, is given in Table 5-4. The saturated CO_2 adsorption quantity increases with an increase in inlet CO_2 concentrations and decreases with an increase in temperature. The highest reported quantity of CO_2 adsorbed was 0.311 mmol/g for CQ006 at 40 °C.

Table 5-4: Summary of the saturated adsorbed CO_2 quantities (q_e in mmol/g) for CQ006, CQ30P, CQ650 and PCX1 at 40, 55, 70 and 85 °C with inlet CO_2 concentrations of 5, 15 and 25 vol%.

Inlet CO_2 concentration	AC sample	40 °C	55 °C	70 °C	85 °C
5 *vol%* CO_2	CQ006	0.109	0.0971	0.0872	0.0789
	CQ30P	0.0652	0.0614	0.0550	0.0509
	CQ650	0.0750	0.0595	0.0568	0.0466
	PCX1	0.100	0.0952	0.0847	0.0679
15 *vol%* CO_2	CQ006	0.237	0.190	0.146	0.0905
	CQ30P	0.153	0.120	0.100	0.0733
	CQ650	0.174	0.158	0.138	0.119
	PCX1	0.161	0.140	0.125	0.117
25 *vol%* CO_2	CQ006	0.311	0.243	0.194	0.129
	CQ30P	0.194	0.167	0.125	0.112
	CQ650	0.189	0.163	0.133	0.101
	PCX1	0.284	0.214	0.156	0.122

The effect of inlet CO_2 concentration is shown in Figure 5-11 for CQ650 at 40, 55, 70 and 85 °C. The adsorption rate increases as the inlet CO_2 concentration increases. A higher inlet CO_2 concentration indicates that there are more CO_2 molecules per volume gas, resulting in more rapid filling of the active sites present in the adsorbent, hence causing the adsorbent to reach equilibrium adsorption faster. A similar trend is observed for CQ006, CQ30P and PCX1: see Figure C- 1, Figure C- 2 and Figure C- 3 (Appendix C).

Comparing the experimental adsorption rate data of CQ006, CQ30P, CQ650 and PCX1 at 40, 55, 70 and 85 °C with an inlet CO_2 concentration of 15 vol%, yields Figure 5-12. CQ30P outperforms the other adsorbents at all the temperatures. At 40 to 70 °C, CQ006 presents as the

slowest adsorbent, but at 85 °C it's adsorption rate picks up and leads to PCX1 being the slowest adsorbent.

Examining Figure C- 4 and Figure C- 5 presenting the comparison of the experimental CO_2 adsorption rate data of CQ006, CQ30P, CQ650 and PCX1 at 40, 55, 70 and 85 °C with CO_2 inlet concentrations of 5 and 25 vol% in Appendix C, CQ650 is the best performing adsorbent at 5 and 25 vol% CO_2 in the temperature range 40–70 °C. At 85 °C the CQ30P adsorbent performs the best for both 5 and 25 vol% CO_2.

CQ006 and PCX1 present as the slowest adsorbents regarding adsorption kinetic rate. Analysing their saturated adsorption quantities, given in Table 5-4, shows that both CQ006 and PCX1 adsorb more CO_2 than CQ650 and CQ30P. Thus, adsorbents with a higher CO_2 adsorption capacity will yield slower adsorption rates due to the extended times required to reach saturated CO_2 adsorption.

A repeatability study was performed on the CQ006, CQ650 and PCX1 adsorbent samples at 40, 55 and 70 $°C$ and 15, 5 and 15 vol% CO_2 inlet concentrations, respectively, with a 95% confidence interval. The experimental adsorption rate error analysis is shown in Figure C- 6, Figure C- 7 and Figure C- 8, with the tabulated data given in Table C- 5, Table C- 6 and Table C- 7. The total experimental error for CQ006 at 40 °C with a CO_2 inlet concentration of 15 vol%, was 12%. The experimental error determined for CQ650 at 55 °C with an inlet CO_2 concentration of 5 vol% was 12.8%. An experimental error of 4.1% was calculated for PCX1 at 70 °C with an inlet CO_2 concentration of 15 vol%.
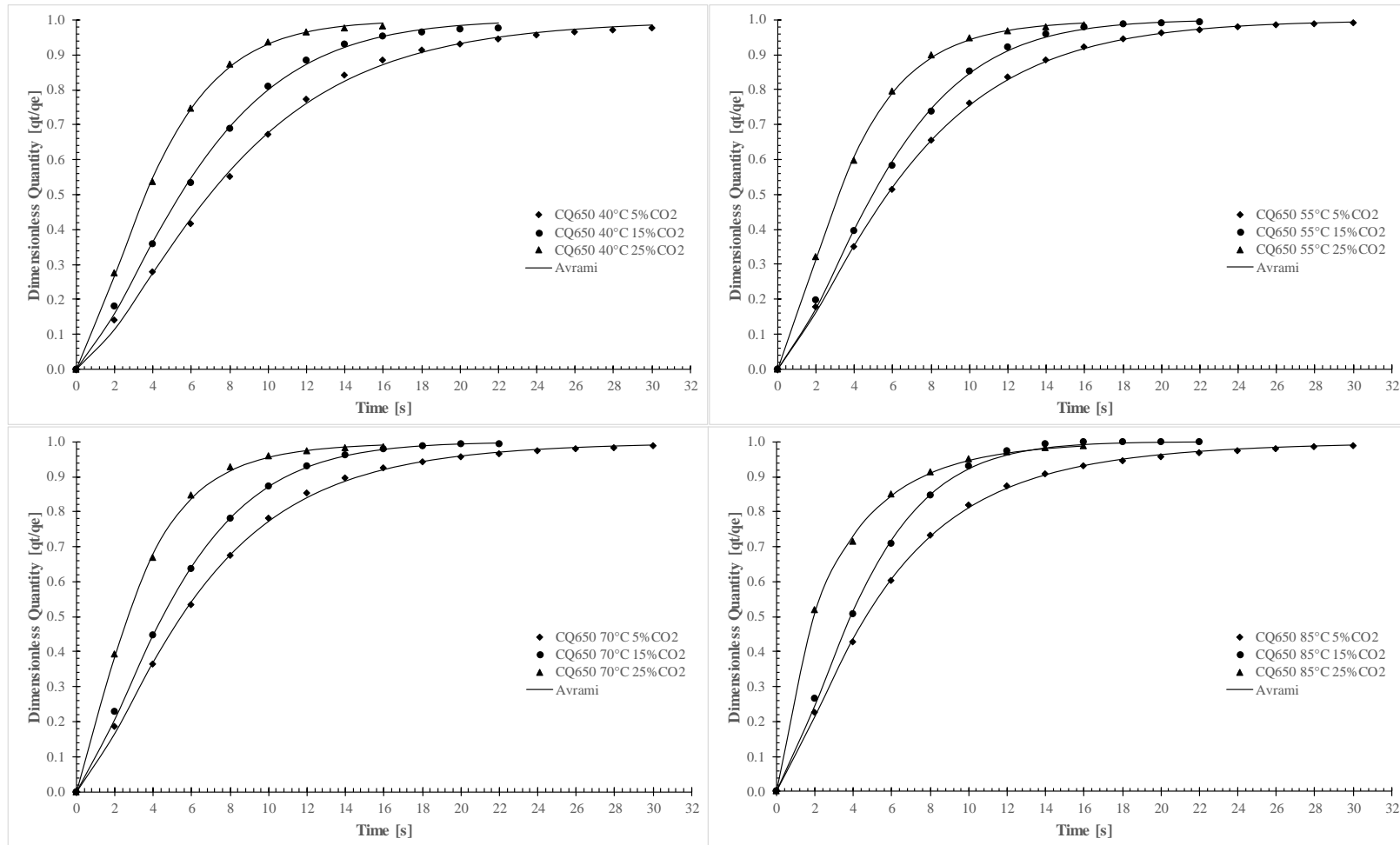
Figure 5-11: Experimental adsorption rate data at 40, 55, 70 and 85 °C for CQ650 at different inlet CO_2 concentration of 5, 15 and 25 vol%, modelled with the Avrami adsorption rate model.
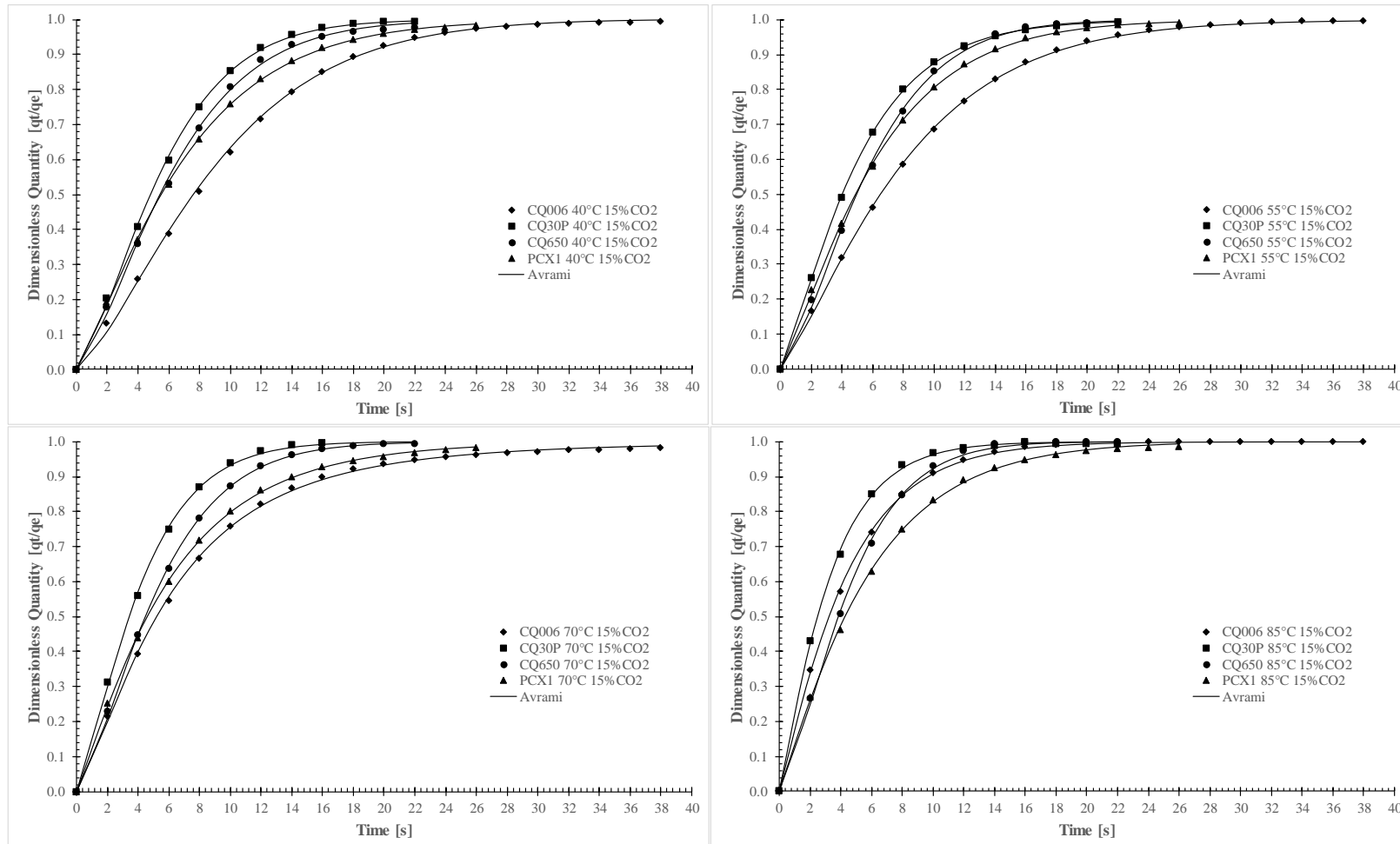
Figure 5-12: Comparing the experimental adsorption rate data of CQ006, CQ30P, CQ650 and PCX1 at 40, 55, 70 and 85 °C for at a fixed inlet CO_2 concentration of 15 vol%, modelled with the Avrami adsorption rate model.

5.4 DETERMINATION OF THE CO_2 DIFFUSION MECHANISM ONTO THE SOLID ADSORBENT

The CO_2 diffusion mechanism onto the activated carbon adsorbents was investigated with the interparticle diffusion, intraparticle diffusion and the Boyd's film-diffusion model, as given in Section 3.5.4. Evaluating the adsorption rate data for interparticle diffusion in the range $0.7 <$ $q_t/q_e < 0.99$, the $1-q_t/q_e$ versus time was plotted for CQ006 at 40 °C, with an inlet CO_2 concentration of 15 vol%. Results are presented in Figure 5-13. The intercepts of the $1-q_t/q_e$ versus time plots of CQ006, PCX1, CQ650 and CQ30P at 40, 55, 70 and 85 °C with inlet CO_2 concentrations of 15, 25, 5 and 15 vol%, respectively, are given in Table 5-5.

If interparticle diffusion applies, then the $1-q_t/q_e$ versus time plot should be linear, with the intercepts (given in Table 5-5) equal to $\ln(6/\pi^2)$. This is clearly not the case in Figure 5-13; the intercepts in Table 5-5 do not agree with $\ln(6/\pi^2)$. Thus, interparticle diffusion does not present the diffusion mechanism experienced by CO_2 onto the adsorbents; it adheres to some other diffusion mechanism.
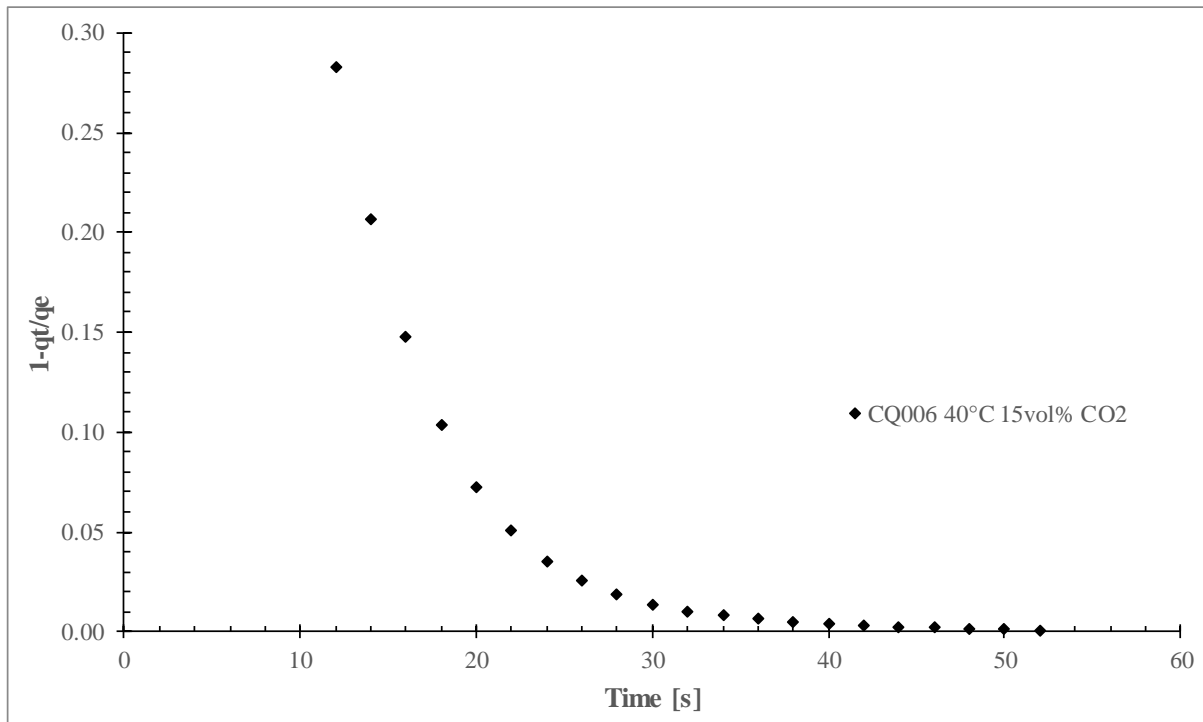
Figure 5-13: $1-q_t/q_e$ versus time plot for CQ006 at 40 °C with a CO_2 inlet concentration of 15 vol%.

Table 5-5: The slopes and intercepts of $1-q_t/q_e$ versus time plots of CQ006, PCX1, CQ650 and CQ30P at 40, 55, 70 and 85 °C with inlet CO_2 concentrations of 15, 25, 5 and 15 vol%, respectively.

Sample	CO_2 inlet concentration, *vol%*	Temperature, °C	Slope	Intercept
CQ006	15	40	-0.0058	0.37
		55	-0.0053	0.34
		70	-0.0048	0.32
		85	-0.0033	0.21
PCX1	25	40	-0.0046	0.29
		55	-0.0038	0.24
		70	-0.0034	0.21
		85	-0.0031	0.20
CQ650	5	40	-0.0055	0.36
		55	-0.0048	0.31
		70	-0.0047	0.30
		85	-0.0044	0.28
CQ30P	15	40	-0.0041	0.26
		55	-0.0038	0.24
		70	-0.0033	0.21
		85	-0.0028	0.18

To evaluate intraparticle diffusion, a Weber–Morris plot of CQ006 at 40 *°C* with an inlet CO_2 concentration of 15 vol% was investigated; see Figure 5-14. If intraparticle diffusion is the CO_2 diffusion mechanism followed when CO_2 diffuses into the activated carbon adsorbent, then the Weber–Morris plot should be linear, and if intraparticle diffusion is the only diffusion mechanism, then the straight line should pass through the origin. However, this is not the case. In Figure 5-14, the plot is not linear and the straight line does not pass through the origin. This leads to the conclusion that the CO_2 adsorption involves a combination of diffusion mechanisms. Three distinct linear regions, regions A, B and C, are observed. Upon inspecting the Weber–Morris plot in Figure 5-15, each linear region can be attributed to different diffusion mechanisms occurring, chronologically, as the CO_2 adsorption takes place on the activated carbon sample.
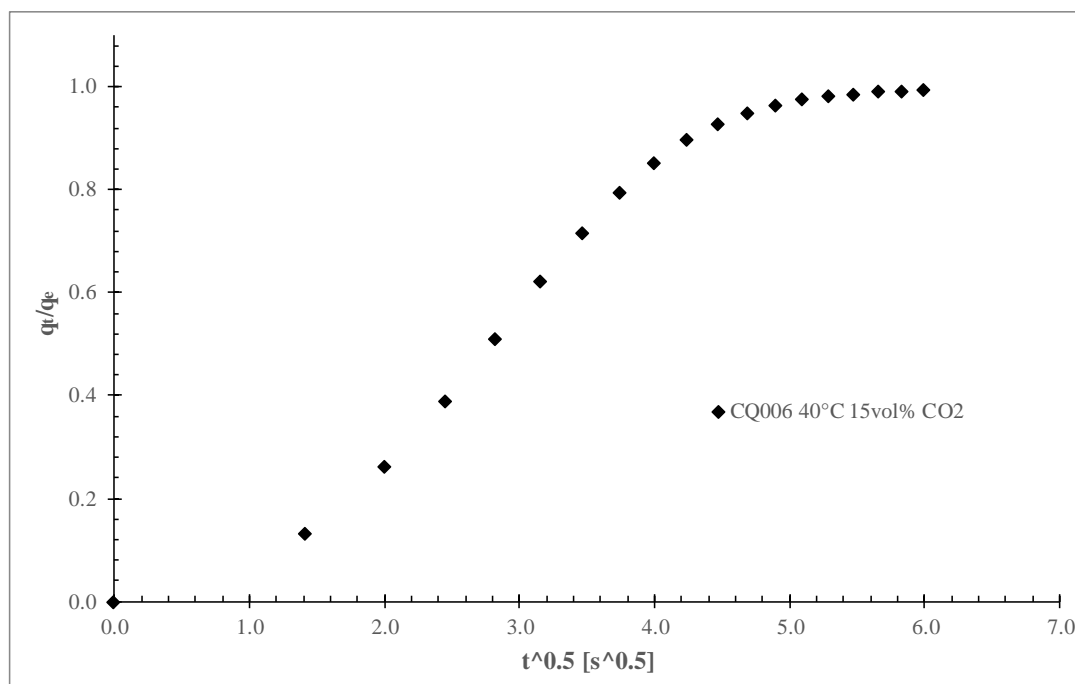
Figure 5-14: Weber–Morris plot of CQ006 at 40 °C with an inlet CO_2 concentration of 15 vol%.
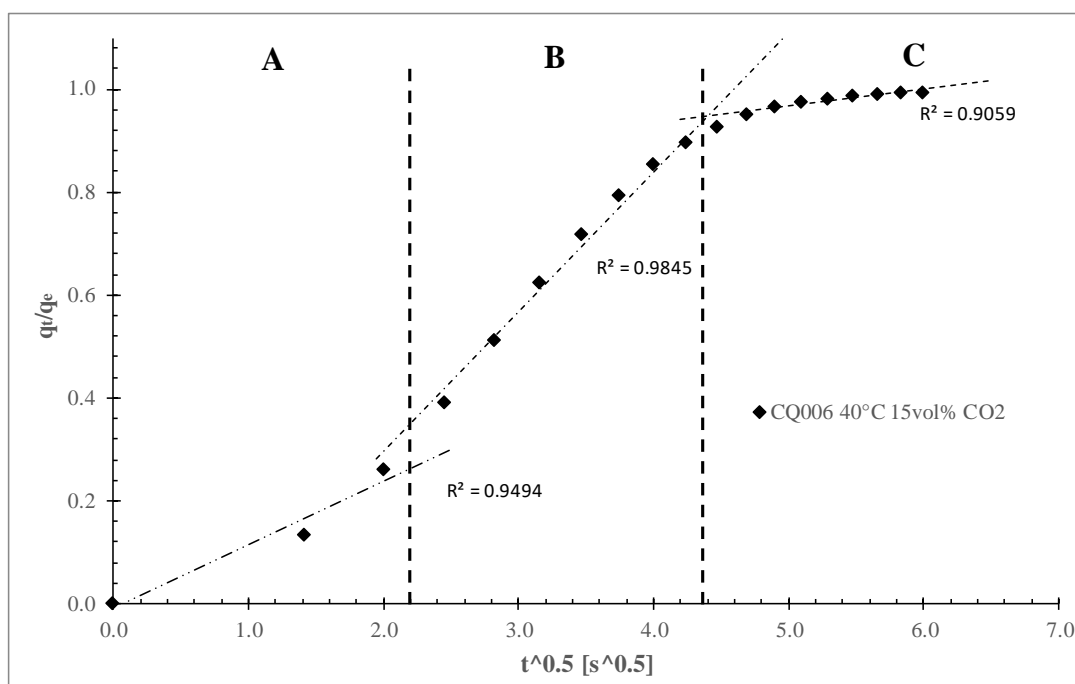
Figure 5-15: Weber–Morris plot of CQ006 at 40 °C with an inlet CO_2 concentration of 15 vol%, indicating linear regions.

126

The first linear region that is observed is associated with film diffusion, where the CO_2 molecules diffuse through the boundary layer surrounding the external surface of the adsorbent. The second linear region is associated with intraparticle diffusion, where the CO_2 molecules diffuses inside the pores of the adsorbent. The third linear region illustrates the final equilibrium stage, where the adsorbent is approaching saturation with CO_2. Each diffusion mechanism occurs in a certain time frame as the CO_2 adsorption on the adsorbent progresses.

Further investigation into the Weber–Morris plots of CQ006, PCX1, CQ650 and CQ30P at 40, 55, 70 and 85 °C with inlet CO_2 concentrations of 15, 25, 5 and 15 vol%, respectively, were carried out; see Figure 5-16. All the sorbents exhibited the same phenomenon, hence indicating that the CO_2 adsorption onto all of the adsorbents is limited by film diffusion, followed by intraparticle diffusion, then leading to CO_2 saturation in the adsorbent.
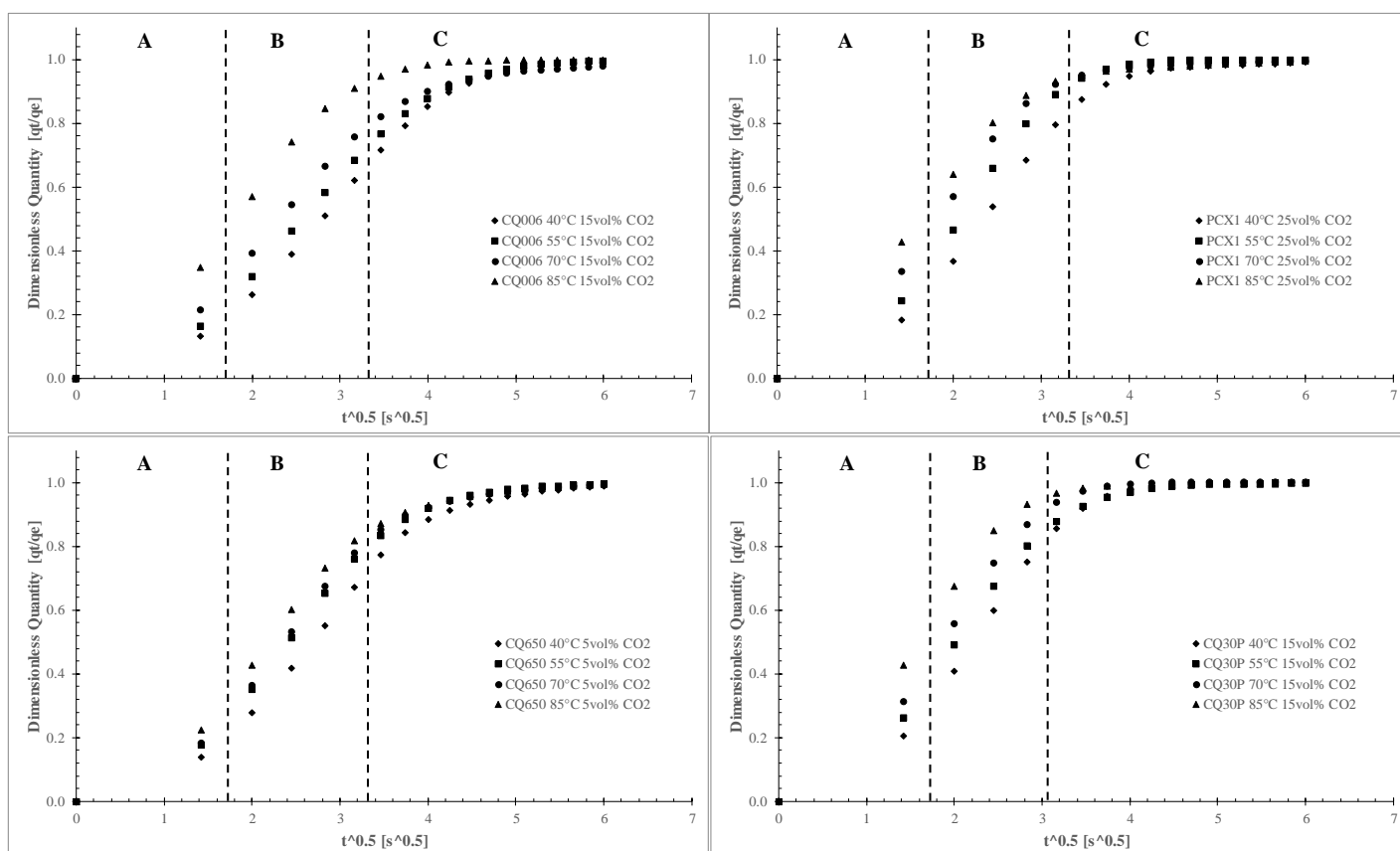
Figure 5-16: The Weber–Morris plots of CQ006, PCX1, CQ650 and CQ30P at 40, 55, 70 and 85 °C with inlet CO_2 concentrations of 15, 25, 5 and 15 vol%, respectively, indicating the different linear regions where the different rate-limiting steps take place.

5.5   ACTIVATION ENERGY

Because the Avrami adsorption rate model displayed an adequate fitting to the experimental adsorption rate data (given in Table 5-3), the Avrami adsorption rate constant (k_A) was used to obtain the Arrhenius plot for CQ006, CQ30P, CQ650 and PCX1; see Figure 5-17. The activation energies determined for the adsorbents are given in Table 5-6. The activation energy is positive at each inlet CO_2 concentration, indicating an increase in adsorption rate as the temperature increases. This further supports the findings discussed in Section 5.2.

Table 5-6: Activation energy for CQ006, CQ30P, CQ650 and PCX1.

Inlet CO_2 concentration, *vol%*	Activation energy, *kJ/mol*			
	CQ006	**CQ30P**	**CQ650**	**PCX1**
5	5.60	5.82	6.38	5.39
15	14.8	11.67	7.09	3.88
25	15.0	8.88	8.19	10.8
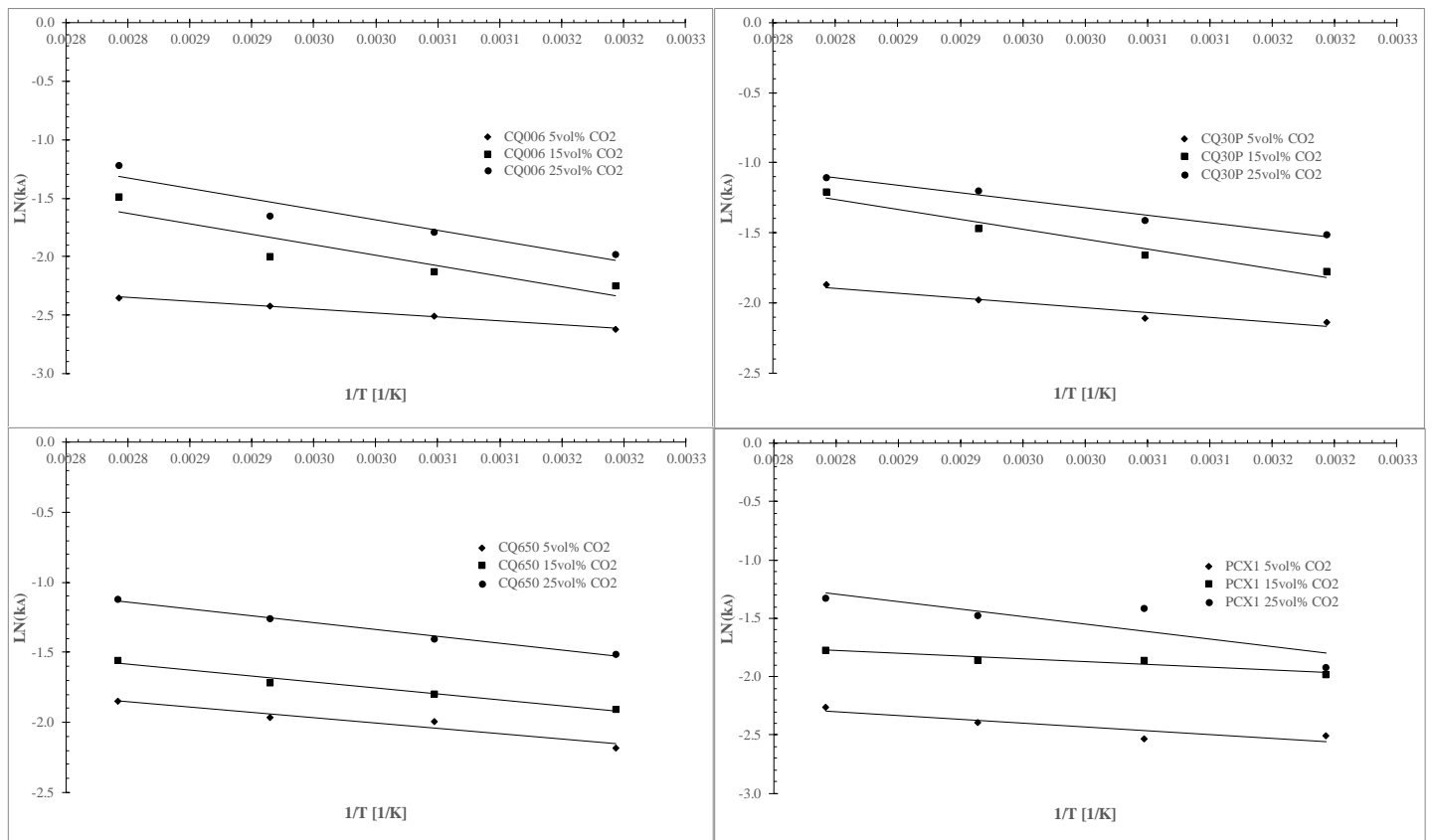
Figure 5-17: Arrhenius plots for CQ006, CQ30P, CQ650 and PCX1.

5.6   COMPARISON WITH LITERATURE

The adsorption rate results determined for the activated carbon samples in this study were compared with the adsorption rate results reported in literature for activated carbon, zeolite, magnetite and silica samples in Table 5-7. The adsorption rate of CO_2 on activated carbon samples GAC and OXA-GAC was investigated by Shafeeyan *et al.* (2015). It was found that the Avrami adsorption rate model fitted the adsorption rate results obtained for GAC and OXA-GAC the best.

The reported saturated adsorption capacities of the adsorbents tabulated in Table 5-7 all decrease as temperature increases and the adsorption rate constant increases with temperature increase. This phenomenon was also observed for the activated carbons samples investigated in this study.

The saturated CO_2 adsorption capacity reported for GAC and OXA-GAC at 45 °C with an inlet CO_2 concentration of 15 vol% was 0.19 and 0.51 mmol/g, respectively. The saturated CO_2 adsorption capacity determined for CQ006 at 40 °C with an inlet CO_2 concentration of 15 vol% was 0.24 mmol/g, which outperform the GAC activated carbon sample but not the OXA-GAC activated carbon sample. Adelodun *et al.* (2016) and Ammendola *et al.* (2017) studied the adsorption rate of CO_2 on activated carbon samples (G1, N-G1, N-O-G1, G2 and DARCO-FGD) and found saturated CO_2 adsorption capacities ranging from 0.074 to 0.86 mmol/g, which outperform the saturated CO_2 adsorption capacities determined for the activated carbon samples in this study, under similar conditions.

The activation energy reported for DARCO-FGD, C700, GAC and OXA-GAC ranged from 7.11 to 10.1 kJ/mol, which compares well with the activation energies determined for CQ006, CQ30P, CQ650 and PCX1, which range from 3.88 to 15.0 kJ/mol.

Table 5-7: CO_2 adsorption kinetic rate onto activated carbon results published in literature compared to the CO_2 adsorption kinetic rate onto activated carbon results recorded in this study.

Sample name	Pressure, bar	Temperature range, °C	Inlet CO_2 concentration, vol%	Flow rate, L/min	Temperature, °C	Saturated adsorption capacity, mmol/g	ARM	ARM parameter symbol	ARM parameter value	ARM parameter symbol	ARM parameter value	Activation energy, kJ/mol	Author(s)
CQ006	1	40-85	15	0.25	40	0.237	Avrami	k_A, 1/s	0.105	b	1.34	14.8	This study
					55	0.190			0.119		1.22		
					70	0.146			0.136		1.05		
					85	0.0905			0.226		1.09		
CQ30P	1	40-85	15	0.25	40	0.153	Avrami	k_A, 1/s	0.169	b	1.38	11.67	
					55	0.120			0.191		1.21		
					70	0.100			0.230		1.26		
					85	0.0733			0.299		1.12		
CQ650	1	40-85	15	0.25	40	0.174	Avrami	k_A, 1/s	0.148	b	1.37	7.09	
					55	0.158			0.166		1.41		
					70	0.138			0.180		1.32		
					85	0.119			0.212		1.37		
PCX1	1	40-85	15	0.25	40	0.161	Avrami	k_A, 1/s	0.138	b	1.20	3.88	
					55	0.140			0.156		1.20		
					70	0.125			0.156		1.07		
					85	0.117			0.170		1.10		
DARCO FGD	1	18-130	15	1	18	0.387	P1O	k_1, 1/s	0.00183	-	-	7.13	Ammendola et al. (2017)
					40	0.530			0.00315		-		
					70	0.146			0.00557		-		
					100	0.0960			0.00920		-		
					130	0.0740			0.01167		-		
GAC	1	30-60	15	0.05-0.1	30	0.260	Avrami	k_A, 1/s	0.00797	b	1.03	10.1	Shafeeyan et al. (2015)
					45	0.190			0.01010		0.96		
					60	0.110			0.01140		0.91		
OXA-GAC	1	30-60	15	0.05-0.1	30	0.600	Avrami	k_A, 1/s	0.03110	b	1.74	7.11	
					45	0.510			0.03530		1.53		
					60	0.400			0.04010		1.38		
C-700	1	30-100	100	0.05	30	0.795	P1O	k_1, 1/s	0.029		-	9.87	Goel et al. (2016)
AC1	0 - 20	25-200	-	-	25	0.167	P1O	k_1, 1/s	0.000972	-	-	-	Çağlayan and Aksoylu (2016)
AC4-200	0 - 20	25-200	-	-	120	0.326	P1O	k_1, 1/s	0.00102	-	-	-	
G1	1	0-35	10	-	30	0.483	P2O	k_2, s/mmol.s	0.523	-	-	-	Adelodun et al. (2016)
N-G1	1	0-35	10	-	30	0.662	P2O	k_2, s/mmol.s	0.0242	-	-	-	
N-O-G1	1	0-35	10	-	30	0.860	P2O	k_2, s/mmol.s	0.0188	-	-	-	
G2	1	0-35	10	-	30	0.474	P2O	k_2, s/mmol.s	0.516	-	-	-	

The experimental CO_2 adsorption kinetic rate results of the different activated carbon and zeolite samples (Darco FGD, GAC, OXA-GAC, Norit RB3, Zeolite 5A and Norit R2030), determined utilizing physisorption as the adsorption mechanism for CO_2, were obtained from literature (Ammendola *et al.*, 2017; Dantas *et al.*, 2011; Shafeeyan *et al.*, 2015; Singh & Kumar, 2016), and compared; see Figure 5-18. The experimental CO_2 adsorption kinetic rate results of different alkali carbonate and metal oxide samples (K_2CO_3, MgO, KMgI30-500 and KMgP30-500) determined utilizing chemisorption as the adsorption mechanism for CO_2 were obtained from literature (Lee *et al.*, 2008; Park *et al.*, 2016; Song *et al.*, 2016), and compared; see Figure 5-18. There is a clear difference between these two figures in terms of the adsorption time. The adsorption time of the adsorbents employing physisorption as the adsorption mechanism to adsorb CO_2 is significantly faster than the adsorbents utilizing chemisorption as the adsorption mechanism to adsorb CO_2.
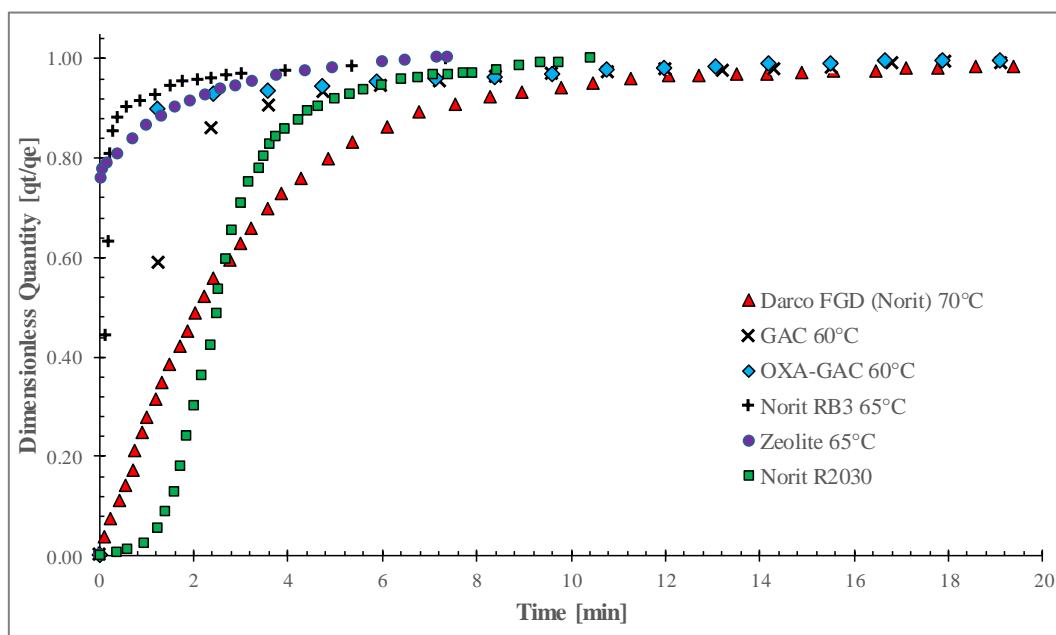
Figure 5-18: CO_2 adsorption kinetic rate result comparison between different activated carbon and zeolite samples utilizing physisorption as the adsorption mechanism, obtained from literature (Ammendola *et al.*, 2017; Dantas *et al.*, 2011; Shafeeyan *et al.*, 2015; Singh & Kumar, 2016).
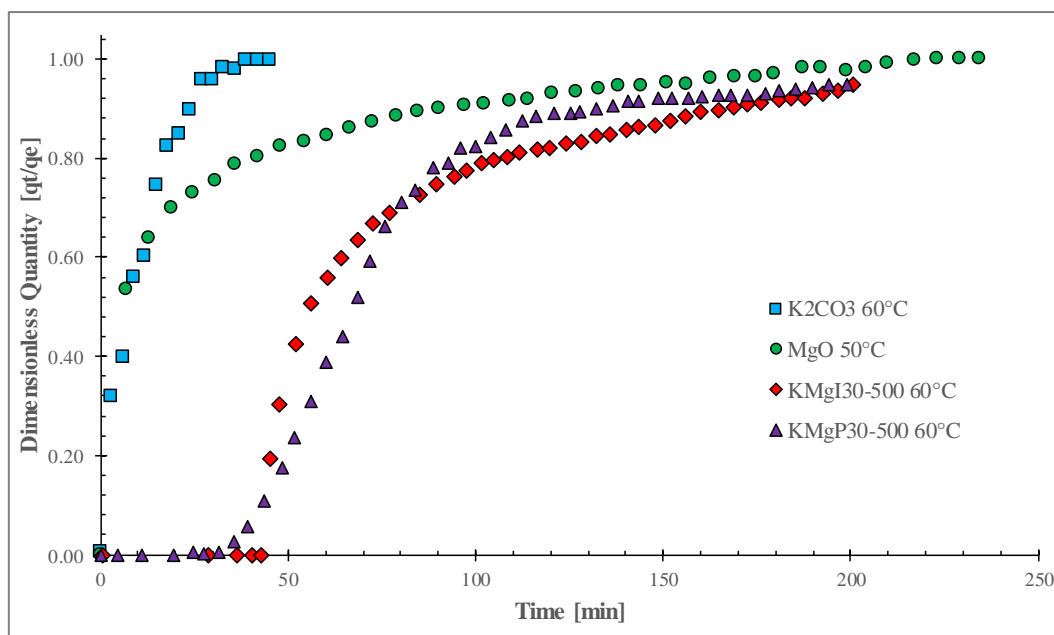
Figure 5-19: CO_2 adsorption kinetic rate result comparison between different alkali carbonate and metal oxide samples utilizing chemisorption as the adsorption mechanism, obtained from literature (Lee *et al.*, 2008; Park *et al.*, 2016; Song *et al.*, 2016)

A visual comparison of the CO_2 experimental adsorption rate kinetic results between the activate carbon samples investigated in this study (CQ006, CQ30P, CQ650 and PCX1) at 70 °C with an inlet CO_2 concentration of 25 vol% and the two best performing adsorbent samples, examined in Figure 5-18, which resulted in an activated carbon sample (RB3) and zeolite sample (5A) investigated by Singh and Kumar (2016) at 65 °C with an inlet CO_2 concentration of 100 vol% is displayed in Figure 5-20. The CO_2 adsorption kinetic rate results of the activated carbons investigated in this study outperform the CO_2 adsorption kinetic rate results of the samples studied by Singh and Kumar (2016).
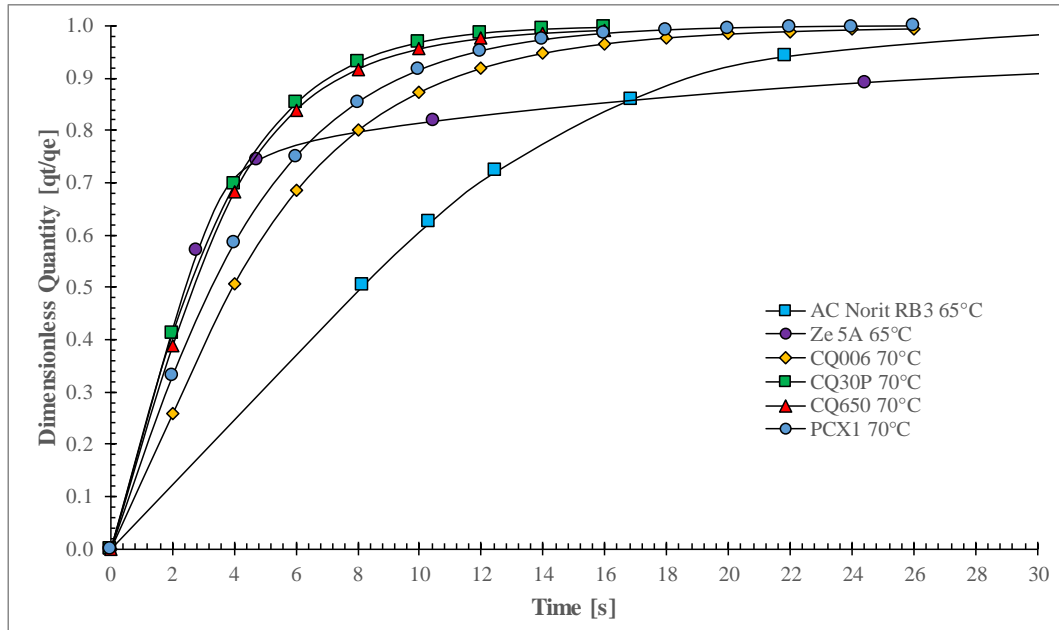
Figure 5-20: The experimental adsorption kinetic rate results of CQ006, CQ30P, CQ650 and PCX1 at 70 °C with inlet CO_2 concentration of 25 vol% compared with the experimental adsorption rate results of activated carbon sample (Norit RB3) and zeolite sample (5A) at 65 °C with inlet CO_2 concentration of 100 vol% (Singh & Kumar, 2016).

Chapter 6

(CONCLUSIONS AND RECOMMENDATIONS)

Chapter 6

(CONCLUSIONS AND RECOMMENDATIONS)

6.1 CONCLUSIONS

Four commercially available activated carbon samples (CQ006, CQ30P, CQ650 and PCX1), obtained from ChemQuest (Germiston, South Africa), were investigated for their suitability in a dry carbon capture process in terms of their adsorption capacity and adsorption kinetic rate.

The activated carbon samples (CQ006, CQ30P, CQ650 and PCX1) were comprehensively characterized using methods such as proximate analysis, ultimate analysis, surface area analysis, pore size distribution and volume analysis as well as scanning electron microscopy (SEM) analysis to compare inherent characteristics of the activated carbon samples with each other and to results published in literature.

The CO_2 adsorption isotherms for each activated carbon sample were evaluated at low pressures, in the range 0–114 kPa, at 0, 10, 20, 30, 40 and 55 °C. The individual adsorption isotherms were modelled with eight adsorption isotherm models: Langmuir, BET, Dubinin–Radushkevich (D-R), Dubinin–Astakhov (D-A), Toth, Freundlich, Temkin and SIPS to find the optimal adsorption isotherm model suitable for CO_2 adsorption isotherm modelling on the activated carbon samples. The goodness of fit for each adsorption isotherm model was evaluated with the quality of fit (QOF%) and average relative error (ARE%). D-R presented as the best fitting adsorption isotherm model to describe the experimental adsorption isotherm data of the activated carbon samples.

A fixed bed reactor was designed and constructed at the North-West University to measure the CO_2 adsorption kinetic rates of CO_2 adsorption onto the activated carbon samples. The CO_2 adsorption kinetic rates of CO_2 adsorption onto the activated carbon samples were evaluated at 40, 55, 70 and 85 °C with inlet CO_2 concentrations of 5, 15 and 25 vol% at a pressure of 1 bar. The individual adsorption rates were modelled with five adsorption rate models—Pseudo first order, pseudo second order, Elovich, Avrami and the fractional order adsorption rate models

to find the optimal adsorption rate model suitable for CO_2 adsorption rate modelling on the activated carbon samples. The goodness of fit for each adsorption isotherm model was evaluated in terms of the QOF% and ARE% values. The Avrami adsorption rate model presented as the best fitting adsorption rate model on the experimental adsorption rate data.

CQ650 was found to be the most suitable adsorbent for CO_2 adsorption in terms of adsorption capacity and kinetic rate. The CQ650 sample is derived from coconut fibres, making it robust and suitable for the use in a CO_2 capture process, such as in a circulating fluidized bed reactor. CQ650 is also impregnated with KOH resulting in an increased adsorption of CO_2. The order of the remaining activated carbon samples regarding suitability ranking in terms of CO_2 adsorption capacity and kinetic rate, are as follows: CQ006, CQ30P and PCX1.

6.2   SUMMARY OF RESULTS

The highest fixed carbon content was obtained for CQ006 at 87.9% and the highest carbon content was experimentally determined for CQ30P at 96.3%. The four activated samples displayed high BET surface areas and extensive inherent micropore structures, with the highest BET surface area and micropore surface area obtained for CQ650 at 735 m^2/g and 517 m^2/g, respectively. The average pore diameter was determined with the Horvath–Kawazoe method; values in the range 3.92–4.13 Å were recorded for the activated carbon samples. The porosity of the activated carbon samples was determined between the pore diameters 3 and 5 Å; and the highest porosity was obtained for CQ006 at 27.7%. SEM analysis revealed intricate cracks and crevasses, displaying a very uneven surface. The characterization results recorded in this study compared well with information in literature.

The maximum adsorption capacities, determined with the D-R adsorption isotherm model, decreased with an increase in temperature. This observation is attributed to the fact that gasses have increased kinetic energy at increased temperatures. The weak adsorption forces adsorbing the CO_2 onto the adsorbent is overcame when the gas has increased kinetic energy at increased temperatures and, therefore, the CO_2 adsorption quantity decreases as temperature increases. The highest adsorption capacity was obtained for CQ650 at 0 $°C$, 7.6 mmol/g. This result was expected because CQ650 has the highest micropore surface area. The adsorption isotherm results obtained in this study for the activated carbon samples compared well with literature.

CHAPTER 6: CONCLUSIONS AND RECOMMENDATIONS

An experimental repeatability study concluded that an experimental error of 1.75% was obtained.

Thermodynamic analysis was conducted on the activated carbon samples to determine the change in enthalpy, entropy, Gibbs free energy and isosteric heat of adsorption. All the values for a change in enthalpy of the activated carbon samples were found to be negative, indicating exothermic adsorption for CO_2 adsorption onto the activated carbon samples. The change in enthalpy of all the sorbents was significantly lower than 80 kJ/mol, indicating that the adsorption mechanism for CO_2 adsorption is physical adsorption.

The change in entropy was negative for all the activated carbon samples, indicating that the CO_2 adsorption progresses from a chaotic state in the bulk phase to a state of order as it adsorbs onto the adsorbent. The change in Gibbs free energy was positive for all the activated carbon samples at all the temperatures studied, which indicates that CO_2 adsorption onto the adsorbents is not favourable. The change in Gibbs free energy increases as the temperature increases indicating that CO_2 adsorption becomes less feasible and spontaneous at higher temperatures.

Analysis of the isosteric heat of adsorption as a function of surface loading indicated that the maximum isosteric heat of adsorption is obtained at low surface loading quantities. The values obtained for the isosteric heat of adsorption of the activated carbon samples were <80 kJ/mol, indicating that the CO_2 adsorption process is physical in nature.

The adsorption rate increased as the temperature and inlet CO_2 concentration increased and the saturated CO_2 adsorption quantity decreased as the temperature increased. This is attributed to the increased kinetic energy that CO_2 possesses at higher temperatures. The CQ30P sample presented as the fastest adsorbent at inlet CO_2 concentrations of 5 and 25 vol%. The CQ650 sample surpassed the CQ30P sample at an inlet CO_2 concentration of 15 vol%. The saturated CO_2 adsorption quantity increased with an increase in inlet CO_2 concentration. The highest saturated CO_2 adsorption quantity was obtained for CQ006 at 40 °C with an inlet CO_2 concentration of 25 vol%, 0.31 mmol/g. The adsorbents that presented the fastest adsorption rate adsorbed the least amount of CO_2, indicating that the adsorption rate and adsorption capacity are inversely proportional.

The activation energies were found to be positive for all the activated carbon samples at all the inlet CO_2 concentrations here, indicating that the CO_2 adsorption rate increases as the temperature increases. The adsorption isotherm results obtained for the activated carbon samples compared well with literature. An experimental repeatability study concluded that an experimental error of 9.8% was obtained.

6.3   RECOMMENDATIONS

➢ Study the adsorption isotherms of the activated carbon samples at the same temperatures at which the adsorption rates are studied.

➢ Obtain a more suitable CO_2 analyser to study a larger range of inlet CO_2 concentration adsorption rates, as well as pure CO_2 adsorption rates.

➢ Investigate adsorption isotherms and adsorption rates of more adsorbent types, such as metal organic frameworks, silica, zeolites, magnetite, MgO, K_2CO_3 and Na_2CO_3, to obtain the best possible adsorbent for CO_2 adsorption in a CFBR.

➢ Explore further characterization methods to characterize the activated carbon adsorbents, then identify correlations between CO_2 adsorption capacity and characteristics and CO_2 adsorption rate and characteristics, to pre-determine whether an activated carbon sample would be suitable for CO_2 adsorption in a CFBR.

➢ Investigate high-pressure CO_2 adsorption kinetic rates for the adsorption of CO_2 at higher pressures.

➢ Investigate the regenerative ability of adsorbents by studying the CO_2 desorption kinetic rates of the adsorbents.

➢ Investigate multi-component mixtures containing CO_2, N_2, O_2, SO_2 and NO_x gases to replicate realistic flue gas conditions.

➢ Activated carbons co-adsorb water and this is detrimental because regeneration energies are increased. Investigating gases containing moisture will be critical for practical application of activated carbons in an industrial capturing process.

➢ In real applications the amount of CO_2 adsorbed at the breakthrough time will be considered rather than the equilibrium adsorbed amount. Indeed, when breakthrough is about to occur, i.e., once the percentage of the adsorbate exiting the column rises above a certain threshold value (i.e., at the breakthrough value), the reactor (typically a fixed bed) is taken off-line and the feed is switched to the second bed. Simultaneously, the first bed is regenerated by either increasing the temperature (temperature swing adsorption, TSA) or decreasing the pressure (pressure swing adsorption, PSA).

6.4   CONTRIBUTION TO EXISTING KNOWLEDGE AND SCIENCE

The following contributions were made to the existing knowledge and field of science:

➢ A fixed bed reactor that accurately measures the kinetic rate of CO_2 adsorption onto dry adsorbents was developed and constructed at the North-West University in South Africa.

➢ The characterization, CO_2 adsorption capacities and kinetic rates of commercially available activated carbon samples in South Africa were investigated and documented. Acceptable CO_2 adsorption capacity and kinetic rates, compared to literature data, was obtained for the activated carbon samples, originally intended for gold capture, ink manufacturing and water purification, respectively.

➢ Confirmed the validity of the Avrami adsorption kinetic rate model to the kinetic rate of CO_2 adsorption onto activated carbon samples. The results recorded in this study is in well agreement with results published in literature.

BIBLIOGRAPHY

Abbasi, E. & Arastoopour, H. 2011. CFD simulation of CO2 sorption in a circulating fluidized bed using deactivation kinetic model.

Abd, A.A., Naji, S.Z., Hashim, A.S. & Othman, M.R. 2020. Carbon dioxide removal through physical adsorption using carbonaceous and non-carbonaceous adsorbents: a review. *Journal of Environmental Chemical Engineering*:104142.

Adelodun, A.A., Ngila, J.C., Kim, D.-G. & Jo, Y.-M. 2016. Isotherm, thermodynamic and kinetic studies of selective CO2 adsorption on chemically modified carbon surfaces. *Aerosol Air Quality Research*, 16(12):3312-3329.

Al-Ghouti, M.A. & Da'ana, D.A. 2020. Guidelines for the use and interpretation of adsorption isotherm models: A review. *Journal of Hazardous Materials*, 393:122383.

Ammendola, P., Raganati, F. & Chirone, R. 2017. CO2 adsorption on a fine activated carbon in a sound assisted fluidized bed: Thermodynamics and kinetics. *Chemical Engineering Journal*, 322:302-313.

Audus, H. 2000. Leading options for the capture of CO2 at power stations. (*In*. Proceedings of the Fifth International Conference on Greenhouse Gas Control Technologies, Cairns, Australia organised by: Citeseer. p. 13-16).

Avrami, M. 1939. Kinetics of phase change. I General theory. *The Journal of chemical physics*, 7(12):1103-1112.

Balsamo, M., Budinova, T., Erto, A., Lancia, A., Petrova, B., Petrov, N. & Tsyntsarski, B. 2013. CO2 adsorption onto synthetic activated carbon: Kinetic, thermodynamic and regeneration studies. *Separation and Purification Technology*, 116:214-221.

Barnes, I. 2015. Upgrading the Efficiency of the World's Coal Fleet to Reduce CO2 Emissions. (*In*. Cornerstone-The Official Journal of the World Coal Industry organised by: Spring. p. 4-9).

Ben-Mansour, R., Habib, M., Bamidele, O., Basha, M., Qasem, N., Peedikakkal, A., Laoui, T. & Ali, M. 2016. Carbon capture by physical adsorption: materials, experimental investigations and numerical modeling and simulations–a review. *Applied Energy*, 161:225-255.

Benjaprakairat, T., Piumsomboon, P. & Chalermsinsuwan, B. 2020. Development of computational fluid dynamics model for two initial CO2 concentration in circulating fluidized bed reactor. *Energy Reports*, 6:137-145.

Boyd, G., Adamson, A. & Myers Jr, L. 1947. The exchange adsorption of ions from aqueous solutions by organic zeolites. II. Kinetics. *Journal of the American Chemical Society*, 69(11):2836-2848.

BIBLIOGRAPHY

Brunauer, S., Emmett, P.H. & Teller, E. 1938. Adsorption of Gases in Multimolecular Layers. *Journal of the American Chemical Society*, 60(2):309-319.

Bubanale, S. & Shivashankar, M. 2017. History, method of production, structure and applications of activated carbon. *International Journal of Engineering Technical Research*, 6:495-498.

Çağlayan, B.S. & Aksoylu, A.E. 2016. CO_2 adsorption behavior and kinetics on chemically modified activated carbons. *Turkish Journal of Chemistry*, 40(4):576-587.

Cazorla-Amorós, D., Alcaniz-Monge, J. & Linares-Solano, A. 1996. Characterization of activated carbon fibers by CO_2 adsorption. *Langmuir*, 12(11):2820-2824.

Chalermsinsuwan, B., Piumsomboon, P. & Gidaspow, D. 2010. A computational fluid dynamics design of a carbon dioxide sorption circulating fluidized bed. *AIChE journal*, 56(11):2805-2824.

Choi, S., Moon, H., Lee, N., Kim, K., Park, Y.-K. & Cho, H.H. 2020. Thermal design of dual circulating fluidized bed reactors for a large-scale CO_2 capture system. *Applied Thermal Engineering*, 171:115114.

Coninck, H.d. & Benson, S.M. 2014. Carbon Dioxide Capture and Storage: Issues and Prospects. *Annual Review of Environment and Resources*, 39(1):243-270.

Crippa, M., Oreggioni, G., Guizzardi, D., Muntean, M., Schaaf, E., Lo Vullo, E., Solazzo, E., Monforti-Ferrario, F., Olivier, J.G. & Vignati, E. 2019. Fossil CO_2 and GHG emissions of all world countries. *Luxemburg: Publication Office of the European Union*.

Cychosz, K.A. & Thommes, M. 2018. Progress in the Physisorption Characterization of Nanoporous Gas Storage Materials. *Engineering*, 4(4):559-566.

Czerw, K., Baran, P. & Zarębska, K. 2017. Application of the stretched exponential equation to sorption of mine gases and sorption induced swelling of bituminous coal. *International Journal of Coal Geology*, 173:76-83.

Dantas, T.L., Luna, F.M.T., Silva Jr, I.J., de Azevedo, D.C., Grande, C.A., Rodrigues, A.E. & Moreira, R.F. 2011. Carbon dioxide–nitrogen separation through adsorption on activated carbon in a fixed bed. *Chemical Engineering Journal*, 169(1-3):11-19.

Davis, M.E. & Davis, R.J. 2012. Fundamentals of chemical reaction engineering. 15 Wellman Avenue, North Chelmsford, Massachusetts 01863, U.S.A.: Courier Corporation.

Dubinin, M. 1960. The potential theory of adsorption of gases and vapors for adsorbents with energetically nonuniform surfaces. *Chemical Reviews*, 60(2):235-241.

Dubinin, M. & Astakhov, V. 1971. Development of ideas of volume filling of micropores during adsorption of gases and vapours by microporous adsorbents. 1. Carbonaceous adsorbents. *Izvestiya Akademii Nauk SSSR-Seriya Khimicheskaya*(1):5-+.

BIBLIOGRAPHY

Dubinin, M.i. 1975. Physical adsorption of gases and vapors in micropores. Progress in surface and membrane science. Elsevier. p. 1-70).

Dubinin, M.M., Zaverina, E. & Radushkevich, L. 1947. Sorption and structure of active carbons. I. Adsorption of organic vapors. *Zhurnal Fizicheskoi Khimii*, 21(3):151-162.

Ebner, A.D. & Ritter, J.A. 2009. State-of-the-art adsorption and membrane separation processes for carbon dioxide production from carbon dioxide emitting industries. *Separation Science and Technology*, 44(6):1273-1421.

Elovich, S.Y. & Larinov, O. 1962. Theory of adsorption from solutions of non electrolytes on solid (I) equation adsorption from solutions and the analysis of its simplest form,(II) verification of the equation of adsorption isotherm from solutions. *Akad. Nauk. SSSR, Otd. Khim. Nauk*, 2(2):209-216.

Everett, D. 1972. Manual of symbols and terminology for physicochemical quantities and units, appendix II: Definitions, terminology and symbols in colloid and surface chemistry. *Pure and Applied Chemistry*, 31(4):577-638.

Feig, G.T., Joubert, W.R., Mudau, A.E. & Monteiro, P. 2017. South African carbon observations: CO2 measurements for land, atmosphere and ocean. *South African Journal of Science*, 113(11-12):1-4.

Figueroa, J.D., Fout, T., Plasynski, S., McIlvried, H. & Srivastava, R.D. 2008. Advances in CO2 capture technology—The U.S. Department of Energy's Carbon Sequestration Program. *International Journal of Greenhouse Gas Control*, 2(1):9-20.

Flanigen, E.M., Broach, R.W. & Wilson, S.T. 2010. Zeolites in industrial separation and catalysis. Vol. 1. Hoboken, New Jersey, U.S.A.: John Wiley & Sons.

Freundlich, H. 1906. Over the adsorption in solution. *J. Phys. Chem*, 57(385471):1100-1107.

Fylstra, D., Lasdon, L., Watson, J. & Waren, A. 1998. Design and use of the Microsoft Excel Solver. *Interfaces*, 28(5):29-55.

Garnier, C., Finqueneisel, G., Zimny, T., Pokryszka, Z., Lafortune, S., Défossez, P. & Gaucher, E.C. 2011. Selection of coals of different maturities for CO2 Storage by modelling of CH4 and CO2 adsorption isotherms. *International Journal of Coal Geology*, 87(2):80-86.

Ge, M. & Friedrich, J. 2020. Charts explain greenhouse gas emissions by countries and sectors. *World Resources Institute*.

Ghanbari, T., Abnisa, F. & Daud, W.M.A.W. 2020. A review on production of metal organic frameworks (MOF) for CO2 adsorption. *Science of The Total Environment*, 707:135090.

Ghoufi, A., Gaberova, L., Rouquerol, J., Vincent, D., Llewellyn, P. & Maurin, G. 2009. Adsorption of CO2, CH4 and their binary mixture in Faujasite NaY: a combination of molecular simulations with gravimetry–manometry and microcalorimetry measurements. *Microporous and Mesoporous Materials*, 119(1-3):117-128.

BIBLIOGRAPHY

Gibbins, J. & Chalmers, H. 2008. Carbon capture and storage. *Energy Policy*, 36(12):4317-4322.

Gielen, D. 2003. The energy policy consequences of future CO2 capture and sequestration technologies. (*In*. Proceedings of the 2nd annual conference on carbon sequestration. Alexandria, VA organised by: Citeseer.

Gil, A., Korili, S. & Vicente, M. 2008. Recent advances in the control and characterization of the porous structure of pillared clay catalysts. *Catalysis Reviews*, 50(2):153-221.

Goel, C., Kaur, H., Bhunia, H. & Bajpai, P.K. 2016. Carbon dioxide adsorption on nitrogen enriched carbon adsorbents: Experimental, kinetics, isothermal and thermodynamic studies. *Journal of CO2 utilization*, 16:50-63.

Goel, N., Kumar, V., Pahan, S., Bhardwaj, Y. & Sabharwal, S. 2011. Development of adsorbent from Teflon waste by radiation induced grafting: Equilibrium and kinetic adsorption of dyes. *Journal of hazardous materials*, 193:17-26.

Gottipati, R. 2012. Preparation and characterization of microporous activated carbon from biomass and its application in the removal of chromium (VI) from aqueous phase. Rourkela, Odisha 769001, India: National Institute of Technology, Rourkela.

Gratuito, M.K.B., Panyathanmaporn, T., Chumnanklang, R.A., Sirinuntawittaya, N. & Dutta, A. 2008. Production of activated carbon from coconut shell: Optimization using response surface methodology. *Bioresource Technology*, 99(11):4887-4895.

Green, D.A., Turk, B.S., Gupta, R.P., Portzer, J.W., McMichael, W. & Harrison, D. 2004. Capture of carbon dioxide from flue gas using solid regenerable sorbents. *International journal of environmental technology and management*, 4(1-2):53-67.

Hauchhum, L. & Mahanta, P. 2014a. Carbon dioxide adsorption on zeolites and activated carbon by pressure swing adsorption in a fixed bed. *International Journal of Energy Environmental Engineering*, 5(4):349-356.

Hauchhum, L. & Mahanta, P. 2014b. Kinetic, thermodynamic and regeneration studies for CO2 adsorption onto activated carbon. *International Journal of Advanced Mechanical Engineering*, 4(1):27-32.

Hauchhum, L. & Mahanta, P. 2017. Performance enhancement of CO2 capture from flue gas in a bubbling fluidized bed. *Journal of the Energy Institute*, 90(5):764-775.

Heydari-Gorji, A. & Sayari, A. 2011. CO2 capture on polyethylenimine-impregnated hydrophobic mesoporous silica: Experimental and kinetic modeling. *Chemical engineering journal*, 173(1):72-79.

Ho, Y.-S. & McKay, G. 1999. Pseudo-second order model for sorption processes. *Process biochemistry*, 34(5):451-465.

143

BIBLIOGRAPHY

Hoffmann, S., Bartlett, M., Finkenrath, M., Evulet, A. & Ursin, T.P. 2008. Performance and Cost Analysis of Advanced Gas Turbine Cycles With Precombustion CO2 Capture. *Journal of Engineering for Gas Turbines and Power*, 131(2):021701-021701-021707.

Jafari, H., Sheikhi, A. & Sotudeh‑Gharebagh, R. 2020. Sequential modular simulation of circulating fluidized bed reactors. *The Canadian Journal of Chemical Engineering*, 98(4):1003-1016.

Kanniche, M., Gros-Bonnivard, R., Jaud, P., Valle-Marcos, J., Amann, J.-M. & Bouallou, C. 2010. Pre-combustion, post-combustion and oxy-combustion in thermal power plant for CO2 capture. *Applied Thermal Engineering*, 30(1):53-62.

Kargari, A. & Ravanchi, M.T. 2012. Carbon dioxide: capturing and utilization. Greenhouse gases-capturing, utilization and reduction. InTech.

Keller, J., Dreisbach, F., Rave, H., Staudt, R. & Tomalla, M. 1999. Measurement of gas mixture adsorption equilibria of natural gas compounds on microporous sorbents. *Adsorption*, 5(3):199-214.

Keller, J.U. & Staudt, R. 2005. Gas adsorption equilibria: experimental methods and adsorptive isotherms. Berlin/Heidelberg, Germany: Springer Science & Business Media.

Khraisheh, M., Mukherjee, S., Kumar, A., Al Momani, F., Walker, G. & Zaworotko, M.J. 2020. An overview on trace CO2 removal by advanced physisorbent materials. *Journal of Environmental Management*, 255:109874.

Kruk, M. & Jaroniec, M. 2001. Gas adsorption characterization of ordered organic− inorganic nanocomposite materials. *Chemistry of materials*, 13(10):3169-3183.

Kumar, S., Saxena, S.K., Drozd, V. & Durygin, A. 2015. An experimental investigation of mesoporous MgO as a potential pre-combustion CO 2 sorbent. *Materials for Renewable Sustainable Energy*, 4(2):8.

Kweku, D.W., Bismark, O., Maxwell, A., Desmond, K.A., Danso, K.B., Oti-Mensah, E.A., Quachie, A.T. & Adormaa, B.B. 2017. Greenhouse effect: greenhouse gases and their impact on global warming. *Journal of Scientific research and reports*:1-9.

Lagergren, S.K. 1898. About the theory of so-called adsorption of soluble substances. *Sven. Vetenskapsakad. Handingarl*, 24:1-39.

Langmuir, I. 1916. The constitution and fundamental properties of solids and liquids. Part I. Solids. *Journal of the American chemical society*, 38(11):2221-2295.

Lee, C.-H., Park, S.-W. & Kim, S.-S. 2014. Breakthrough analysis of carbon dioxide adsorption on zeolite synthesized from fly ash. *Korean Journal of Chemical Engineering*, 31(2):179-187.

Lee, S.C., Chae, H.J., Lee, S.J., Choi, B.Y., Yi, C.K., Lee, J.B., Ryu, C.K. & Kim, J.C. 2008. Development of Regenerable MgO-Based Sorbent Promoted with K2CO3 for CO2 Capture at Low Temperatures. *Environmental Science & Technology*, 42(8):2736-2741.

BIBLIOGRAPHY

Leung, D.Y.C., Caramanna, G. & Maroto-Valer, M.M. 2014. An overview of current status of carbon dioxide capture and storage technologies. *Renewable and Sustainable Energy Reviews*, 39:426-443.

LeVan, M.D., Carta, G. & Yon, C.M. 1997. Adsorption and ion exchange. *Energy*, 16:17.

Lopes, E.C., dos Anjos, F.S., Vieira, E.F. & Cestari, A.R. 2003. An alternative Avrami equation to evaluate kinetic parameters of the interaction of Hg (II) with thin chitosan membranes. *Journal of Colloid Interface Science*, 263(2):542-547.

Lozano-Castelló, D., Suárez-García, F., Cazorla-Amorós, D. & Linares-Solano, A. 2009. Porous texture of carbons. *Carbons for electrochemical energy storage and conversion systems. CRC, Boca Raton*:115-162.

Lu, G., Wei, C., Wang, J., Yan, G., Zhang, J. & Song, Y. 2018. Methane adsorption characteristics and adsorption model applicability of tectonically deformed coals in the Huaibei coalfield. *Energy & Fuels*, 32(7):7485-7496.

Marsh, H., Reinoso, F.R. & Rodriguez-Reinoso, F. 2006. Activated Carbon. Oxford, UNITED KINGDOM: Elsevier Science.

Mayoral, M., Izquierdo, M., Andrés, J. & Rubio, B. 2001. Different approaches to proximate analysis by thermogravimetry analysis. *Thermochimica Acta*, 370(1-2):91-97.

McSweeney, R. & Timperley, J. 2018. The Carbon Brief Profile: South Africa. *Carbon Brief*.

Metz, B., Davidson, O., De Coninck, H., Loos, M. & Meyer, L. 2005. IPCC, 2005: IPCC special report on carbon dioxide capture and storage. Prepared by Working Group III of the Intergovernmental Panel on Climate Change. *Cambridge, United Kingdom and New York, NY, USA*, 442.

Micromeritics, A. 2004. 2020 Accelerated Surface Area and Porosimetry System Operator's Manual: Micromeritics Instrument Corporation, Norcross, GA.

Mohamedali, M., Nath, D., Ibrahim, H. & Henni, A. 2016. Review of recent developments in CO2 capture using solid materials: metal organic frameworks (MOFs). *Greenhouse Gases: Science and Technology*:115-154.

Morris, J.C. & Weber jr, W.J. 1964. Removal of biologically-resistant pollutants from waste waters by adsorption. Advances in water pollution research. Elsevier. p. 231-266).

Müller, U., Schubert, M.M. & Yaghi, O.M. 2008. Chemistry and applications of porous metal–organic frameworks. *Handbook of Heterogeneous Catalysis*:247-262.

Nguyen, C. & Do, D.D. 2001. The Dubinin–Radushkevich equation and the underlying microscopic adsorption description. *Carbon*, 39(9):1327-1336.

Nie, L., Mu, Y., Jin, J., Chen, J. & Mi, J. 2018. Recent developments and consideration issues in solid adsorbents for CO2 capture from flue gas. *Chinese Journal of Chemical Engineering*, 26(11):2303-2317.

BIBLIOGRAPHY

Ogungbenro, A.E., Quang, D.V., Al-Ali, K. & Abu-Zahra, M.R. 2017. Activated Carbon from Date Seeds for CO2 Capture Applications. *Energy Procedia*, 114:2313-2321.

Okolo, G.N. 2017. Adsorption properties of South African bituminous coals relevant to carbon dioxide storage. Potchefstroom, North-West, South Africa: North-West University.

Ozdemir, E. 2005. Chemistry of the adsorption of carbon dioxide by Argonne premium coals and a model to simulate CO2 sequestration in coal seams. Pittsburgh, Pennsylvania, United States: University of Pittsburgh.

Park, S.-W., Sung, D.-H., Choi, B.-S., Lee, J.-W. & Kumazawa, H. 2006. Carbonation kinetics of potassium carbonate by carbon dioxide. *Journal of industrial and engineering chemistry*, 12(4):522-530.

Park, Y., Ju, Y., Park, D. & Lee, C.-H. 2016. Adsorption equilibria and kinetics of six pure gases on pelletized zeolite 13X up to 1.0 MPa: CO2, CO, N2, CH4, Ar and H2. *Chemical Engineering Journal*, 292:348-365.

Qiu, H., Lv, L., Pan, B.-c., Zhang, Q.-j., Zhang, W.-m. & Zhang, Q.-x. 2009. Critical review in adsorption kinetic models. *Journal of Zhejiang University-Science A*, 10(5):716-724.

Raganati, F., Alfe, M., Gargiulo, V., Chirone, R. & Ammendola, P. 2019. Kinetic study and breakthrough analysis of the hybrid physical/chemical CO2 adsorption/desorption behavior of a magnetite-based sorbent. *Chemical Engineering Journal*, 372:526-535.

Rashidi, N.A., Yusup, S. & Borhan, A. 2014. Development of novel low-cost activated carbon for carbon dioxide capture. *International Journal of Chemical Engineering and Applications*, 5(2):90-95.

Rashidi, N.A., Yusup, S. & Borhan, A. 2016. Isotherm and thermodynamic analysis of carbon dioxide on activated carbon. *Procedia Engineering*, 148:630-637.

Ruthven, D.M. 1984. Principles of adsorption and adsorption processes. Hoboken, New Jersey, United States: John Wiley & Sons.

Ruthven, D.M. 2006. Fundamentals of adsorption equilibrium and kinetics in microporous solids. Adsorption and Diffusion. New York City, New York, United States: Springer. p. 1-43).

Samokhvalov, A. 2015. Adsorption on mesoporous metal–organic frameworks in solution: aromatic and heterocyclic compounds. *Chemistry–A European Journal*, 21(47):16726-16742.

Sayari, A. 1996. Periodic mesoporous materials: synthesis, characterization and potential applications. *Studies in Surface Science Catalysis*, 102:1-46.

Serna-Guerrero, R. & Sayari, A. 2010. Modeling adsorption of CO2 on amine-functionalized mesoporous silica. 2: Kinetics and breakthrough curves. *Chemical Engineering Journal*, 161(1-2):182-190.

BIBLIOGRAPHY

Shafeeyan, M.S., Daud, W.M.A.W., Shamiri, A. & Aghamohammadi, N. 2015. Modeling of carbon dioxide adsorption onto ammonia-modified activated carbon: kinetic analysis and breakthrough behavior. *Energy Fuels*, 29(10):6565-6577.

Silva, S.M., Sampaio, K.A., Ceriani, R., Verhé, R., Stevens, C., De Greyt, W. & Meirelles, A.J. 2013. Adsorption of carotenes and phosphorus from palm oil onto acid activated bleaching earth: Equilibrium, kinetics and thermodynamics. *Journal of Food Engineering*, 118(4):341-349.

Sing, K.S. 1985. Reporting physisorption data for gas/solid systems with special reference to the determination of surface area and porosity (Recommendations 1984). *Pure and applied chemistry*, 57(4):603-619.

Singh, J., Bhunia, H. & Basu, S. 2019. Adsorption of CO2 on KOH activated carbon adsorbents: Effect of different mass ratios. *Journal of Environmental Management*, 250:109457.

Singh, V.K. & Kumar, E.A. 2016. Comparative Studies on CO2 Adsorption Kinetics by Solid Adsorbents. *Energy Procedia*, 90:316-325.

Singh, V.K. & Kumar, E.A. 2017. Measurement of CO2 adsorption kinetics on activated carbons suitable for gas storage systems. *Greenhouse Gases: Science and Technology*, 7(1):182-201.

Sips, R. 1948. On the structure of a catalyst surface. *The Journal of Chemical Physics*, 16(5):490-495.

Song, G., Zhu, X., Chen, R., Liao, Q., Ding, Y.-D. & Chen, L. 2016. An investigation of CO2 adsorption kinetics on porous magnesium oxide. *Chemical Engineering Journal*, 283:175-183.

Styring, P. 2015. Novel Sorbent Materials for Carbon Capture. Novel Materials for Carbon Dioxide Mitigation Technology. Elsevier. p. 207-229).

Subramoney, J., Van Wyk, J., Dithupe, M., Molapo, A., Mahlangu, N. & Morumudi, R. 2009. Digest of South African Energy Statistics 2009: Pretoria: Department of Energy Republic of South Africa.

Tekalgne, M.A., Do, H., Hasani, A., Van Le, Q., Jang, H., Ahn, S. & Kim, S. 2020. Two-dimensional materials and metal-organic frameworks for the CO2 reduction reaction. *Materials Today Advances*, 5:100038.

Temkin, M. 1940. Kinetics of ammonia synthesis on promoted iron catalysts. *Acta physiochim. URSS*, 12:327-356.

Thomas, J. & Damberger, H.H. 1976. Internal surface area, moisture content, and porosity of Illinois coals: Variations with coal rank. *Circular no. 493*.

Thommes, M. 2010. Physical adsorption characterization of nanoporous materials. *Chemie Ingenieur Technik*, 82(7):1059-1073.

BIBLIOGRAPHY

Toth, J. 1971. A multicomponent isotherm for liquid adsorption. *Acta Chim. Acad. Sci. Hung*, 69:311-322.

Tsai, W.-T., Chang, C.-Y., Ho, C.-Y. & Chen, L.-Y. 2000. Adsorption properties and breakthrough model of 1, 1-dichloro-1-fluoroethane on granular activated carbon and activated carbon fiber. *Separation Science and Technology*, 35(10):1635-1650.

Ullah, R., Saad, M.A.H.S., Aparicio, S. & Atilhan, M. 2018. Adsorption equilibrium studies of CO2, CH4 and N2 on various modified zeolites at high pressures up to 200 bars. *Microporous Mesoporous Materials*, 262:49-58.

US-Embassy. 2017. South Africa - Electrical Power Systems. https ://www.export.gov/article?id=South-Africa-electrical-power Date of access: 5 July 2018.

Valenzuela, D. & Myers, A. 1984. Gas adsorption equilibria. *Separation and Purification Methods*, 13(2):153-183.

Veawab, A., Aroonwilas, A. & Tontiwachwuthikul, P. 2002. CO 2 absorption performance of aqueous alkanolamines in packed columns. *Fuel Chemistry Division Preprints*, 47(1):49-50.

Viljoen, J., Stapelberg, F. & Cloete, M. 2010. Technical report on the geological storage of carbon dioxide in South Africa. *Pretoria: Council for Geoscience*:236.

Wang, J. & Guo, X. 2020. Adsorption kinetic models: physical meanings, applications, and solving methods. *Journal of Hazardous Materials*, 390:122156.

Weber Jr, W.J. & Morris, J.C. 1963. Kinetics of adsorption on carbon from solution. *Journal of the Sanitary Engineering Division*, 89(2):31-59.

Yahia, M.B., Torkia, Y.B., Knani, S., Hachicha, M., Khalfaoui, M. & Lamine, A.B. 2013. Models for type VI adsorption isotherms from a statistical mechanical formulation. *Adsorption Science Technology*, 31(4):341-357.

Yang, P. 2003. The chemistry of nanostructured materials. Vol. 1. Ichibanchō, Chiyoda City, Singapore: World Scientific.

Yates, J.G. & Lettieri, P. 2016. Fluidized-bed reactors: processes and operating conditions. New York City, New York, United States: Springer.

Zanco, S.E., Mazzotti, M., Gazzani, M., Romano, M.C. & Martínez, I. 2018. Modeling of circulating fluidized beds systems for post‐combustion CO2 capture via temperature swing adsorption. *AIChE Journal*, 64(5):1744-1759.

Zhang, W., Sun, C., Snape, C.E., Irons, R., Stebbing, S., Alderson, T., Fitzgerald, D. & Liu, H. 2017. Process simulations of post-combustion CO2 capture for coal and natural gas-fired power plants using a polyethyleneimine/silica adsorbent. *International Journal of Greenhouse Gas Control*, 58:276-289.

BIBLIOGRAPHY

Zhou, X., Yi, H., Tang, X., Deng, H. & Liu, H. 2012. Thermodynamics for the adsorption of SO_2, NO and CO_2 from flue gas on activated carbon fiber. *Chemical Engineering Journal*, 200:399-404.

Appendix A

(EXPERIMENTAL DATA PROCESSING)

$\mathbf{A}$ppendix A

(EXPERIMENTAL DATA PROCESSING)

A-1.   BREAKTHROUGH CO_2 CONCENTRATION   DATA PROCESSING

The experimental breakthrough CO_2 concentration curve obtained from the adsorption rate FBR for CQ650 is shown in Figure A- 1.
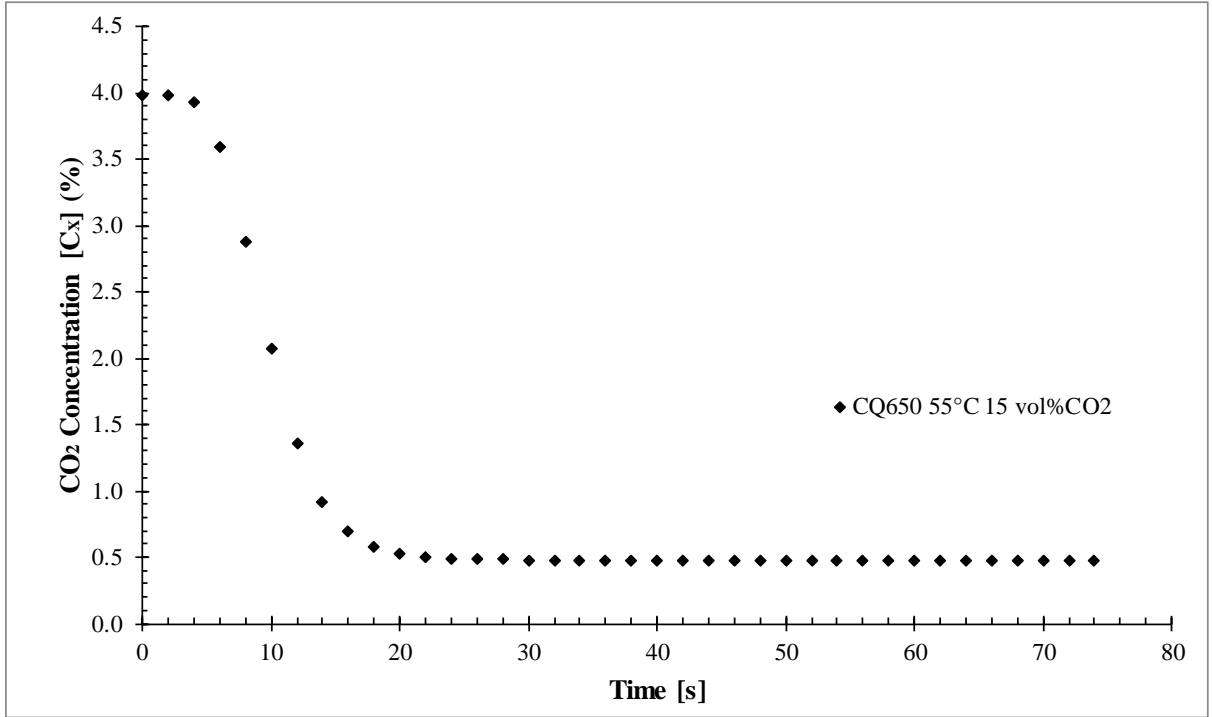
Figure A- 1: Experimental CO_2 concentration data (C_X) curve obtained from the adsorption rate FBR for CQ650 at 55 °C and 15 vol% CO_2.

To obtain the actual CO_2 concentration before the second dilution step, and incorporating the calibration data obtained for this individual experiment, Equation A-1 is applied to the data.

$$C_A = C_{C_{MIN}} + \left(C_{C_{MAX}} - C_{C_{MIN}}\right)\left[\frac{C_X - C_{Z_{MIN}}}{C_{Z_{MAX}} - C_{Z_{MIN}}}\right]\left(\frac{C_Y}{C_D}\right) \qquad \text{(A-1)}$$

$C_{C_{MIN}}$ and $C_{C_{MAX}}$ represents the calibration gas minimum and maximum which is 0% and 2.85%, respectively. C_X is the concentration measured with the CO_2 analyser. $C_{Z_{MIN}}$ and $C_{Z_{MAX}}$ represent the minimum and maximum concentrations read on the CO_2 analyser at 0 vol% CO_2 and 2.85 vol% CO_2, respectively. C_Y is the experimental concentration, which in this case is 15 vol%. C_D is the true steady state concentration of the gas mixture when the gas mixture is directly sent through the bypass line to the CO_2 analyser. C_D is calculated with Equation A-2

$$C_D = C_{C_{MIN}} + \left(C_{C_{MAX}} - C_{C_{MIN}}\right)\left[\frac{C_R - C_{Z_{MIN}}}{C_{Z_{MAX}} - C_{Z_{MIN}}}\right] \tag{A-2}$$

where C_R represents the CO_2 concentration measured with the CO_2 analyser when the gas mixture is directly sent through the bypass line to the CO_2 analyser. When Equation A-1 and Equation A-2 are applied to the data, Figure A- 2 is obtained.
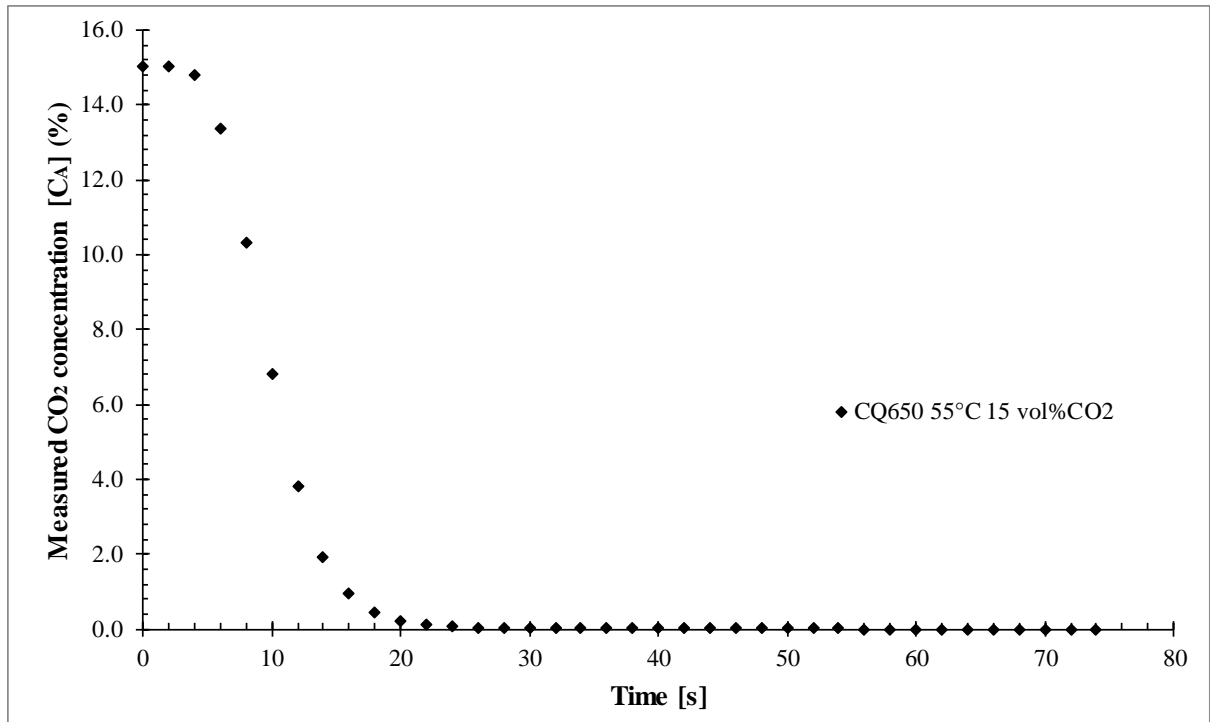
Figure A- 2: Experimental breakthrough CO_2 concentration (C_A) curve obtained from the adsorption rate FBR for CQ650 at 55 °C and 15 vol% CO_2.

Equation A-3 is applied to the experimental CO_2 concentration data represented in Figure A-2.

$$C_A^* = (C_{A_0} - C_A) \qquad\qquad\qquad \text{(A-3)}$$

where C_{A_0} represents the initial concentration at time $t = 0$ and C_A represents the concentration at time $t = t$ at each time interval. Figure A-3 represents the experimental C_A^* versus time graph. The experimental data is then normalized to obtain Figure A-4.
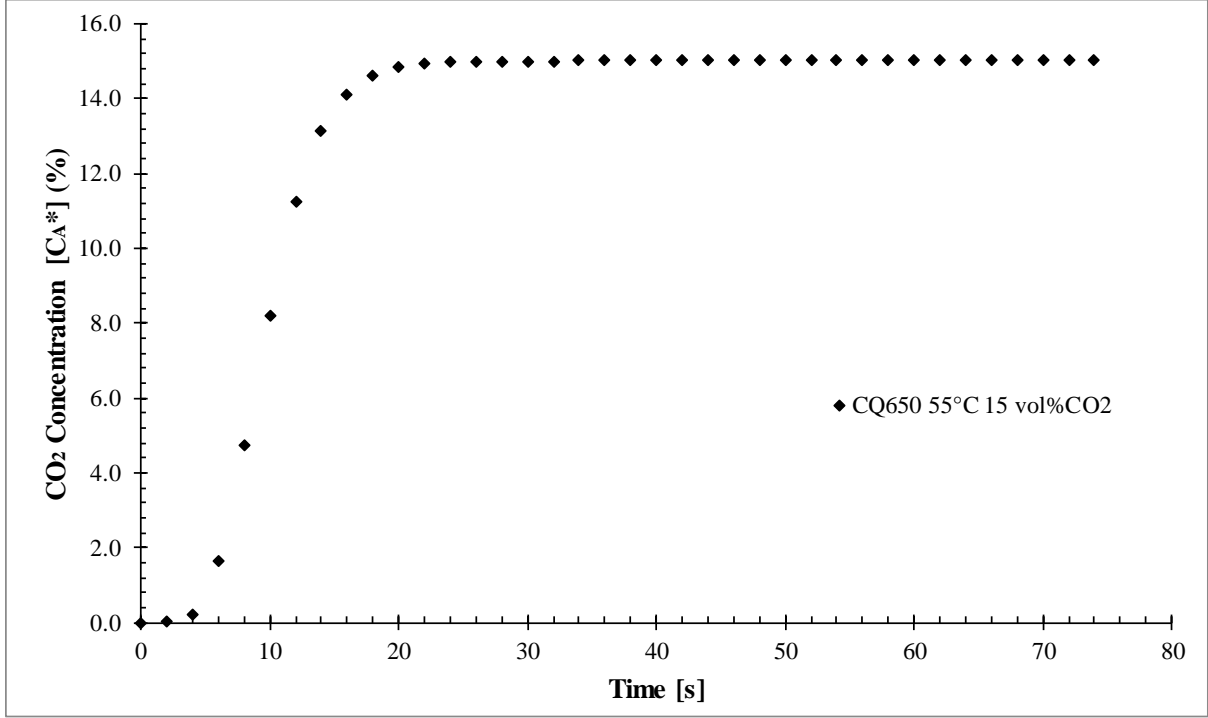
Figure A-3: Experimental breakthrough CO_2 concentration (C_A^*) curve obtained from the adsorption rate FBR for CQ650 at 55 °C and 15 vol% CO_2.

153
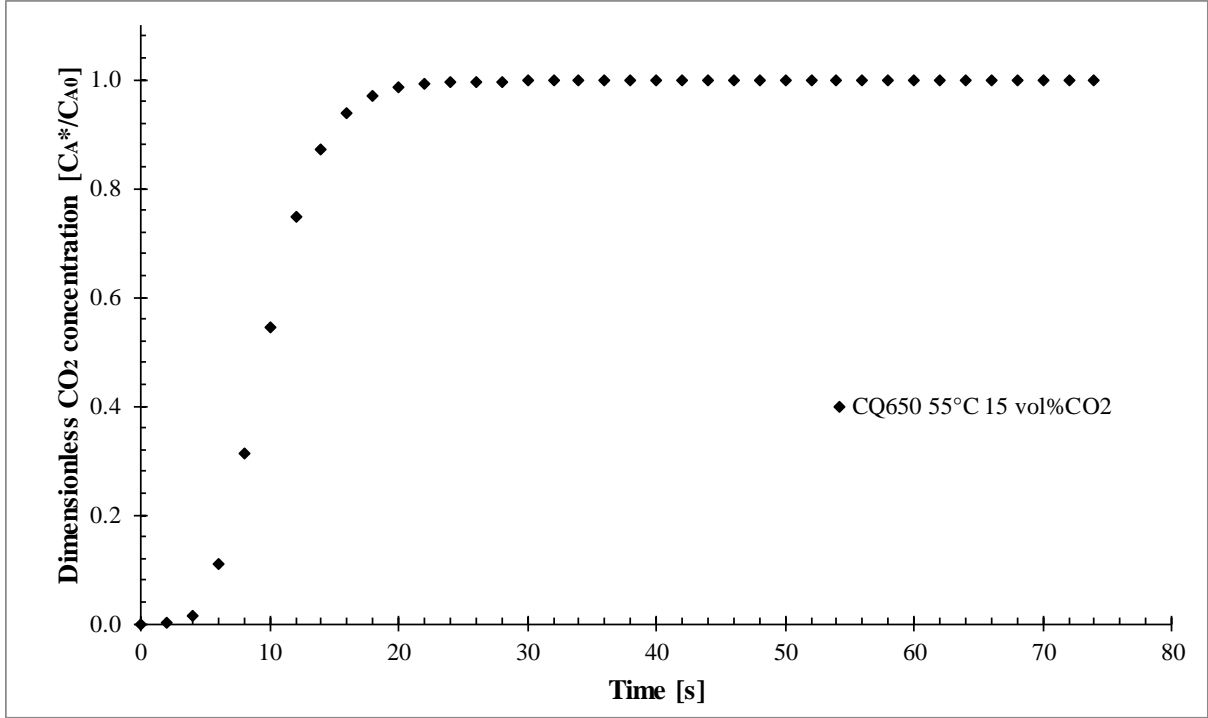
Figure A- 4: Normalized experimental breakthrough CO_2 concentration (C_A^*/C_{A0}) curve obtained from the adsorption rate FBR for CQ650 at 55 °C and 15 vol% CO_2.

The quantity adsorbed is determined from the normalized experimental breakthrough CO_2 concentration (C_A/C_{A0}): Equation A-4 and Equation A-5

$$\frac{q_t}{q_0} = 1 - \frac{1}{t_f} \int_0^{t_f} \frac{C_A^*}{C_{A_0}} dt \tag{A-4}$$

$$q_0 = \frac{C_i P Q_0 t_f}{R T M_w} \times 1000 \tag{A-5}$$

where q_t and q_0 presents the adsorption capacity at a time instance and the equilibrium capacity measured in mmol/g, t_f is the time measured in seconds, C_i is the inlet concentration (5, 15 and 25 vol%), P is the operating pressure in bar, Q_0 is the flow rate in L/s, R is the gas constant in L.bar/mol.K, T is the operating temperature and M_w is the sorbent mass loaded in the FBR (Lee *et al.*, 2014). Substituting C_A^*, defined in Equation A-3, into Equation A-4, yields Equation A-6.

$$\frac{q_t}{q_0} = 1 - \frac{1}{t_f} \int_0^{t_f} \frac{C_{A_0} - C_A}{C_{A_0}} dt \qquad \text{(A-6)}$$

Simplifying Equation A-7 yields Equation A-12.

$$\frac{q_t}{q_0} = 1 - \frac{1}{t_f} \int_0^{t_f} \frac{C_{A_0} - C_A}{C_{A_0}} dt \qquad \text{(A-7)}$$

$$\frac{q_t}{q_0} = 1 - \frac{1}{t_f} \left[\int_0^{t_f} \frac{C_{A_0}}{C_{A_0}} dt - \int_0^{t_f} \frac{C_A}{C_{A_0}} dt \right] \qquad \text{(A-8)}$$

$$\frac{q_t}{q_0} = 1 - \frac{1}{t_f} \left[\int_0^{t_f} 1 \, dt - \int_0^{t_f} \frac{C_A}{C_{A_0}} dt \right] \qquad \text{(A-9)}$$

$$\frac{q_t}{q_0} = 1 - \frac{1}{t_f} \left[t_f - \int_0^{t_f} \frac{C_A}{C_{A_0}} dt \right] \qquad \text{(A-10)}$$

$$\frac{q_t}{q_0} = 1 - 1 + \frac{1}{t_f} \int_0^{t_f} \frac{C_A}{C_{A_0}} dt \qquad \text{(A-11)}$$

$$\frac{q_t}{q_0} = \frac{1}{t_f} \int_0^{t_f} \frac{C_A}{C_{A_0}} dt \qquad \text{(A-12)}$$

The integration of the (C_A/C_{A0}) curve was determined with the trapezoidal rule for integration, given in Equation A-13. The result was verified with the integration function of ORIGIN 2019b.

$$\int_a^b f(x)dx = \int_{x_0}^{x_0 + nh} y \, dx$$

$$\text{(A-13)}$$

$$\int_a^b f(x)dx = \frac{h}{2}[(y_0 + y_n) + 2(y_1 + y_2 + \cdots + y_{n-1})]$$

Applying Equation A-12, Equation A-5 and Equation A-13 to the dimensionless CO_2 experimental data C_A/C_{A0} presented in Figure A- 4 yields Figure A- 5. Normalizing the CO_2 adsorption quantity presented in Figure A- 5 (q_t/q_e) yields Figure A- 6, representing the data to be modelled by each adsorption rate model, discussed in Section 3.4.4.
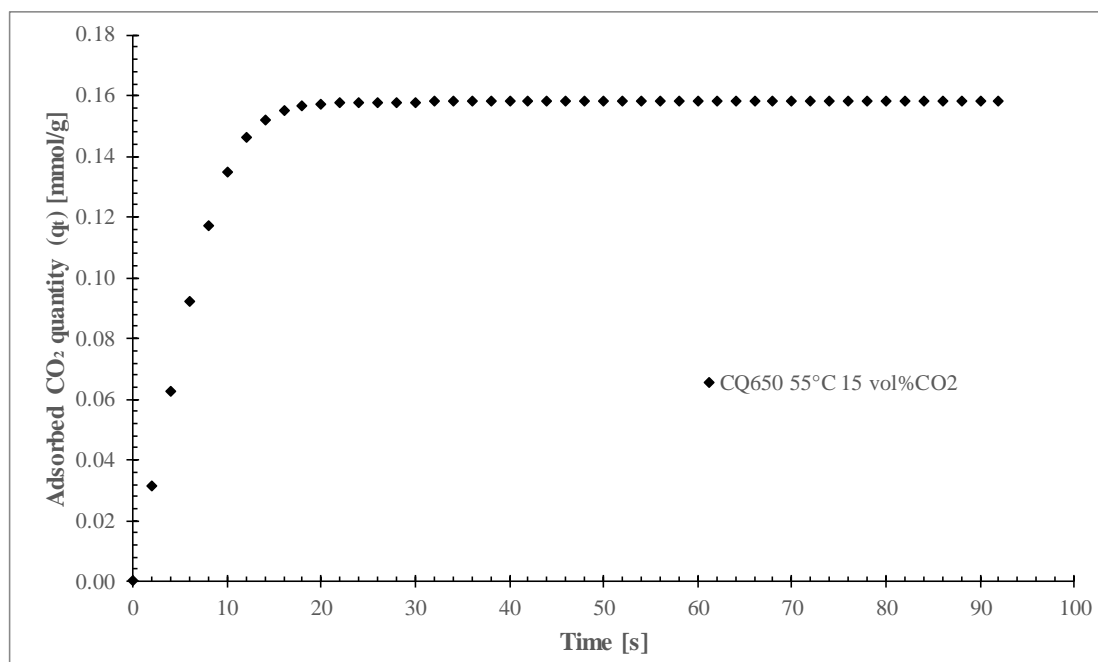
Figure A- 5: Adsorbed CO_2 quantity (mmol/g) for CQ650 at 55 °C and 15 vol% CO_2.
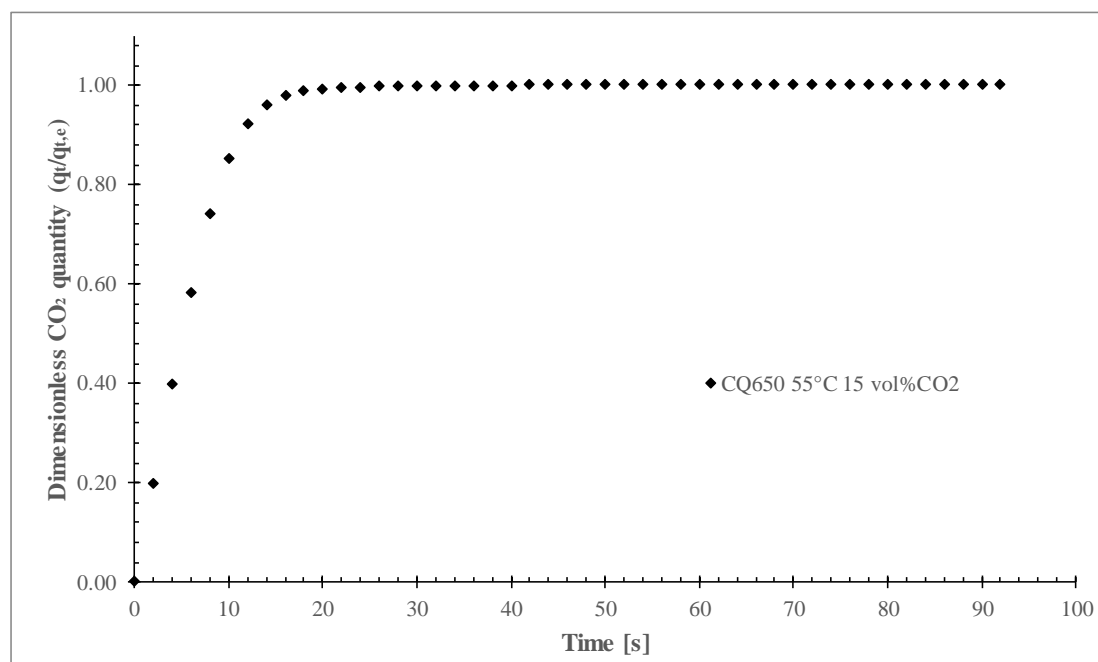
Figure A- 6: Normalized adsorbed CO_2 quantity ($q_t/q_{t,e}$) curve for CQ650 at 55 °C and 15 vol% CO_2.

APPENDIX A

A-2. POROSITY CALCULATION

The porosity is calculated with the Horvath–Kawazoe cumulative pore volume, plotted against the pore width obtained from the Micromeritics ASAP 2020 measured with CO_2 adsorption at 0 °C. The area under the curve was determined with ORIGIN 2019; see Figure A- 7.
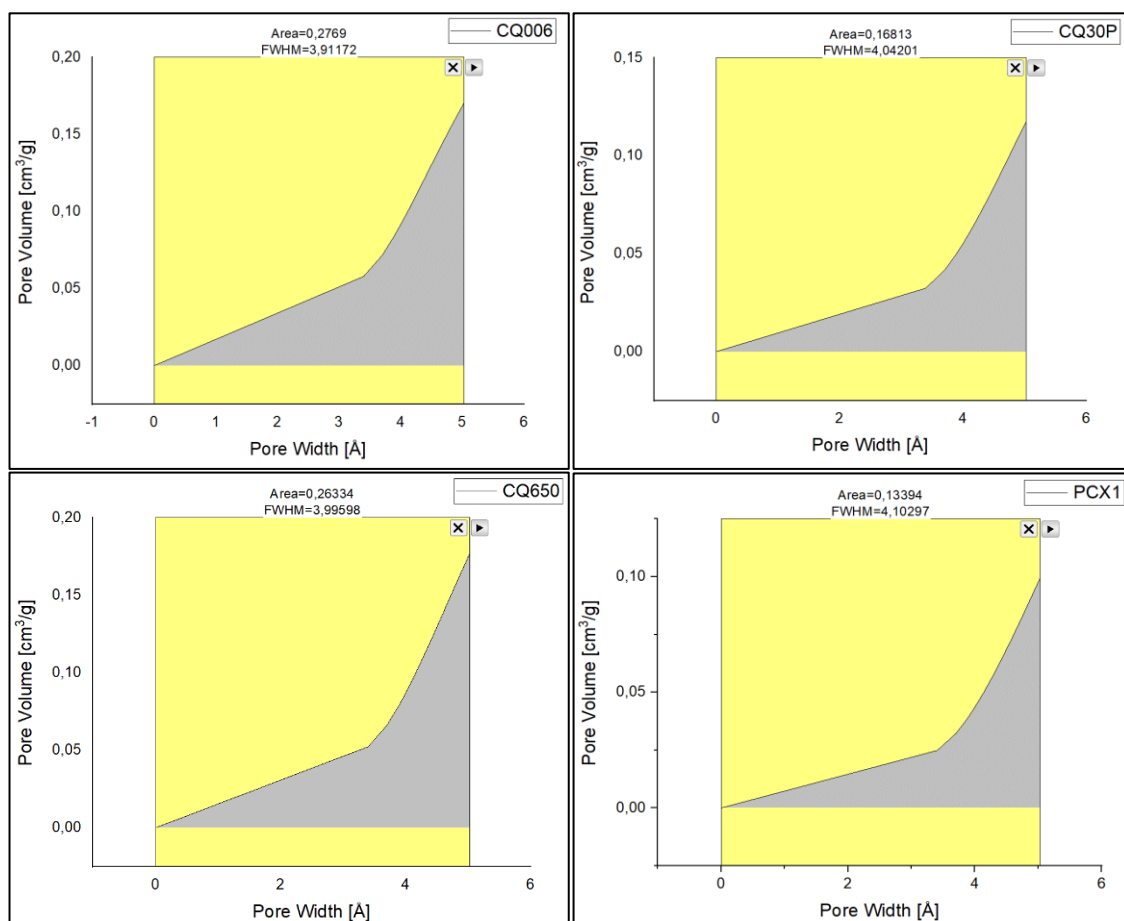
Figure A- 7: Area determination from the cumulative pore volume plotted against pore width curve.

Appendix B

(SUPPLEMENTARY ADSORPTION ISOTHERM DATA)

$\mathbf{A}$ppendix $\mathbf{B}$

(SUPPLEMENTARY ADSORPTION ISOTHERM DATA)

B-1.   ADSORPTION ISOTHERM MODEL PARAMETERS

The adsorption isotherm model parameters of Langmuir, BET, D-R, D-A, Temkin, Toth, Freundlich and SIPS for CQ006, CQ30P, CQ650 and PCX1 at 0, 10, 20, 30, 40 and 55 °C are given in Table B- 1 to Table B- 4.

Table B- 1: Experimental CO_2 adsorption isotherm data of CQ006 at 0, 10, 20, 30, 40 and 55 °C modelled with Langmuir, BET, D-A, D-R, Toth, Freundlich, Temkin and SIPS adsorption isotherm model (AIM) parameters.

AIM	Parameter	0 °C	10 °C	20 °C	30 °C	40 °C	55 °C
Langmuir	q_L, *mmol/g*	5.340	5.313	4.121	3.720	2.804	2.311
	K_L, *1/kPa*	0.02218	0.01602	0.01714	0.01437	0.00790	0.00669
	ARE%	10.68	6.97	7.05	4.64	1.27	0.71
	QOF%	77.87	78.96	81.76	85.29	96.12	97.09
BET	P_o, *kPa*	3485	4501	5727	7211	8967	12131
	C	83.90	77.79	103.6	109.6	74.4	84.4
	q_{BET}, *mmol/g*	5.019	5.010	3.945	3.563	2.682	2.229
	ARE%	10.28	6.700	6.863	4.539	1.241	0.689
	QOF%	78.32	79.40	82.04	85.59	96.19	97.14
D-R	P_o, *kPa*	3485	4501	5727	7211	8967	12131
	q_{DR}, *mmol/g*	7.598	7.148	6.553	6.240	4.728	4.207
	D_{DR}	0.2387	0.2363	0.2373	0.2391	0.2576	0.2565
	ARE%	5.337	5.112	3.550	2.297	0.698	0.405
	QOF%	86.27	87.63	89.16	91.50	97.42	98.02
D-A	P_o, *kPa*	3485	4501	5727	7211	8967	12131
	q_{DA}, *mmol/g*	12.91	12.85	12.29	12.53	7.34	6.22
	D_{DA}	0.3282	0.3239	0.3383	0.3493	0.3192	0.3073
	n_{DA}	1.385	1.473	1.381	1.374	1.594	1.660
	ARE%	0.3501	0.09379	0.3187	0.2107	0.1274	0.1098
	QOF%	98.97	96.45	98.62	99.08	99.55	99.59
Toth	K_{TOTH}, *1/kPa*	0.01397	0.00458	0.00530	0.002838	0.000617	0.001584
	t_T	0.1727	0.1940	0.1750	0.1825	0.2243	0.3749
	q_T, *mmol/g*	176.1	176.0	190.8	191.6	136.0	17.3
	ARE%	0.5217	0.5554	0.4009	0.2457	0.3534	0.1554
	QOF%	98.47	96.01	98.33	98.87	99.03	99.57
Freundlich	k_F, *mmol/g.kPa$^{(1/n)}$*	0.3162	0.2188	0.1858	0.1373	0.0532	0.0344
	n_F	1.856	1.695	1.736	1.656	1.462	1.398
	ARE%	3.711	0.000	2.113	1.496	0.980	0.810
	QOF%	91.34	80.08	94.68	95.47	96.87	96.73
Temkin	K_{TEM}, *1/kPa*	1.470	4.810	0.832	0.588	0.212	0.174
	B	0.6241	0.3866	0.5072	0.4679	0.3739	0.3010
	ARE%	39.48	54.85	27.08	19.12	9.53	6.81
	QOF%	17.08	-1828	36.26	41.87	71.36	75.20
SIPS	K_{SIPS}, *1/kPa*	0.002000	0.001929	0.001327	0.001663	0.002315	0.002732
	m_{SIPS}	1.568	1.447	1.519	1.433	1.228	1.161
	q_{SIPS}, *mmol/g*	14.2084	13.5879	12.5614	9.9196	5.3177	3.7592
	ARE%	0.0482	0.2611	0.0082	-0.0427	0.0189	0.0030
	QOF%	99.42	95.49	99.68	99.53	99.69	99.76

Table B- 2: Experimental CO_2 adsorption isotherm data of CQ30P at 0, 10, 20 and 30 °C modelled with Langmuir, BET, D-A, D-R, Toth, Freundlich, Temkin and SIPS adsorption isotherm model (AIM) parameters.

AIM	Parameter	0 °C	10 °C	20 °C	30 °C
Langmuir	q_L, *mmol/g*	4.389	3.754	3.078	2.713
	K_L, *1/kPa*	0.01288	0.01114	0.01147	0.01036
	ARE%	4.21	3.09	2.31	1.36
	QOF%	93.34	93.82	94.68	95.51
BET	P_o, *kPa*	3485	4501	5727	7211
	C	49.73	54.47	69.90	78.50
	q_{BET}, *mmol/g*	4.033	3.497	2.916	2.596
	ARE%	3.98	2.95	2.24	1.33
	QOF%	93.56	94.00	94.80	95.59
D-R	P_o, *kPa*	3485	4501	5727	7211
	q_{DR}, *mmol/g*	5.859	5.329	4.771	4.543
	D_{DR}	0.2617	0.2614	0.2546	0.2544
	ARE%	2.503	1.884	1.221	0.717
	QOF%	95.13	95.45	96.66	97.20
D-A	P_o, *kPa*	3485	4501	5727	7211
	q_{DA}, *mmol/g*	10.34	10.01	7.93	7.42
	D_{DA}	0.3659	0.3730	0.3338	0.3256
	n_{DA}	1.359	1.367	1.484	1.541
	ARE%	0.1613	0.1629	0.1260	0.0498
	QOF%	99.51	99.53	99.65	99.84
Toth	K_{TOTH}, *1/kPa*	0.00336	0.00182	0.00153	0.00087
	t_T	0.1833	0.1968	0.1896	0.2030
	q_T, *mmol/g*	192.9	169.5	178.5	168.6
	ARE%	0.1070	0.1039	0.2488	0.2654
	QOF%	99.55	99.56	98.93	98.77
Freundlich	k_F, *mmol/g.kPa$^{(1/n)}$*	0.1700	0.1163	0.0947	0.0677
	n_F	1.717	1.620	1.605	1.514
	ARE%	1.415	0.000	1.071	0.830
	QOF%	96.23	96.51	96.24	96.36
Temkin	K_{TEM}, *1/kPa*	0.515	0.408	0.354	0.299
	B	0.5699	0.4785	0.4167	0.3620
	ARE%	22.66	17.56	13.48	9.26
	QOF%	55.30	57.62	62.99	65.50
SIPS	K_{SIPS}, *1/kPa*	0.001550	0.001345	0.001422	0.001907
	m_{SIPS}	1.455	1.405	1.394	1.306
	q_{SIPS}, *mmol/g*	11.4116	10.2889	8.3916	6.3889
	ARE%	0.0354	0.0425	0.0730	0.0447
	QOF%	98.93	98.93	98.65	98.94

Table B- 3: Experimental CO_2 adsorption isotherm data of CQ650 at 0, 10, 20 and 30 °C modelled with Langmuir, BET, D-A, D-R, Toth, Freundlich, Temkin and SIPS adsorption isotherm model (AIM) parameters.

AIM	Parameter	0 °C	10 °C	20 °C	30 °C
Langmuir	q_L, mmol/g	5.340	5.313	4.121	3.720
	K_L, 1/kPa	0.02218	0.01602	0.01714	0.01437
	ARE%	10.68	6.97	7.05	4.64
	QOF%	77.87	78.96	81.76	85.29
BET	P_o, kPa	3485	4501	5727	7211
	C	83.90	77.79	103.6	109.6
	q_{BET}, mmol/g	5.019	5.010	3.945	3.563
	ARE%	10.28	6.700	6.863	4.539
	QOF%	78.32	79.40	82.04	85.59
D-R	P_o, kPa	3485	4501	5727	7211
	q_{DR}, mmol/g	7.598	7.148	6.553	6.240
	D_{DR}	0.2387	0.2363	0.2373	0.2391
	ARE%	5.337	5.112	3.550	2.297
	QOF%	86.27	87.63	89.16	91.50
D-A	P_o, kPa	3485	4501	5727	7211
	q_{DA}, mmol/g	12.91	12.85	12.29	12.53
	D_{DA}	0.3282	0.3239	0.3383	0.3493
	n_{DA}	1.385	1.473	1.381	1.374
	ARE%	0.3501	0.09379	0.3187	0.2107
	QOF%	98.97	96.45	98.62	99.08
Toth	K_{TOTH}, 1/kPa	0.01397	0.00458	0.00530	0.002838
	t_T	0.1727	0.1940	0.1750	0.1825
	q_T, mmol/g	176.1	176.0	190.8	191.6
	ARE%	0.5217	0.5554	0.4009	0.2457
	QOF%	98.47	96.01	98.33	98.87
Freundlich	k_F, mmol/g.kPa$^{(1/n)}$	0.3162	0.2188	0.1858	0.1373
	n_F	1.856	1.695	1.736	1.656
	ARE%	3.711	0.000	2.113	1.496
	QOF%	91.34	80.08	94.68	95.47
Temkin	K_{TEM}, 1/kPa	1.470	4.810	0.832	0.588
	B	0.6241	0.3866	0.5072	0.4679
	ARE%	39.48	54.85	27.08	19.12
	QOF%	17.08	-1828	36.26	41.87
SIPS	K_{SIPS}, 1/kPa	0.002000	0.001929	0.001327	0.001663
	m_{SIPS}	1.568	1.447	1.519	1.433
	q_{SIPS}, mmol/g	14.2084	13.5879	12.5614	9.9196
	ARE%	0.0482	0.2611	0.0082	-0.0427
	QOF%	99.42	95.49	99.68	99.53

Table B- 4: Experimental CO_2 adsorption isotherm data of PCX1 at 40 and 55 °C modelled with Langmuir, BET, D-A, D-R, Toth, Freundlich, Temkin and SIPS adsorption isotherm model (AIM) parameters.

AIM	Parameter	40 °C	55 °C
Langmuir	q_L, *mmol/g*	2.484	2.224
	K_L, *1/kPa*	0.00707	0.00529
	ARE%	1.08	0.55
	QOF%	96.17	97.31
BET	P_o, *kPa*	8967	12131
	C	66.70	67.13
	q_{BET}, *mmol/g*	2.369	2.131
	ARE%	1.05	0.54
	QOF%	96.23	97.35
D-R	P_o, *kPa*	8967	12131
	q_{DR}, *mmol/g*	4.090	3.829
	D_{DR}	0.2615	0.2642
	ARE%	0.769	0.463
	QOF%	97.07	97.47
D-A	P_o, *kPa*	8967	12131
	q_{DA}, *mmol/g*	7.58	7.02
	D_{DA}	0.3543	0.3492
	n_{DA}	1.485	1.537
	ARE%	0.1090	0.0565
	QOF%	99.80	99.74
Toth	K_{TOTH}, *1/kPa*	0.00048	0.00114
	t_T	0.2352	0.4093
	q_T, *mmol/g*	116.1	15.6
	ARE%	0.1988	0.0555
	QOF%	99.26	99.76
Freundlich	k_F, *mmol/g.kPa$^{(1/n)}$*	0.0404	0.0237
	n_F	1.421	1.323
	ARE%	0.669	0.533
	QOF%	97.27	97.20
Temkin	K_{TEM}, *1/kPa*	0.193	0.153
	B	0.3217	0.2617
	ARE%	7.87	5.93
	QOF%	73.70	73.32
SIPS	K_{SIPS}, *1/kPa*	0.001763	0.001959
	m_{SIPS}	1.231	1.148
	q_{SIPS}, *mmol/g*	5.2448	3.9523
	ARE%	0.0203	0.0080
	QOF%	99.41	99.57

B-2.   EXPERIMENTAL ADSORPTION ISOTHERM REPEATABILITY AND REPRODUCIBILITY STUDY

The CO_2 adsorption isotherm experimental error analysis was performed on the CQ650 adsorbent sample at 10 °C with a 95% confidence interval. The experimental adsorption isotherm error analysis is visually displayed in Figure B- 1 with the tabulated data given in Table B- 5. A total experimental error of 1.75% was determined for the experimental CO_2 adsorption isotherm data done on the CQ650 sample at 10 °C.
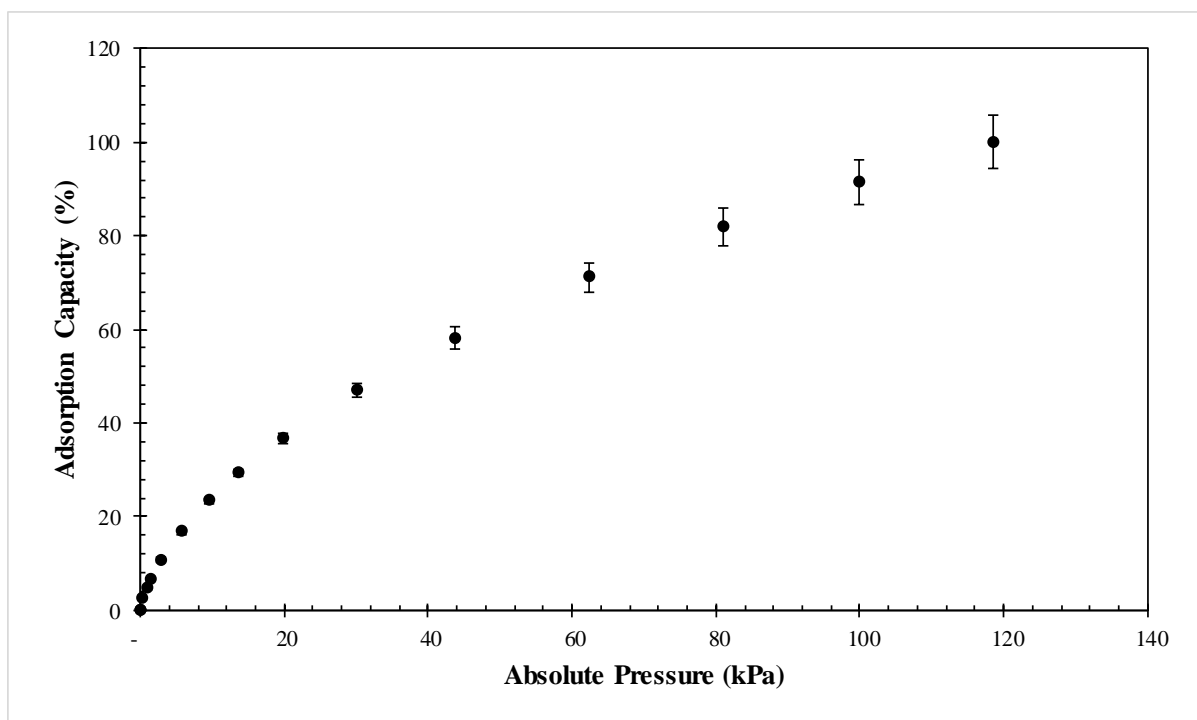

Figure B- 1: Experimental adsorption isotherm error analysis on CQ650 at 10 °C.

Table B- 5: Statistical experimental error analysis on the experimental CQ650 CO_2 adsorption isotherm at 10 °C.

P, *kPa*	Run 1, *cm³/g*	Run 2, *cm³/g*	Run 3, *cm³/g*	Avg ads capacity, *cm³/g*	Std dev	Avg dev	Conf int.	% Expt error	Expt error, *cm³/g*	Final adsorption capacity, *cm³/g*		
0	0	0	0	0	0	0	2.78	0	0	**0**	±	**0**
0.00793	0.097	0.079	0.109	0.0951	0.0126	0.0110	2.78	36.8	0.0350	**0.0951**	±	**0.0350**
0.343	1.85	1.75	1.99	1.86	0.101	0.087	2.78	15.1	0.282	**1.86**	±	**0.282**
0.845	3.54	3.44	3.77	3.58	0.140	0.126	2.78	10.9	0.389	**3.58**	±	**0.389**
1.38	4.99	4.91	5.28	5.06	0.159	0.147	2.78	8.75	0.442	**5.06**	±	**0.442**
2.88	8.27	8.27	8.65	8.40	0.178	0.168	2.78	5.90	0.495	**8.40**	±	**0.495**
5.67	12.9	13.1	13.4	13.1	0.184	0.159	2.78	3.88	0.510	**13.1**	±	**0.510**
9.48	17.9	18.3	18.4	18.2	0.204	0.191	2.78	3.10	0.565	**18.2**	±	**0.565**
13.6	22.5	23.1	22.9	22.9	0.257	0.231	2.78	3.12	0.714	**22.9**	±	**0.714**
19.9	28.3	29.2	28.7	28.7	0.369	0.323	2.78	3.57	1.03	**28.7**	±	**1.03**
30.1	36.3	37.6	36.4	36.8	0.575	0.539	2.78	4.34	1.60	**36.8**	±	**1.60**
43.6	45.0	46.7	44.8	45.5	0.838	0.788	2.78	5.12	2.33	**45.5**	±	**2.33**
62.5	55.0	57.2	54.5	55.6	1.18	1.09	2.78	5.89	3.27	**55.6**	±	**3.27**
81.0	63.5	66.0	62.5	64.0	1.48	1.34	2.78	6.43	4.12	**64.0**	±	**4.12**
99.8	71.0	73.8	69.6	71.5	1.77	1.57	2.78	6.86	4.90	**71.5**	±	**4.90**
118.5	77.8	80.9	75.9	78.2	2.03	1.78	2.78	7.20	5.63	**78.2**	±	**5.63**
									1.75			

Appendix C

(ADSORPTION KINETIC RATE MODEL PARAMETERS)

Appendix C

(ADSORPTION KINETIC RATE MODEL PARAMETERS)

C-1.   COMPARATIVE ANALYSIS BETWEEN THE ADSORBENTS, TEMPERATURES AND INLET CO_2 CONCENTRATIONS

This section provides supplementary graphs on the effect of temperature on the adsorption rate of the CQ006, CQ30P and PCX1 adsorbents in Figure C- 1 to Figure C- 3. The adsorbents are then compared with each other at fixed temperatures and inlet CO_2 concentrations and results shown in Figure C- 4 and Figure C- 5.
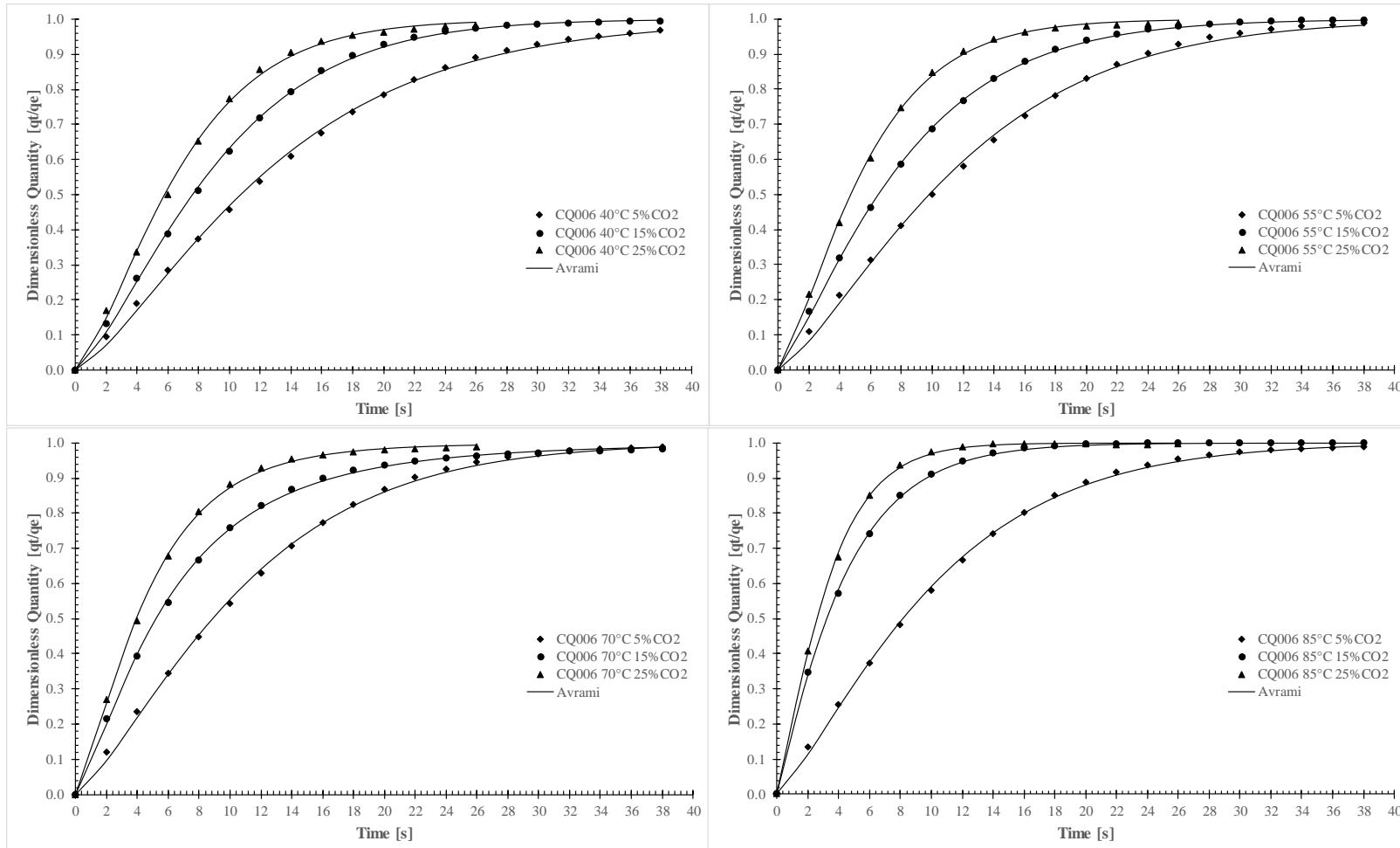
Figure C- 1: Experimental adsorption rate data at 40, 55, 70 and 85 °C for CQ006 at different inlet CO_2 concentration of 5, 15 and 25 vol%, modelled with the Avrami adsorption rate model.
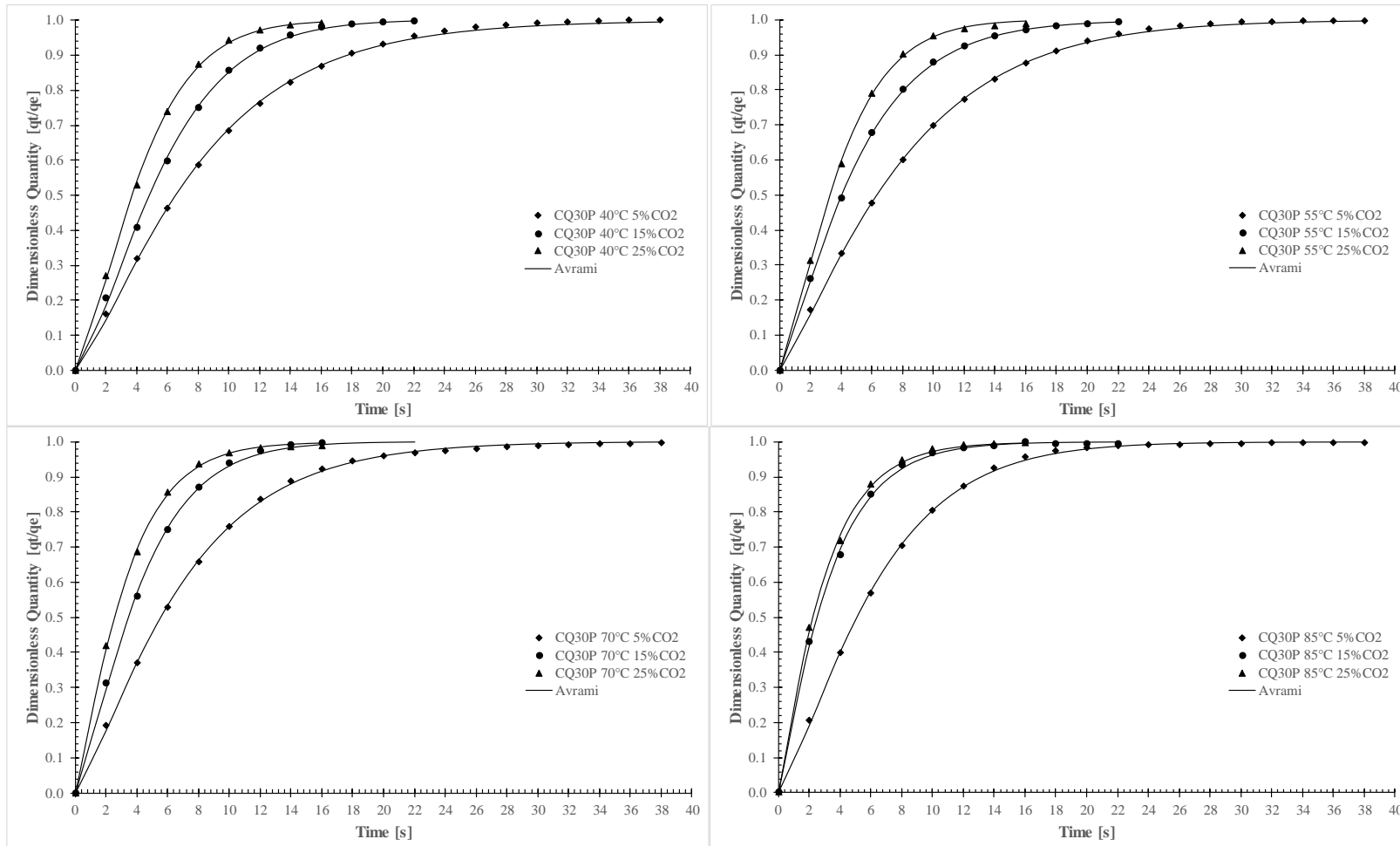
Figure C- 2: Experimental adsorption rate data at 40, 55, 70 and 85 °C for CQ30P at different inlet CO_2 concentration of 5, 15 and 25 vol%, modelled with the Avrami adsorption rate model.
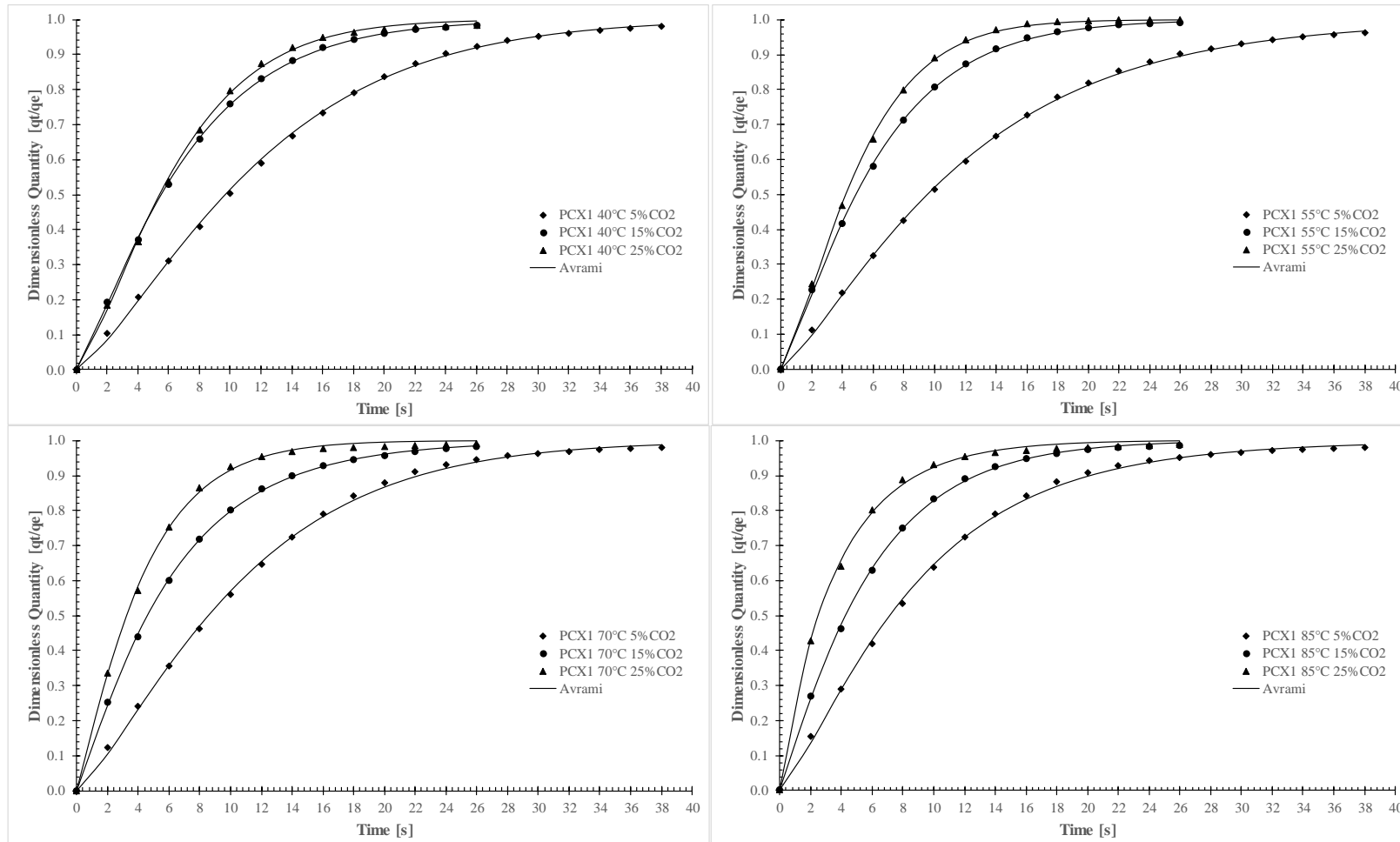
Figure C- 3: Experimental adsorption rate data at 40, 55, 70 and 85 °C for PCX1 at different inlet CO_2 concentration of 5, 15 and 25 vol%, modelled with the Avrami adsorption rate model.
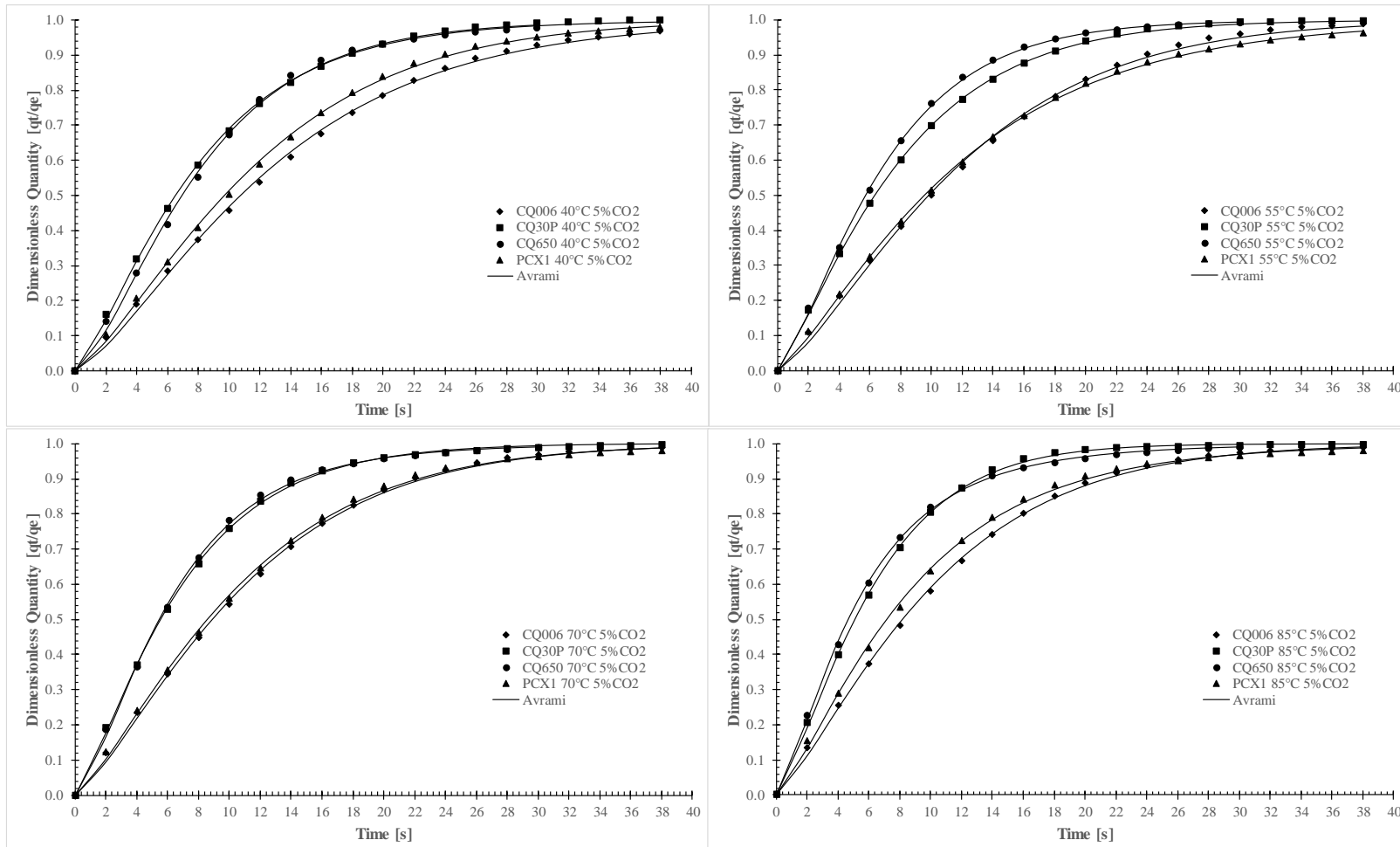
Figure C- 4: Comparing the experimental adsorption rate data of CQ006, CQ30P, CQ650 and PCX1 at 40, 55, 70 and 85 °C for at a fixed inlet CO_2 concentration of 5 vol%, modelled with the Avrami adsorption rate model.
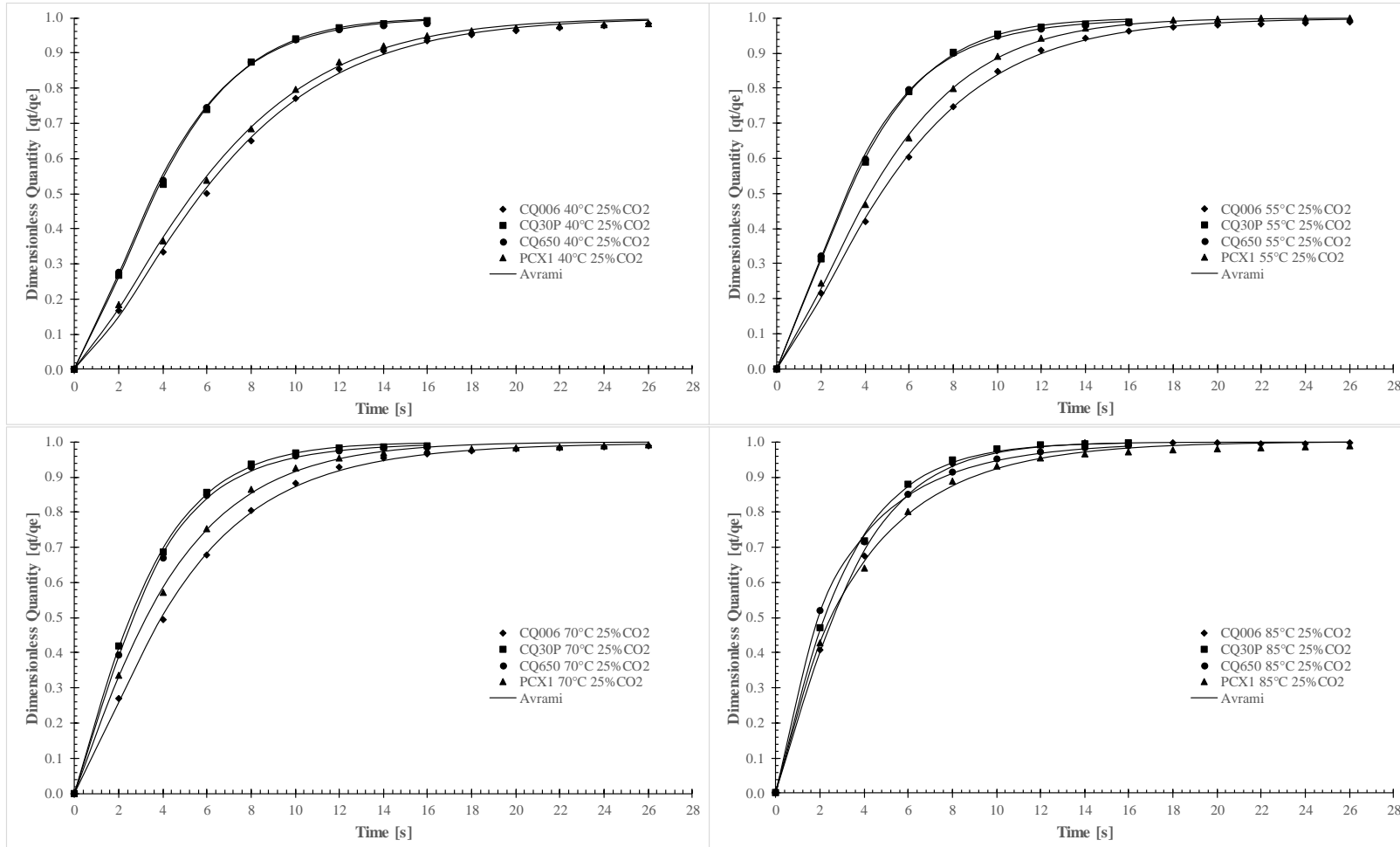
Figure C- 5: Comparing the experimental adsorption rate data of CQ006, CQ30P, CQ650 and PCX1 at 40, 55, 70 and 85 °C for at a fixed inlet CO_2 concentration of 25 vol%, modelled with the Avrami adsorption rate model.

C-2.   ADSORPTION RATE MODEL PARAMETERS

The adsorption rate model parameters of pseudo first order (P1O), pseudo second order (P2O), Elovich, Avrami and the fractional order (FOM) adsorption rate model for CQ006, CQ30P, CQ650 and PCX1 at 40, 55, 70 and 85 °C are tabulated in Table C- 1 to Table C- 4.

Table C- 1: Pseudo first order (P1O), pseudo second order (P2O), Elovich, Avrami and fractional order adsorption rate model parameters when fitted to the experimental adsorption rate data of CQ006 at 40, 55, 70 and 85 °C and an inlet CO_2 concentration of 5, 15 and 25 vol%.

Sample	Parameter	5 vol% CO_2				15 vol% CO_2				25 vol% CO_2			
		40 °C	55 °C	70 °C	85 °C	40 °C	55 °C	70 °C	85 °C	40 °C	55 °C	70 °C	85 °C
P1O	k_1, $1/s$	0.073	0.081	0.089	0.095	0.105	0.119	0.136	0.226	0.138	0.166	0.191	0.296
	ARE%	2.12	2.188	1.780	1.480	1.70	1.11	0.694	0.291	1.205	0.857	0.568	0.439
	QOF%	95.5	95.6	96.4	97.0	96.4	97.9	99.0	99.6	97.4	98.3	99.0	99.4
P2O	k_2, $mmol/g.s$	0.168	0.192	0.231	0.229	0.255	0.293	0.335	0.605	0.340	0.419	0.490	0.815
	ARE%	9.01	8.88	9.03	7.82	7.80	6.88	5.30	4.26	6.53	5.61	4.79	3.55
Elovich	α	0.185	0.24	0.31	0.38	0.49	0.76	1.35	23.7	1.2	2.9	6.7	108
	β	3.79	4.09	4.39	4.63	4.91	5.43	6.16	9.32	5.98	6.99	7.9	11.0
	ARE%	6.77	7.22	7.13	6.97	7.46	6.92	5.77	5.35	7.11	6.47	5.79	5.04
Avrami	k_A, $1/s$	0.070	0.077	0.085	0.091	0.100	0.114	0.134	0.221	0.131	0.159	0.185	0.284
	b	1.28	1.31	1.29	1.25	1.34	1.22	1.05	1.09	1.35	1.29	1.18	1.19
	ARE%	0.317	0.427	0.317	0.279	0.244	0.131	0.655	0.097	0.353	0.306	0.319	0.166
	QOF%	98.7	98.8	99.1	99.3	99.3	99.6	99.4	99.8	99.4	99.5	99.6	99.8
FOM	k_{FOM}, $g^{n-1}/s^m g^{n-1}$	0.039	0.045	0.053	0.062	0.061	0.086	0.121	0.210	0.085	0.120	0.161	0.267
	n_{FOM}	1.10	1.01	1.01	1.01	1.01	1.01	1.33	1.01	1.07	1.04	1.16	1.01
	m_{FOM}	1.35	1.32	1.29	1.26	1.35	1.23	1.28	1.10	1.40	1.32	1.29	1.203
	ARE%	0.407	0.446	0.323	0.282	0.248	0.145	0.357	0.105	0.329	0.295	0.280	0.169

APPENDIX C

Table C- 2: Pseudo first order (P1O), pseudo second order (P2O), Elovich, Avrami and fractional order adsorption rate model parameters when fitted to the experimental adsorption rate data of CQ30P at 40, 55, 70 and 85 °C and an inlet CO_2 concentration of 5, 15 and 25 vol%.

Sample	Parameter	5 vol% CO_2				15 vol% CO_2				25 vol% CO_2			
		40 °C	55 °C	70 °C	85 °C	40 °C	55 °C	70 °C	85 °C	40 °C	55 °C	70 °C	85 °C
P1O	k_1, *l/s*	0.117	0.121	0.138	0.154	0.169	0.191	0.230	0.299	0.220	0.244	0.301	0.331
	ARE%	1.08	0.970	0.763	0.895	1.14	0.57	0.674	0.312	0.806	0.582	0.363	0.222
	QOF%	97.9	98.2	98.4	98.3	97.8	99.0	99.0	99.6	98.5	99.0	99.5	99.7
P2O	k_2, *mmol/g.s*	0.290	0.301	0.357	0.388	0.429	0.492	0.614	0.825	0.574	0.646	0.825	0.942
	ARE%	6.88	6.68	6.44	5.94	5.93	4.98	4.61	3.41	4.87	4.28	3.40	3.15
Elovich	α	0.732	0.82	1.32	2.09	3.14	6.66	25.43	111.4	16.5	33.5	139.2	166
	β	5.39	5.53	6.08	6.59	7.04	7.91	9.38	11.00	8.90	9.69	11.2	11.4
	ARE%	6.88	6.79	6.61	6.67	6.84	6.01	5.73	4.92	5.97	5.48	4.85	4.89
Avrami	k_A, *l/s*	0.113	0.117	0.133	0.147	0.160	0.184	0.219	0.291	0.208	0.233	0.290	0.323
	b	1.21	1.19	1.21	1.27	1.38	1.21	1.26	1.12	1.38	1.30	1.16	1.10
	ARE%	0.135	0.136	0.246	0.181	0.167	0.105	0.186	0.193	0.132	0.163	0.217	0.122
	QOF%	99.5	99.7	99.6	99.7	99.6	99.9	99.7	99.8	97.2	98.0	98.5	99.8
FOM	k_{FOM}, $g^{n-1}/s^m g^{n-1}$	0.083	0.092	0.104	0.112	0.109	0.156	0.186	0.282	0.000	0.000	0.000	0.319
	n_{FOM}	1.10	1.01	1.07	1.01	1.01	1.04	1.01	1.01	20.87	20.87	46.82	1.01
	m_{FOM}	1.28	1.20	1.25	1.27	1.39	1.23	1.27	1.13	26.07	27.45	58.45	1.106
	ARE%	0.282	0.150	0.218	0.184	0.173	0.091	0.192	0.194	2.059	1.562	1.385	0.124

Table C- 3: Pseudo first order (P1O), pseudo second order (P2O), Elovich, Avrami and fractional order adsorption rate model parameters when fitted to the experimental adsorption rate data of CQ650 at 40, 55, 70 and 85 °C and an inlet CO_2 concentration of 5, 15 and 25 vol%.

Sample	Parameter	5 vol% CO_2				15 vol% CO_2				25 vol% CO_2			
		40 °C	55 °C	70 °C	85 °C	40 °C	55 °C	70 °C	85 °C	40 °C	55 °C	70 °C	85 °C
P1O	k_1, l/s	0.113	0.136	0.141	0.157	0.148	0.166	0.180	0.212	0.221	0.246	0.286	0.327
	ARE%	1.34	0.960	0.782	0.470	1.14	1.20	0.913	0.977	0.745	0.530	0.350	0.320
	QOF%	96.9	98.0	98.2	99.0	97.6	97.6	98.3	98.4	98.7	99.1	99.5	99.6
P2O	k_2, $mmol/g.s$	0.274	0.338	0.363	0.396	0.369	0.418	0.460	0.554	0.572	0.647	0.775	0.926
	ARE%	7.21	6.33	6.38	5.31	6.31	6.08	5.49	5.14	4.64	4.14	3.56	2.75
Elovich	α	0.617	1.22	1.39	2.38	1.67	2.78	4.64	13.0	16.7	36.2	88.1	154
	β	5.19	5.98	6.14	6.76	6.33	6.90	7.49	8.63	8.94	9.79	10.7	11.3
	ARE%	7.16	6.84	6.63	6.06	7.00	6.94	6.48	6.25	5.72	5.32	4.97	4.44
Avrami	k_A, l/s	0.109	0.131	0.136	0.154	0.141	0.156	0.171	0.199	0.211	0.236	0.277	0.342
	b	1.32	1.26	1.23	1.13	1.37	1.41	1.32	1.37	1.33	1.26	1.17	0.87
	ARE%	0.482	0.208	0.365	0.376	0.357	0.231	0.121	0.234	0.273	0.218	0.205	0.129
	QOF%	99.2	99.7	99.5	99.7	99.4	99.5	99.7	99.6	99.7	99.8	99.8	99.8
FOM	k_{FOM}, $g^{n-1}/s^m g^{n-1}$	0.065	0.095	0.099	0.132	0.093	0.102	0.124	0.150	0.167	0.207	0.272	0.344
	n_{FOM}	1.15	1.07	1.20	1.27	1.02	1.01	1.01	1.01	1.06	1.16	1.19	1.01
	m_{FOM}	1.43	1.31	1.38	1.33	1.39	1.42	1.36	1.38	1.37	1.38	1.32	0.877
	ARE%	0.379	0.168	0.246	0.202	0.355	0.235	0.112	0.241	0.263	0.186	0.169	0.130

Table C- 4: Pseudo first order (P1O), pseudo second order (P2O), Elovich, Avrami and fractional order adsorption rate model parameters when fitted to the experimental adsorption rate data of CQ650 at 40, 55, 70 and 85 °C and an inlet CO_2 concentration of 5, 15 and 25 vol%.

Sample	Parameter	5 vol% CO_2				15 vol% CO_2				25 vol% CO_2			
		40 °C	55 °C	70 °C	85 °C	40 °C	55 °C	70 °C	85 °C	40 °C	55 °C	70 °C	85 °C
P1O	k_1, *1/s*	0.082	0.079	0.091	0.105	0.138	0.156	0.156	0.170	0.147	0.244	0.228	0.265
	ARE%	2.00	1.313	1.464	0.892	0.77	0.70	0.257	0.395	1.040	1.129	0.445	0.402
	QOF%	95.7	97.0	96.8	98.1	98.5	98.7	99.5	99.4	97.8	97.3	99.3	99.5
P2O	k_2, *mmol/g.s*	0.192	0.186	0.248	0.253	0.345	0.396	0.397	0.436	0.364	0.646	0.599	0.710
	ARE%	8.68	8.02	9.09	6.88	6.06	5.70	5.20	5.02	6.15	4.74	4.13	3.28
Elovich	α	0.244	0.24	0.34	0.52	1.36	2.31	2.45	3.7	1.6	33.5	22.9	61
	β	4.11	4.11	4.50	5.02	6.12	6.71	6.80	7.28	6.31	9.69	9.3	10.4
	ARE%	7.10	6.33	6.90	6.48	6.54	6.43	5.89	5.83	6.80	5.79	5.19	4.51
Avrami	k_A, *1/s*	0.078	0.077	0.088	0.102	0.134	0.151	0.154	0.167	0.140	0.180	0.223	0.269
	b	1.30	1.19	1.26	1.17	1.20	1.20	1.07	1.10	1.32	1.32	1.13	0.95
	ARE%	0.298	0.329	0.474	0.504	0.244	0.146	0.196	0.249	0.394	0.148	0.312	0.364
	QOF%	99.1	99.4	99.1	99.2	99.6	99.7	99.7	99.6	99.4	96.1	97.7	99.6
FOM	k_{FOM}, $g^{n-1}/s^m g^{n-1}$	0.046	0.054	0.058	0.076	0.108	0.124	0.144	0.154	0.098	0.000	0.000	0.296
	n_{FOM}	1.01	1.08	1.01	1.14	1.01	1.01	1.09	1.01	1.04	20.87	36.96	1.23
	m_{FOM}	1.31	1.25	1.27	1.27	1.20	1.20	1.13	1.10	1.35	27.45	44.59	1.108
	ARE%	0.298	0.265	0.472	0.406	0.243	0.147	0.147	0.245	0.385	2.357	1.791	0.297

C-3.   EXPERIMENTAL ADSORPTION RATE REPEATABILITY AND REPRODUCIBILITY STUDY

The adsorption rate experimental error analysis was performed on the CQ006, CQ650 and PCX1 adsorbent samples at 40, 55 and 70 °C and 15, 5 and 15 vol% CO_2 inlet, respectively, with a 95% confidence interval. The experimental adsorption rate error analysis is shown in Figure C- 6, Figure C- 7 and Figure C- 8, with the tabulated data given in Table C- 5, Table C- 6 and Table C- 7. The total experimental error for CQ006 at 40 $°C$ and 15 vol% CO2 was determined to be 12%. The experimental error determined for CQ650 at 55 $°C$ and 5 vol% was determined to be 12.8%. An experimental error of 4.1% was calculated for PCX1 at 70 °C and 15 vol% CO_2.
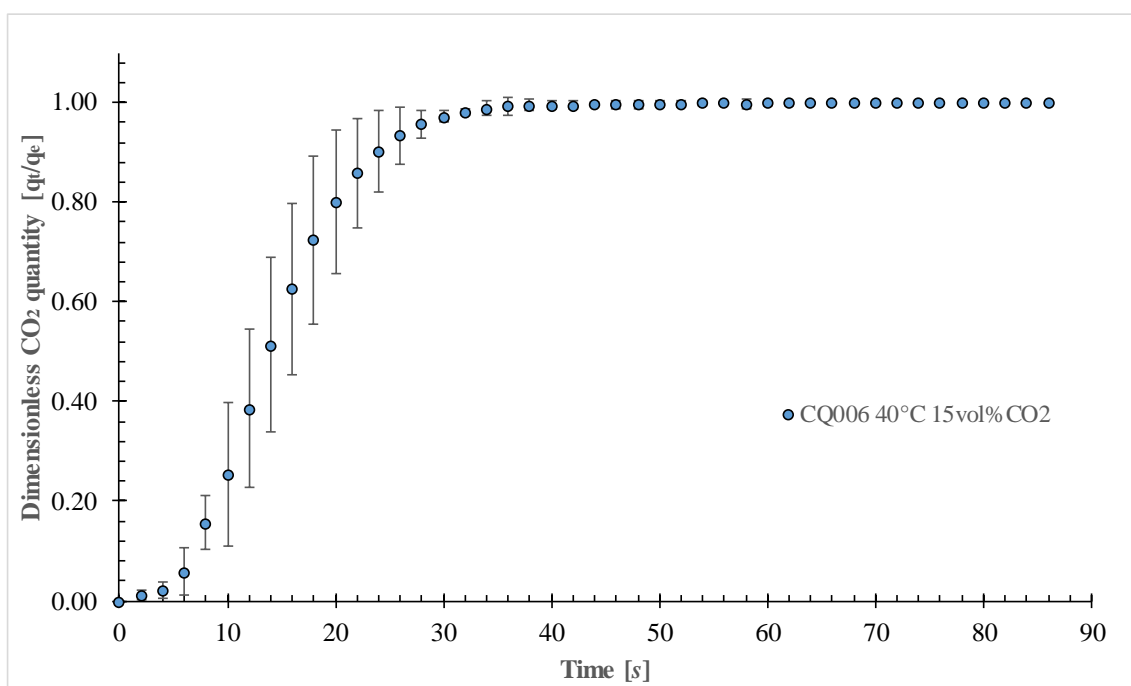

Figure C- 6: Experimental adsorption rate error analysis done on CQ006 at 40 °C and 15 vol% CO_2.
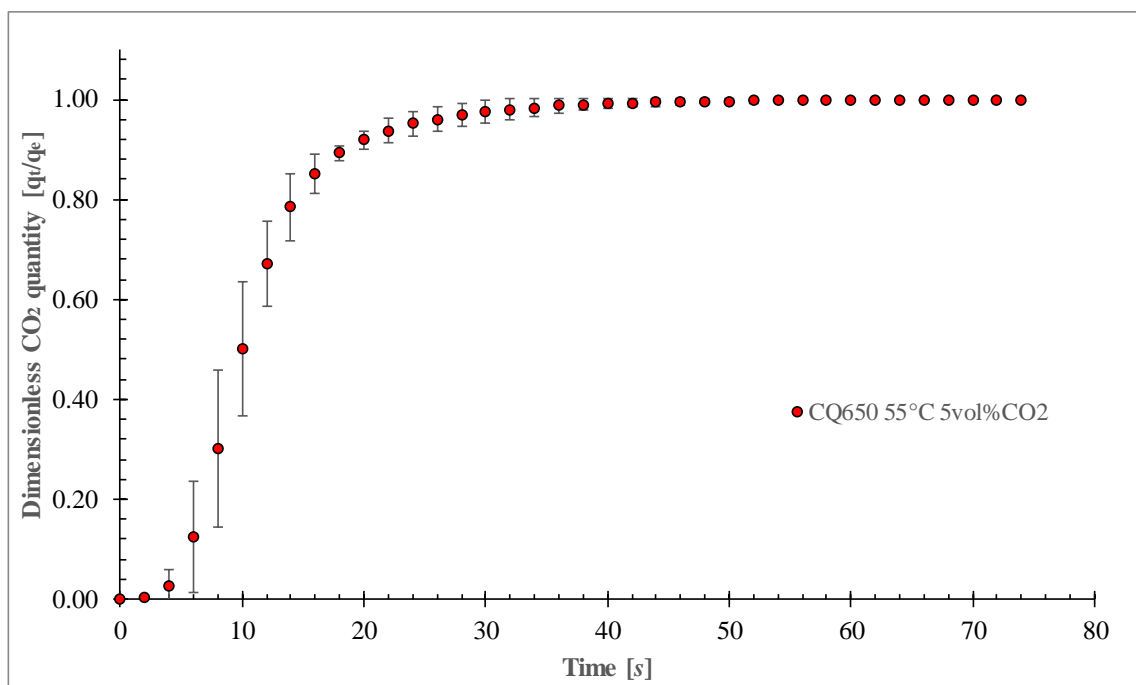
Figure C- 7: Experimental adsorption rate error analysis done on CQ006 at 55 °C and 5 vol% CO_2.
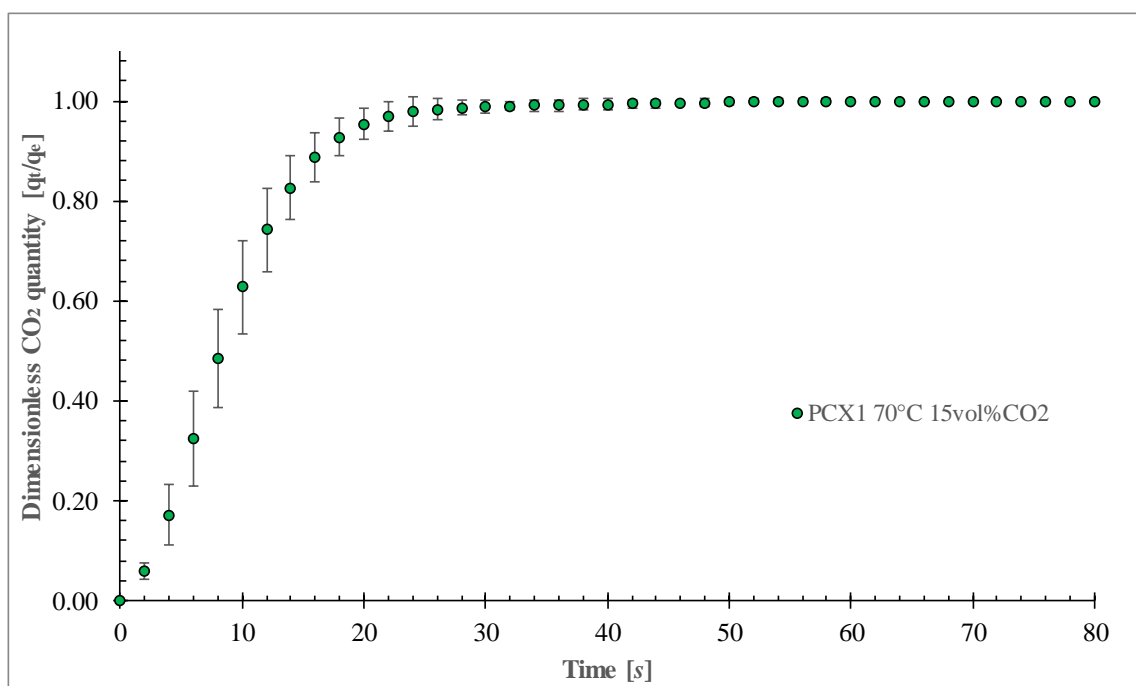

Figure C- 8: Experimental adsorption rate error analysis done on CQ006 at 70 °C and 15 vol% CO_2.

Table C- 5: Experimental adsorption rate error analysis done on CQ006 at 40 °C and 15 vol% CO_2.

Time [s]	Run 1 (qt/qe)	Run 2 (qt/qe)	Run 3 (qt/qe)	Avg ads kinetics	Std dev	Avg dev	Conf int	% Expt error	Expt error	Final data		
0	0.00	0.00	0.00	0.0	0.00	0.00	0.00	0.0	0.0	0.00	±	0.00
2	0.01	0.01	0.01	0.0	0.00	0.00	4.30	84.2	0.0	0.01	±	0.01
4	0.02	0.02	0.02	0.0	0.00	0.00	4.30	80.2	0.0	0.02	±	0.02
6	0.05	0.06	0.07	0.1	0.01	0.01	4.30	81.5	0.0	0.06	±	0.05
8	0.16	0.14	0.17	0.2	0.01	0.01	4.30	34.6	0.1	0.16	±	0.05
10	0.21	0.25	0.30	0.3	0.03	0.03	4.30	57.2	0.1	0.25	±	0.15
12	0.35	0.37	0.44	0.4	0.04	0.03	4.30	41.4	0.2	0.39	±	0.16
14	0.49	0.48	0.57	0.5	0.04	0.04	4.30	34.1	0.2	0.51	±	0.18
16	0.62	0.58	0.68	0.6	0.04	0.04	4.30	27.6	0.2	0.63	±	0.17
18	0.72	0.68	0.77	0.7	0.04	0.03	4.30	23.3	0.2	0.72	±	0.17
20	0.80	0.76	0.84	0.8	0.03	0.03	4.30	18.1	0.1	0.80	±	0.15
22	0.86	0.82	0.89	0.9	0.03	0.02	4.30	12.7	0.1	0.86	±	0.11
24	0.91	0.88	0.92	0.9	0.02	0.02	4.30	9.0	0.1	0.90	±	0.08
26	0.94	0.92	0.95	0.9	0.01	0.01	4.30	6.1	0.1	0.93	±	0.06
28	0.96	0.95	0.96	1.0	0.01	0.01	4.30	3.0	0.0	0.96	±	0.03
30	0.97	0.97	0.98	1.0	0.00	0.00	4.30	1.2	0.0	0.97	±	0.01
32	0.98	0.98	0.98	1.0	0.00	0.00	4.30	0.7	0.0	0.98	±	0.01
34	0.99	0.99	0.99	1.0	0.00	0.00	4.30	1.4	0.0	0.99	±	0.01
36	0.99	1.00	0.99	1.0	0.00	0.00	4.30	1.7	0.0	0.99	±	0.02
38	0.99	1.00	0.99	1.0	0.00	0.00	4.30	1.2	0.0	0.99	±	0.01
40	0.99	1.00	0.99	1.0	0.00	0.00	4.30	0.7	0.0	1.00	±	0.01
42	0.99	1.00	0.99	1.0	0.00	0.00	4.30	0.7	0.0	1.00	±	0.01
44	1.00	1.00	1.00	1.0	0.00	0.00	4.30	0.4	0.0	1.00	±	0.00
46	1.00	0.99	1.00	1.0	0.00	0.00	4.30	0.9	0.0	1.00	±	0.01
48	1.00	0.99	1.00	1.0	0.00	0.00	4.30	0.9	0.0	1.00	±	0.01
50	1.00	1.00	1.00	1.0	0.00	0.00	4.30	0.6	0.0	1.00	±	0.01
52	1.00	1.00	1.00	1.0	0.00	0.00	4.30	0.6	0.0	1.00	±	0.01
54	1.00	1.00	1.00	1.0	0.00	0.00	4.30	0.6	0.0	1.00	±	0.01
56	1.00	1.00	1.00	1.0	0.00	0.00	4.30	0.0	0.0	1.00	±	0.00
58	1.00	1.00	1.00	1.0	0.00	0.00	4.30	1.0	0.0	1.00	±	0.01
60	1.00	1.00	1.00	1.0	0.00	0.00	4.30	0.5	0.0	1.00	±	0.00
62	1.00	1.00	1.00	1.0	0.00	0.00	4.30	0.5	0.0	1.00	±	0.00
64	1.00	1.00	1.00	1.0	0.00	0.00	4.30	0.0	0.0	1.00	±	0.00
66	1.00	1.00	1.00	1.0	0.00	0.00	4.30	0.0	0.0	1.00	±	0.00
68	1.00	1.00	1.00	1.0	0.00	0.00	4.30	0.0	0.0	1.00	±	0.00
70	1.00	1.00	1.00	1.0	0.00	0.00	4.30	0.0	0.0	1.00	±	0.00
72	1.00	1.00	1.00	1.0	0.00	0.00	4.30	0.0	0.0	1.00	±	0.00
74	1.00	1.00	1.00	1.0	0.00	0.00	4.30	0.0	0.0	1.00	±	0.00
76	1.00	1.00	1.00	1.0	0.00	0.00	4.30	0.0	0.0	1.00	±	0.00
78	1.00	1.00	1.00	1.0	0.00	0.00	4.30	0.0	0.0	1.00	±	0.00
80	1.00	1.00	1.00	1.0	0.00	0.00	4.30	0.0	0.0	1.00	±	0.00

12.0

Table C- 6: Experimental adsorption rate error analysis done on CQ650 at 55 °C and 5 vol% CO_2.

Time [s]	Run 1 (qt/qe)	Run 2 (qt/qe)	Run 3 (qt/qe)	Run 4 (qt/qe)	Avg ads kinetics	Std dev	Avg dev	Conf int	% Expt error	Expt error	Final data		
0	0.00	0.00	0.00	0.00	0.0	0.00	0.00	3.18	0.0	0.0	**0.00**	±	**0.00**
2	0.00	0.00	0.00	0.00	0.0	0.00	0.00	3.18	141.6	0.0	**0.00**	±	**0.00**
4	0.04	0.02	0.04	0.01	0.0	0.01	0.01	3.18	121.2	0.0	**0.03**	±	**0.03**
6	0.15	0.11	0.16	0.07	0.1	0.04	0.03	3.18	89.3	0.1	**0.12**	±	**0.11**
8	0.34	0.30	0.35	0.22	0.3	0.05	0.04	3.18	52.3	0.2	**0.30**	±	**0.16**
10	0.54	0.50	0.53	0.43	0.5	0.04	0.03	3.18	26.8	0.1	**0.50**	±	**0.13**
12	0.71	0.66	0.69	0.64	0.7	0.03	0.02	3.18	12.6	0.1	**0.67**	±	**0.08**
14	0.81	0.76	0.80	0.77	0.8	0.02	0.02	3.18	8.5	0.1	**0.78**	±	**0.07**
16	0.87	0.84	0.86	0.84	0.9	0.01	0.01	3.18	4.6	0.0	**0.85**	±	**0.04**
18	0.90	0.89	0.89	0.89	0.9	0.00	0.00	3.18	1.5	0.0	**0.89**	±	**0.01**
20	0.92	0.93	0.92	0.91	0.9	0.01	0.00	3.18	2.0	0.0	**0.92**	±	**0.02**
22	0.94	0.95	0.93	0.93	0.9	0.01	0.01	3.18	2.4	0.0	**0.94**	±	**0.02**
24	0.95	0.96	0.95	0.95	1.0	0.01	0.01	3.18	2.6	0.0	**0.95**	±	**0.02**
26	0.95	0.97	0.96	0.96	1.0	0.01	0.01	3.18	2.6	0.0	**0.96**	±	**0.02**
28	0.96	0.98	0.97	0.97	1.0	0.01	0.01	3.18	2.5	0.0	**0.97**	±	**0.02**
30	0.97	0.99	0.97	0.97	1.0	0.01	0.01	3.18	2.3	0.0	**0.97**	±	**0.02**
32	0.97	0.99	0.98	0.98	1.0	0.01	0.01	3.18	2.1	0.0	**0.98**	±	**0.02**
34	0.98	0.99	0.98	0.98	1.0	0.01	0.00	3.18	1.8	0.0	**0.98**	±	**0.02**
36	0.98	0.99	0.99	0.98	1.0	0.00	0.00	3.18	1.5	0.0	**0.99**	±	**0.02**
38	0.99	1.00	0.99	0.99	1.0	0.00	0.00	3.18	1.2	0.0	**0.99**	±	**0.01**
40	0.99	1.00	0.99	0.99	1.0	0.00	0.00	3.18	1.0	0.0	**0.99**	±	**0.01**
42	0.99	1.00	0.99	0.99	1.0	0.00	0.00	3.18	0.9	0.0	**0.99**	±	**0.01**
44	0.99	1.00	1.00	0.99	1.0	0.00	0.00	3.18	0.8	0.0	**0.99**	±	**0.01**
46	0.99	1.00	1.00	0.99	1.0	0.00	0.00	3.18	0.7	0.0	**1.00**	±	**0.01**
48	0.99	1.00	1.00	1.00	1.0	0.00	0.00	3.18	0.6	0.0	**1.00**	±	**0.01**
50	0.99	1.00	1.00	1.00	1.0	0.00	0.00	3.18	0.5	0.0	**1.00**	±	**0.00**
52	1.00	1.00	1.00	1.00	1.0	0.00	0.00	3.18	0.4	0.0	**1.00**	±	**0.00**
54	1.00	1.00	1.00	1.00	1.0	0.00	0.00	3.18	0.3	0.0	**1.00**	±	**0.00**
56	1.00	1.00	1.00	1.00	1.0	0.00	0.00	3.18	0.3	0.0	**1.00**	±	**0.00**
58	1.00	1.00	1.00	1.00	1.0	0.00	0.00	3.18	0.3	0.0	**1.00**	±	**0.00**
60	1.00	1.00	1.00	1.00	1.0	0.00	0.00	3.18	0.3	0.0	**1.00**	±	**0.00**
62	1.00	1.00	1.00	1.00	1.0	0.00	0.00	3.18	0.3	0.0	**1.00**	±	**0.00**
64	1.00	1.00	1.00	1.00	1.0	0.00	0.00	3.18	0.1	0.0	**1.00**	±	**0.00**
66	1.00	1.00	1.00	1.00	1.0	0.00	0.00	3.18	0.1	0.0	**1.00**	±	**0.00**
68	1.00	1.00	1.00	1.00	1.0	0.00	0.00	3.18	0.1	0.0	**1.00**	±	**0.00**
70	1.00	1.00	1.00	1.00	1.0	0.00	0.00	3.18	0.1	0.0	**1.00**	±	**0.00**
72	1.00	1.00	1.00	1.00	1.0	0.00	0.00	3.18	0.2	0.0	**1.00**	±	**0.00**
74	1.00	1.00	1.00	1.00	1.0	0.00	0.00	3.18	0.0	0.0	**1.00**	±	**0.00**

12.8

Table C- 7: Experimental adsorption rate error analysis done on CQ650 at 70 °C and 15 vol% CO_2.

Time [s]	Run 1 (q_t/q_e)	Run 2 (q_t/q_e)	Run 3 (q_t/q_e)	Run 4 (q_t/q_e)	Avg ads kinetics	Std dev	Avg dev.	Conf int	% Expt error	Expt error	Final data		
0	0.00	0.00	0.00	0.00	0.0	0.00	0.00	0.00	0.0	0.0	0.00	±	0.00
2	0.05	0.06	0.06	0.06	0.1	0.00	0.00	3.18	26.4	0.0	0.06	±	0.02
4	0.16	0.15	0.20	0.18	0.2	0.02	0.02	3.18	35.8	0.1	0.17	±	0.06
6	0.32	0.28	0.36	0.34	0.3	0.03	0.03	3.18	29.0	0.1	0.32	±	0.09
8	0.48	0.44	0.52	0.51	0.5	0.03	0.03	3.18	20.1	0.1	0.48	±	0.10
10	0.62	0.58	0.66	0.65	0.6	0.03	0.02	3.18	14.8	0.1	0.63	±	0.09
12	0.74	0.70	0.77	0.76	0.7	0.03	0.02	3.18	11.1	0.1	0.74	±	0.08
14	0.82	0.80	0.84	0.85	0.8	0.02	0.02	3.18	7.8	0.1	0.83	±	0.06
16	0.88	0.86	0.90	0.90	0.9	0.02	0.01	3.18	5.6	0.0	0.89	±	0.05
18	0.92	0.91	0.94	0.94	0.9	0.01	0.01	3.18	4.2	0.0	0.93	±	0.04
20	0.94	0.94	0.97	0.96	1.0	0.01	0.01	3.18	3.1	0.0	0.95	±	0.03
22	0.96	0.96	0.98	0.97	1.0	0.01	0.01	3.18	3.0	0.0	0.97	±	0.03
24	0.97	0.98	0.99	0.98	1.0	0.01	0.01	3.18	2.9	0.0	0.98	±	0.03
26	0.97	0.98	0.99	0.99	1.0	0.01	0.01	3.18	2.1	0.0	0.98	±	0.02
28	0.98	0.99	0.99	0.99	1.0	0.00	0.00	3.18	1.4	0.0	0.99	±	0.01
30	0.98	0.99	0.99	0.99	1.0	0.00	0.00	3.18	1.3	0.0	0.99	±	0.01
32	0.99	0.99	0.99	0.99	1.0	0.00	0.00	3.18	0.7	0.0	0.99	±	0.01
34	0.99	0.99	0.99	1.00	1.0	0.00	0.00	3.18	1.2	0.0	0.99	±	0.01
36	0.99	0.99	0.99	1.00	1.0	0.00	0.00	3.18	1.2	0.0	0.99	±	0.01
38	1.00	0.99	0.99	1.00	1.0	0.00	0.00	3.18	1.3	0.0	0.99	±	0.01
40	1.00	0.99	0.99	1.00	1.0	0.00	0.00	3.18	1.3	0.0	0.99	±	0.01
42	1.00	0.99	0.99	1.00	1.0	0.00	0.00	3.18	0.9	0.0	0.99	±	0.01
44	1.00	0.99	0.99	1.00	1.0	0.00	0.00	3.18	0.9	0.0	0.99	±	0.01
46	1.00	0.99	1.00	1.00	1.0	0.00	0.00	3.18	0.4	0.0	1.00	±	0.00
48	1.00	0.99	1.00	1.00	1.0	0.00	0.00	3.18	0.7	0.0	1.00	±	0.01
50	1.00	1.00	1.00	1.00	1.0	0.00	0.00	3.18	0.5	0.0	1.00	±	0.00
52	1.00	1.00	1.00	1.00	1.0	0.00	0.00	3.18	0.4	0.0	1.00	±	0.00
54	1.00	1.00	1.00	1.00	1.0	0.00	0.00	3.18	0.4	0.0	1.00	±	0.00
56	1.00	1.00	1.00	1.00	1.0	0.00	0.00	3.18	0.4	0.0	1.00	±	0.00
58	1.00	1.00	1.00	1.00	1.0	0.00	0.00	3.18	0.4	0.0	1.00	±	0.00
60	1.00	1.00	1.00	1.00	1.0	0.00	0.00	3.18	0.0	0.0	1.00	±	0.00
62	1.00	1.00	1.00	1.00	1.0	0.00	0.00	3.18	0.0	0.0	1.00	±	0.00
64	1.00	1.00	1.00	1.00	1.0	0.00	0.00	3.18	0.0	0.0	1.00	±	0.00
66	1.00	1.00	1.00	1.00	1.0	0.00	0.00	3.18	0.0	0.0	1.00	±	0.00
68	1.00	1.00	1.00	1.00	1.0	0.00	0.00	3.18	0.0	0.0	1.00	±	0.00
70	1.00	1.00	1.00	1.00	1.0	0.00	0.00	3.18	0.0	0.0	1.00	±	0.00
72	1.00	1.00	1.00	1.00	1.0	0.00	0.00	3.18	0.0	0.0	1.00	±	0.00
74	1.00	1.00	1.00	1.00	1.0	0.00	0.00	3.18	0.0	0.0	1.00	±	0.00

	4.1

C-4.   EXPERIMENTAL: ADSORPTION KINETIC RATE DATA

The adsorption rate data obtained from the experimental fixed bed reactor setup is given in Figure C- 9, Figure C- 11 and Figure C- 10 as the absolute CO_2 adsorbed quantity (q_t) versus time plots.
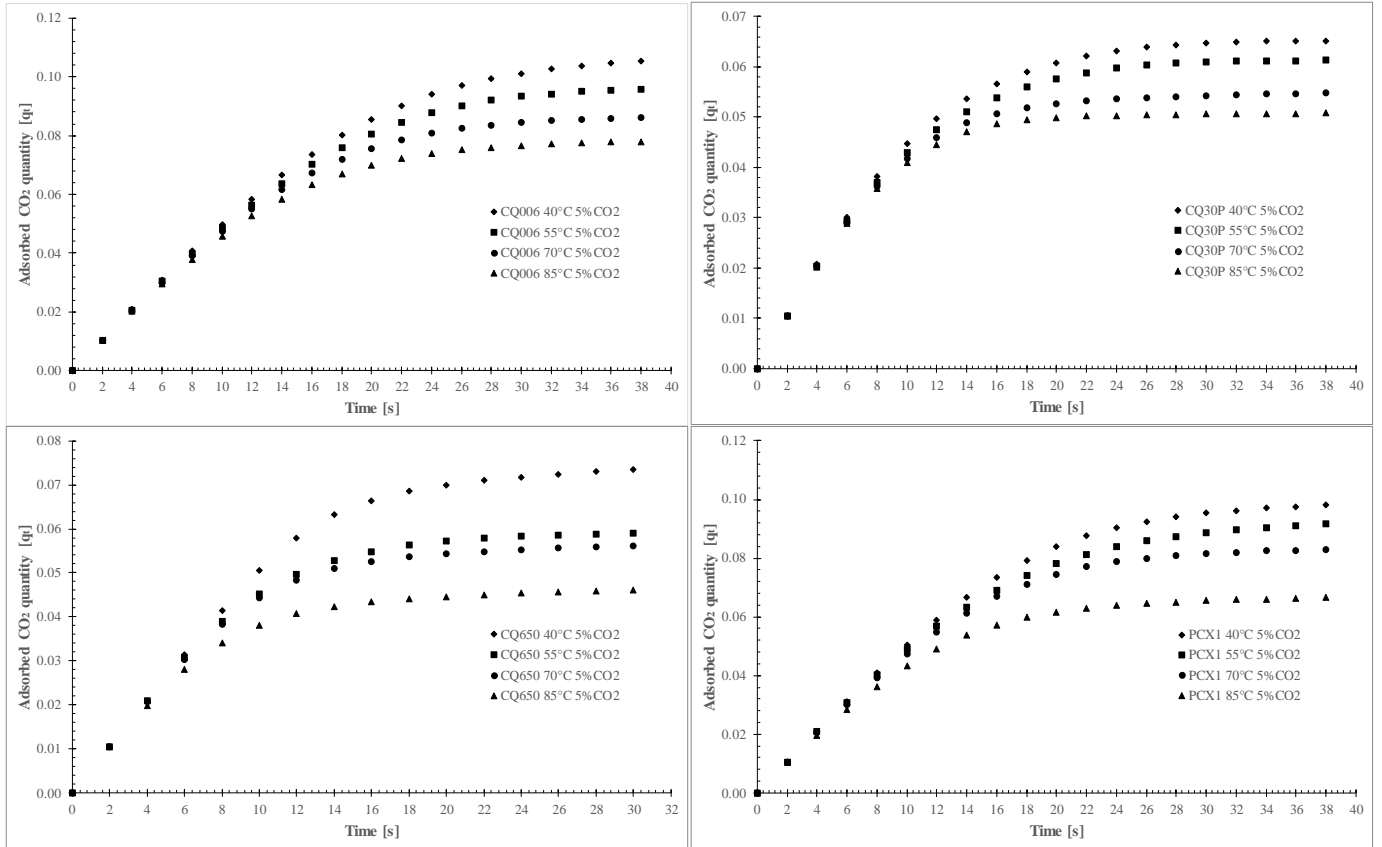

Figure C- 9: Absolute CO_2 quantity adsorbed (q_t in mmol/g) at 40, 55, 70 and 85 °C for CQ006, CQ30P, CQ650 and PCX1 at a fixed inlet CO_2 concentration of 5 vol% and fixed flow rate of 250 cm³/min.
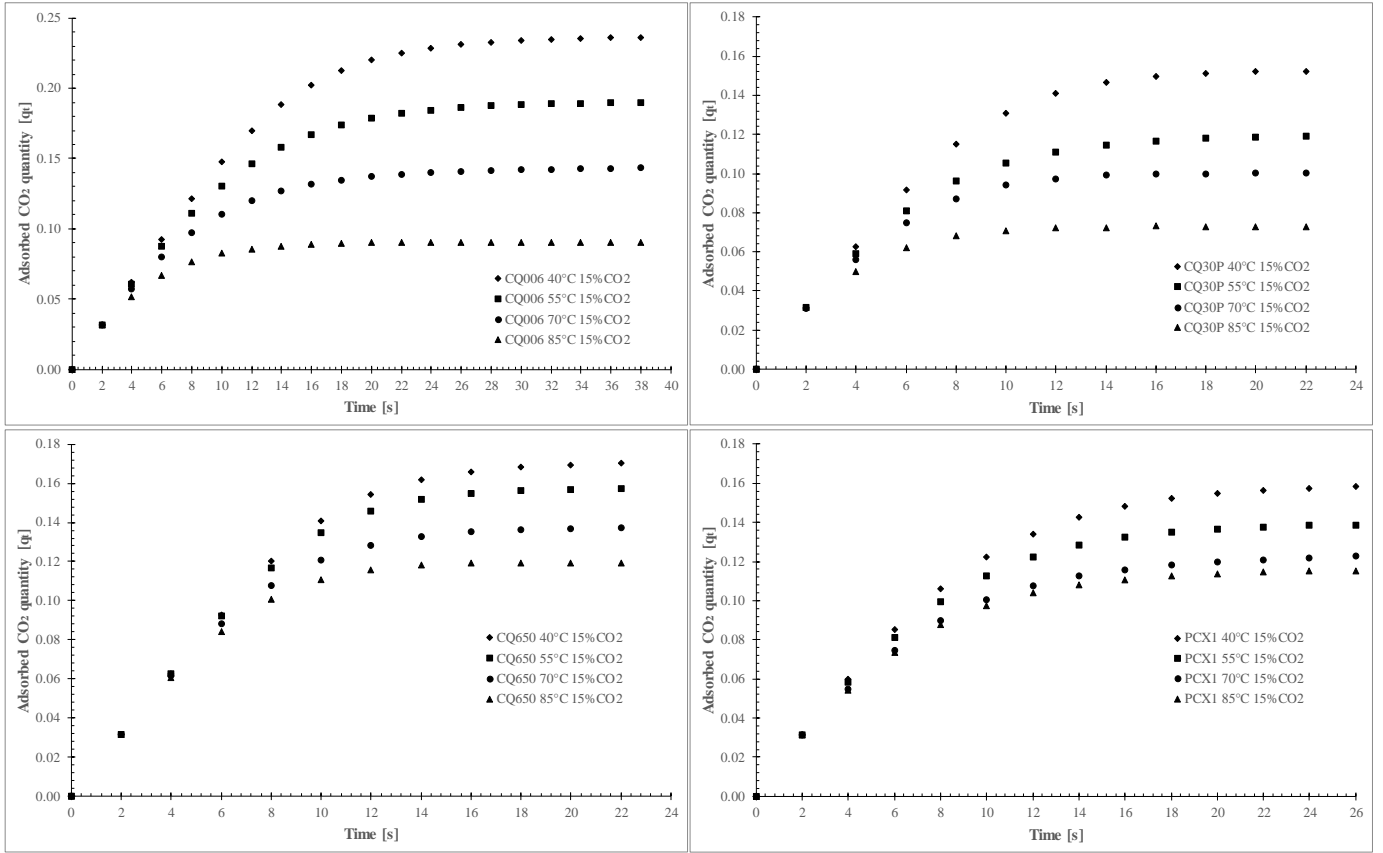
Figure C- 10: Absolute CO_2 quantity adsorbed (q_t in mmol/g) at 40, 55, 70 and 85 °C for CQ006, CQ30P, CQ650 and PCX1 at a fixed inlet CO_2 concentration of 15 vol% and fixed flow rate of 250 cm^3/min.
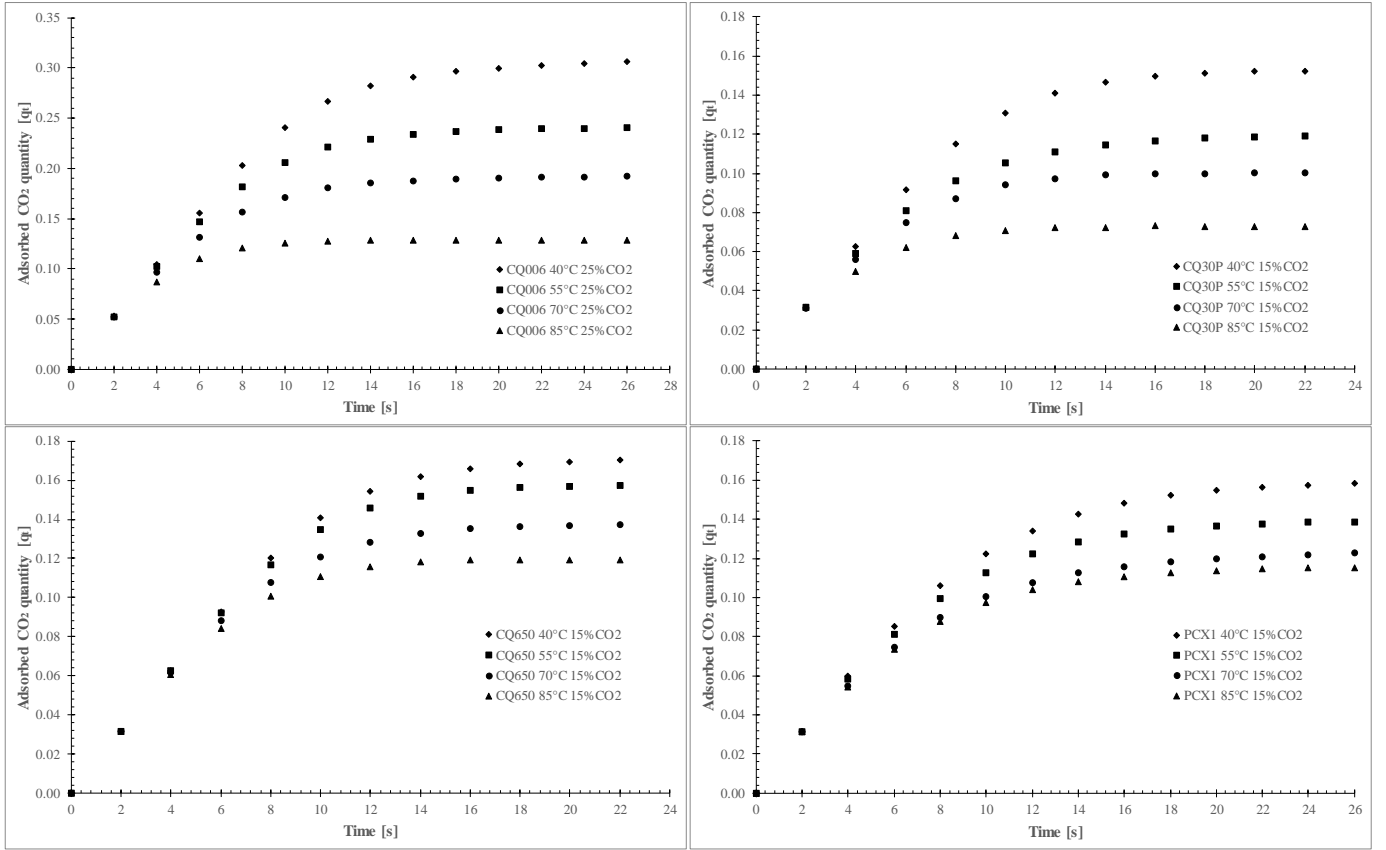
Figure C- 11: Absolute CO_2 quantity adsorbed (q_t in mmol/g) at 40, 55, 70 and 85 °C for CQ006, CQ30P, CQ650 and PCX1 at a fixed inlet CO_2 concentration of 25 vol% and fixed flow rate of 250 cm^3/min.